UNIVERSIDADE ESTADUAL DE CAMPINAS

INSTITUTO DE QUÍMICA

MANAZAEL ZULIANI JORA

pH-responsive wormlike micelle and its application in acid stimulation in oilfield exploration

Micelas gigantes responsivas a pH e sua aplicação na etapa de estimulação ácida na produção de petróleo

CAMPINAS

2020

Manazael Zuliani Jora

pH-responsive wormlike micelle and its application in acid stimulation in oilfield exploration

Micelas gigantes responsivas a pH e sua aplicação na etapa de estimulação ácida na produção de petróleo

Tese de Doutorado apresentada ao Instituto de Química da Universidade Estadual de Campinas como parte dos requisites exigidos para a obtenção do título de Doutor em Ciências.

Doctor's Thesis presented to the Institute of Chemistry of the University of Campinas as part of the requirements to obtain the title of Doctor in Sciences.

Supervisor: Dr. Edvaldo Sabadini

O arquivo digital corresponde à versão final da Tese defendida pelo aluno Manazael Zuliani Jora e orientada pelo Prof. Dr. Edvaldo Sabadini.

CAMPINAS

2020

Ficha catalográfica
Universidade Estadual de Campinas
Biblioteca do Instituto de Química
Simone Luiz Alves - CRB 8/9094

J75p

Jora, Manazael Zuliani, 1990-
pH-responsive wormlike micelle and its application in acid stimulation in oilfield exploration / Manazael Zuliani Jora. – Campinas, SP : [s.n.], 2020.

Orientador: Edvaldo Sabadini.
Tese (doutorado) – Universidade Estadual de Campinas, Instituto de Química.

1. Micelas gigantes. 2. Estimulação ácida. 3. Acidificação matricial. 4. Calorimetria de titulação isotérmica. 5. Reologia. 6. Colóides. I. Sabadini, Edvaldo, 1962-. II. Universidade Estadual de Campinas. Instituto de Química. III. Título.

Informações para Biblioteca Digital

Título em outro idioma: Micelas gigantes responsivas a pH e sua aplicação na etapa de estimulação ácida na produção de petróleo
Palavras-chave em inglês:
Giant micelles
Acid stimulation
Matrix acidizing
Isothermal titration calorimetry
Rheology
Colloids
Área de concentração: Físico-Química
Titulação: Doutor em Ciências
Banca examinadora:
Edvaldo Sabadini [Orientador]
Watson Loh
Paulo de Tarso Vieira e Rosa
Guilherme Augusto Ferreira
Tito José Bonagamba
Data de defesa: 29-10-2020
Programa de Pós-Graduação: Química

Identificação e informações acadêmicas do(a) aluno(a)
- ORCID do autor: https://orcid.org/0000-0002-4680-4691
- Currículo Lattes do autor: http://lattes.cnpq.br/0094513251232643

Banca examinadora

Prof. Dr. Edvaldo Sabadini (Orientador)

Prof. Dr. Watson Loh (Universidade Estadual de Campinas)

Prof. Dr. Paulo de Tarso Vieira e Rosa (Universidade Estadual de Campinas)

Prof. Dr. Guilherme Augusto Ferreira (Universidade Federal da Bahia)

Prof. Dr. Tito José Bonagamba (Universidade de São Paulo)

A ata da defesa assinada pelos membros da Comissão Examinadora, consta no SIGA/Sistema de Fluxo de Dissertação/Tese e na Secretaria do Programa da Unidade.

Este exemplar corresponde à redação final da Tese de Doutorado defendida pelo aluno **Manazael Zuliani Jora**, aprovada pela Comissão Julgadora em 29 de outubro de 2020.

Acknowledgements

I would like to initially thank my wife, Monize Helena Bini, who accompanied and supported me throughout my school education, going through high school, graduation, master's degree and, now, my doctorate. Thank you for being this wonderful person, companion, comprehensive, loving, passionate, and especially, friend, for more than a decade that we are together. I love you.

I would also like to thank my parents, Nilson Jora and Celia Silvana Zuliani Jora, and my father-in-law and my mother-in-law, who are like parents to me, Oswaldo Bini and Maria Helena Bini, for all the support of all kinds that they gave me. Unfortunately, my parents did not have the opportunity to complete even the elementary school, but they always worked very hard so that my brother and I had the study opportunities that they did not have. I will be forever grateful to you for that.

To my supervisor, Prof. Dr. Edvaldo Sabadini, for the opportunity to develop the project under his supervising and for the friendship we have developed during these almost seven years that we have worked together.

To my friends Renato Nunes de Souza and Matheus da Silva Barbosa who are also researchers in the PETROBRAS project. Much of the results that I will present in this thesis were planned, carried out and the results discussed with their help. Without their help, I am sure that most of these results, published articles and patent application would not have been made in time. The friendship we have, and the memory of our excellent teamwork is one of the things I want to keep in mind forever.

To the collaborators, Prof. Dr. Tito Bonagamba (and students) and Prof. Dr. Fernando Paiva (and students) from the University of São Paulo, for all their support with x-ray tomography and nuclear magnetic resonance. The works in programming, x-ray tomography, NMR and MRI that you do are really impressive, and part of our collaborations will be presented in at least two of the works in this thesis.

And finally to UNICAMP and the Chemistry Institute for the infrastructure, PETROBRAS for the scholarship (2015/00103-0) and the technical interlocutor of our project, Carlos Speglich, for all the help and explanations of the acid stimulation stage and for our friendship.

I also would like to thank to Conselho Nacional de Desenvolvimento Científico e Tecnológico (CNPq) for six months of scholarship (140391/2016-9) in the beginning of the program.

This study was financed in part by the Coordenação de Aperfeiçoamento de Pessoal de Nível Superior - Brasil (CAPES) - Finance Code 001

With great affection, my sincere thanks.

“All we have to decide is what to do with the time that is given us”

J.R.R. Tolkien, The Fellowship of the Ring

Resumo

Entre as complexas operações envolvidas na produção de petróleo, a acidificação matricial é uma das etapas envolvidas na recuperação avançada e tem o objetivo de aumentar a eficiência de produção de um poço produtor através da remoção de danos e aumento de permeabilidade da rocha reservatório. Este aumento de permeabilidade se baseia na reação química entre o fluido estimulante de natureza ácida e a matriz rochosa de natureza carbonácea como as que são encontradas no Polígono do Pré-Sal brasileiro. Para que o processo de estimulação seja bem sucedido, o ácido utilizado deve formar canais de alta permeabilidade na rocha reservatório conhecidos como *wormholes* cuja formação é controlada pelo fluxo do fluido estimulante injetado e a taxa de dissolução ácida do carbonato. Um dos desafios da acidificação matricial é a estimulação das regiões de menor permeabilidade natural e, para isso, existem os fluidos ácido divergentes que modulam sua viscoelasticidade de acordo com a neutralização do fluido. Fluidos contendo agregados coloidais de surfactante conhecidos como micelas gigantes (MG), podem ser formulados para modular sua viscoelasticidade de acordo com a acidez e concentrações de íons em solução e são, portanto, potenciais fluidos para serem utilizados como divergentes na etapa de estimulação de poços produtos de petróleo.

As micelas gigantes são agregados dinâmicos de grande razão de aspecto que são formados a partir de interações intermoleculares. Dependendo das condições físico-químicas do sistema, como temperatura, pH, concentração ou força-iônica, as MG podem variar seu comprimento de contorno de alguns nanômetros a dezenas de micrometros e tais mudanças causam grandes variações reológicas nos fluídos que as contêm, possibilitando a aplicação em fluidos para a estimulação ácida.

Assim, neste trabalho, foram desenvolvidos fluídos contendo MG responsivas a estímulos externos, em especial ao pH. Uma parte do projeto foi dedicada ao desenvolvimento de pesquisa fundamental, buscando entender a natureza das moléculas que poderiam gerar micelas gigantes em condições variadas. Para isto foram

feitas caracterizações reológicas, calorimétricas, entre outras, buscando correlações entre estrutura e propriedade. Com base nestes resultados, em colaboração com o Centro de Pesquisa PETROBRAS (CENPES-PETROBRAS), foram desenvolvidos fluidos, que possuem tecnologia protegida por pedido de patente que deverão ser aplicados em campo pela PETROBRAS em 2021.

Abstract

Among the complex operations involved in oil production, matrix acidification is one of the steps involved in advanced recovery and aims to increase the production efficiency of a wellbore by removing damage and increasing the permeability of the reservoir rock. This increase in permeability is based on the chemical reaction between the stimulating fluid of acidic nature and the matrix of carbonaceous nature such as those found in the Brazilian Pre-Salt Polygon. For the stimulation process to be successful, the acid used must form high permeability channels in the reservoir rock known as wormholes whose formation is controlled by the flow rate of the injected stimulating fluid and the acidic dissolution rate of the carbonate. One of the challenges of matrix acidification is the stimulation of the regions with less natural permeability and, for this, there are diverting acid fluids that modulate their viscoelasticity according to the neutralization of the fluid. Colloidal fluids containing surfactant aggregates known as wormlike micelles (WLM), can be formulated to modulate their viscoelasticity according to acidity and ion concentrations in solution and, then, are potential fluids to be used as diverting fluids in the matrix acidizing step.

Wormlike micelles are dynamic aggregates of great aspect ratio that are formed through intermolecular interactions. Depending on the physicochemical conditions of the system, such as temperature, pH, concentration or ionic strength, WLM can vary its contour length from a few nanometers to dozens of micrometers and such changes can cause great rheological changes allowing the fluids to be used for acid stimulation.

In this thesis, fluids containing WLM responsive to external stimuli, especially pH, were e developed. Part of the project was dedicated to the development of fundamental research, seeking to understand the nature of the molecules that could generate wormlike micelles under different conditions. For this, rheological and calorimetric characterizations were made, among others, looking for the correlations between structure and properties. Based on these results, in collaboration with PETROBRAS Research Center (CENPES-PETROBRAS), diverting acid fluids were developed and had its

technology protected by a patent application whose use in the field is planned to be carried out by PETROBRAS in 2021.

List of Figures

List of Tables

Parameters and acronyms

α (Chapter 4)	=	Ionization degree
α (Section 7.7.4)	=	Regulation parameter of the inverse Laplace transform in time domain nuclear magnetic ressonance
γ (Chapter 2)	=	Surface tension
γ (Chapter 3)	=	Shear strain
$\dot{\gamma}$	=	Shear rate
γ_0	=	Maximum shear strain
$\dot{\gamma}_{critical}$	=	Critical shear rate
$\gamma_{el.}$	=	Deformation in a spring
$\gamma_{visc.}$	=	Deformation in a dashpot
δ	=	Diffusion-encoding gradient pulse width in DOSY NMR
Δ	=	Diffusion delay in DOSY NMR
$\Delta C_{p,ag}^{o}$	=	Thermal heat capacity of aggregation
ΔG_{ag}^{o}	=	Standard molar Gibbs free energy of aggregation
ΔG_{mic}^{o}	=	Standard molar Gibbs free energy of micellization
ΔH	=	Enthalpy variation
ΔH_{ag}^{o}	=	Standard molar enthalpy of aggregation
ΔH_{m}^{o}	=	Standard molar enthalpy
ΔH_{mic}^{o}	=	Standard molar enthalpy of micellization
ΔH_{tra}	=	Enthalpy of the aggregate morphology change
ΔH_{WLM}^{o}	=	Standard molar enthalpy of wormlike micelleformation
ΔS_{ag}^{o}	=	Standard molar entropy of aggregation
ΔS_{mic}^{o}	=	Standard molar entropy of micellization
η	=	Viscosity
η_0	=	Zero-shear viscosity
$\eta_{ap}(\dot{\gamma})$	=	Apparent viscosity
$\lvert\eta^*\rvert$	=	Complex viscosity

θ (Eq. 8)	=	Angle of rotation
θ (Eq. 13)	=	Phase lag
θ (Section 7.4)	=	Scattering angle of the light scattering technique
κ	=	Overall dissolution rate between the acid fluid and the carbonate rock
ξ	=	Hydrodynamic correlation length or mesh-size of wormlike micelle chain
ρ_2	=	Surface relaxivity in nuclear magnetic resonance
σ	=	Shear stress
σ_0	=	Maximum shear stress
τ	=	Interpulse time in NMR
$\tau_{b.}$	=	Breaking/recombining time of a wormlike micelle chain
$\tau_{rel.}$	=	Relaxation time
$\tau_{rep.}$	=	Reptation time
τ_y	=	Yield stress
φ	=	Volumetric fraction
ϕ	=	Surfactant weight percentage
Φ	=	Carbonate porosity
ω	=	Disturbance frequency in oscillatory shear rheology
ω_{co}	=	Cross-over frequency
∇P	=	Pressure differential

2Cl	=	2-Chlorobenzoate
2,3Cl	=	2,3-Dichlorobenzoate
2,4Cl	=	2,4-Dichlorobenzoate
2,6Cl	=	2,6-Dichlorobenzoate
3Cl	=	3-Chlorobenzoate
3,4Cl	=	3,4-Dichlorobenzoate
3PPA	=	3-Phenylpropanoic acid
4-HB	=	4-hydroxybenzoate
4Br	=	4-Bromobenzoate

4Cl	=	4-Chlorobenzoate
4F	=	4-Fluorobenzoate
4H	=	Sodium salicylate
4I	=	4-Iodobenzoate
$a_{Cl}^{micellar}$	=	Activity of the chlorobenzoate at the micellar phase
$a_{Cl}^{solution}$	=	Activity of the chlorobenzoate at the aqueous phase
A (Chapter 2)	=	Surface area
A (Chapter 3)	=	Contact area
a_0	=	Optimum head group area of the surfactant
ACA	=	4-azobenzene carboxylic acid
b	=	Kuhn length ($b = 2\ l_p$)
BA	=	Benzoic acid
CDTA	=	1,2-cyclohexane-diaminetetraacetic acid
CMC	=	Critical micelle concentration
CPMG	=	Carr-Purcell-Meiboom-Gill pulse sequence in NMR
CPP	=	Critical packing parameter
$C_{12}EO_{3\text{-}4}$	=	Polyoxyethylene dodecyl ethers
C_{12}TAC	=	Dodecyltrimethylammonium chloride
C_{12}TAB	=	Dodecyltrimethylammonium bromide
C_{14}TAB	=	Tetradecyltrimethylammonium bromide
C_{16}mimBr	=	1-hexadecyl-3-methylimidazolium bromide
C_{16}TAB	=	Hexadecyltrimethylammonium bromide
C_nDMAO	=	Alkyldimethylamine oxides
d	=	Diameter of the wormhole or the carbonate outcrop
d_{16}	=	Gradient recovery in DOSY NMR
$D_{4-halogenbenzoate,i}$	=	Self-diffusion coefficient of 4-halogenzoate at i concentration of surfactant
$D^{*}_{4-halogenbenzoate}$	=	Self-diffusion coefficient of 4-halogenbenzoate in aqueous solution
$D^{C_{14}TAB}_{4-halogenbenzoate}$	=	Self-diffusion coefficient of 4-halogenbenzoate totally incorporated at C_{14}TAB aggregate

$D_{4Cl,i}$	=	Self-diffusion coefficient of 4-chlorobenzoate at i concentration of surfactant
D_{4Cl}^{*}	=	Self-diffusion coefficient of 4-chlorobenzoate in aqueous solution
$D_{4Cl}^{C_{14}TAB}$	=	Self-diffusion coefficient of 4-chlorobenzoate totally incorporated at C_{14}TAB aggregate
D_C	=	Curvilinear diffusion constant of the colloidal chain
De	=	Deborah number
DHB	=	1,2-dihydroxybenzene
DLS	=	Dynamic light scattering
DOSY	=	Diffusion ordered spectroscopy
DP	=	Desert pink carbonate
DTPA	=	Diethylenetriaminepentaacetic acid
e	=	Euler's number
E_C	=	End-cap energy of wormlike micelle chain
E_e	=	Energy associated with the repulsion of charges of the wormlike micelle backbone
EDB	=	Edwards brown carbonate
EDTA	=	Ethylenediaminetetraacetic acid
EDW	=	Edwards white carbonate
EHAC	=	Erucylbis(hydroxyethyl)methylammonium chloride
EtP	=	Ethyl-4-hydroxybenzoate
F_{shear}	=	Shear force
f	=	Friction coefficient
G (Chapter 2)	=	Surface Gibbs free energy
G (Chapter 3)	=	Elasticity constant
G'	=	Storage modulus
$G"$	=	Dissipative modulus
G_0	=	Elastic moduli at infinity frequency of disturbance in oscillatory-shear rheology
$G"_{min}$	=	Minimum of viscous modulus in oscillatory-shear rheology
G1	=	QuoVadis first generation

G2	=	QuoVadis second generation
G3	=	QuoVadis third generation and its variations, G3 A, G3 B and G3 C
HAc	=	Acetic acid
HCl	=	Hydrochloric acid
HPD	=	High porosity dolomite
IB	=	Iodobenzene
IND	=	Indian limestone carbonate
ILT	=	Inverse Laplace transform
k	=	Carbonate permeability
k_B	=	Boltzmann constant
$k_{b.}$	=	Rate of breaking/recombining of a wormlike micelle chain
L (Chapter 1)	=	Length of the wormhole
L (Chapter 12/13)	=	Length of the carbonate plug or carbonate outcrop
$\bar{L}$	=	Contour length of wormlike micelles
l_B	=	Bjerrum length
l_e	=	Entanglement length of wormlike micelle chain
l_p	=	Persistence length of wormlike micelle chain
ℓ	=	Critical length of the surfactant hydrophobic tail
LPD	=	Low porosity dolomite
MeP	=	Methyl-4-hydroxybenzoate
MRI	=	Nuclear magnetic resonance imaging
NaOH	=	Sodium hydroxide
n_{echo}	=	Number of echoes in NMR
NaSal	=	Sodium salicylate
NaTos	=	Sodium tosylate
NS	=	Number of accumulated scans
OMBA	=	2-methoxybenzoic acid
OMCA	=	Ortho-methoxycinnamic acid
OHCA	=	O-hydroxycinnamic acid
OHPA	=	3-Hydroxyphenylpropanoic acid
P	=	Pressure

P_i (Chapter 8/9)	=	Partition coefficient of the organic salt at i concentration of surfactant
p_{19}	=	Gradient purge pulse in DOSY NMR
PA	=	Phthalic acid
PAG	=	Photoacid generator
$PhyEO_{30}$	=	Polyoxyethylene phytosteryl ether
q (Chapter 1)	=	Flow rate
q (Chapter 4)	=	Energy as heat
q_p	=	Heat transfer with constant pressure
R (Chapter 3)	=	Radius of the rheometer rotor
R	=	Universal constant of gases
R_v	=	Carbonate plug radii calculated from the volume
R_s	=	Carbonate plug radii calculated from the surface area
R_{CS}	=	Cross-sectional radius of the wormlike micelle chain
RD	=	Recycle delay in NMR
S	=	Surface area of the carbonate plug
SHNC	=	Sodium hydroxynaphthalene carboxylate
T	=	Temperature
T_1	=	Longitudinal relaxation time in NMR
T_2	=	Transverse relaxation time in NMR
t_{50}	=	Time to dissolve about 50% of the mass of carbonate plug with acid
$t_{obs.}$	=	Observation time
TEM	=	Transmission electron microscopy
$UC_{22}AMPM$	=	N-erucamido-N,N-dimethylamine
V (Chapter 2)	=	Volume of the surfactant hydrophobic portion
V (Section 7.7.5)	=	Volume of the carbonate plug
VES	=	Viscoelastic surfactant
v	=	Effective charge per unit length of wormlike micelle
x_{CMC}	=	Molar fraction of surfactant at critical micelle concentration
WLM	=	wormlike micelle

Summary

Thesis division

The introductory part will begin with the presentation of the application investigated in this thesis, which would be the matrix acidification in the process of stimulation in oil wells, explaining how this step is performed in the field and which parameters are important for the formation of high conductivity channels in the reservoir rock known as wormholes and how the diverting acid fluids can be used to promote a successful stimulation step. As the diverting fluids are mostly composed of solutions containing high concentrations of surfactant and also, fundamentally, the colloidal aggregates formulated and characterized in the thesis are composed of surfactants, the next chapter was dedicated to the fundamentals of the surfactant molecules and in its property of self-aggregation in solution. As will be presented, surfactants can self-aggregate in different morphologies, but the morphology of interest for this thesis will be the wormlike micelles (WLMs), that are elongated dynamic aggregates formed through intermolecular interactions. The technological basis of diverting acid fluids can be through WLMs responsive to pH and ionic strength, and, for this reason, this second chapter was completed presenting the concept of smart WLMs and their different external stimuli possible. Finally, the introduction ended with the presentation of the rheology and the isothermal titration calorimetry fundamentals, which were the two main techniques used for the characterization of the investigated fluids. In addition to the general aspects of the techniques, part of the chapters were intended to explain how these techniques can be used to characterize fluids containing WLMs and, also, a history of the proposals for interpreting the enthalpograms of WLM formation was presented and as our research group contributed scientifically to this understanding.

The results and discussion can be understood by dividing in 3 blocks involving 2 studies each. In the first block, the formation of WLMs with aminoquaternary cationic surfactant and derivatives of chlorobenzoate or 4-halogenbenzoate was investigated in order to study the role of the positions and the nature of the substituent of the aromatic benzoate ring to favor the formation of WLM in solution; in the second block, smart

fluids containing WLMs responsive to pH or also to ultraviolet light were investigated. One of these fluids, the one responsive exclusively to pH, was investigated because it has the ideal rheological profile expected for a diverting fluid. Finally, in the third block, important aspects for acid stimulation were investigated, such as how the acid dissolution rate of carbonate is influenced by changing the nature of the carbonate and the acid used; how the rheological profile of a diverting acid fluid should be and its flow tests in core-flooding experiments. For this last block, the experiments were done for two commercial diverting acid fluids used today in the field and, also, using our own diverting fluid developed over the project called QuoVadis, product of a patent application.

Part I: Introduction

1. Acid stimulation in oilfield industry

Although investments in studies for the generation of efficient, clean and sustainable energies are continually increasing, especially in recent years, the use of oil for power generation (and derivative products) is still a very important and omnipresent source for this purpose [1]. In the oil field, the increase in extraction efficiency is quite challenging but has been growing with the development of new techniques and fluids in the stimulation stage of oil extraction. Stimulation techniques aim to increase productivity by increasing the permeability of the reservoir rock and also by removing damage of the reservoir in stages prior to stimulation stage [2–5]. In this sense, several stimulation techniques were developed and, among them, there are two that are worth mentioning which are the hydraulic fracturing (physical process) and the matrix acidification (chemical process).

In hydraulic fracturing, a fluid is injected under high pressure, well above the reservoir pressure, in order to create cracks in the reservoir rock which increase the reservoir permeability [6]. This technique is vastly used in wells where the reservoir rock is of siliciclastic nature and/or reservoirs of low permeabilities, where the incorporation of stimulating fluids into the formation becomes unfeasible. When successfully applied, this technique has strong penetration and the cracks generated can easily reach hundreds of meters of penetration radially to the wellbore. After these cracks are opened, the trend is that they tend to close when the injection pressure is relieved and, so as avoid this, a support material called proppant (solid particulates) [7] is injected together with the fluid. It is also possible to use acid fluids for hydraulic fracturing in order to combine the efficiency of crack formation, due to high injection pressure, with the reaction power of the acid fluid for the application in carbonaceous reservoir rock. This application is called acid fracturing [8]. Fracturing has several difficulties and strategies for using the fluid depending on the well that will be stimulated, but as fracturing is not the stimulation of interest in this thesis, these difficulties will not be addressed.

Matrix acidizing, stimulation method of interest of this thesis, is a technique that has become essential in the production of oil in wells of carbonaceous nature and still has a strong investment in the development of new methods, fluids and technologies for stimulation since more than half of the world's oil and gas reservoirs are still carbonaceous in nature [9,10] (including the largest reservoir in the world, Guawar Field, in Saudi Arabia) and, in particular, those found in the Brazilian pre-salt polygon, between Campos and Santos Basins.

In matrix acidification, a reactive acid fluid is injected into the reservoir, slightly above the reservoir pressure, in order to dissolve the formation rock and the materials that plug the pore spaces [11]. The dissolution removes particles that create resistance to flow and, mainly, creates high permeability flow channels known as wormholes [3,12] as can be seen in Figure 1 as an illustrative example.

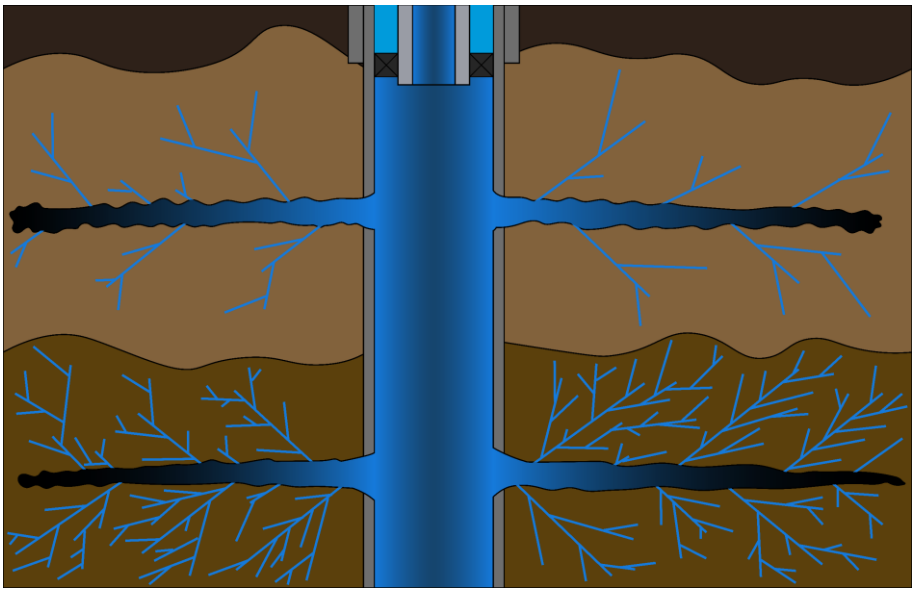

Figure 1. Oil well stimulated by the matrix acidification process. Horizontal inlets refer to the perforating channels and the branches to the wormholes formed through the reaction of the acid fluid with the carbonaceous rock of the reservoir. Perforation channels and the wellbore dimensions are out of scale for illustration purposes only.

The matrix acidification process increases the flow capacity close to the wellbore, at distances less than 10 meters of high density radially from the well [9]. The key parameters that govern the formation of the wormhole are the rate of reaction of the stimulating acid with the carbonaceous rock of the formation and the rate of convective and diffusive transport of the acid through the carbonate. These parameters can be related using the Damköhler number shown in Eq. 1.

$$N_{Da} = \frac{\pi d L \kappa}{q} \qquad \text{Eq. 1}$$

Where q is the flow rate into the wormholes, d and L the diameter and length of the wormhole, respectively, and κ is the overall dissolution rate that depends on the fluid-rock system [13–15]. When the Damköhler number is high, as in the case of low flow rates and/or high reactivity of the fluid with the carbonaceous rock, the dissolution is predominantly facial with low or no penetration into the reservoir rock, which is not desired. For cases where the Damköhler number is low, characteristic of injections with high flow and/or low reactivity, the penetration and dissolution of the reservoir by the acid fluid is intense which can lead to great damage in the formation and a large volume of acid is required per meter of wormhole formed. The ideal condition then is one where the Damköhler number is intermediate, where high conductivity flow channels are created, with controlled reactivity and low acid fluid consumption per meter of wormhole formed. Thus, the control of the reaction rate of the acid fluid with the carbonaceous rock (through the use of different acid fluids) and the flow used in the stimulation process are fundamental for the type of dissolution and wormhole formed [16,17]. Figure 2 shows the dependence of the pore volume to breakthrough (PVBT, which is the volume of acid needed, in units of porous volume of the rock, to run through the entire carbonate throughout the dissolution process) for acid fluids with different reactivities and carbonaceous rocks shown through the inverse of the Damköhler number.

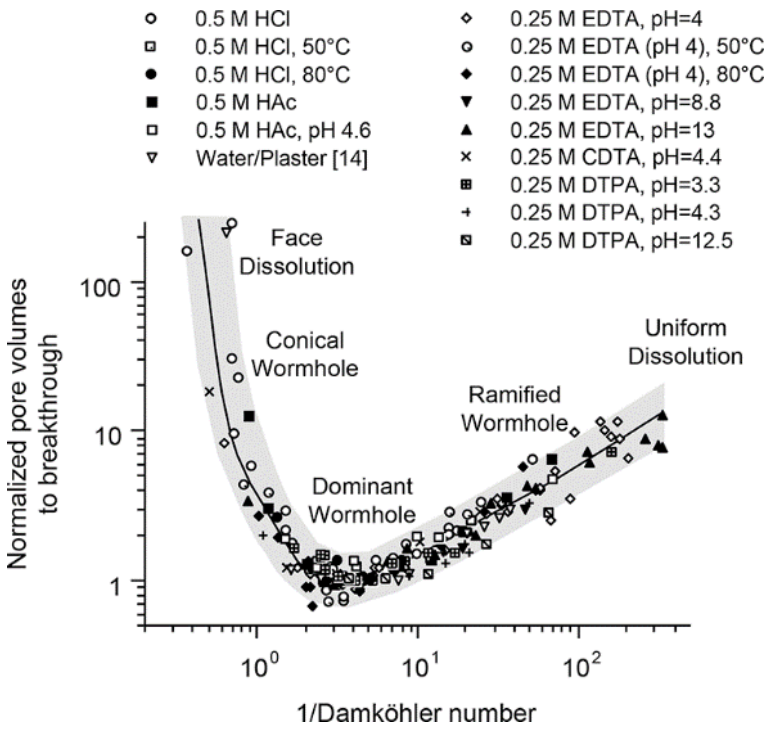

Figure 2. Normalized number of pore volumes to breakthrough as function of the inverse of the Damköhler number for a wide range of fluid/mineral systems. HCl means hydrochloric acid; HAc acetic acid; EDTA ethylenediaminetetraacetic acid; CDTA 1,2-cyclohexane-diaminetetraacetic acid and DTPA diethylenetriaminepentaacetic acid. Adapted with permission from reference [13].

It is possible to observe a master curve in Figure 2, where the different types of dissolution patterns are highlighted: face dissolution; conical wormhole; dominant wormhole; ramified wormhole and uniform dissolution. These different types of dissolution pattern can be visualized in Figure 3.

It is possible to observe in Figure 3 (from top to bottom) that the dissolution pattern obtained in stimulation can vary from facial dissolution to uniform dissolution, changing the reactivity of the injected acid fluid to one that has less reactivity with the carbonate matrix and/or increasing the injection flow in the formation. In facial dissolution, due to high reactivity and/or low injection flow, the penetration of the fluid in the formation is negligible and practically all of it is consumed in the face of the formation. At the other end, when fluid reactivity is extremely low with the carbonate and/or high flow rates are used, uniform consumption of the rock matrix occurs and a large volume of the

stimulating fluid is consumed. These both conditions are not desired during the stimulation process and there is no formation of wormholes.

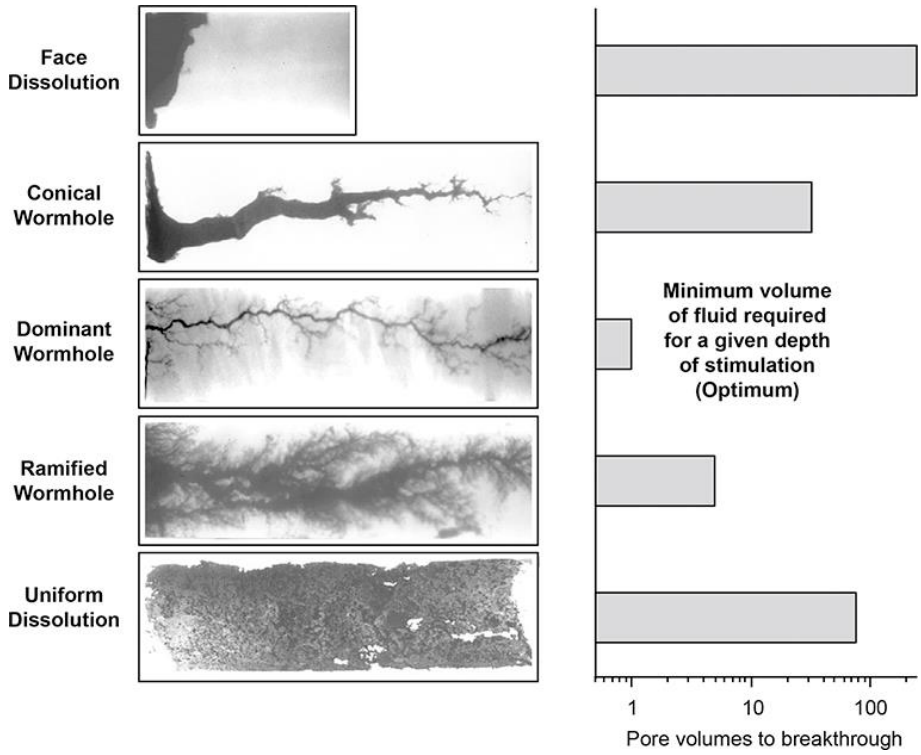

Figure 3. Dissolution patterns formed during reactive flow in carbonaceous rocks and the corresponding volume to break through the carbonate. The fluids were injected from left to right and the images were acquired by neutron radiography using hydrochloric acid (HCl) or ethylenediaminetetraacetic acid (EDTA) as a reactive fluid. Adapted with permission from reference [13].

So as to induce the formation of high permeability channels in the interior of the carbonates (wormholes), intermediate reaction and flow conditions must be employed. For these cases, when the fluid still has relatively high reactivity and/or low flow is employed, the wormhole formed is of the conical type where the main channel is relatively wide and of low penetration. Decreasing the reactivity a little more and/or increasing the flow, the wormhole formed is of the dominant type, where the main channel is narrower and of high penetrating power. This is the type of wormhole most desired in matrix acidification because it is the one that has the greatest penetration by

the injected acid fluid and represents the most effective conditions for stimulation [13]. Finally, by decreasing the fluid reactivity and/or the injection rate a little more, the wormhole formed is extremely branched and to have the same depth in stimulation, large volumes of acid are needed.

In the acid carbonate dissolution reaction, in addition to the acid used, the mineralogical nature and the composition of the carbonate used also has a great influence on the reaction rate as well as its petrophysics [18]. Carbonaceous reservoirs are generally composed of limestones ($CaCO_3$) and/or dolomites ($CaMg(CO_3)_2$) of different petrophysical nature (permeability and porosity) that vary considerably in their reactivity to different acid fluids. As an example, it is known [19–22] that the acid dissolution rate of limestone or dolomites is higher when aqueous hydrochloric acid solutions are used instead of organic acids such as acetic acid which means that, for reservoirs or stimulation zones composed mostly by dolomites (naturally less reactive), the use of acetic acid can make the stimulation process a failure due to the very low reactivity between species. Thus, the previous prospecting of the mineralogical nature of the well and the acid fluid that will be used in the matrix acidification stage is essential for a successful stimulation process.

Conventional acids such as hydrochloric acid are widely used as stimulating fluids in matrix acidification [23], but their use has several disadvantages such as high reactivity, corrosion and, mainly, incorporation of the stimulating fluid in the regions of high permeabilities of the stimulation zone. As consequence, the zones of less natural permeability remain practically unstimulated. Acids such as acetic, hydrofluoric, citric acid, among others, can also be used to overcome some of the problems associated with high reactivity, but, as will be shown in Chapter 12, the reactivity of the acid fluid with the carbonate and, consequently, the formation of the wormhole, in addition to the flow parameters, are strongly influenced by the petrophysical and the composition of the carbonate and the acid fluid.

To circumvent the problem of incorporating the stimulating fluid only in the areas of greatest natural permeability, diverting acid fluids can be used in the acid stimulation stage and they aim to "diverge" the virgin acid fluid to areas of less natural permeability after reacting with the carbonate reservoir and alter its rheological properties such as

viscosity and viscoelasticity. As with conventional acid fluids, diverting acid fluids also have low initial viscosity to facilitate their pumping down the well and incorporation into the reservoir rock and they also are incorporated into regions with high permeabilities in the stimulation zone. After being incorporated, initially in the zone of high permeability, they react and trigger the increase of the fluid viscosity and, consequently, decrease the local permeability, as if it were a plug in the region incorporated, causing the virgin fluid to be redirected to the areas of less natural permeability and also stimulate and form wormholes in these regions. As the reaction progresses, so that it does not cause permanent damage to the formation, after a given neutralization degree, the viscosity of the reacted fluid drops avoiding the obstruction (mechanical) of the wormholes formed, and, then increasing the permeability of the reservoir and the stimulated zone. A schematic illustration of the matrix acidification process using diverting acid fluids can be seen in Figure 4.

Polymeric fluids (gelled) [15,24–27] or fluids containing wormlike micelles (viscoelastic surfactants, VES) [15,28–31] are used as diverting fluids by oil companies in the stimulation stage of oil extraction. Polymeric fluids are widely used due to their ease of preparation and low production cost, but fluids containing wormlike micelles (WLM, colloidal self-assembly structure discussed in section 2.3) are often more interesting because in addition to having the properties of reducing friction and suspending and carrying solid particles such as the polymeric fluids, they also have the advantages of reconstituting the rheological properties of the fluid after high shear and temperature since they are structures formed by intermolecular interactions and not covalent bonds as in polymers. Therefore, their properties can be tuned for each step of the acid stimulation, such as low viscosity, in the beginning of the stimulation, high viscosity after some degree of neutralization and, again, low viscosity at the end of the process. This later characteristic is very advantageous relative to the polymeric fluid, in which their chains must be destroyed by adding chemical additives at the end of the stimulation and, for fluids containing WLM, this is not necessary because once it comes in contact with oil or with the with the advance of reaction, its viscosity naturally decreases due to the disruption or decrease in size of the wormlike micelle structures.

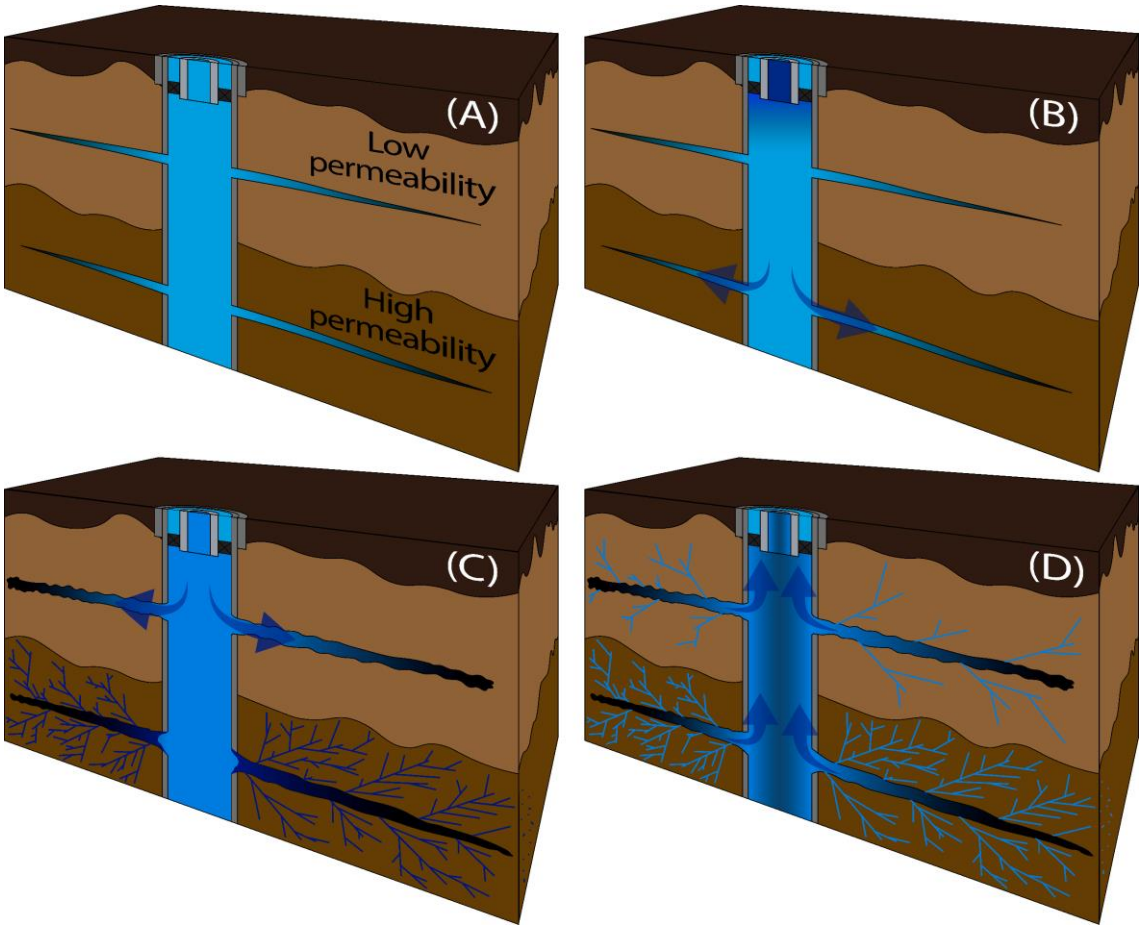

Figure 4. Matrix acidification using a diverting acid fluid. (A) Stimulation zone (post-perforation) containing carbonaceous rocks of two different natures, the upper one being less permeable than the lower one. (B) The virgin low-viscosity fluid is incorporated into the region of greatest natural permeability. (C) The reaction of the stimulating fluid with the carbonaceous rock causes the formation of wormholes and, with neutralization, the increase of the fluid viscosity and the decrease in local permeability. The virgin fluid is diverted to areas of less natural permeability, causing these regions to be stimulated as well. (D) As the neutralization reaction of the acid stimulating fluid advances, the viscosity of the fluid decreases, making it to be recovered and, then, increasing the productivity of the stimulated zone. Perforation channels and the wellbore dimensions are out of scale for illustration purposes only.

Part of the project and then, the thesis, was intended for the development and characterization of a diverting acid fluid based on pH-responsive wormlike micelle. Therefore, for a better comprehension why we chose this system and the results

obtained, Chapter 2 is dedicated to the fundamentals of surfactants and its property of self-aggregation.

2. Surfactants and self-assembly [32–39]

2.1. Surfactants and their properties

Surfactant is a class of molecules that has surface activity and can self-assemble in solution in specific conditions. They are amphiphile molecules, where part of the surfactant molecule has favorable interactions with the solvent (lyophilic) and the other part not so good interactions with the solvent (lyophobic). When in aqueous solutions, the lyophilic and lyophobic parts are called, respectively, as hydrophilic or "head" group and hydrophobic or "tail" group. In water, the head group has solubilizing functionality and it can be an ionic (cationic, anionic or zwitterionic) or a highly polar non-ionic group such as poly(ethylene glycol) or polyol groups (as sugars) and the tail is generally a hydrocarbon chain varying from a straight-chain alkyl groups (C_8-C_{22}), branched-alkyl groups, unsaturated akenyl chains, alkylbenzenes, and so on. Some common examples of surfactant chemical structures can be seen in Figure 5. From now on, the fundaments will be presented with the continuous phase being water which makes the lyophilic and lyophobic parts of the surfactant implicit.

Molecules at the interface solution/air experience fewer attractions when compared with the molecules of the bulk phase and hence have a higher chemical potential than the ones in the bulk. So, to transport molecules from the bulk to the surface to increase the surface area, A, a positive work is necessary. The surface tension, γ, is "the work required to increase the area of a surface reversibly and isothermally by a unit amount" and is represented by Eq. 2.

$$\gamma = \left(\frac{\partial G}{\partial A}\right)_{T,P,n} \qquad \text{Eq. 2}$$

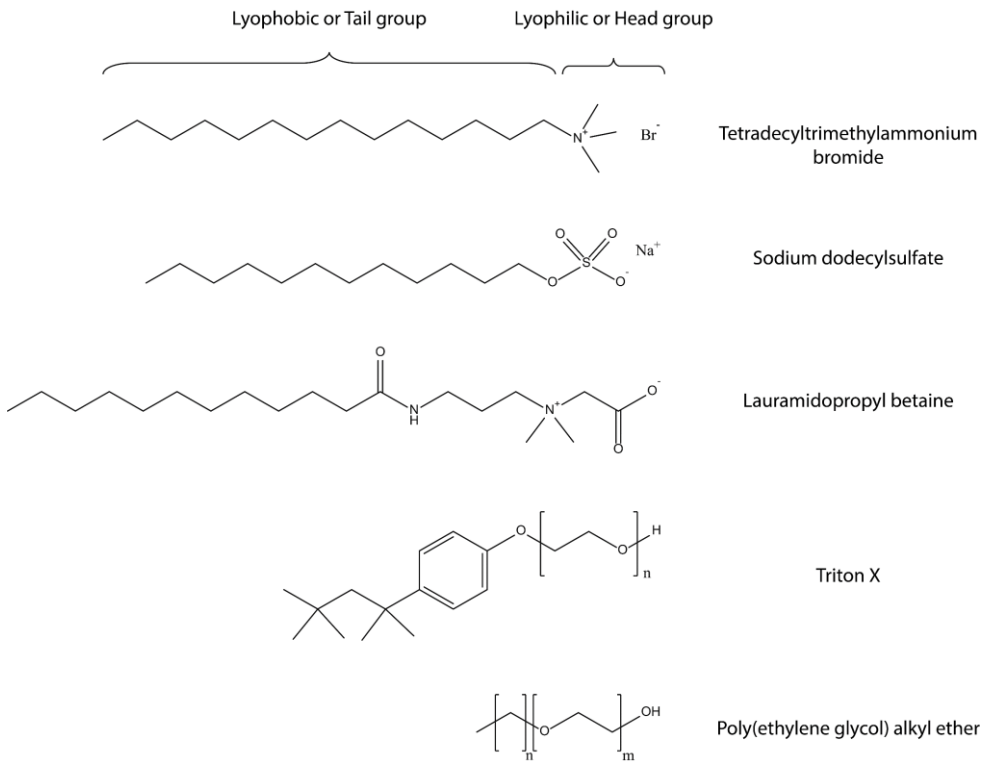

Figure 5. Examples of surfactant molecules of different natures. From top to bottom, cationic (tetradecyltrimethylammonium bromide), anionic (sodium dodecylsulfate), zwitterionic (lauramidopropyl betaine) and two non-ionic surfactants (triton X and poly(ethylene glycol) alkyl ether). At the top it is also highlighted the lyophobic or tail group and lyophilic or head group parts of the cationic surfactant.

Liquids with strong intermolecular interactions, as water, have high values of surface tension ($71.99\ mN\ m^{-1}$ at $25\ °C$ [40]) and the dissolution of solutes can increase or decrease its value, being the last much more common. When surfactant molecules are dissolved in water, the lyophobic group causes a restructuring of the solvent molecules leading to an increase of the free energy of the system. To reduce this energy, in very dilute conditions, the surfactant molecules concentrate at the solution/air interface, with the tails and head group pointed to the air and aqueous phases, respectively. Due to this configuration, surfactants drastically change the surface properties of the solution, being able to easily reduce the solution interfacial tension by more than 90% when compared to pure water depending on the molecular structure of the surfactant and its concentration.

2.2. Surfactant self-assembly

As the interfaces begin to be saturated with the increase of surfactant concentration, the overall energy reduction may continue through other mechanisms like the self-aggregation in the bulk phase. The most known and the first aggregate to be formed in solution in the majority of the surfactants is the spherical micelle, where the surfactant head group remains in direct contact with the solvent molecules and the tail group in the interior of the aggregate as can be seen in Figure 6. The term “micelle” was created by K. Nägeli in 1858 but it was first used in the sense of surfactant self-assemble by McBain in 1914 in one of his own publication [41] and it was initially harshly criticized by scientific community mainly by Hartley, who, in the late of 1930s correctly proposed the configuration of the spherical micelles [42,43]. A schematic illustration of spherical micelles is represented in Figure 6.

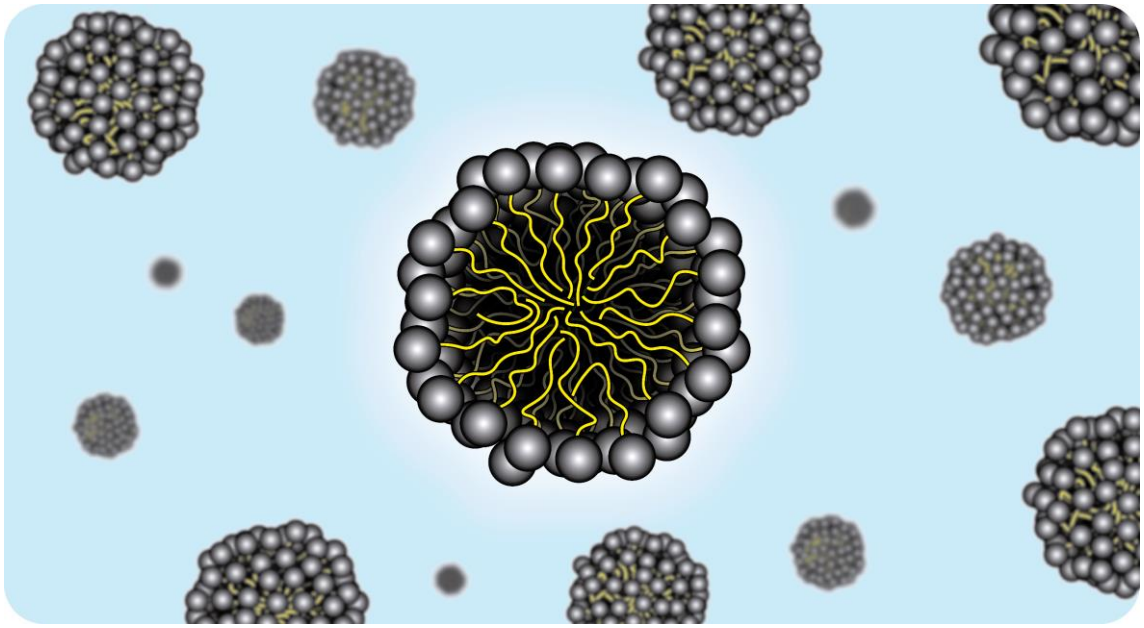

Figure 6. Schematic representation of a spherical micelle formed by surfactant in an aqueous system.

The surfactant concentration where the aggregate is formed is called critical micelle concentration (CMC) and the concentration of unimers in solution after the CMC remains virtually unchanged and only more aggregates are formed with the increase of surfactant concentration. With the process of aggregation, several bulk solution properties change its trend as function of the surfactant concentration like osmotic pressure, electrical conductivity, turbidity, calorimetry, fluorescence, surface tension and so on and they can be used to measure the surfactant CMC [32].

The driving force for micelle formation is a balance of the forces favoring and retarding the molecular aggregation process. From the surfactant molecules point of view, the initial state is the molecules solubilized in water and at interfaces and the final state is the spherical micelle, with the headgroup interacting with the water molecules and the apolar part with each other in micelle core. From the water molecules point of view, the initial state is the consequence of the rupture of the icelike structure in pure water and the solvation of the surfactant molecule, both the hydrophilic and hydrophobic part, and the final state is the water molecules interacting with each other and with the surfactant headgroup. In terms of Gibbs free energy, even though the surfactant molecules lose mobility due to the micellization process and great steric and/or ionic repulsion occurs between the heads of the surfactant, the entropic gain that occurs due to the release of the water molecules that were previously hydrating the hydrophobic part of the surfactant is much greater (called as hydrophobic effect), making the whole process of aggregation entropically favorable. Additionally, the steric/ionic repulsion between the surfactant headgroup and the strong ion-dipole interaction between the water molecules and the surfactant headgroups is crucial for the system do not phase separate with the micelle formation [32].

Even though the structure of the spherical micelle is dynamic, the size distribution, surface area and the core volume of the aggregates are consequences of the packing of the surfactants into the aggregates. Depending on the system investigated (type and structure of the surfactant considered, presence or not of a third or fourth component, physicochemical conditions, etc.) it is possible to perceive other forms of aggregates in solution as for example elongated structures called wormlike micelles (WLM), bilayers structures as lamellae or vesicles, and more complex structures like hexagonal, cubic or

even inverse structures. Israelachvili [44–46] has shown that the structure formed can be foreseen looking at the geometric factors that the surfactant molecule assumes when it is in the aggregate. This relation, called critical packing parameter, CPP, is defined as the relation between the lyophilic and lyophobic dimension of the surfactant molecule by $(V/\ell)/a_0$ where V and ℓ are the volume and the critical length of the hydrophobic tail of the surfactant and a_0 is the optimum head group area. The CPP relation can be seen in Figure 7 for the spherical micelle shown in Figure 6.

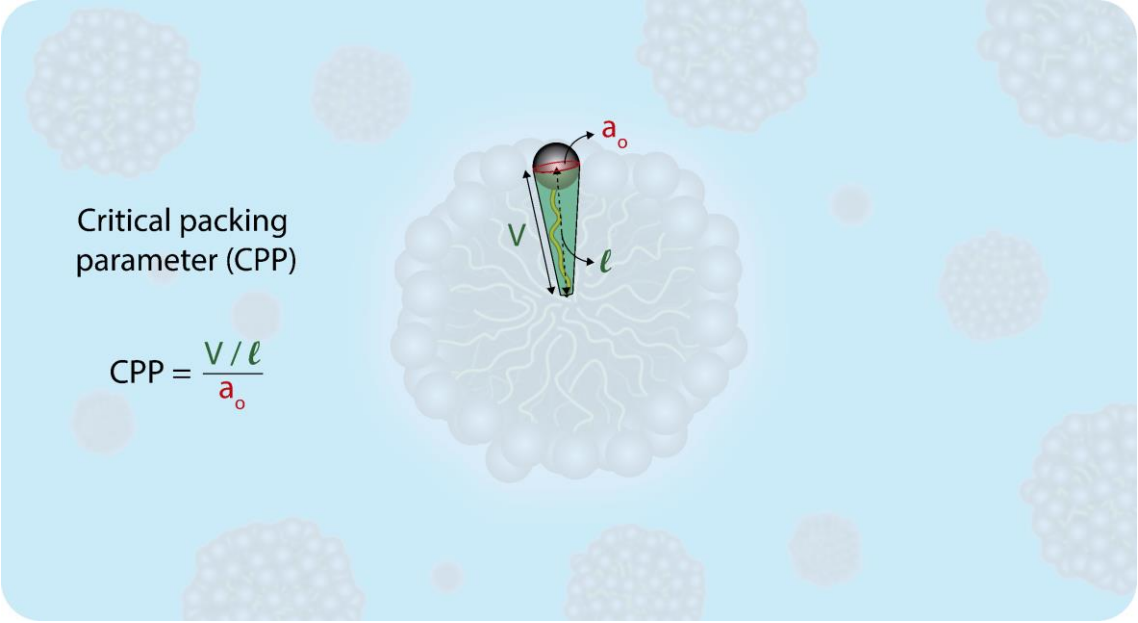

Figure 7. Critical packing parameter definition and the relevant structural parameters of the surfactant in a spherical aggregate in aqueous solution.

As lower the curvature of the aggregate, higher is the surfactant CPP. For spherical micelles the CPP expected is lower than 1/3, WLMs or rod-like micelles between 1/3 and 1/2, vesicles and flexible bilayers between 1/2 and 1, planar bilayers structure have CPP around 1 and inversed structures (with the tail and headgroup toward to solvent and structure core, respectively, commonly observed in apolar solvents) with CPP higher than 1. Even being possible [47], in general the calculation of surfactant CPP is not necessary during the investigations but it is an interesting relation to keep in mind to predict and discuss changes in the bulk solution properties and even predict the

surfactant equilibrium structure in specific physicochemical conditions prior its investigation. For example, if high curvature aggregates in solution are desirable (low CPP), surfactants with single chain and/or relatively large head groups are chosen and, if low curvature aggregates are required (high CPP), double-chain and/or small head groups are chosen. The WLMs are the morphology of interest in this thesis and the discussion from now on will be targeted at this type of aggregate.

2.3. Wormlike micelles [48–50]

It is possible to manipulate the surfactant CPP changing the physicochemical properties of the solution like concentration [51,52], temperature [53–55], pH [51,56,57], ionic strength [58–60], and so on. As an example of aggregate morphology change, let us take the quaternary ammonium salt like cetyltrimethylammonium bromide (C_{16}TAB) which is vastly used in colloidal science. The phase diagram of C_{16}TAB in water can be easily found elsewhere [61] and it shows that the Krafft temperature (temperature for the phase transition from solvated solid surfactant to the solution phase or liquid crystalline phase) is about $25\ °C$, its critical micelle concentration is about $0.92\ mmol\ L^{-1}$ and it can form hexagonal phase above $19.0\ wt\%$ ($\sim 640.0\ mmol\ L^{-1}$). So, supposing that the system is in this intermediate conditions, spherical-like micelles are formed in solution. To induce the formation of WLM in this system one can add inorganic salts [62–64] or specific organic salts [65–67], so as the Coulombic forces between the dissociated salts and the surfactant headgroup decrease the head group area of the surfactant, leading it to a higher value of CPP and eventually favoring the formation of WLM. The concentration required to form WLM in solution is specific for each combination of surfactant/salt. The use of organic salt to form WLM is much more convenient when compared with the inorganic salt due to the concentration required, which is much lower in the case of organic salt. Oelschlaeger *et al.* [59] showed that in a system containing $350\ mmol\ L^{-1}$ C_{16}TAB, long WLM were obtained using around $200\ mmol\ L^{-1}$ of sodium salicylate, but for $NaClO_3$, $NaNO_3$ and KBr, the concentration required was $350\ mmol\ L^{-1}$, $1000\ mmol\ L^{-1}$ and $> 3000\ mmol\ L^{-1}$, respectively. In

inorganic salts, the main driving force to form the WLM is the Coulombic interaction mentioned above, but for organic salts, like for example the sodium salicylate, much used for this purpose [59,68–75], additional interactions can take place due to the conformation that the organic salt assumes when interact with the surfactant as can be seen in Figure 8 and some of them are the dispersive interactions (non-polar interactions) and cation-π interactions [76,77] in the case of the organic salt being an aromatic salt.

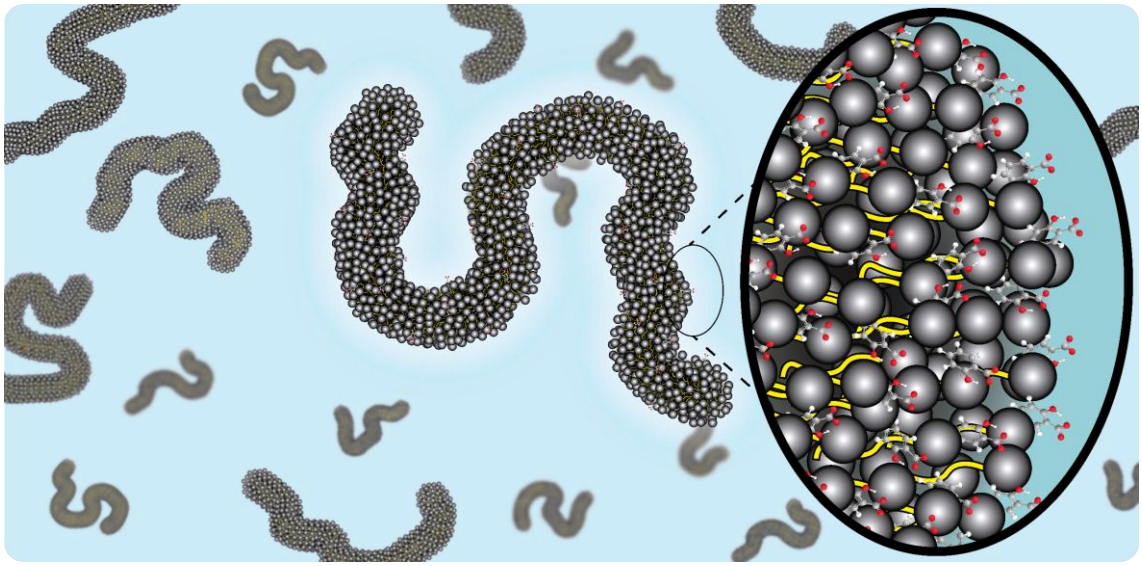

Figure 8. Wormlike micelle aggregate in aqueous solution showing the disposition of the organic salt molecules at the micellar interface formed by a cationic surfactant.

WLMs are flexible elongated structures which is constantly breaking and recombining in solution due to its nature of formation. Two regions of the WLM structure can be considered; the region of high curvature called end caps and its cylindrical body, which presents low curvature. For this structure, the chemical potential of the surfactants that are in the end caps is higher than the surfactant molecules that are in the cylindrical body and, then, the growth of the WLM is a consequence of the system in minimize the excess free energy by reducing the number of end caps.

In diluted regime, the WLMs chains are distant from one another and the solution viscosity increases linearly with the surfactant concentration [78,79] but, above the

critical concentration [80] (not the CMC mentioned previously), where the chains start to entangle, the solution viscosity increases rapidly and can presents remarkably viscoelasticity. Depending on the components and the physicochemical conditions, the entangled WLM can form points of branching or entanglement [81–83] that can slide along the chains, providing additional mechanisms for relaxing the mechanical tension as will be seen in section 3.6. Due to this behavior, solutions containing WLM are quite interesting from an academic and application point of views. From an academic perspective, the investigation of the conditions that favor the WLM micellar phase is always very intriguing, considering the forces and the characteristics of the molecules involved. From the practical side, WLM can be used to modulate the viscosity and the viscoelasticity for different fields of action and, in addition to enhanced oil recovery presented in Chapter 1, they also find application in drug delivery systems [84], rheological controller [85,86], drag reduction agents [87–89] and home and personal care products [90,91].

WLMs have some characteristic lengths that can be correlated with parameters obtained in oscillatory-shear rheology (introduced in section 3.6). Starting from the largest to the smallest size, the first one is the overall length of the WLM, which is related as the contour length, $\bar{L}$, and it can vary from few nanometers to some micrometers. For neutral or highly screened micelles [92] the contour length can be related in terms of volume fraction φ, the temperature T and the end-cap energy, E_C, which is the energy required to form two hemispherical end-caps as a consequence of the disruption of the giant micelle body, as can be seen in Eq. 3.

$$\bar{L} \sim \varphi^{\frac{1}{2}} \exp\left(\frac{E_c}{k_B T}\right) \qquad \text{Eq. 3}$$

For charged micelles in the absence of salt, an additional term, E_e, must be taken into account to also consider the repulsion of charges along the backbone that favor shorter micelles. $\bar{L}$ for this case is shown in Eq. 4.

$$\bar{L} \sim \varphi^{\frac{1}{2}} \left(\exp\left(\frac{E_c - E_e}{2k_B T} \right) \right) \quad \text{Eq. 4}$$

Where E_c is given by Eq. 5.

$$E_c \sim k_B T l_B R_{CS} v^2 \varphi^{\frac{1}{2}} \quad \text{Eq. 5}$$

Where l_B is the Bjerrum length (distance where the Coulombic energy between two charges are the same as the thermal energy, $k_B T$), R_{CS} is the cross-sectional radius of the WLM body and v is the effective charge per unit length.

The next characteristic length of WLM is the persistence length, l_p, the length over which the WLM is considered rigid and it is related with the flexibility of the chains (Kuhn length $b = 2l_p$). In large scale, the WLM chains can achieve conditions where they can be quite flexible (in low superficial charge) but, in low scale, it can be considered as a combination of several rigid rods of length l_p. The persistence length varies significantly with the system investigated, but typical values of l_p are $20 - 50$ nm [48] (much smaller than the polymers which are typically in order of some nanometers [93]).

For semi-diluted and concentrated regimes, two additional parameters can be defined and are related to the entanglement density of the chains. The first one is the entanglement length, l_e, which is the length of a section of the WLM between two entanglement points, and the hydrodynamic correlation length, ξ, related with the mesh size of the micellar network.

As it will be presented in section 3.6, knowing the persistence length of the WLM system investigated (normally determined by neutron/x-ray scattering techniques), all these structural parameters can be estimated in oscillatory-shear rheology. For a better comprehension of them, Figure 9 shows the typical lengths discussed for WLM in semi-diluted regime.

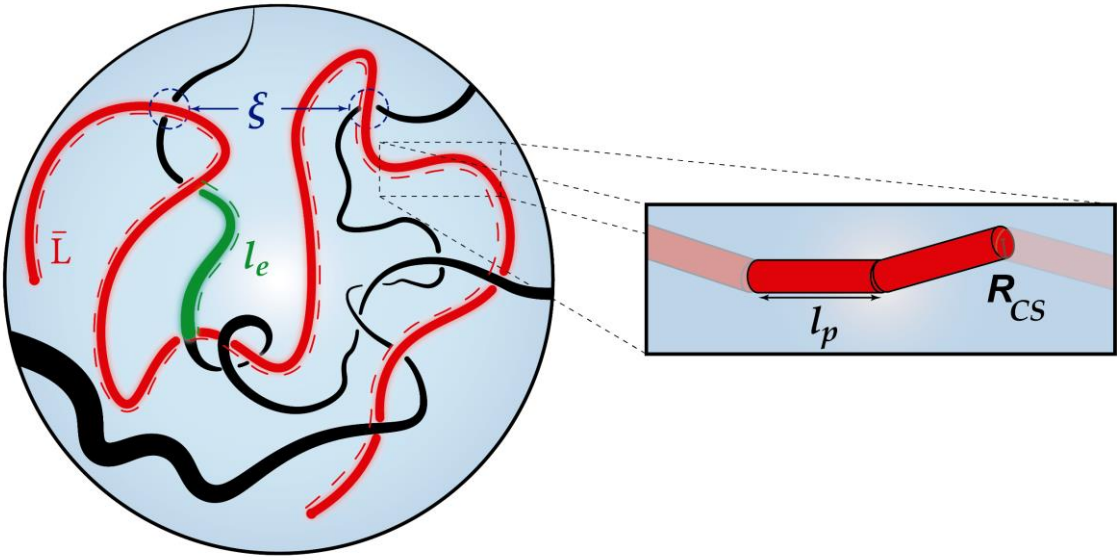

Figure 9. Characteristic lengths of the wormlike micelles in a semi-diluted regime.

Fluids containing WLMs can be formulated to respond to external stimuli such as pH, temperature, ionic strength, and so on, which considerably expands its application possibilities. These fluids are known as “smart wormlike micelles” [94,95] and are the technological basis of several applications. The next section will discuss the main stimuli reported in the literature, the strategies in the formulation of each stimulus and some examples.

2.4. WLM fluids responsive to external stimuli [94,95]

Several applications demand that the fluid used increase or decrease its viscosity and viscoelasticity after the application of some external stimulation and some fluids with WLMs (before and/or after the stimulation) can be formulated to do so. The fundamental aspect behind this responsiveness is the change in the aggregate CPP leading to aggregate growth (shorter to higher WLM chains) or vice versa.

The most common stimuli are temperature, UV/visible light, pH and CO_2/N_2 bubbling, and some of them can be cyclic or not, that is, it is possible to reverse the initial

formulation by going in the “opposite direction” to the initial stimulus. Still, it is interesting to note that the stimuli are often independent, being possible to formulate fluids that are multi-responsive [54,96,97].

Temperature stimulus possibly is the simplest one between them and, as discussed in section 2.3 with Eq. 3 and Eq. 4, the typical behavior of the WLM when the temperature is raised is an exponential decrease of its length and, consequently, a decrease in the solution viscosity. Even though some studies associate this thermo-thinning behavior as a smart fluid [54], this is the common behavior expected. The cases in which the viscosity increases with the increase of temperature (thermo-thickening), are in fact, a “non expected behavior”. Fluids that behave this way generally show a gain in viscosity over a finite temperature range and, after this range, the usual behavior of wormlike micelles take place, causing the decrease in the solution viscosity.

Non-ionic surfactants derived from polyoxyethylene alkyl ethers are commonly used in thermo-thickening fluids containing WLM since the hydration of the oxyethylene units is dramatically affected by temperature [98], but a few studies involving charged surfactants are also found [55,99]. As examples, Sharma *et al.* [98] showed that the system composed by $5.0\ wt\%$ of the mixture polyoxyethylene phytosteryl ether ($PhyEO_{30}$)/polyoxyethylene dodecyl ethers ($C_{12}EO_{3\text{-}4}$) containing $36.0\ molar\%$ of PhyEO, exhibited a viscosity increase of about fifty-times, by changing the temperature from 15 to $30\ °C$. In a similar way but for a gemini surfactant, Wei *et al.* [55] showed that aqueous solution of 2-Hydroxypropyl-1,3-bis(hexadecildimethylammonium chloride) presented a thermo-thickening behavior of almost $1{,}000\ times$ increasing the temperature from 30 to $37\ °C$. In a different fashion, Raghavan *et al.* [99] developed a thermo-thickening fluid composed by a C_{22} cationic surfactant, erucylbis(hydroxyethyl)methylammonium chloride (EHAC), with sodium hydroxynaphthalene carboxylate (SHNC) in different concentrations that showed viscosity increase of about fifty-times using SHNC $360\ mmol\ L^{-1}$ and EHAC $40.0\ mmol\ L^{-1}$ if the solutions is heated. The authors' strategy for this system was to prepare it in an excess SHNC regime. At low temperatures, the excess of SHNC incorporated in the micellar environment makes the charge density of the micellar surface high and, thus, it favors the short aggregates and low viscosity. With the increase

in temperature, part of the SHNC is partitioned in the aqueous phase, which reduces the surface charge of the aggregate and, thus, favors the formation of wormlike micelles as can be seen in Figure 10.

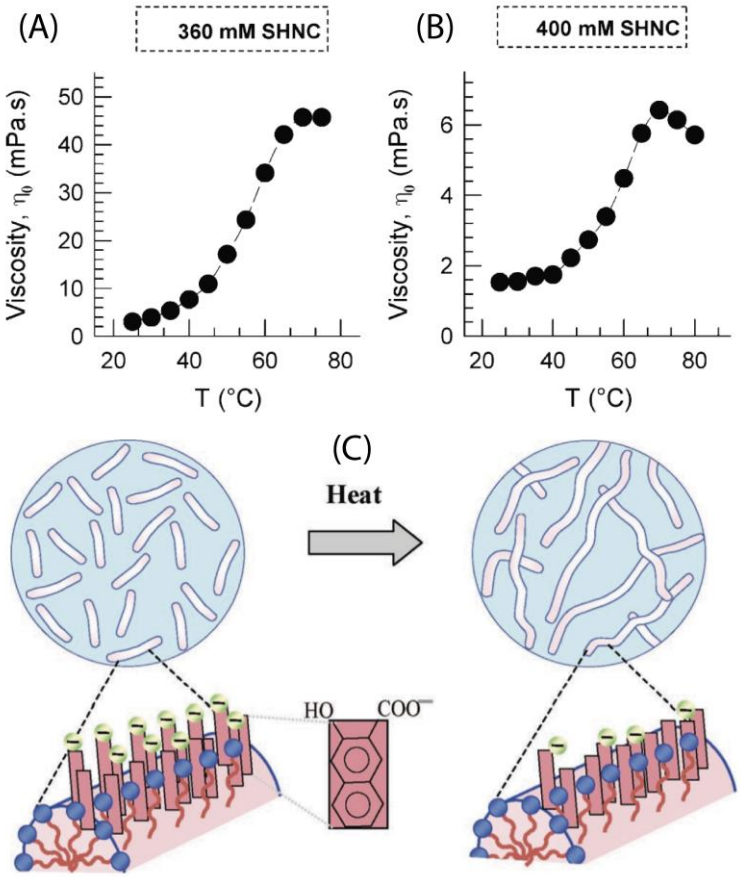

Figure 10. Viscosity as function of temperature for a solution containing EHAC $40.0\ mmol\ L^{-1}$ and (A) SHNC $360.0\ mmol\ L^{-1}$ or (B) $400.0\ mmol\ L^{-1}$. (C) Molecular interpretation proposed by the authors to justify the WLM growth with the increase of temperature. Adapted with permission from reference [99].

Light stimulus presents some advantages compared to the others, like a non-invasive stimulus, simple, cheap, and readily available. It can be directed at a precise spatial location which allows several applications and its use avoid changes in the composition and the physicochemical properties of the solution. WLM that respond to light stimuli exploit mainly the dimerization [100,101] or cis-trans isomerization [97,102–104] of the

molecules that compose the fluid and the photosensitive compound can be additives [102,103,105] or directly the surfactant [97,104].

Azobenzene derivatives ($R-N \equiv N-R'$) are extensively used for UV/Vis responsive systems containing WLM, either by the addition of an azobenzene into a conventional solution of WLM like C_{16}TAB/NaSal [106], incorporating the azobenzene directly in the additive that promotes the formation of WLM without the necessity of an co-additive [106,107] or even incorporating the azobenzene group directly on the surfactant molecule [97,108,109]. In these three cases, the idea is the same: the UV irradiation changes the trans-form to the cis-form (and the visible irradiation to the opposite direction making it a cyclic stimulus) which drastically changes the surfactant CPP and, then, the solution viscosity. As an example, Raghavan *et al.* [107] showed a fluid composed by EHAC $40.0\ mmol\ L^{-1}$ and 4-azobenzene carboxylic acid (ACA) $20.0\ mmol\ L^{-1}$ that the incidence of UV light by $30\ min$ changed the solution viscosity by more than 5 orders of magnitude as can be seen in Figure 11. Raghavan *et al.* [105,110] also published photo-responsive fluids containing WLM composed by ortho-methoxycinnamic acid (OMCA) instead of azo derivates showing a photo-thinning [110] and a photo-thickening behavior [105]. In this case, the UV incidence also isomerizes the OMCA from trans to cis conformation and the cis isomer has a much weaker interaction with the cationic surfactant C_{16}TAB used since its geometry does not favor the incorporation into the micellar interface.

Probably, the pH responsive smart WLM fluids are the most investigated systems. There are several studies that relate smart WLM responsive to the solution pH. The main strategies in these studies are the use of a surfactant pH responsive [67,97,111], mixtures of surfactants of different nature [97,111], combination of a conventional surfactants and a pH responsive organic compound like oxalic acid [67], coumaric acid isomers [112], phthalic acid isomers [113], and others. It is possible to formulate pH responsive WLM in any pH range, acid [114,115], neutral [54] or basic conditions [116,117] and WLM that have responsiveness in acid conditions has a very important application in the oil field as acid diverting fluid in carbonate matrix acidizing step [9,23] (Chapter 1), which is the main interest of application of this thesis.

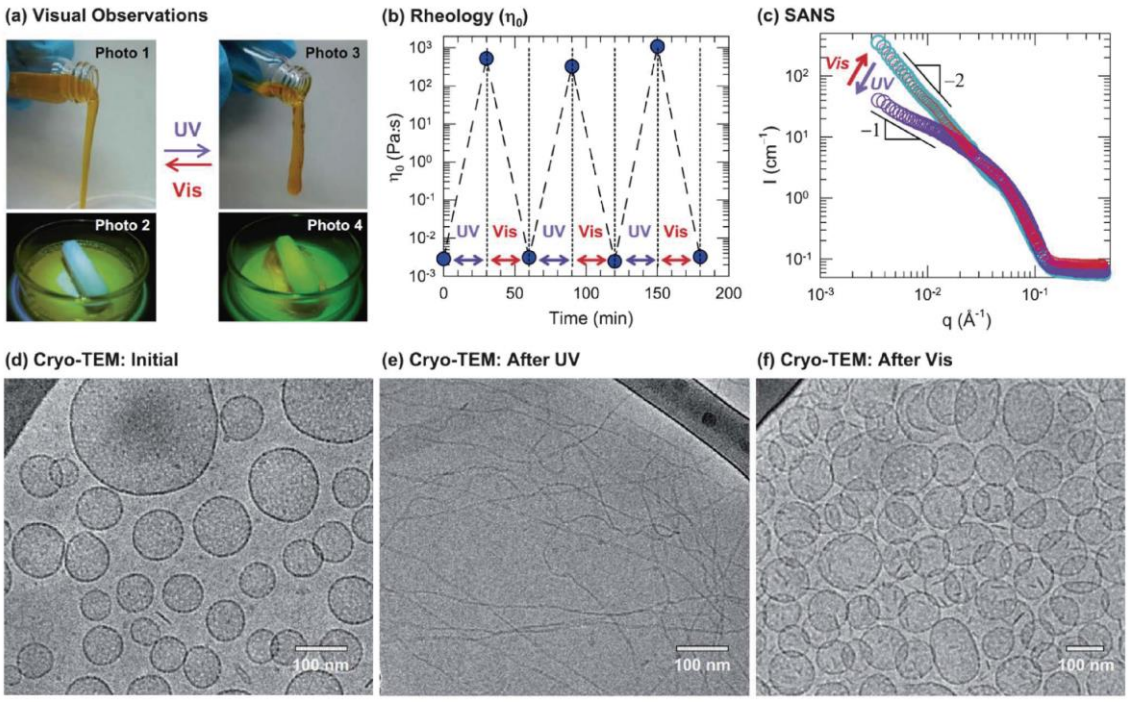

Figure 11. Photosensitive WLM fluid composed by EHAC $40.0\,mmol\,L^{-1}$ and 4-azobenzene carboxylic acid (ACA) $20.0\,mmol\,L^{-1}$. (a) Visual observation before and after UV irradiation; (b) The cyclic profile of viscosity upon UV/Vis irradiation; (c) small angle neutron scattering before and after UV irradiation and (d) to (f) cryogenic transmission electron microscopy of the fluid before and after UV/Vis irradiation. Adapted with permission from reference [107].

Alkyldimethylamine oxides (C_nDMAO) are vastly used to formulate systems composed only by surfactants that are pH-responsive [118–120]. They spontaneously self-assembly into long, flexible WLMs without the help of any additives in specific conditions. In low pH, below the isoelectric point, C_nDMAO is in its cationic form where great ionic repulsion is presented in the aggregate surface and, hence, only spherical micelles are formed. However, near the point of half-ionization ($\alpha = 0.5$), the net superficial charge of the aggregate decreases and strong hydrogen bonds among the surfactants are formed which favors the formation of long WLMs and, then, solutions with high viscosity.

The introduction of a pH-responsive additive to a conventional surfactant solution undoubtedly is the most common way to formulate pH-responsive system with only

commercial-available chemicals. Lin *et al.* [86] showed facile ways to formulate viscoelastic pH-responsive fluids of cationic surfactants and different aromatic organic acids derived from phenyl or naththyl compounds. In all cases, the idea of the pH-responsiveness is the same: in pH where the aromatic acid is totally protonated or totally unprotonated in the case of molecules with two pK_a, spherical or short WLMs are obtained and the solution presents low viscosity due to the high solubility in water of the organic compounds; when the solution pH is adjusted so as the aromatic acid is anionic (in the case of only one pK_a) or monoanionic (in the case of more than one pK_a), the interactions of the organic salt with the cationic surfactant is very strong, driving the formation of long WLM in solution and enhancing the viscosity of the solution. Another very interesting way to formulate pH-responsive fluids is by the formation of "pseudo-gemini surfactants" in solution. Feng *et al.* [57,121] showed results of a pH-responsive fluid composed by N-erucamido-N,N-dimethylamine (UC_{22}AMPM) $50.0\ mmol\ L^{-1}$ and maleic acid $25.0\ mmol\ L^{-1}$ that, decreasing the solution pH lower than 7.20, a sharp increase of five orders of magnitude in the solution viscosity is obtained and the results were associated with the formation of pseudo-gemini surfactant, as can be seen in Figure 12. Below pH 7.0 the secondary amine surfactant UC_{22}AMPM is mostly in its cationic form and strong Coulombic interactions take place with the dianionic maleate and the pseudo-gemini surfactant is formed resulting in a very high solution viscosity.

In general, fluids that are responsive to pH through the addition of HCl/NaOH have a limit of reversibility due to the added counterions (Cl^- and Na^+) that increase the ionic strength of the solution. This effect is even more pronounced for fluids composed of high-concentration ionic surfactants, where large concentrations of acid or base are required to change a pH unit. To work around this situation in pH-responsive fluids, acidification can be done by pumping CO_2 into the solution instead of adding HCl or any other acid [97,122–124]. The limitation of this would be for fluids that respond in very acid conditions, where even solutions saturated with CO_2 are not able to reach such a pH. To remove the excess of CO_2 from the solution (and shift the H_2CO_3 and HCO_3^- equilibria), an inert gas such as N_2 is normally used, which is able to restore exactly the initial conditions prior to acidification. With this approach, the same strategies

presented above for pH-responsive fluids can be formulated, even those where the pseudo-gemini surfactant is formed.

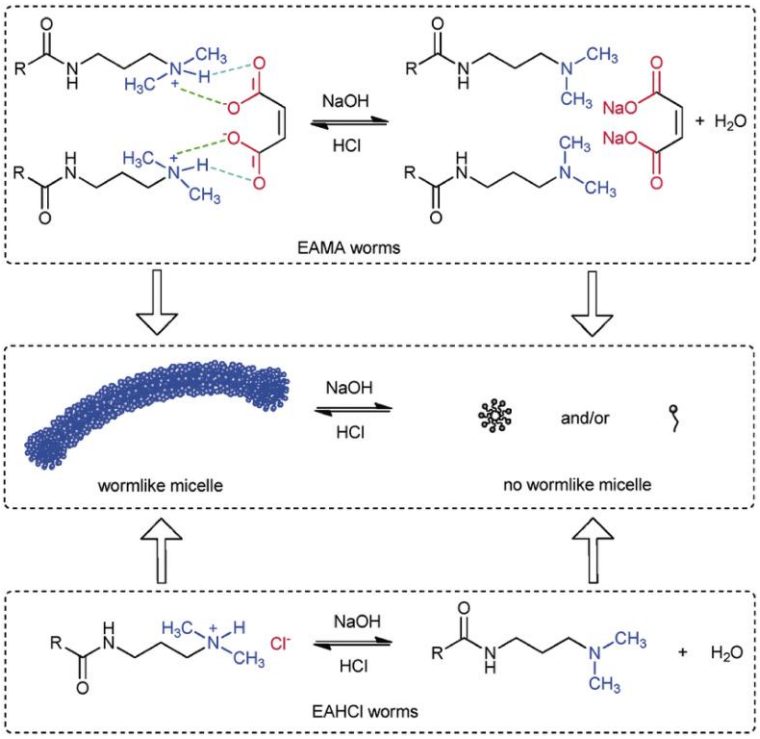

Figure 12. pH responsive fluid composed by N-erucamido-N,N-dimethylamine ($UC_{22}AMPM$) $50.0\ mmol\ L^{-1}$ and maleic acid $25.0\ mmol\ L^{-1}$ below (HCl) and above (NaOH) pH 7.20. Wormlike micelles and then the highly viscous solution is obtained with the addition of HCl below pH 7.20 due to the formation of pseudo-gemini surfactant. Adapted with permission from reference [57].

Certainly, the most import property of WLM systems is associated with their special rheological nature. In Chapter 3, fundaments in rheology with special emphasis to WLMs are presented. On the other hand, thermodynamic dictates how likely is the formation of WLM when a cationic surfactant is combined with an aromatic anion. Therefore, in Chapter 4, thermodynamic aspects relative to formation of WLM is presented, with emphasis on the variation of enthalpy for the process, measured in a isothermal calorimetric titration.

3. Rheology [78,79,125–129]

3.1. Introduction

Rheology is the science field that study the flow and the deformation of the matter resulting from the application of a mechanical force and it was coined by Bingham in 1929 [130]. The response of the materials to the application of the force will depend on the nature of the material and the observation time after the application of the force. For totally solid materials (known as Hookean solids), the mechanical force deforms the material and the transferred energy is stored, with the material being able to return to its initial shape or not, depending on the magnitude of the applied force. For totally liquid materials (known as Newtonian fluids), the deformation and energy transferred is dissipated in flow. However, for most of the applied materials, their responsiveness can vary, being liquid-like or solid-like depending on the force applied, classifying them as viscoelastic materials.

Beyond its nature, upon a mechanical stimulus, the responsiveness of materials can be correlated with the relation between the relaxation time of the material, $\tau_{rel.}$, which is an inherent time of each material to achieve the low energy state after the application of the force, and the observation time, $t_{obs.}$, after the application of the force. Such relation is defined as Deborah number, De, showed in Eq. 6.

$$De = \frac{\tau_{rel.}}{t_{obs.}} \qquad \text{Eq. 6}$$

For a liquid-like system, the relaxation time is very short and thus $De \ll 1$. On the other hand, the material is classified as solid-like if $De \gg 1$, and in intermediary situations, around $De \sim 1$, as viscoelastic. This relation is simple to understand considering the application of a force in a string. As soon as the force is applied, the material responds in an elastic way (strong mechanical resistance) as a result of the deformation, however,

if this deformation is applied for a long time, the string will no longer return to its initial state, as a reflection of its flow. Yet, in a funny way, this relation can also be remembered as “pain” after your first “belly flop” in a swimming pool. In a rapid disturbance, the water responds as solid-like, and in a relatively low disturbance (compared to its relaxation time), as liquid-like.

3.2. Shear strain, shear stress and shear rate definitions

To understand how some experiments are done in rheology, some definitions need to be presented as the shear strain, γ, shear stress, σ, and the shear rate, $\dot{\gamma}$. All the characterizations that are acquired in rheology is a consequence of the relationship among these quantities and the way the material is sheared (steady shear or oscillatory shear), and some of them are the viscosity, elasticity constant, viscoelastic moduli, and so on.

Figure 13A shows a photograph of a rheometer (HAAKE MARS 60, Thermo Fisher Scientific) where it is possible to observe a plate-type rotor coupled to the equipment. Figure 13B shows a scheme of the rotor and the position of the sample after being crushed by the rotor. The mechanical force applied in the investigated material is done by the rotor and the height between the base and the rotor is called *gap* and it is an important height which is predefined for each type rotor but which can also be manipulated.

The shear stress, σ, is defined as the shear force (force parallel to the action plan), F_{shear}, divided by the contact area, A, between the rotor and the sample as can be seen in Eq. 7. The unit of shear stress is Pa, a “shear pressure”. The deformation generated in the material or strain, γ, due to the shear stress is registered by the angle of rotation, θ, or the rotation arc length ($\theta \cdot R$) of the rotor, considering the sample gap as it is shown in Eq. 8, where R is the radius of the rotor. Strain is a dimensionless unit and sometimes it is represented as a percentage of strain. As it will be shown, it is more convenient to use the strain in the form of shear rate, $\dot{\gamma}$, which also takes into account the time

required to make such strain due to the application of such stress and its definition is shown in Eq. 9. The unit normally used for the shear rate is s^{-1}.

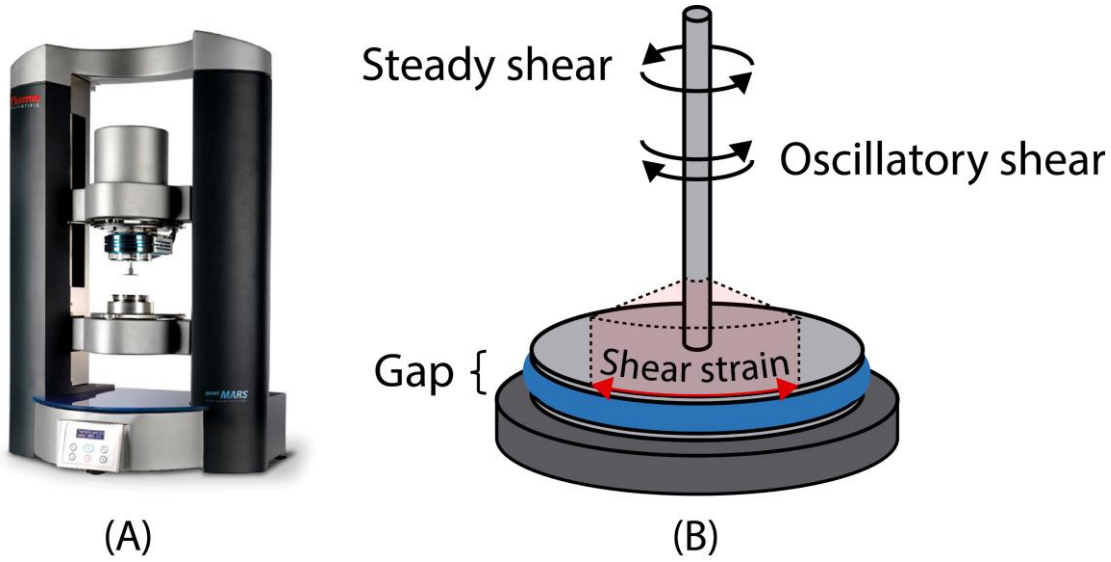

Figure 13. (A) Photograph of a rheometer and (B) scheme of a plate rotor and the shear strain generated by the application of shear stress. In (B) it is also shown the height gap and two methods of operation of the rheometer, steady or oscillatory shear.

$$\sigma = \frac{F_{shear}}{A} \qquad \text{Eq. 7}$$

$$\gamma = \frac{arc\ length}{gap} = \frac{\theta \cdot R}{gap} \qquad \text{Eq. 8}$$

$$\dot{\gamma} = \frac{\partial \gamma}{\partial t} \qquad \text{Eq. 9}$$

It is possible to apply the stress in two major ways in rheology: steady-shear and oscillatory-shear, and they can be seen in Figure 13B. In steady-shear (sections 3.3 and 3.4), where viscosities can be obtained, the shear is applied in a single direction of rotation, meaning that large deformation is caused in the material. In oscillatory-shear (section 3.5 and 3.6), where the viscoelasticity of the materials can be investigated, the maximum strain (or stress) is fixed and the strain (or stress) is applied in a cyclic way at

different frequencies. The stress applied in this case is very low and only internal structural rearrangements are induced in the material.

In addition to the way that stress/strain is applied, during the rheological experiments, it is possible to control which properties you would like to control: stress (controlled stress mode, CS) or strain (controlled rate mode, CR). The CS mode is more indicated when very low stress will be applied in the material.

3.3. Newtonian fluids, Hookean solids and non-Newtonian fluids

Newtonian fluids and Hookean solids are those materials that present only one proportionality constant that relates the shear stress applied, respectively with the shear rate and the strain. For the Newtonian fluids, this constant is the viscosity, Eq. 10, and for solids, the elasticity constant, G, showed in Eq. 11.

$$\sigma = \eta \cdot \dot{\gamma} \qquad \text{Eq. 10}$$

$$\sigma = G \cdot \gamma \qquad \text{Eq. 11}$$

As the interest in this thesis is for colloidal materials that show fluidity, I will focus this Chapter from now on in how to obtain the viscosity and viscoelasticity of these materials.

The Eq. 10 is also known as the Newton equation (dashpot model) and Figure 14 shows a typical result obtained for this type of material (flow curve). As can be seen in Figure 14A, the Newtonian fluids present only one angular coefficient, which is directly the viscosity of the fluid, showed in Figure 14B.

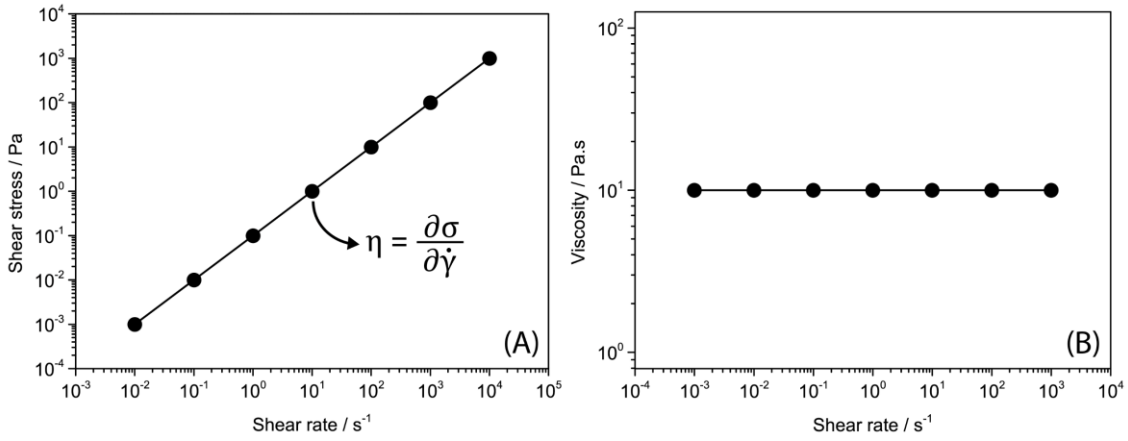

Figure 14. (A) Shear stress as function of the shear rate and (B) viscosity as function of the shear rate for a Newtonian fluid with viscosity of $10.0\ Pa.s$. (B) is obtained from the angular coefficient of (A) at the different shear rate.

3.4. Non-Newtonian fluids

Non-Newtonian fluids are those materials in which the "viscosity" is dependent on the shear stress applied. The viscosity for these materials is called apparent viscosity and the shear stress needs to be specified, $\eta_{ap}(\dot{\gamma})$. Most of the applied fluids belong to this classification and depending on its responsivity for the shear, they can be characterized as plastic, pseudoplastic or dilatant. The definitions of them can be seem below and an example of its apparent viscosity as function of the shear rate in Figure 15.

- Plastic: High initial viscosity (theoretically, infinity viscosity) and only deforms after a specific shear stress (called yield stress, σ_y). Examples: plastic bag, metals, concrete.
- Pseudoplastic or shear-thinning: present constant viscosity at low shear rate; after a critical shear stress, its viscosity decreases and another constant viscosity region at high shear rate. Examples: fluids containing WLMs, paint.

- Dilatant or shear-thickening: present constant viscosity at low shear rate and after the critical shear rate, its viscosity increases continuously. Examples: wet sand on the edge of the beach, concentrated solution of starch.

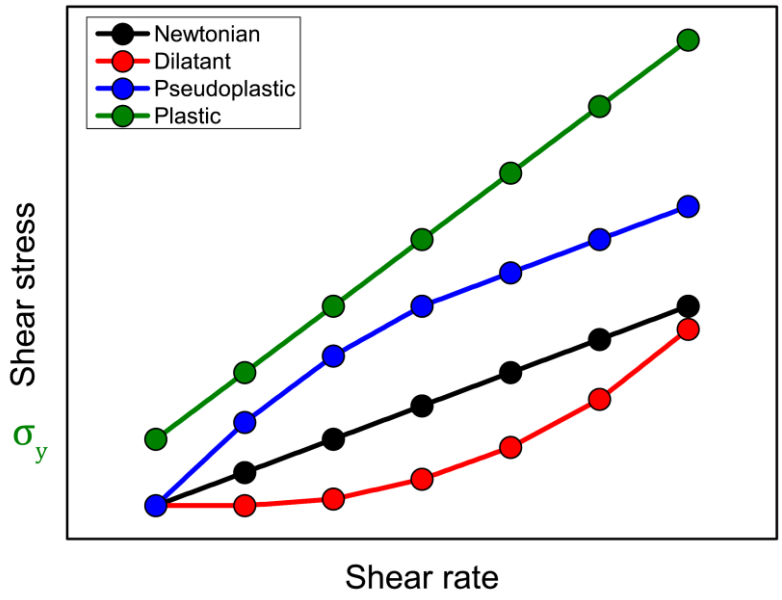

Figure 15. Shear stress as function of shear rate for different types of material: Newtonian, dilatant, pseudoplastic and plastic. σ_y is the yield stress for plastic materials.

Due to the long length of WLM and its entanglement, solutions containing WLM in semi-diluted or concentrated regime present a pseudoplastic flow curve. In low shear rates, the solution viscosity is practically the same and its "zero-shear viscosity", η_0, (its "viscosity at rest") is obtained through the extrapolation of the $\eta_{ap}(\dot{\gamma})$ in the Newtonian region up to $\dot{\gamma} = 0$. The viscosity is virtually unchanged in this region because the shear rate applied is not high enough to change the average conformation adopted by WLMs in the Brownian regime. Increasing the shear, the critical shear rate is achieved and the WLM begins to align with the flow which decreases the resistance to the flow and the apparent viscosity of the solution. The chains continue to align with the shear up to the point where most of the chains are aligned and a new constant viscosity region is achieved, mainly related with the viscosity of the solvent. This last region is very difficult to be obtained for solutions containing WLM because the shear rate for it is very high

and the turbulent flow occurs first. Thus, a typical flow curve for WLM in semi-diluted regime can be seen in Figure 16, together with a scheme representing the changes in the conformation of the WLM chains.

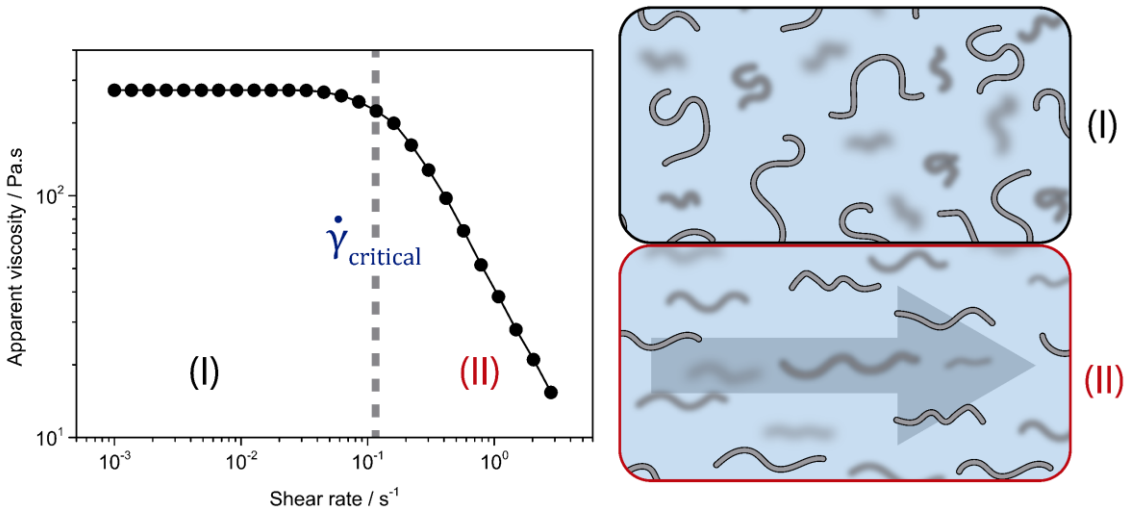

Figure 16. Typical flow curve for a fluid containing wormlike micelle in semi-diluted regime highlighting the average conformation of the chains in Brownian (I) and above the critical shear rate, $\dot{\gamma}_{critical}$.

As it was shown, the dependence of the $\sigma(\dot{\gamma})$ not always is a linear relationship and then the flow curve are addressed as experiments outside the linear responsiveness regime or “non-linear regime”. Even so, experiments in linear regime is very interesting, not to obtain direct viscosity relations, but to characterize the viscoelasticity of the solutions. The introductory aspects of the oscillatory-shear rheology will be presented in the next section and how it is possible to correlate the viscoelasticity with structural parameters of WLM in section 3.6.

3.5. Oscillatory-shear rheology [78,129]

Viscoelastic materials can change its elastic and viscous response depending on the stress/strain applied and, mainly, the mechanical frequencies that the disturbance is applied. The dependence of the viscoelastic moduli can be obtained with oscillatory-shear experiments in the linear responsiveness region and, to understand these experiments, some fundaments and mathematics need to be introduced. The cyclic strain applied can be represented by Eq. 12.

$$\gamma(t) = \gamma_0 \cos(\omega t) \qquad \text{Eq. 12}$$

Where γ_0 is the maximum strain and ω the disturbance frequency. Depending on the nature of the material investigated, the strain and the stress can have a phase lag. Solid materials respond immediately to applied deformation by a contrary force and liquid materials only shows a significant resistance to the flow when the direction of deformation is changed, that is, there is a phase lag between the maximum of strain and stress of $\pi/2$ rad. As viscoelastic systems have elastic and viscous components, its phase lag is intermediate between the solid and liquid (that is, between zero and $\pi/2$ rad). Figure 17 shows simulations of the stress obtained to the applied strain for solid, liquid and viscoelastic fluids, with phase lags of 0 for solid, $\pi/2$ for liquid and $0 < \theta < \pi/2$ for viscoelastic systems. The stress, considering the phase lag, can be represented by equation Eq. 13.

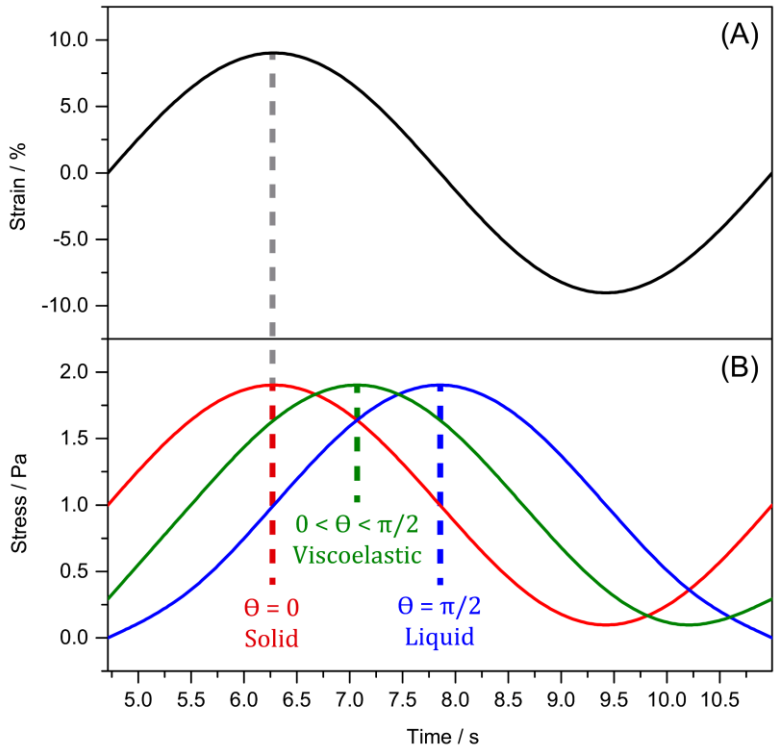

Figure 17. Simulated (A) strain and (B) stress as function of time in oscillatory rheology for solid, liquid and viscoelastic materials. θ is the phase lag. The values used for simulation was $\gamma_0 = 10\%$; $\eta = 10.0\ Pa\ s$ and $\omega = 1.0\ rad\ s^{-1}$.

$$\sigma(t) = \sigma_0 \sin(\omega t - \theta) \qquad \text{Eq. 13}$$

σ_0 is the maximum stress and θ is the phase lag. Eq. 12 and Eq. 13 can be conventionally rewritten to the complex plane using the Euler relation (Eq. 14), showed in Eq. 15 and Eq. 16, respectively.

$$e^{i\theta} = \cos\theta + i \sin\theta \qquad \text{Eq. 14}$$

$$\gamma(t) = \gamma_0\, e^{i\omega t} \qquad \text{Eq. 15}$$

$$\sigma(t) = \sigma_0\, e^{i(\omega t - \theta)} \qquad \text{Eq. 16}$$

Using the Hooke relation, Eq. 11, it is possible to write the elastic constant in the complex plane using the Euler relation as it is showed in Eq. 17 and Eq. 18.

$$\sigma = G\,\gamma \rightarrow G = \frac{\sigma}{\gamma} = \frac{\sigma_0\, e^{i(\omega t-\theta)}}{\gamma_0\, e^{i\omega t}} \rightarrow G = \frac{\sigma_0}{\gamma_0}\, e^{-i\theta} \qquad \text{Eq. 17}$$

$$G = \frac{\sigma_0}{\gamma_0}\,(\cos\theta - i\sin\theta) \qquad \text{Eq. 18}$$

The real component of Eq. 18 is the component that is in phase with the strain and it is called “storage modulus”, G', which is a measure of the amount of the stored energy during the periodic strain or stress and the out of phase or imaginary component ($\theta = (n + 1/2)\,\pi$, where n is an integer) is the “dissipative modulus”, $G"$, which is related with the amount of energy lost during the periodic application of stress or strain. Mathematically, these two moduli can be written as in Eq. 19 and Eq. 20, respectively, and G as in Eq. 21.

$$G' = \frac{\sigma_0}{\gamma_0}\cos\theta \qquad \text{Eq. 19}$$

$$G" = \frac{\sigma_0}{\gamma_0}\sin\theta \qquad \text{Eq. 20}$$

$$G = G' - iG" \qquad \text{Eq. 21}$$

The σ_0/γ_0 ratio gives the modulus of G, $|G^*|$, showed in Eq. 22 and the phase angle can be calculated through the relation $G"/G'$ showed in Eq. 23.

$$|G^*| = \frac{\sigma_0}{\gamma_0} = \sqrt{G'^2 + G"^2} \qquad \text{Eq. 22}$$

$$\tan\theta = \frac{\sin\theta}{\cos\theta} = \frac{G"}{G'} \qquad \text{Eq. 23}$$

With that, the storage and dissipative moduli can be rewritten as $|G^*|\cos\theta$ and $|G^*|\sin\theta$, respectively, and the complex viscosity, $|\eta^*|$, can be defined as in Eq. 24.

$$|\eta^*| = \frac{|G^*|}{\omega} \qquad \text{Eq. 24}$$

The complex viscosity values at the different frequency of disturbance in $rad\ s^{-1}$ has the same values of the dynamic viscosity obtained from flow curves in non-linear regime. This relation is known as Cox-Merz empirical rule and some application of this rule can be seen in [131–134].

The experiments to obtain the dependence of G' and G" as function of the shear stress or frequency of disturbance is the “stress sweep” and “frequency sweep”, respectively. As the frequency sweep needs to be performed in the linear responsiveness region of the material, the stress sweep experiment needs to be performed previously to characterize this region.

In a stress sweep experiment, the material is sheared with different shear stresses (in a strain sweep, with different shear strains) keeping the frequency of disturbance constant during the whole experiment. For the frequency sweep, a constant shear stress is applied (in the linear region previously determined in the stress sweep experiment) with different frequencies of disturbance so as to obtain the storage and dissipative moduli of the material at different frequencies. Examples of stress sweep and frequency sweep, together with the viscosity obtained by flow curves, can be seen in Figure 18 for a solution containing WLM in semi-diluted regime.

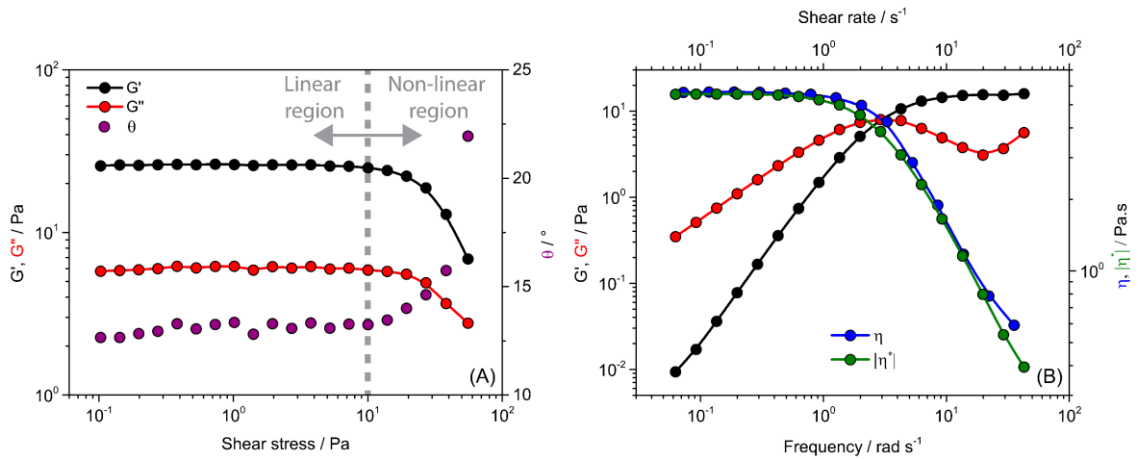

Figure 18. (A) Stress sweep and (B) frequency sweep together with the flow curve for a solution containing WLM in semi-diluted regime. In (A) it is also showed the phase lag, θ in degrees. In (B) the curves for $|\eta^*|$ and η are overlaid, indicating in this case the validity of the Cox-Merz empirical rule.

Another interesting parameter that is possible to correlate with the dynamic moduli is the relaxation time, $\tau_{rel.}$, which is the time for the material dissipates the stress applied to σ_0/e (where e is the Euler's number), that is, dissipation of 63% of σ_0. Applying a fixed strain in any material, the observation of $\sigma(s)$ dissipation leads to the conclusion that: Newtonian liquids tends to dissipate the stress almost instantly; Hookean solids will take the eternity to dissipate the stress, and real material will dissipates the stress exponentially.

For some viscoelastic material, it is possible to use the Maxwell model (string in series with a dashpot, Figure 19) to correlate the dissipation of the stress with the dynamic moduli G' and $G"$. The deformation generated in a single Maxwell element is given by $\gamma = \gamma_{el.} + \gamma_{visc.}$, where $\gamma_{el.}$ is the deformation in the string and $\gamma_{visc.}$ is the deformation on the dashpot due to the application of the stress. Differentiating this relation with respect to time and using the string and dashpot relations, gives Eq. 25.

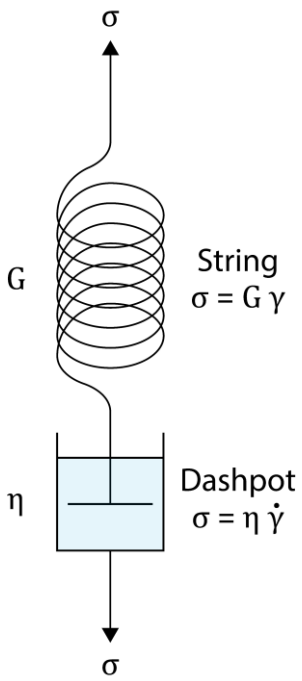

Figure 19. Maxwell model with a single element, string in series with a dashpot.

$$\frac{d\gamma}{dt} = \dot{\gamma} = \dot{\gamma}_{el.} + \dot{\gamma}_{visc.} = \frac{1}{G}\frac{d\sigma}{dt} + \frac{\sigma}{\eta} \qquad \text{Eq. 25}$$

For a constant strain, $d\gamma/dt = 0$, Eq. 25 can be rewritten as in Eq. 26.

$$\frac{\sigma}{\eta} + \frac{1}{G}\frac{d\sigma}{dt} = 0 \qquad \text{Eq. 26}$$

Whose differential solution is represented by Eq. 27.

$$\sigma(t) = \sigma_0 \exp\left(-\frac{G}{\eta}t\right) \qquad \text{Eq. 27}$$

Which is an expression for the stress dissipation as function of time depending on the elastic and viscous moduli of the material. The exponential term in Eq. 27 is, by definition, the relaxation time $\tau_{rel.} = \eta/G$ and so it is a relation between the elastic and viscous moduli of the material, rewritten in Eq. 28.

$$\sigma(t) = \sigma_0 \exp\left(-\frac{t}{\tau_{rel.}}\right) \qquad \text{Eq. 28}$$

In Eq. 28, when $t = \tau_{rel.}$, $\sigma(\tau_{rel.}) = \sigma_0/e$ as it was discussed before. Using the relaxation time definition and the definitions of $\gamma(t)$ and $\sigma(t)$ on the complex plane, showed by Eq. 15 and Eq. 16, respectively, Eq. 25 can be rewritten as in Eq. 29.

$$\frac{d\gamma}{dt} = \frac{1}{G}\frac{d\sigma}{dt} + \frac{\sigma}{\eta} \rightarrow \sigma = -\tau_{rel.}\frac{d\sigma}{dt} + \eta\frac{d\gamma}{dt} \rightarrow$$

$$\sigma_0 e^{i(\omega t-\theta)} = -\tau_{rel.}\frac{d}{dt}\left(\sigma_0 e^{i(\omega t-\theta)}\right) + \eta\frac{d}{dt}\left(\sigma_0 e^{i\omega t}\right) = \qquad \text{Eq. 29}$$

$$= -\tau_{rel.}\sigma_0 i\omega e^{i(\omega t-\theta)} + \eta\gamma_0 i\omega e^{i\omega t}$$

Dividing Eq. 29 by $e^{i\omega t}$ in both sides and using again the definition of relaxation time, it can be rewritten as in Eq. 30.

$$\sigma_0 e^{-i\theta}(1 + i\omega\tau_{rel.}) = i\omega G\tau_{rel.}\gamma_0 \rightarrow \sigma_0 e^{-i\theta} = \frac{i\omega G\tau_{rel.}\gamma_0}{1 + i\omega\tau_{rel.}} \qquad \text{Eq. 30}$$

Dividing both sides by γ_0 and using the definition of the elastic constant showed in Eq. 17, Eq. 30 can be rewritten as Eq. 31.

$$G = \frac{\sigma_0 e^{-i\theta}}{\gamma_0} = \frac{i\omega G\tau_{rel.}}{1 + i\omega\tau_{rel.}} \quad \text{Eq. 31}$$

Multiplying Eq. 31 by $\frac{1-i\omega\tau_{rel.}}{1-i\omega\tau_{rel.}}$ and isolating the real part from the imaginary part, we have Eq. 32.

$$G = \frac{\omega^2 G\tau_{rel.}^2}{1 + \omega^2\tau_{rel.}^2} + i\frac{\omega G\tau_{rel.}}{1 + \omega^2\tau_{rel.}^2} \quad \text{Eq. 32}$$

Using the same strategy that the elastic constant G can be written as a dissipative and storage modulus, Eq. 21, the final expression of G' and G" can be obtained as in Eq. 33 and Eq. 34, respectively [78].

$$G'(\omega) = \frac{\omega^2 G\tau_{rel.}^2}{1 + \omega^2\tau_{rel.}^2} \quad \text{Eq. 33}$$

$$G"(\omega) = \frac{\omega G\tau_{rel.}}{1 + \omega^2\tau_{rel.}^2} \quad \text{Eq. 34}$$

When $G' = G"$, $\tau_{rel.} = 1/\omega_{co}$, and then the relaxation time is numerically the inverse of the cross-over frequency, ω_{co}. With that, if the viscoelastic system investigated behaves like a Maxwellian model, Eq. 33 and Eq. 34 can be used to predict its elastic and viscous modulus and the relaxation time can be estimated when $G' = G"$.

Most of the times, aqueous solution containing WLMs in semi-diluted regime behaves as Maxwell fluid in low and intermediate frequencies, where only one relaxation time is enough to describe the elastic and viscous moduli as function of the frequency of disturbance. But for high frequencies, the dynamic moduli significantly diverge from the Maxwell model because additional relaxation mechanisms of the chains, as the Rouse movements and breathing modes [81,135,136], are not included on the model. Figure

20 shows the application of the Maxwell model in the results obtained in the frequency sweep experiment presented in Figure 18B for a solution containing WLM in semi-diluted regime.

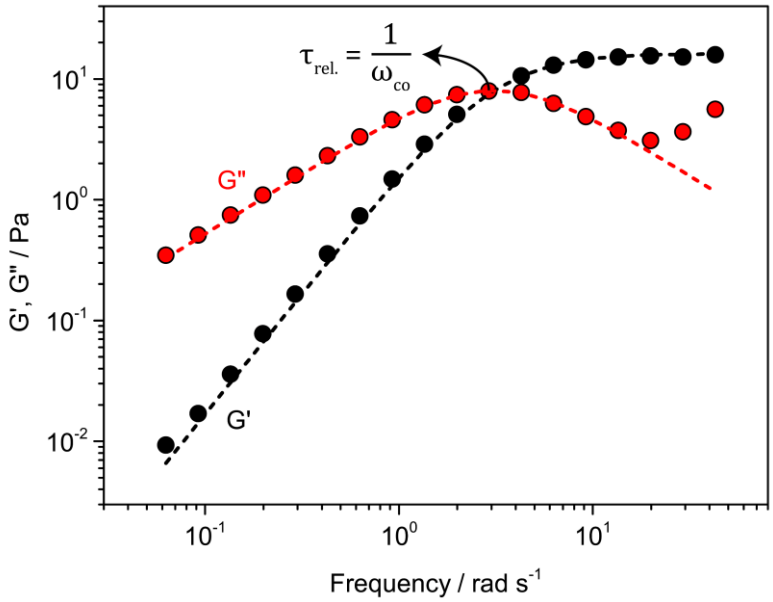

Figure 20. G' and $G"$ as function of the frequency of disturbance in a frequency sweep experiment for a solution containing wormlike micelles in semi-diluted regime. Circles are experimental values and the dashed lines the Maxwell model represented by Eq. 33 and Eq. 34. The relaxation time is obtained through the inverse of the cross-over frequency as it is shown in the Figure when $G' = G"$.

As can be seen, at low and intermediate frequencies, the Maxwell model fits very well the experimental curves, and diverges for high frequencies. The $\tau_{rel.}$ is obtained from the inverse of the frequency where $G' = G"$ which is also highlighted in Figure 20. There are more complex models available with different strategies to also fit the high frequency regions [78,137,138], but they will not be presented here because only the Maxwell model was applied in some of the solutions containing WLMs investigated in this thesis.

3.6. Oscillatory rheology of fluids containing WLM

Solutions containing wormlike micelles in the semi-diluted or concentrated regime (where chains are entangled) show an elastic behavior when a mechanical stress is applied. As seen in the previous section, the presence of the elastic behavior, in addition to dissipative, alters the entire tension relaxation dynamic and a very peculiar mechanical spectrum is observed.

The processes of stress relaxation of solutions containing WLMs are very different from that observed for polymeric solutions in the dilute or concentrate regime and, in order to investigate the origin of this difference, Cates [135] proposed that, in addition to the classic reptation movements of the polymer chains, in which the chains slide as snakes among the points of entanglements through an imaginary tube formed by the contact points of the chain with the neighboring chains, represented in Figure 21, the wormlike micelles (at that time called "living polymers") had an additional feature that was the breaking/recombination of the chains (Figure 22) that could occur throughout the relaxation process due to the nature of WLM formation (intermolecular interactions instead of covalent bonds as in polymers).

Cates and Candau [139] showed that both the reptation and the breaking/recombining time is associated with the contour length of the WLM by the relations showed by Eq. 35 and Eq. 36, respectively.

$$\tau_{rep.} = \frac{\bar{L}_c^2}{D_c} \qquad \text{Eq. 35}$$

$$\tau_{b.} = \frac{1}{k_{b.}\bar{L}_C} \qquad \text{Eq. 36}$$

Where D_C is the curvilinear diffusion constant of the chain in its tube and $k_{b.}$ is the rate associated with the breaking.

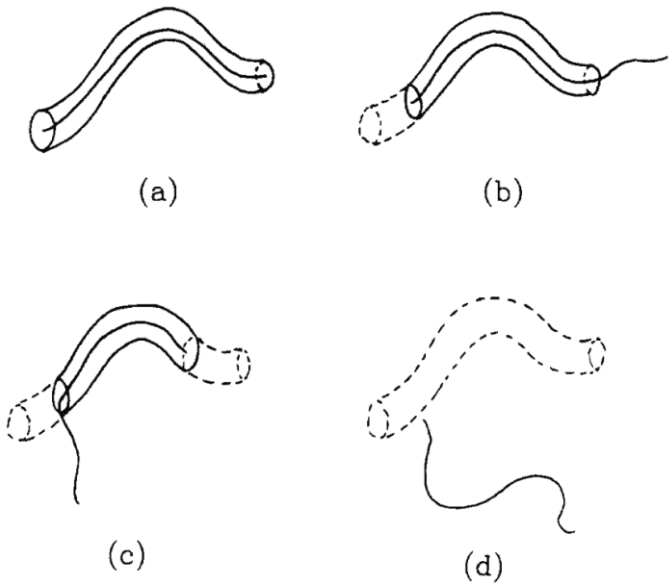

Figure 21. Classical reptation movement of a polymer chain that can also be applied for wormlike micelle chains in the regime where the reptation time is much higher than the breaking/recombining time, $\tau_{rep.} \gg \tau_{b.}$. The letters (a) to (d) indicates the chronological progress of the reptation movement. Adapted with permission from reference [135].

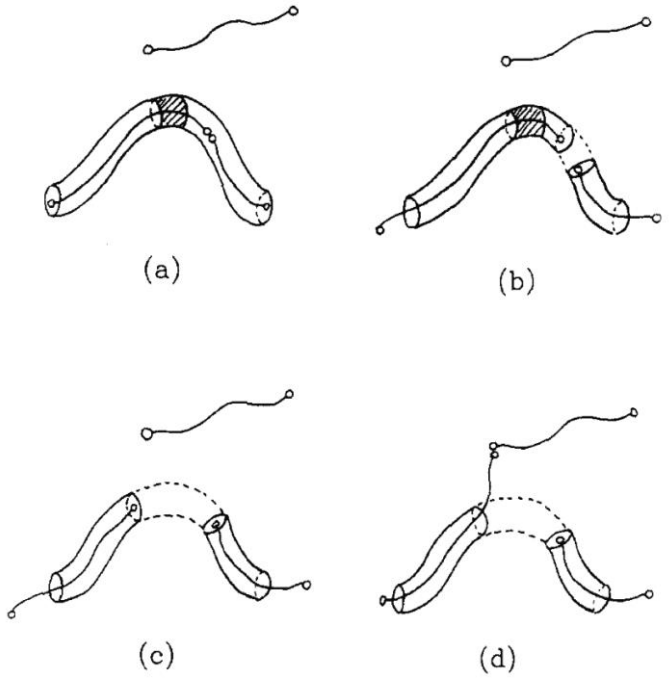

Figure 22. Breaking/recombining mechanism proposed by Cates for a wormlike micelle chain in the fast-breaking regime, $\tau_{b.} \gg \tau_{rep.}$.The WLM chain breaks in (b) and recombines with a lateral WLM chain in (d). Adapted with permission from reference [135].

Even the WLMs showing two characteristic times, Cates and Candau [139] showed that it was possible to use the Maxwell model with one relaxation time ($\tau_{rel.}$) to fit the oscillatory-shear behavior of solutions containing WLM in entangled regime assuming that the breaking time is much faster than the reptation time, $\tau_{b.} \gg \tau_{rep.}$. In this condition, the unique relaxation time of the solution summarizes to Eq. 37.

$$\tau_{rel.} = \sqrt{\tau_{b.}\tau_{rep.}} \qquad \text{Eq. 37}$$

For low and intermediate disturbance frequencies, the Maxwell model in general is a very good model to predict the elastic and viscous moduli of WLM solutions. Another way to visualize the deviation region of the Maxwell model is using the Cole-Cole plot showed by Eq. 38 and illustrated by Figure 23 for a solution containing cetylpyridinium chloride and sodium salicylate [136]. The dashed semi-circle (Intercepting $G'/G_0 = 1$) in Figure 23 represent the behavior of a Maxwell fluid with a unique relaxation time. The deviations of the semi-circle, which is higher for lower surfactant concentrations (also showed in Figure 20) occurs due to the predominance of additional relaxation times like breathing motions (tube-length fluctuations) and Rouse movements (non-cooperative movements of the chains), which are more dominant in higher frequencies.

$$\left(G' - \frac{G_0}{2}\right)^2 + G''^2 = \frac{G_0^2}{4} \qquad \text{Eq. 38}$$

In addition to the relaxation time, it is also possible to obtain structural parameters of WLMs with the oscillatory-shear rheology [48,139]. The mesh size, ξ, is obtained by comparison of G_0 (which depends on the volumetric fraction of micelles in solution and is obtained from the elastic moduli in oscillatory-shear experiments when $\omega \to \infty$) with thermal energy through the relationship shown by Eq. 39.

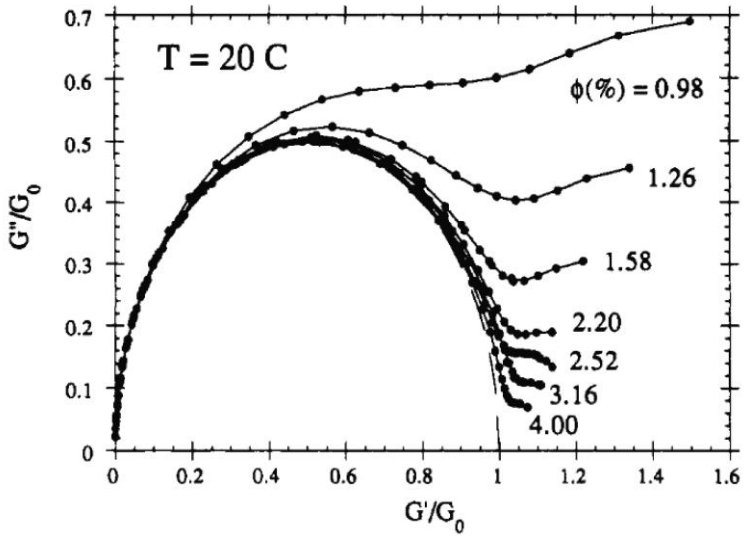

Figure 23. Cole-Cole plot for a WLM solution containing cetylpyridinium chloride and sodium salicylate in molar proportion of 0.5 varying the surfactant weight percentage, ϕ, from 0.98 to 4.0% at $20\,°C$. The half circle (dashed line) corresponds to an ideal Maxwell element with a unique relaxation time. Adapted with permission from reference [136].

$$\xi = \left(\frac{k_B T}{G_0}\right)^{\frac{1}{3}} \qquad \text{Eq. 39}$$

Knowing the persistence length with scattering techniques, it is possible to estimate the entanglement length relating it with the mesh size by the Eq. 40.

$$l_e = \frac{\xi^{5/3}}{l_p^{2/3}} \qquad \text{Eq. 40}$$

The contour length can be obtained using the l_e, $G"_{min}$ and G_0 through the relation showed by Eq. 41.

$$\frac{l_e}{\bar{L}} = \frac{G"_{min}}{G_0} \qquad \text{Eq. 41}$$

Some works [140–144] used the frequency where the Maxwell model diverge from the experimental data or the frequency at $G"_{min}$ to isolate the breaking/recombining time from the reptation time, but not all authors fully agree with this as there is no theoretical support by the model proposed by Cates and Candau [139].

As described in the previous Chapter (Chapter 2), the combination of cationic surfactant with some aromatic anions can induce the formation of WLM. The spontaneity for formation of this self-assembly, intrinsically depends on the interactions between the two species. The energy involved in the process can be measured in calorimetric experiments, in which the main points is presented in Chapter 4.

4. Isothermal titration calorimetry

4.1. Introduction

Isothermal titration calorimetry, ITC, is a titration automation technique that monitors the energy in the form of heat released or absorbed by the system throughout the titration. In the equipment, there are two cells, the "reference cell" containing the solvent of the solution investigated (normally water for aqueous systems) and the "reaction cell", where in fact the titration is performed. Throughout the titration, the reference cell receives constant heat from a heater and the reaction cell a variable heat from another heater. When an aliquot is added to the reaction cell, depending on the titrant/titrand interactions, energy in the form of heat can be released (exothermic) or absorbed (endothermic) by the system, creating a temperature difference between the cells. To compensate this temperature variation (in order of $0.1\ °C$), the reaction cell heater is adjusted so that to keep the temperature variation as close to isothermal as possible throughout the experiment. Figure 24A shows a typical example of ITC equipment (PEAQ-ITC, Malvern) and Figure 24B a schematic of the main parts of the equipment.

If with the titration the difference of the temperature between the reaction to reference cell becomes negative, the equipment increases the heat supplied to the reaction cell and if it is positive, the equipment decreases the heat supplied. This manipulation of the heater is the raw data obtained in an ITC experiment where each titrant injection is associated with a peak in the raw data. The peaks can be upwards (increase in the electric power due to a endothermic process) or downwards (decrease in the electric power due to a exothermic process) and the integration of each peak gives the energy as heat, q, involved in the injection. As the reaction cell in general is an open system, the heat is the same as the enthalpy, $q_p = \Delta H$, and if the enthalpy is divided by the titrant molar amount in the standard conditions, the standard molar enthalpy is obtained, ΔH_m^o, in $kJ\ mol^{-1}$ of titrant. Figure 25A shows a typical raw data obtained from the titration of C_{14}TAB $11.0\ mmol\ L^{-1}$ in a reaction cell containing aqueous

solution of sodium salicylate $1.2\,mmol\,L^{-1}$ and in Figure 25B the enthalpogram, showing the integration of each peak.

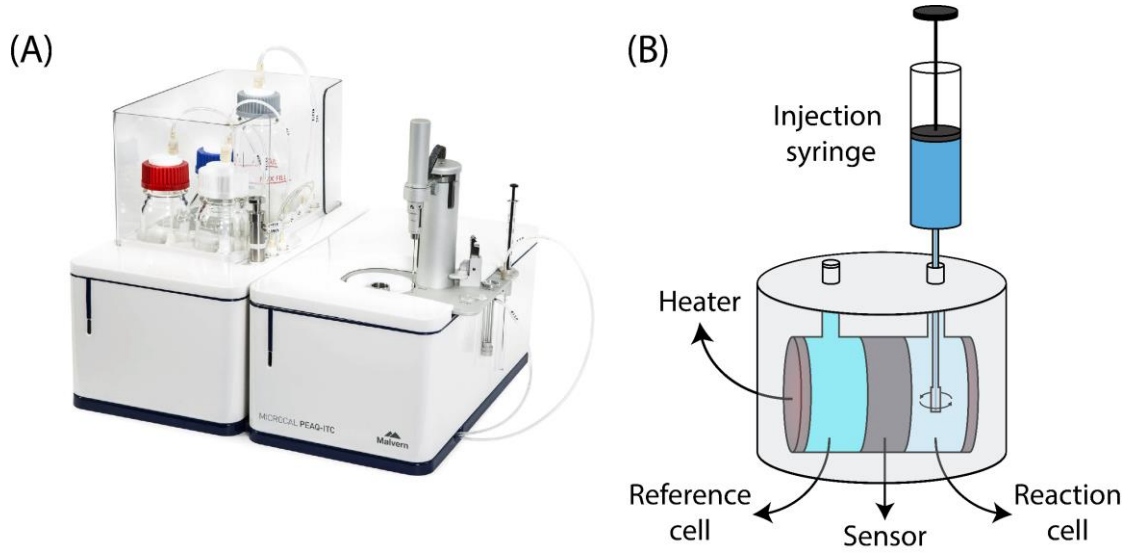

Figure 24. (A) Photograph of a typical isothermal titration calorimetry and (B) equipment diagram showing the injection syringe, reference and reaction cell, the sensor, and the heaters.

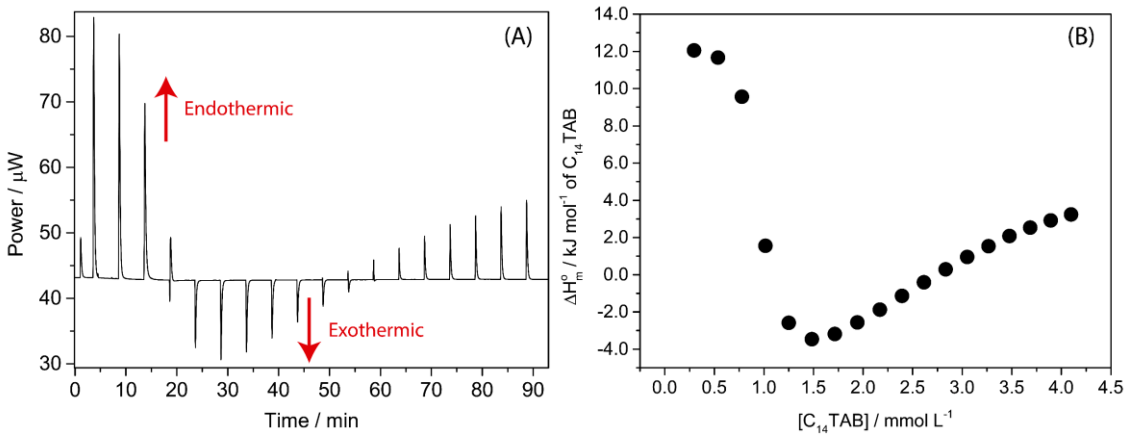

Figure 25. (A) Raw data of an ITC experiment, electric power as function of the time and (B) standard molar enthalpy obtained from the integration of each peak from (A). Titration of $C_{14}TAB$ $11.0\,mmol\,L^{-1}$ in a reaction cell containing sodium salicylate $1.2\,mmol\,L^{-1}$ [68].

4.2. Thermodynamic parameters of aggregation through calorimetry

Due to its high sensitivity, ITC is a very powerful technique to investigate colloidal systems containing surfactants. With the thermograms, it is possible to obtain the CMC and several thermodynamic parameters associated with the aggregation phenomenon as for example the standard molar enthalpy, ΔH_{ag}^{o}, Gibbs free energy, ΔG_{ag}^{o}, entropy, ΔS_{ag}^{o}, and others [145]. For these experiments, normally an aqueous solution containing surfactant in concentration higher than its CMC is titrated in a reaction cell containing or not an analyte of interest. Figure 26 shows a typical enthalpogram obtained from the titration of $C_{14}TAB$ $40.0\ mmol\ L^{-1}$ in a reaction cell containing only water where spherical micelles are formed in the reaction cell when the [$C_{14}TAB$] is around the CMC value.

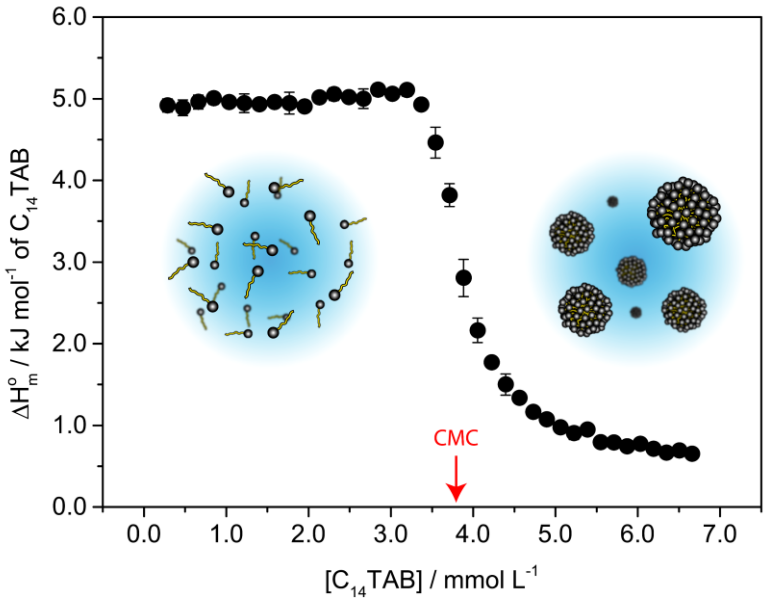

Figure 26. Enthalpogram obtained from the titration of $C_{14}TAB$ $40.0\ mmol\ L^{-1}$ in a reaction cell containing water. Before the CMC the surfactant molecules are in the form of unimers in solution and after CMC in spherical aggregates.

As can be seen in Figure 26, thermograms of spherical micelle formation presents an initial region with constant slope, which is associated with the demicellization process of the titrant (once its concentration is higher than the surfactant CMC in the syringe) followed by a very cooperative process (in this case, exothermic), associated with the formation of aggregates in the reaction cell. The inflection point of the cooperative region (maximum/minimum value of the first derivative or second derivative equal to zero) determines the CMC value of the surfactant titrated at the specific conditions investigated (temperature and presence or not of an analyte) and the ΔH^o_{mic} is calculated from the difference between the linear extrapolation of enthalpy at the CMC before and after the aggregation process. Figure 27 shows how the CMC value is obtained from the second derivative method and how the ΔH^o_{mic} is obtained using the linear extrapolations from Figure 26.

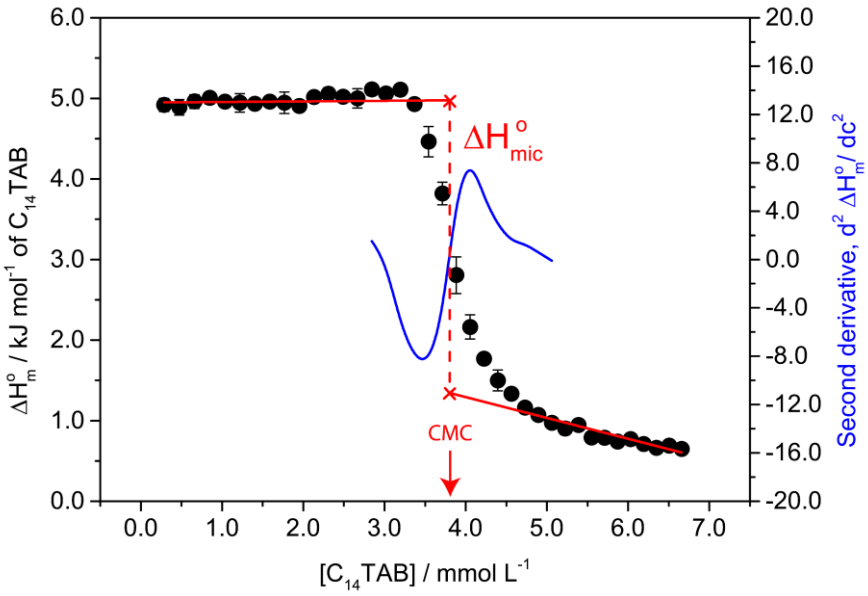

Figure 27. Enthalpogram obtained from the titration of C_{14}TAB $40.0\ mmol\ L^{-1}$ in a reaction cell containing water, showing how the CMC is obtained from the second derivative method and the calculation of ΔH^o_{mic} from linear extrapolations.

The Gibbs free energy for the aggregation process can be calculated using the CMC value and depends on the nature of the surfactant used as can be seen in Eq. 42. [146]

$$\Delta G_{mic}^{o}\begin{cases}= RT\ln x_{CMC} & non-ionic\ surfactants\\ = (2-\alpha)RT\ln x_{CMC} & ionic\ surfactants\end{cases} \quad \text{Eq. 42}$$

Where x_{CMC} is the molar fraction of surfactant at the CMC and α is the ionization degree of the micelle (fraction of counterions not bound to the micelle). ΔG_{mic}^{o} expression presented in Eq. 42 for ionic surfactants is valid only for aqueous solutions and/or low ionic strength [146] and the value of α can be experimentally determined from the slopes of the conductivity plots below and above the CMC [147].

The standard entropy for the micellization can be calculated using the Gibbs relation as it is shown in Eq. 43 [146].

$$\Delta G_{mic}^{o} = \Delta H_{mic}^{o} - T\Delta S_{mic}^{o} \rightarrow T\Delta S_{mic}^{o} = \Delta H_{mic}^{o} - \Delta G_{mic}^{o} \quad \text{Eq. 43}$$

The variation of ΔH_{ag}^{o} with the temperature or the thermal heat capacity of aggregation, $\Delta C_{p,ag}^{o}$, is another interesting thermodynamic parameter to be considered in calorimetric experiments and it can be calculated using the Eq. 44.

$$\Delta C_{p,ag}^{o} = \left(\frac{\partial \Delta H_{ag}^{o}}{\partial T}\right)_{p} \quad \text{Eq. 44}$$

$\Delta C_{p,ag}^{o}$ is related with the reduction of the hydrophobic area exposed to the aqueous phase with the aggregation [148]. Spherical micelle aggregation presents a negative value of $\Delta C_{p,mic}^{o}$ [68,149] showing that the aggregation leads to a decrease in hydrated hydrophobic area.

The same concepts of calculation and determination of thermodynamic parameters presented for spherical micelles can also be used for systems that form WLM in solution [68,150,151]. The thermogram obtained for WLMs is considerably different from that obtained for spherical micelle formation depending on the combination of

surfactant/analyte used and the Figure 25B already presented is a typical example of thermogram for WLM formation. The CMC and ΔH^o_{WLM} determination for WLM formation in ITC can be seen in Figure 28.

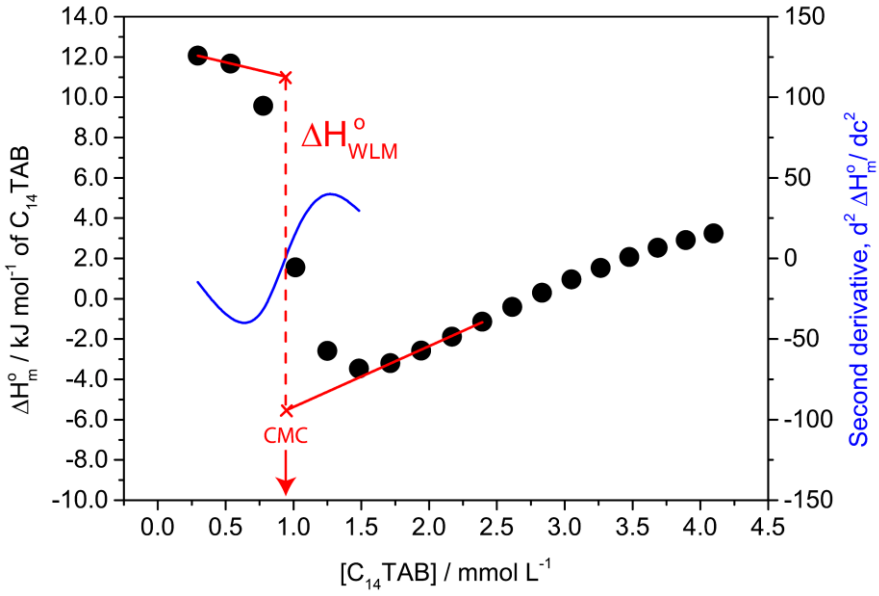

Figure 28. Enthalpogram obtained from the titration of $C_{14}TAB$ $11.0\ mmol\ L^{-1}$ in a reaction cell containing sodium salicylate $1.2\ mmol\ L^{-1}$, showing how the CMC is obtained from the second derivative method and the calculation of ΔH^o_{mic} from linear extrapolations.

The interpretation of the different regions of the thermogram with the morphology of the aggregate is not so simple as in the case of spherical micelles and it is worth mention the historical contribution for the interpretations that we have today.

For this historical survey, a search was made on the Web of Science for articles containing calorimetric study with any elongated micelles (the exact research was: *TS=(((worm-like* OR wormlike* OR threadlike* OR cylindrical* OR elongated*) micelle*) AND (calorim* OR ITC) AND titration))*. The research returned as results, on 08/18/2020, 36 works, of which 6 are from our research group.

The first relevant result to mention was published by Matthew *et al.* in 2010 [142] where the authors induced the formation of WLM using $C_{16}TAB$ with $NaNO_3$ in different

concentrations and characterized the solution with ITC, rheology and small-angle neutron scattering (SANS). In high concentration, above $40.0\ mmol\ L^{-1}$ of surfactant, WLMs are clearly induced and explain the results of rheology and SANS but, for the ITC experiments, the surfactant concentration titrated was $10.0\ mmol\ L^{-1}$ with the reaction cell containing 0, 10, 20 or $30\ mmol\ L^{-3}$ $NaNO_3$. As interpreted by the authors, it was observed changes in the enthalpogram (Figure 29) with the $NaNO_3$ addition but these concentrations were not high enough to induce the formation of WLMs in the calorimeter. Even though this work clearly does not deliver promising results for WLM formation in ITC, it was relevant to the research because it shows that the induction of WLM using inorganic salts by calorimetry is relatively complex due to the high concentration required to induce its formation.

The first enthalpy obtained from ITC which the authors associated with the morphology changes from spherical to WLM was published by Liu *et al.* in 2011 [152]. The authors titrated a solution containing a mixture of 1-hexadecyl-3-methylimidazolium bromide (C_{16}mimBr) $40.0\ mmol\ L^{-1}$/sodium tosylate (NaTos) $160.0\ mmol\ L^{-1}$ (or NaSal $1{,}000\ mmol\ L^{-1}$) into a reaction cell containing the same concentration of C_{16}mimBr. For this concentration of surfactant, it is known that NaTos and NaSal favor the formation of WLM in the salt range concentration of 20 to $60\ mmol\ L^{-1}$ and 30 to $180\ mmol\ L^{-1}$, respectively [152]. According to the authors, with the titration, three main process occur and is related with the enthalpy obtained: aggregate dilution; organic salt dilution and the change of the aggregate morphology. The thermogram obtained for the NaTos after the subtraction of the NaTos dilution (obtained from the titration of NaTos at the same concentration into the reaction cell containing only water) can be seen in Figure 30B, together with the solution viscosity at the same concentration of the reaction cell in Figure 30A. The authors proposed that, the enthalpy associated with the morphology change (from spherical to WLM), can be calculated as demonstrated by ΔH_{tra} showed in Figure 30B, which is the difference between the enthalpy of aggregate dilution (obtained through the extrapolation of the fit in the regions where only spherical micelles are present) and the experimental curve. It is worth noting that the ΔH_{tra} changes with the analyte/surfactant ratio along the ITC.

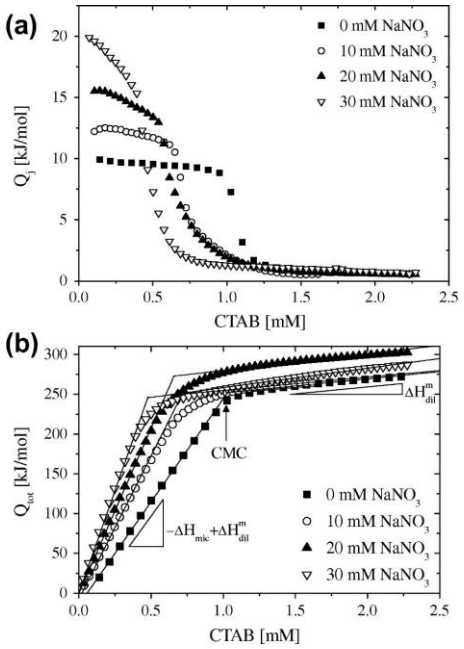

Figure 29. (a) Molar heat of injection and (b) total molar heat measured using ITC for demicellization of C_{16}TAB $10.0\ mmol\ L^{-1}$ at $NaNO_3$ concentrations shown at $25\ °C$. Lines show fits of the data at low and high C_{16}TAB concentration for determination of thermodynamic parameters. Adapted with permission from reference [142].

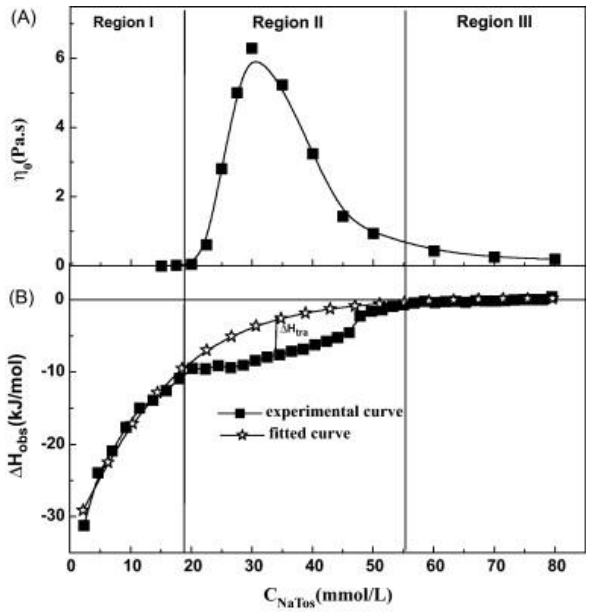

Figure 30. (A) Zero-shear viscosity versus NaTos concentration at a fixed C_{16}mimBr concentration of $40.0\ mmol\ L^{-1}$; (B) Dependence of enthalpy change with the titration of C_{16}mimBr/NaTos $40.0\ mmol\ L^{-1}/160.0\ mmol\ L^{-1}$ in a reaction cell containing C_{16}mimBr $40.0\ mmol\ L^{-1}$. Adapted with permission from reference [152].

The next chronological contribution for the comprehension of ITC of WLM formation, was published by Bešter-Rogač *et al.* in 2014 [153] where they investigated the titration of dodecyltrimethylammonium chloride (C_{12}TAC) in different concentrations in a reaction cell containing 4-hydroxybenzoate (4-HB) or methyl-4-hydroxybenzoate (MeP) or ethyl-4-hydroxybenzoate (EtP) $10.0\ mmol\ L^{-1}$ at different temperatures, from 278 to 328 K. For 4-HB and MeP the enthalpograms obtained at different temperature were the sigmoid expected for the formation of spherical aggregates, but EtP presented remarkably different enthalpograms. Figure 31 shows the enthalpogram obtained for EtP at different temperatures. Bešter-Rogač interpreted the different regions of the enthalpogram, according to Figure 31, as follow: the light-brown region was associated with the demicellization of the micelles of C_{12}TAC titrated; the white region between the light and dark brown was associated with the formation of spherical micelles; the dark brown region is where the concentration of C_{12}TAC in the reaction cell has reached sufficient values to induce the formation of elongated micelles in the reaction cell (corroborated with conductivity and viscosity) and, finally, the blue region is where the spherical micelles are again induced in the reaction cell due to the high [C_{12}TAC]/[EtPNa] ratio.

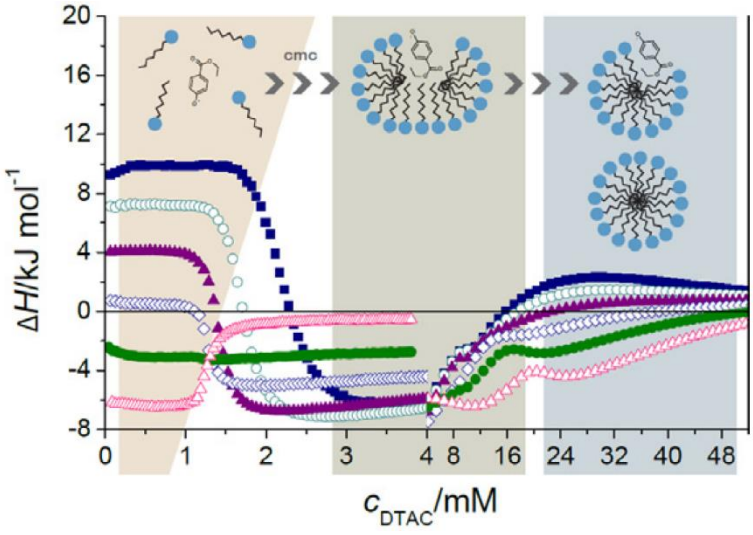

Figure 31. Enthalpograms obtained for the titration of 50.0 or $280.0\ mmol\ L^{-1}$ C_{12}TAC in a reaction cell containing $10.0\ mmol\ L^{-1}$ EtPNa at different temperatures, (from blue to pink, the temperature were, in this order: 328.15, 318.15, 308.15, …, $278.15\ K$). Both solutions were in pH higher than 9.8. Adapted with permission from reference [153].

After that, it was published the first article of professor Edvaldo Sabadini research group by Ito *et al.* in 2015 [154] followed by another publication in 2016 [155] and a book chapter by Sabadini and Karl Clinckspoor in 2017 [156]. All these three publications followed the same interpretation for the thermogram of WLM formation proposed by Ito in 2015. All these studies involved the titration of C_{14}TAB in a reaction containing different aromatic salts at $298\ K$ and some of these results are presented in Figure 32. As Bešter-Rogač, some of the aromatic salts also presented only the sigmoid profile expected for spherical micelle formation, but, for some of them, an intense endothermic process was observed after the minimum of the enthalpogram. Being fairly fair, Bešter-Rogač also observed an increase in enthalpy after the minimum of the enthalpogram in some cases (Figure 31), but in her case the increase was much more subtle due to experimental conditions and the attribution of this increase with the WLM was not done. Beyond that, the interpretation of the different regions of the thermogram by Ito with the morphology of the aggregate was quite different from that proposed by Bešter-Rogač. According to Ito, four main regions can be highlighted in these enthalpograms (Figure 32) and two inflection points are pointed out: the first one is related with the mixed spherical micelle formation and the second one with the WLM growth (the WLM is formed, according to Ito, before the beginning of the second cooperative exothermic process, region 3), being the minimum of the enthalpogram the physicochemical conditions where the aggregate reached its maximum length (corroborated by viscosity and light scattering) and the increase of enthalpy is associated with the shrinkage of the WLM aggregate up to only mixed spherical micelles are present in the reaction cell. After that, the research group published more two articles in the subject by Clinckspoor *et al.* [73] and Creatto *et al.* [157] in 2018, keeping the same interpretation of Ito.

Part of this interpretation made by Ito was complemented only in 2019 by de Souza *et al.* with the publication entitled “A new interpretation of the mechanism of WLM formation involving a cationic surfactant and salicylate” [68] where the thermogram of WLM formation using C_{14}TAB and sodium salicylate was brought back. The interpretation of de Souza is summarized in Figure 33 where the thermogram was plotted together with the surface tension and the percentage of salicylate incorporated measured by time resolved fluorescence. With this new interpretation, three regions

were characterized: I – demicellization and ionic-pair formation; II – Aggregate formation and growth and, III – Redistribution of salicylate and shrinkage of the WLM. Unlike what had been proposed, de Souza proposed that the first micellar aggregate to be formed was in fact the wormlike micelle, because, due to the excess of salicylate ions in the reaction cell, the spherical micelle was not favorable to be formed as the first aggregate and a region on the thermogram associated only with the spherical micelle formation was not assigned. The exothermic cooperative region was directly associated with the formation of this elongated aggregate and, concomitantly, with its growth. Similarly to the definition of CMC for spherical micelles in calorimetry (the inflection point of the sigmoid region), the critical concentration of wormlike micelle formation was defined as the inflection point of this cooperative region and the enthalpy of aggregate formation as the difference in enthalpy values extrapolated from the regions before and after the formation of the aggregate, at the inflection point, as it was shown in Figure 28.

Part of Ito's interpretation, which was complemented by de Souza, is quite efficient for the enthalpogram of C_{14}TAB and sodium salicylate and has been used to interpret similar systems [150,151] but several questions still persist like what is the endothermic process that becomes extremely relevant after the formation of the wormlike micelles to the point of reversing the enthalpogram trend? Where does the transition between the elongated aggregate and the mixed spherical micelle occur? Are we in fact correct in assuming that the first aggregate to be formed is the elongated one, or are we just not having a sensitive enough technique to observe that in the cooperative exothermic region and what we have is a very quick transition from spherical to wormlike micelle?

As it will be presented in Chapter 8 and 9 (already published, [150,151]), the enthalpogram showed for salicylate is also observed for different aromatic salts with C_{14}TAB that favors the formation of WLM in ITC conditions, but new feature and interpretations also emerge.

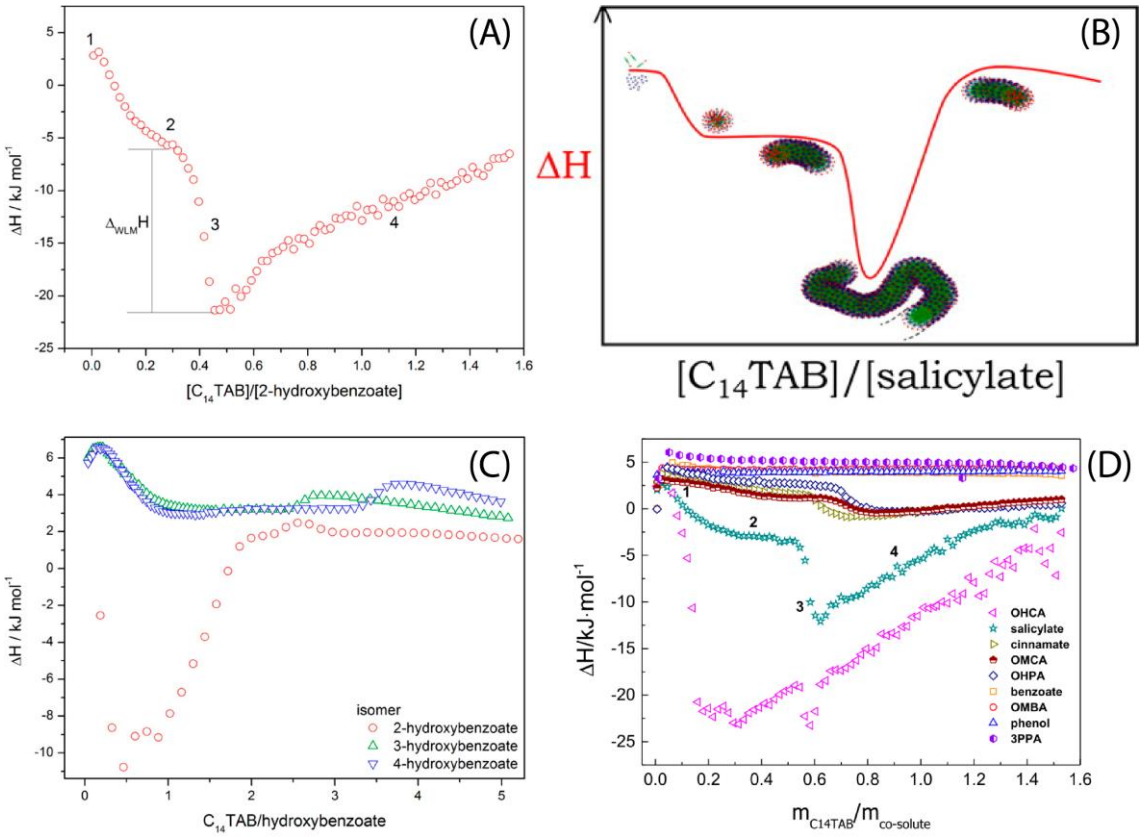

Figure 32. (A) Titration of $C_{14}TAB$ $14.0\ mmol\ L^{-1}$ into a reaction cell containing sodium salicylate $1.5\ mmol\ L^{-1}$ and the numbers along the enthalpogram is related with aggregate morphology showed in (B), 1 – mixed micelle formation, 2 – partial micelle growth, 3 – WLM formation and 4 – shortening of WLM [154]. (C) Enthalpograms for the titration of $C_{14}TAB$ $100.0\ mmol\ L^{-1}$ in 2 (NaSal), 3 and 4-hydroxybenzoate $1.5\ mmol\ L^{-1}$ [154] and (D) Enthalpograms for different aromatic salts at the same conditions of (A) where OHCA means o-hydroxycinnamic acid, OMCA o-methoxycinnamic acid, OHPA 3-Hydroxyphenylpropanoic acid, OMBA 2-methoxybenzoic acid and 3PPA for 3-Phenylpropanoic acid [155]. All the experiments were carried out at $25\ °C$ and all the Figures were used with permissions from the cited references.

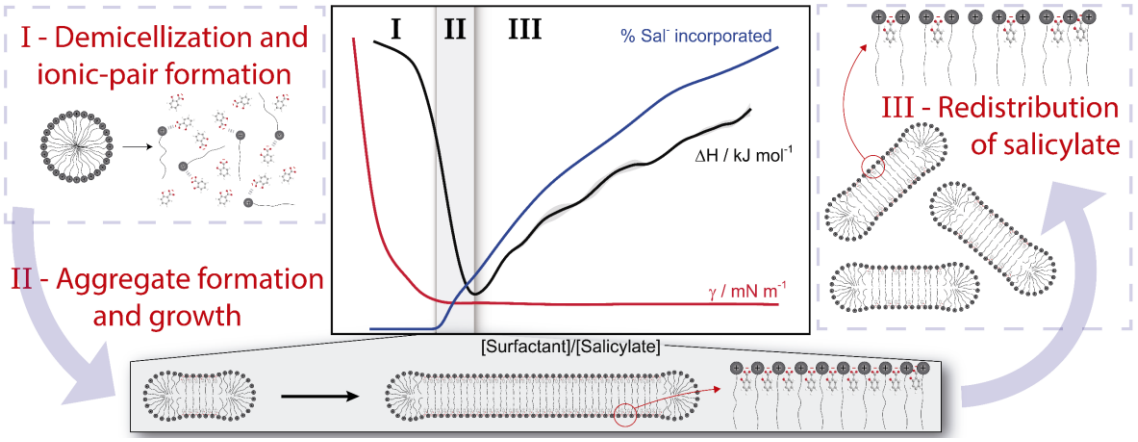

Figure 33. de Souza *et al.* interpretation of the thermogram for wormlike micelle formation for the system of $C_{14}TAB$ and sodium salicylate together with the surface tension, γ, and the percentage of salicylate incorporated as function of the [$C_{14}TAB$]/[salicylate] ratio measured by time resolved fluorescence. The three regions are: I – Demicellization and ionic-pair formation; II – Aggregate formation and growth and III – redistribution of salicylate molecules and the consequent decrease in aggregate size.

It is worth noting that, if the strategy to favors the formation of wormlike micelle changes (keeping the titration of surfactant into the reaction cell containing or not an analyte), like changing the nature of the surfactant (non-ionic, anionic, zwitterionic, gemini surfactants, etc) and/or the nature (or absence) of the analyte, the enthalpogram of the wormlike micelle formation considerable changes. Some of these works for non-ionic surfactant [158,159], anionic [160], zwitterionic [161–164], gemini [164–168], mixtures of surfactants of different natures [169,170] and for inorganic salt [142,162] or other organic salts [150,151,157,168,171,172] can be seem in the cited references.

5. Objectives

Propose a fluid composed of wormlike micelle responsive to pH and metal ions that can be a candidate for use as a diverting fluid in the stage of acid stimulation in oil production. For this, some preliminary steps were necessary: (i) Fundamental investigation of fluids that form wormlike micelle and the different strategies to induce their growth through the use of different aromatic organic salts; (ii) Investigate the behavior of fluids containing wormlike micelle responsive to different external stimuli and, finally, (iii) Investigate the acid dissolution rate of carbonates against acids of different natures and the rheological and the flow behavior of diverting acid fluids.

Part II: Materials and methods

6. Materials

All reagents used, unless otherwise stated, were purchased from Sigma-Aldrich and were used without prior treatment. The surfactant erucylbis(hydroxyethyl)methylammonium chloride (EHAC) was supplied by Akzo Nobel (now Nouryon) whose trade name is ETHOQUAD E/12-75. The product consists of a $75\ wt\%$ solution of surfactant in isopropanol alcohol. Before its use, the isopropanol was removed in a vacuum oven at room temperature and the surfactant was then freeze-dried overnight before use. The photoacid generator (PAG), diphenyliodonium-2-carboxylate monohydrate, was purchased from TCI Chemicals.

Milli-Q water was used to prepare the solutions, except for the preparation of acid stimulating fluids (commercial or QuoVadis) and for the study involving the photoacid generator (Chapter 10), where distilled water was used. The solutions that were analyzed by nuclear magnetic resonance were prepared in deuterated water with isotopic abundance higher than 99.9% of deuterium.

All pH adjustments, unless otherwise stated, were made using aqueous solutions or pure reagents of sodium hydroxide (NaOH) or hydrochloric acid (HCl) with accuracy of $\pm$ 0.1 units.

The solutions containing wormlike micelle were left at rest for at least one week in room temperature prior to any analysis to guarantee the homogenization and avoid any mechanical memory associated with the preparation.

7. Methods

7.1. UV irradiation and spectroscopy

UV irradiation and UV spectra were done only for the study involving the photoacid generator (Chapter 10). Aqueous solution containing PAG were irradiated with UV light from an Oriel $200\ W$ mercury arc lamp. A dichroic beam turner with a mirror reflectance range of 350 to $450\ nm$ was used to access the UV range of the emitted light. The sample ($10.0\ mL$) was placed in a $20\ mL$ vial, and the irradiation was done top to bottom for a specific duration (typically $30\ min$) under mild stirring at $25\ °C$. Then, $0.5\ mL$ of sample was removed for measuring the rheology. The remainder of the sample was then irradiated for a second duration and the above process was repeated. UV-vis spectra were obtained in a spectrophotometer (Hewlett–Packard, model 8453) for aqueous solutions of PAG or 1,2-dihydroxybenzene (DHB) at pH 7.0 and also after irradiating the PAG solution for $2\ h$.

7.2. Isothermal titration calorimetry (ITC)

The thermograms were obtained with an ITC (MicroCal PEAQ-ITC, Malvern) operating at $25\ °C$. The parameters used for all the analyses were: reference power $7.0\ \mu W$, stir speed $750\ rpm$ and no feedback. The number of injections, the volume of each injection and the time between successive injections varied according to the energy involved in each combination of reagents, but typical values were 20 to 40 injections, volume of 1.0 to $2.0\ \mu L$ of each injection and 400 to $800\ s$ between consecutive injections. The experiments were planned so that the next injection was only performed when the power variation associated with the previous injection reached the baseline. The data of the first injection was always discarded.

7.3. Rheology

Steady-shear and oscillatory-shear rheology were conducted in rheometer (HAAKE MARS III or HAAKE MARS 40, Thermo Scientific; AR2000, TA Instruments) operating at controlled-rate (CR) mode for steady-shear and controlled-stress (CS) mode for oscillatory-shear. All the analysis was carried out at $25\ °C$ and after being crushed by the rotor, the samples were thermostatized for at least 10 minutes before the application of the shear to ensure thermal equilibrium and total relaxation of the solution.

For the flow curves (apparent viscosity as function of the shear rate) the samples were pre-sheared for $60\ s$ at $10^{-2}\ s^{-1}$ to attenuate the inertial effects at low shear rates and, then, step-sheared from 10^{-2} to $1000\ s^{-1}$ with 40 steps distributed in logarithmic scale. Flow curves were also obtained by using a pressure cell (Thermo Fisher Scientific) made of Hastelloy. A coaxial cylinder geometry was adopted, in this case PZ38 Ha, and the parameters for the experiments were the same as described previously. Experiments were performed using this facility under atmospheric pressure and under $35\ bar$ using carbon dioxide (CO_2) to pressurize it. In the latter case, system was kept pressurized at rest for at least $30\ min$ prior to the measurement.

For the oscillatory-shear, stress sweep experiments were performed with disturbance frequency of $1.0\ Hz$ and stress from 0.1 to $10\ Pa$ distributed in logarithmic scale and 20 steps. Identified the linear mechanical region, the frequency sweep experiments were conducted from $0.01\ s^{-1}$ to $100\ s^{-1}$ (0.06283 to $628.3\ rad\ s^{-1}$) distributed in logarithmic scale with 6 steps per decade.

7.4. Light scattering

Dynamic light scattering (DLS) experiments were conducted in a goniometer (CGS-3, ALV-GmbH) equipped with a detection system in pseudocross geometry with a $22\ mW$ laser (He-Ne) and wavelength of $632.8\ nm$. The correlation function was acquired using

ALV-7004 multitau correlator. All the material used for sample preparation were pre-washed with Hellmanex for at least two hours and washed with abundant Milli-Q water. About $1.0\,mL$ of sample was filtered (hydrophilic PTFE, $0.45\,\mu m$) prior to the measurement. The sample holder was connected to a thermostatic bath at $25\,°C$ and cis-decalin was used as refractive index matching liquid. All the correlation function was acquired at scattering angle, θ, of $45°$ and control measurements in $60°$ and $130°$ were also performed to assure the correlation time and, consequently, the apparent hydrodynamic radius determined is not function of the scattering angle.

7.5. Nuclear magnetic resonance

^{1}H chemical shift and ^{1}H self-diffusion coefficient (DOSY) was obtained in a $400\,MHz$ spectrometer (Bruker). DOSY experiments were acquired using the Oneshot45 pulse sequence [173,174]. The net diffusion-encoding gradient pulse width (δ) and diffusion delay (Δ) varied with the sample investigated and they will be approached in each Chapter but the gradient recovery ($d16$) and duration of the gradient purge pulse ($p19$) were fixed for all samples at 0.2 and $0.6\,ms$, respectively. The sequence was conducted using sixteen values of nominal gradient amplitudes, from 4.8 to $38.5\,G\,cm^{-1}$, squared distributed and carried out at a nominal probe temperature of $25\,°C$. The DOSY experiments were processed with the DOSY Toolbox package [175] using $32{,}768$ data points, phase and baseline correction and reference deconvolution with a $3.0\,Hz$ wide Lorentzian target line-shape.

7.6. Cryogenic transmission electron macroscopy (Cryo-TEM)

Before sample application on the grids, the grids were subjected to a glow discharge treatment (Pelco easiGlow, Ted Pella) with $15.0\,mA$ current for $25.0\,s$ in air atmosphere. Then, $3.0\,\mu L$ sample was dropped on a 300-mesh lacey carbon-coated copper grid (Ted Pella) in a controlled environment vitrification system (Vitrobot Mark

IV, Thermo Fischer Scientific) with controlled temperature at $22.0\ °C$ and humidity of 100%. Vitrobot preparation parameters used for each grid varied according to the solution properties and they will be stated in each Chapter. Samples were analyzed in low-dose condition using a transmission electron microscope operating at $200.0\ kV$ (TALOS F200C, Thermo Fischer Scientific) or $120.0\ kV$ (JEM-1400 Plus, Jeol). Images were acquired using a CMOS 4000×4000 camera (CETA 16 M, Thermo Fischer Scientific). Sample preparation and image acquisition with cryo-TEM was carried out at Brazilian Nanotechnology National Laboratory (LNNano) in Brazilian Center for Research in Energy and Materials (CNPEM).

7.7. Carbonate acid dissolution

7.7.1. Plug preparation

All carbonate outcrops used in this study were provided by Brazilian oil and gas company (PETROBRAS) and were purchased from Kocurek Industries with dimensions of about $30\ cm$ in length and $3\ cm$ in diameter. The geological background of each sample is presented in Table 1.

Table 1. Geological background of the carbonate outcrops used.

Rock type	Basin	Formation	Environment	Age
Indian Limestone	Illinois	Bedford	Marine	Mississippian
Silurian Dolomite	Illinois	Thornthon	Marine	Silurian
Desert Pink	Maverick	Edwards Plateau	Marine	Early Cretaceous
Edwards White	Maverick	Edwards Plateau	Marine	Early Cretaceous
Edwards Brown	Maverick	Edwards Plateau	Marine	Early Cretaceous

Half of each cylinder were reserved to petrophysical analysis, x-ray fluorescence and thin layer microscopy and the remaining were cut in pieces of about $1.3\ cm$ in height, using a radial arm saw and, posteriorly, cut in smaller plugs of about $1.0\ cm$ height and $0.8\ cm$ in diameter using a hole saw.

Prior acid dissolution, these smaller plugs were heated in a muffle furnace (3000 10P, EDG) for $3\ hours$ at $400\ °C$, with a heat rate of $10\ °C/min$, to remove any organic and water residue. After that, the mass of each plug was determined and they were used in experiments of acid dissolution, NMR and micro-CT.

7.7.2. Carbonate rocks characterization

Thin layer microscopy of each carbonate outcrop was obtained by using a ZEISS AxioImager A2m petrographic microscope. The morphology, diagenetic features and the permo-porous-system, beside fractures and the type of filling were analyzed.

For the petrophysical analysis of the carbonates, it was used the procedure API RP 40:1998 [176]. First, the samples were cleaned by solvent extraction and then dried at oven (relative humidity of 45% and $60\ °C$) until it reached mass stabilization. Grain density, effective gas porosity and gas permeability were obtained using Weatherford DV-4000 device. Permeabilities were corrected by Klinkenberg effect and the measurements were taken under confining stress.

The atomic composition was determined by X-ray fluorescence (XRF1800, Shimadzu). The X-ray fluorescence spectra for the carbonate samples are shown in Appendix E, from Figure E1 to Figure E6. Only the components with percentage higher than 0.1% were considered for discussion.

7.7.3. Acid dissolution

As carbonates of different natures have different reactivities with inorganic and organic acid, before the definitive dissolution experiments were carried out (mass loss × dissolution time), an exploratory experiment was carried out in order to estimate the time required to dissolve approximately 50% of the plug with HCl, a parameter which was called t_{50}. For this experiment, one plug of known mass of each carbonate was partially dissolved in $40.0\ mL$ of aqueous acid solution of HCl $0.5\ mol\ L^{-1}$ and the other in HAc $2.5\ mol\ L^{-1}$ without stirring. This volume of acid was used, because on it contains H^+ ions in excess compared to the mass plug used and, thus, the acid dissolution of the carbonate will not be influenced by the concentration of H^+ ions in solution. After a time required to dissolve around 50% of the plug (visually), the plugs were removed from the acid solution, washed with abundant water, dried in a muffle at $250\ °\ C$ by $5\ h$ and then their masses were determined gravimetrically. Although the mass loss in such situations is not represented by a linear dependence (mass loss × dissolution time), this approximation was adopted to calculate the time required to reduce the mass of the sample to about 50% of dissolution, which characterizes the parameter t_{50}. Table 2 shows the t_{50} values for each carbonate used together with their abbreviations that will be used for each carbonate sample.

Table 2. Dissolution time in minutes required to reduce the mass of the carbonate plugs to about 50% (t_{50}) using hydrochloric acid.

Rock type	Abbreviation	Dissolution time (t_{50}) / min
Silurian Dolomite (low permeability)	LPD	160
Silurian Dolomite (high permeability)	HPD	96
Edwards Brown	EDB	64
Edwards White	EDW	40
Indian Limestone	IND	32
Desert Pink	DP	32

t_{50} values were used only to plan the further experiments in which a triplicate of each carbonate plugs were submerged into $40.0\ mL$ of an acid solution, either HCl $0.5\ mol\ L^{-1}$ or HAc $2.5\ mol\ L^{-1}$ (totalizing 6 plugs of each matrix, 3 for each acid), for

periods of time multiples of a quarter of t_{50} (¼, ½, ¾ and t_{50}). As the chemical reactions were systematically interrupted, during the intervals between each quarter of time, the carbonate rocks were investigated by low field ^{1}H-NMR in order to follow the carbonate surface variation caused due to chemical reaction with the acid solutions. It is worth to mention that it was used the very same carbonate outcrop during the whole procedure and special cares were taken to make sure that the NMR data were correlated to respective samples. The procedure for this investigation is as it follows.

First, a "blank" procedure was carried out, where the plugs, prior to the reaction, were subjected to vacuum of $10\ mbar$ for $7\ h$ and, still under vacuum, deionized water was admitted into the system, submerging the carbonate samples. The plugs were kept at rest, at room temperature for at least $64\ h$ prior to the NMR experiments in order to absorb as much water as possible. The excess of water on the surface of the rock was carefully removed with aluminum foil and the absorbed water was gravimetrically determined. After that, the ^{1}H-NMR experiments were carried out, the plugs were dried in a muffle furnace at $250\ °C$ for $5\ h$ and weighted.

Then, the first cycle of acid dissolution begins with the reaction between the carbonate rocks and the acid solution for a quarter of t_{50}. After each dissolution, the acid solutions used were reserved for further pH analysis. The carbonate plugs, in contrast, were immediately washed with plenty water, dried in muffle furnace at $250\ °C$ for $5\ h$ and, then, the mass loss was gravimetrically determined. For the NMR analysis, the blank procedure described was repeated. This sequence characterizes a full cycle, which was repeated 4 times, so that the cumulative dissolution time reached 100% of t_{50}.

The pH of each acid solution was determined by using an pHmeter after each dissolution (848 Titrino plus, Metrohm). The variation in pH values obtained during these experiments indicate that the carbonate mass loss corresponds exclusively to the chemical reaction.

7.7.4. Time domain ^{1}H-NMR

Transverse relaxation times (T_2) of water hydrogen were obtained in a benchtop low-field nuclear magnetic resonance spectrometer (mq20, Bruker) of $0.47\ Tesla$ ($20\ MHz$ for ^{1}H). Before acquiring the signal, the plugs (with water incorporated) were kept at rest in a thermostatic bath at $25\ °C$ for at least $15\ min$. The pulse sequence used was the Carr-Purcell-Meiboom-Gill (CPMG) [177,178], which can be represented by $\left[RD - 90^{o}_{x}\left[-\tau - 180^{o}_{\pm y} - \tau - echo\right]_{n_{echo}}\right]_{NS}$, where RD is the recycle delay, which is the time necessary for the complete longitudinal magnetization recovery (five times the longitudinal relaxation time, T_1), and a time of $15\ s$ was used; 90° and 180° are the pulse angulation by the application of the radiofrequency pulse of 8.0 and $16.0\ \mu s$ respectively; the 'x' and 'y' index are related with the phase pulse; τ is the interpulse time, fixed at $100\ \mu s$; $echo$ is the spin echo where the amplitude is acquired; n_{echo} is the number of echoes necessary for the complete transverse relaxation and it was used values between $6{,}000$ up to $32{,}000$ as required and the NS is the number of accumulated scans to improve the signal-to-noise ratio, 16 scans was used. With the transverse relaxation raw data, it was applied the inverse Laplace transform (ILT) to obtain the relaxograms, where the distribution of the transverse relaxation time with its amplitudes is shown. The ILT was applied using the SLK Neo Multiexp software, with regulation parameter $\alpha = 100$, minimum and maximum relaxation time of 10^{-3} and $10^{4}\ ms$ respectively and 200 points as output of the ILT.

7.7.5. Micro computed tomography

3D Digital images were obtained in collaboration with Prof. Dr. Tito José Bonagamba and the postdoc of his group, Dr. Everton Lucas de Oliveira, from University of São Paulo, before and after dissolved the carbonate samples for a period that corresponds to half of t_{50}. The images were acquired in an X-ray micro tomography (SkyScan 1272, Bruker) with voltage and current of $100\ kV$ and $100\ \mu A$, respectively. The projections were acquired with $4904\ x\ 3280\ pixels$ resulting in an isometric voxel resolution of $2.5\ \mu m$.

The scanning time was approximately $10\ h$ for each measurement. Reconstruction was performed on the integrated SkyScan software NRecon (version: 1.7.0.4).

Then, using DataViewer software (version 1.5.2.4), the image registration was performed using the images obtained before and after the acid dissolution. This process consists in transforming the two sets of data into one coordinate system, where the structure differences can be compared and visualized. Thus, for each image, the solid space was identified in PerGeos software and the top and bottom of the images were cut to avoid areas that have not been scanned in both stages.

First, to quantify the thickness that was dissolved a mesh was created from the external surface and the distance between the surfaces before and after the acid dissolution was calculated. For this, the Surface Distance method implemented in the PerGeos software was applied, which allows the calculation of the distance between two triangular surfaces.

Furthermore, the respective volumes (V) and the surface areas (S) were determined. For each plug, an equivalent radius was calculated considering them as cylinders. The Eq. 45 and Eq. 46 were used to calculate the radius:

$$V = \pi R_v^2 L \qquad \text{Eq. 45}$$

$$S = 2\pi R_s L + 2\pi R_s^2 \qquad \text{Eq. 46}$$

Where R_v and R_s are the radii calculated from the volume and surface of each plug, respectively. The outcrops before dissolution present imperfections on the external surface, mainly due to the macroporosity, visible in the resolution used. In cases where even the largest pores are not sampled by microCT, the sample is more like a perfect cylinder, and in this case $R_v \cong R_s$. However, after the acid dissolution an irregular surface can be formed and, then, $R_v \neq R_s$. When calculating both values of radii, it is possible to estimate a parameter d that describe how regular is the surface, described by Eq. 47.

$$d = 1 - \frac{R_v}{R_s} \qquad \text{Eq. 47}$$

For this equation, the closer d is to zero, the closer the plug is to a perfect cylinder. Volumes and surface areas for the outcrops before and after the dissolution process are presented in Table E1 (Appendix E). R_v, R_s and the parameter d were also calculated before and after the acid dissolution for HCl and are shown in Table E2 and for HAc in Table E3.

7.8. Diverting fluids

7.8.1. Fluid preparation

Beyond our own diverting formulation (QuoVadis), we also had the opportunity to work with two commercially available diverting fluid which will be designed here by VES 1 and VES 2. The materials and chemicals required to prepare VES 1 and VES 2 were provided by the Brazilian company of oil and gas (PETROBRAS), except for the hydrochloric acid which was purchased from Sigma Aldrich ($37\ wt\%$). The exact amount of each component used to prepare these commercially available fluids will not be described in order to protect their formulation. Generally describing, diverting acid solutions are often composed by surfactants, HCl ($15\ wt\%$), corrosion inhibitor and other additives.

The preparation of $500\ mL$ of VES 1 were carried out following the procedures provided by PETROBRAS. All the components were added at their specific concentrations into a beaker containing HCl solution and the other ingredients. The mixture was kept under mechanical agitation (Fisatom, model 713D) at $1000\ rpm$ for $10\ min$. Following, the prepared fluid was kept at rest for at least $10\ min$ to reduce the foam formed during the shearing. VES 2 was prepared by a company employee in our laboratory and has already been supplied in its final formulation, to be neutralized and characterized rheologically.

At last, QuoVadis fluids were prepared similarly to VES 1. A surfactant stock solution, at high concentration, was previously prepared to be used as the active component. The active component was added into a beaker containing HCl, water and the other components and kept under mechanical agitation, as mentioned for VES 1. Depending on the composition and the identity of the active components for the QuoVadis, it was determined different generations and they will be stated as G1, G2 and G3. In the case of the later generation, there are three variations that will be stated as G3 A, G3 B and G3 C. Considering this, it was studied five different diverting acid fluids proposed by our research group. More information about the QuoVadis and its generations can be found in INPI patent application BR102020006183-6.

7.8.2. Neutralization procedure

$50.0\ mL$ of the diverting fluid were neutralized with the required amount of either $Ca(OH)_2$ or $CaCO_3$. The percentage of neutralized HCl was in range of 0% up to 100%, depending on the diverting fluid, and it was investigated in intervals of 10%. Both $Ca(OH)_2$ and $CaCO_3$ were manipulated in powder and their quantities were weighed by using a precision balance. Samples were kept under mild agitation for at least $1\ h$ to assure the complete reaction and, as the reaction is very exothermic, to allow the samples to reach the room temperature before any measurement. The flasks were kept closed to avoid gas release, which would decrease the acid concentration and it would not be associated to reaction procedure.

It is worth mentioning that special cares were taken to avoid transferring the remaining foam and bubbles from the stock acid fluid to the small flasks. Also, the neutralization procedure was used throughout the study regardless the fluid neutralized and those fluids that phase separated after the neutralization were not characterized by rheology.

7.8.3. Core-flooding

The matrix acidizing process was simulated in a core-flooding simulator (MAT700, Vinci Technologies) in order to understand and investigate the diverting phenomena in different carbonate outcrops. The outcrops used were left submerged in brine for at least one night before being used in the core-holder. For the core-flooding experiment, first it was injected brine until the slope of the graph of pressure × pore volume injected (dP/PV) was at least 0.5; then the stimulating acid fluid was injected until the pressure drops was observed due to the direct connection between the ends of the plug and, finally, brine was again pumped to wash the interior of the core and cease the acid-base reaction. It was pumped VES 1 and different generations of QuoVadis into the system containing Indian Limestone outcrops with different petrophysical features, i.e. permeability and porosity, where the difference in pressure between the extremities of each plug was measured as a function of the injected porous volume. The characteristics of the plugs, such as length (L), diameter (d), permeability (k), porosity (Φ) and the injection flow (q) are presented in Table 3. The confinement pressure and backpressure used in all experiments were $2{,}600$ and $1{,}100$ psi, respectively.

For the plug 122, which was treated with the first generation of QuoVadis, three-dimensional tomography was obtained using nuclear magnetic resonance imaging (MRI) in collaboration with Prof. Dr. Fernando Paiva and the postdoc of his group, Dr. Bernd Uwe Foerster, from University of São Paulo, to identify the pattern of the wormhole formed in the carbonate rock.

Table 3. Characteristics of the Indian Limestone plugs used and the injection flow (q) used for each injection. Properties presented are length (L), diameter (d), permeability (k) and porosity (Φ) of the carbonate outcrop.

Plug	$d\ /\ cm$	$L\ /\ cm$	$K\ /\ mD$	$\Phi\ /\ \%$	$q\ /\ cm^3\ min^{-1}$
111	3.81	7.59	13.0	15.40	1.0
121	3.75	15.23	275.0	15.70	1.0
122	3.75	15.23	275.0	15.70	0.5
123	3.76	15.25	427.0	16.00	1.0
125	3.82	15.29	394.0	15.80	1.0
243	3.82	7.38	514.0	17.30	1.0
244	3.82	7.38	486.0	16.50	1.0
245	3.82	7.35	470.0	16.20	1.0
321	3.78	7.48	98.0	16.90	1.0

Part III: Results and discussion

8. Probing the formation of wormlike micelles formed by cationic surfactant with chlorobenzoate derivatives [150]

8.1. Results and discussion

The affinity of aromatic derivatives for the formation of wormlike micelles with cationic aminoquaternary surfactant varies greatly with the substituent nature and the position of the substituent on the aromatic ring [86,155]. In this study, we investigated the formation of WLM with C_{14}TAB and different isomers of chlorobenzoate, where we changed both the position of the chlorine atom (ortho, meta or para) and the quantity of chlorine atoms (one or two substituents) in the chlorobenzoate derivatives. The organic compounds and the abbreviations used for each one can be seen in Figure 34.

The organic salts were acquired in their acid form and the anionic species were obtained by pH adjustment. As indicated in Table A1 (Appendix A), the pK_a values of the chlorobenzoic acids depend on the number and position of the chlorine atom in the aromatic ring, ranging from 1.8 to 4.2. In order to ensure the titration of the anionic form of chlorobenzoates, the pH of all solutions used in the calorimetric titration were fixed at pH 10 ± 0.1, including the solutions of C_{14}TAB. Figure 35 shows the titration of C_{14}TAB 10.0 (A and B) or $40.0\ mmol\ L^{-1}$ (C and D) in a reaction cell containing water or the organic salt at $1.40\ mmol\ L^{-1}$. Figure 35A and C are the results for the chlorobenzoates with one chlorine atom together with the sodium benzoate (4H) as a comparative and Figure 35B and D for those with two chlorine atoms. The ITC raw data for all the curves can be seen in Figure A1 to Figure A18.

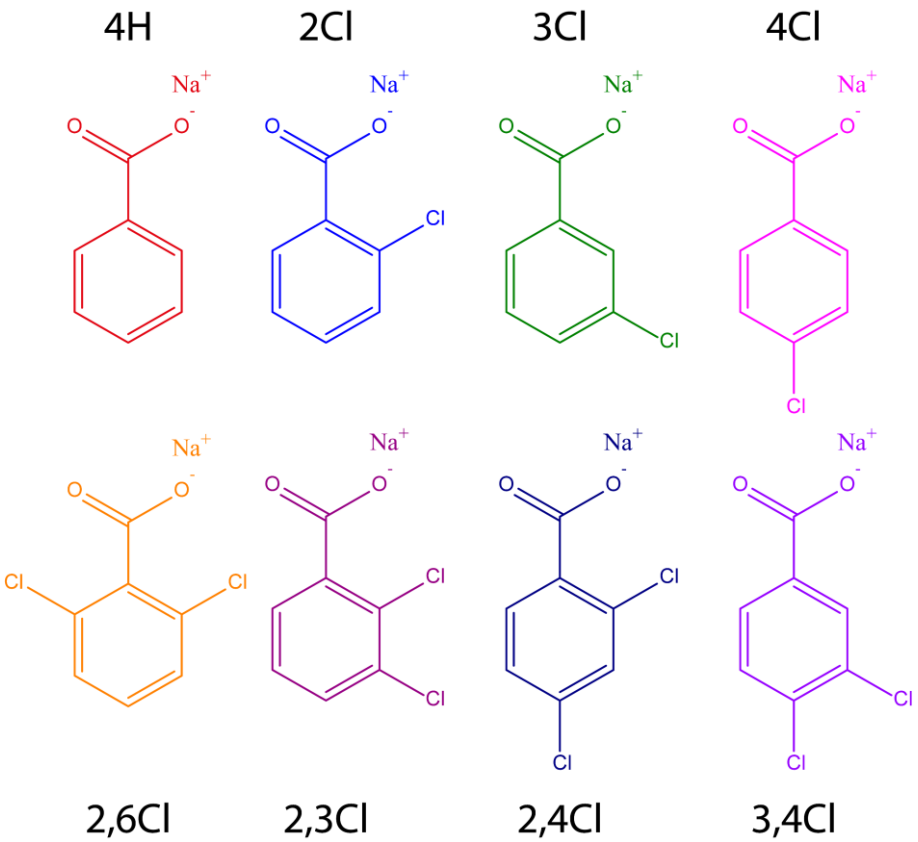

Figure 34. Molecular structure of the benzoate derivatives and their abbreviations. The color of the molecules matches with the color used for the data presentation of each one.

In the case of organic salts that have high affinity for the formation of aggregates, the use of high concentrations of titrant can make that important regions of the enthalpogram are lost. As an example, it is possible to mention the 3Cl or 4Cl, as can be seen in Figure 35A and C. While with the use of C_{14}TAB $10.0\ mmol\ L^{-1}$ it was possible to observe the region of demicellization of the spherical micelles (initial plateau in Figure 35A), the use of C_{14}TAB $40.0\ mmol\ L^{-1}$ makes the first titrated drop of C_{14}TAB already be in the region of formation and growth of the wormlike micelles for some chlorobenzoates. Thus, in many cases, the use of different concentrations of titrant, fixing the titrand concentration, is interesting so that none of these regions are lost. For Figure 35, the use of C_{14}TAB $10.0\ mmol\ L^{-1}$ focused on events that occur in concentrations of C_{14}TAB in the reaction cell of up to $\sim 1.6\ mmol\ L^{-1}$ while the use of C_{14}TAB $40.0\ mmol\ L^{-1}$ in events that occur up to $\sim 7.0\ mmol\ L^{-1}$. The only direct

implication of the use of multiple titrant concentrations (in addition to the displacement on the abscissa axis of the enthalpogram) is that the events become more energetic (look at Figure 35A and C, for example), keeping the events like micellization, aggregate transition, etc., at the same concentrations.

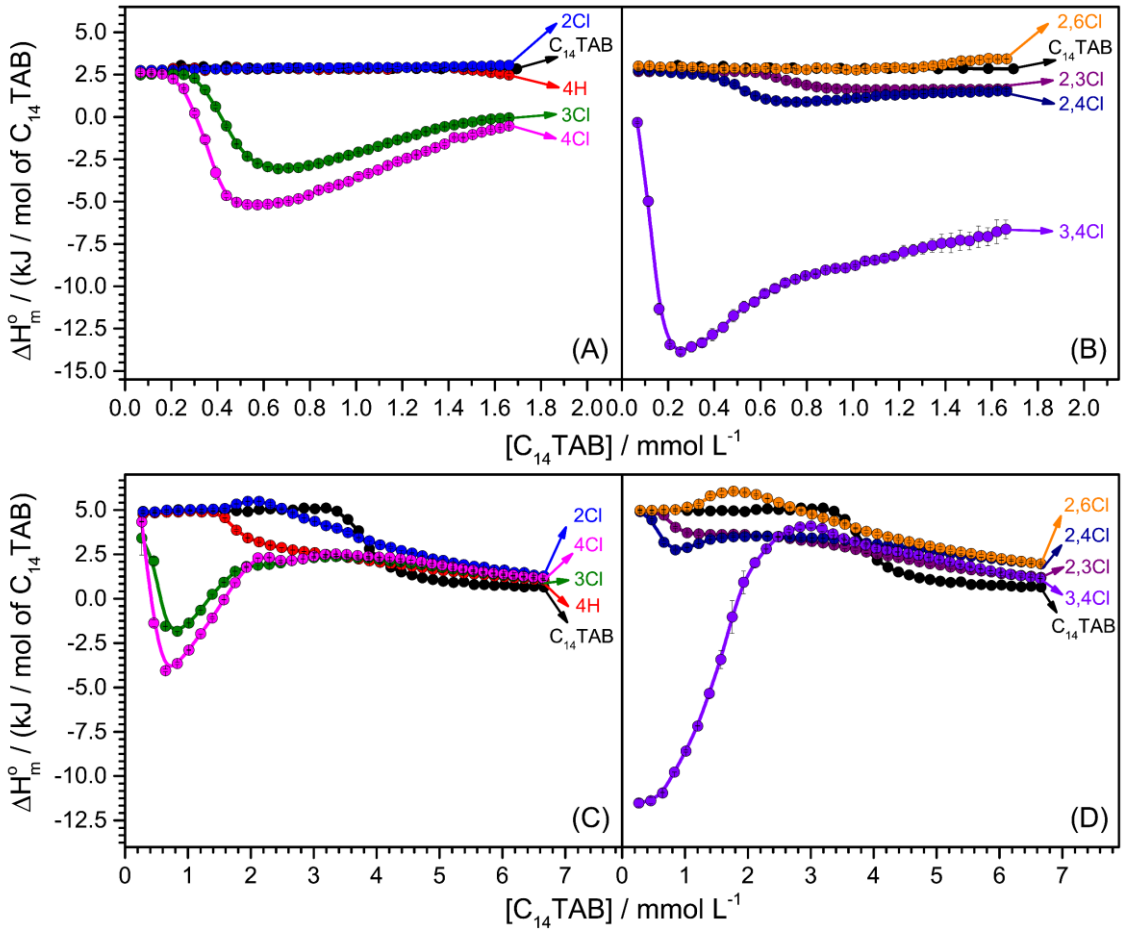

Figure 35. Enthalpy in kJ per mol of $C_{14}TAB$ as a function of the surfactant concentration in the reaction cell. Water or $1.40\ mmol\ L^{-1}$ of salt was fixed in the reaction cell and (A, B) $10.0\ mmol\ L^{-1}$ or (C, D) $40.0\ mmol\ L^{-1}$ of $C_{14}TAB$ in the syringe. In (A) and (C) are shown the salts without and with one substitution in the aromatic ring and in (B) and (D) with two substitutions. The black curve of $C_{14}TAB$ refers to the titration of $C_{14}TAB$ in water as a reference, 4H refers to sodium benzoate and the others to chlorobenzoates where the numbers refer to the substitution position of the chlorine atom in the aromatic ring. Values have been obtained from at least duplicated and the lines are only guide for the eyes.

The presence of the chlorobenzoates in the titrated solution leads to major implications in the calorimetric profile, this is evident when compared with the titration of C_{14}TAB in pure water. For the case of C_{14}TAB in water, the aggregation of the C_{14}TAB at the CMC, characterized by the exothermic signal, is observed at about $4.0\ mmol\ L^{-1}$ which agrees with the value already reported [179]. For the titration of C_{14}TAB in chlorobenzoate solutions, the pattern of the thermograms change considerably. The formation of the aggregates is still associated with change on the profile of the thermogram, but it is observed at lower C_{14}TAB concentrations instead. The critical surfactant concentration in which these aggregates are formed can be determined by the inflection point of the thermogram through the second derivative method (showed in Figure 28). Remarkably, the critical concentration is directly related to the spontaneity of the chlorobenzoate derivatives to thread into the micellar surface. This can be exemplified by considering the results for 2Cl and 3,4Cl, in which the values observed for the critical concentration are $1.8\ mmol\ L^{-1}$ and $\sim 0.1\ mmol\ L^{-1}$, respectively.

The curves were separated in three main groups based on the magnitude of their variation of energies: low energy, observed for titration of 4H, 2Cl and 2,6Cl; intermediary energy, for 2,3Cl, 2,4Cl, 3Cl and 4Cl and high energy observed for 3,4Cl. The last two groups present a specific thermogram profile, which is considered as signature of WLM formation when aromatic anions are titrated with cationic surfactants [73,154,155]. Since the concentration of C_{14}TAB in the syringe is higher than its CMC, the variation of energy observed in the beginning of the titration is associated with the breaking of the C_{14}TAB micelles and the subsequent formation of ionic pairs between the unimers of surfactant and the aromatic anions. Adding more C_{14}TAB, the critical concentration value is reached, and the aggregate is formed. The magnitude of the energy released is another indicative factor of the spontaneity of the chlorobenzoate to form WLM with C_{14}TAB. Indeed, the Coulombic nature of the interaction existing between the cationic surfactant headgroup and the carboxylate group of the organic salt is the same for all chlorobenzoates investigated. Therefore, the differences observed in the magnitude of the exothermic process cannot be attributed only to the electrostatic screening. The position of the chlorine atom clearly plays a main role concerning the embedding of the aromatic anion into the micellar interface. The cation-

π interactions between the positive charges and the electronic cloud of the aromatic have important contribution to the stabilization of WLM [76,77]. Therefore, the chlorine atoms can affect the electronic cloud of the chlorobenzoates. Another important aspect is the distance between the chlorine and the micelle-water interface. Clearly the chlorine in positions 2 is unfavorable for incorporations of 2Cl and 2,6Cl.

The fraction of aromatic molecules incorporated into the micelles can be correlated with the partition coefficient $P = \frac{a_{Cl}^{micellar}}{a_{Cl}^{solution}}$, where a is the activity of chlorobenzoate in the micellar phase, $a_{Cl}^{micellar}$, and in the solution phase, $a_{Cl}^{solution}$. In a thermodynamic equilibrium state, according to the concept of pseudo-phases, the chemical potential of the chlorobenzoate in water is equal to its chemical potential in the microphase. As indicated in Eq. 48, P is correlated with the difference in the standard chemical potential of the chlorobenzoate, μ_{Cl}^{o}, in the two regions (see for instance reference [180]).

$$\mu_{Cl,micellar}^{o} - \mu_{Cl,solution}^{o} = RTlnP \qquad \text{Eq. 48}$$

μ_{Cl}^{o} has entropic and enthalpic contributions and the ITC experiments allow direct considerations about the latter factor. ΔH_{ag}^{o} can be defined as the standard molar enthalpy of the aggregate formation at the critical C_{14}TAB concentration, and the correspondent value can be determined from the ITC experiments. Yet, ΔG_{mic}^{o} and $T\Delta S_{mic}^{o}$ for the aggregate formation can be obtained through the relations showed in Eq. 42 and Eq. 43, respectively, using the ionization degree of C_{14}TAB in water of 0.28 [181]. Probably, the ionization degree of C_{14}TAB in presence of the organic salts investigated varies, but as we are more interested in the trend and the nature of the direction of aggregate formation (enthalpic or entropic), variations in the absolute value are not important for this evaluation. Table 4 shows the values of standard molar enthalpy, Gibbs free energy and entropy and the critical C_{14}TAB concentration for the aggregate formation. The results are also presented in Figure 36 as a plot of enthalpy as function of the entropy showing the enthalpy-entropy compensation [182] for the aggregation formation.

Table 4. Standard molar enthalpy, ΔH^o_{ag},Gibbs free energy, ΔG^o_{ag}, and entropy, ΔS^o_{ag}, of aggregate formation and the critical $C_{14}TAB$ concentration in $mmol\ L^{-1}$, $cc_{C_{14}TAB}$, and molar fraction, $x_{c_{14}TAB,cc}$, determined by the titration of $C_{14}TAB$ $40.0\ mmol\ L^{-1}$ in a reaction cell containing water or organic salt $1.40\ mmol\ L^{-1}$.

Reaction cell	$cc_{C_{14}TAB}$ / $mmol\ L^{-1}$	$x_{c_{14}TAB,cc}$	ΔH^o_{ag} / kJ mol $^{-1}$	ΔG^o_{ag} / kJ mol $^{-1}$	$T\Delta S^o_{ag}$ / kJ mol $^{-1}$
Water	3.80	$6.84\ 10^{-5}$	-4.10	-40.89	36.79
2Cl	1.73	$3.11\ 10^{-5}$	0.95	-44.25	45.20
4H	1.71	$3.08\ 10^{-5}$	-1.72	-44.30	42.58
2,6Cl	1.31	$2.36\ 10^{-5}$	2.03	-45.43	47.46
2,3Cl	0.68	$1.22\ 10^{-5}$	-1.32	-48.23	46.91
2,4Cl	0.52	$9.36\ 10^{-6}$	-2.70	-49.37	46.67
3Cl	0.42	$7.56\ 10^{-6}$	-8.97	-50.28	41.31
4Cl	0.36	$6.48\ 10^{-6}$	-11.36	-50.94	39.58
3,4Cl	0.11	$1.98\ 10^{-6}$	-23.45	-55.99	32.54

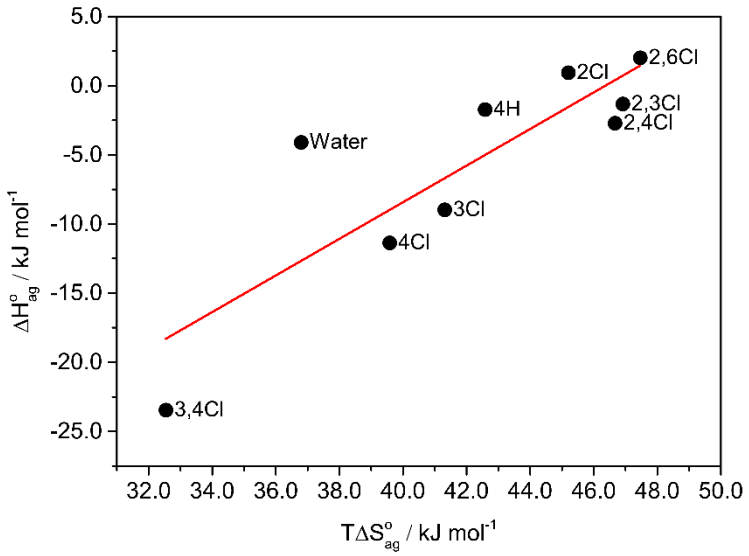

Figure 36. Standard molar enthalpy of aggregate formation (ΔH^o_{ag}) as function of standard molar entropy of aggregate formation ($T\Delta S^o_{ag}$) for all the organic salts investigated. It is also showed the results for the titration of $C_{14}TAB$ in water. The line in red is a linear regression considering all data.

As can be seen in Table 4, regardless of the affinity of the organic salt used, the formation of the spherical mixed micelle (4H, 2,3Cl and 2,6Cl) or wormlike micelle (all others) had an entropic direction, since the entropy modulus is greater than the enthalpy modulus in all cases. This is the expected behavior for the formation of spherical micelles composed only of surfactant, as seen for the formation of C_{14}TAB, and, interestingly, this was also observed for the formation of mixed spherical micelles and wormlike micelles. Based on the values of critical concentration and ΔG^{o}_{WLM}, the following spontaneity for incorporation was obtained:

$$2{,}3ClBz < 2{,}4ClBz < 3ClBz < 4ClBz < 3{,}4ClBz$$

The profile of the enthalpogram is highly dependent on the position of the chlorine in the aromatic ring. If the chlorine is at the position 3 or 4, the formation of the aggregate is very favorable, although the same is not observed if the halogen atom is at position 2. If a second chlorine atom is present, the affinity of the chlorobenzoate to the micelle interface is even higher, however, only if the two halogens are at positions 3 or 4. Moreover, as observed by Smith et al. [183], the further is the chlorine of the carboxyl group, the more favorable is the embedding of the aromatic molecule into the micellar environment, and thus, the number of both species constituting the aggregate is increased. Therefore, a correlation between ΔH^{o}_{WLM} and the contour length of the WLM may be expected. In this way, the viscosities of the solutions measured at the same molar ratios of that obtained in the reaction cell of the ITC experiments during the titration were determined (shown in Figure 37). As the concentrations of C_{14}TAB and chlorobenzoates used in ITC experiments are relatively low, to improve the viscosity measurements, the concentrations of the two components were proportionally increased 5 times. All the flow curves can be seen in Figure A19 to Figure A23.

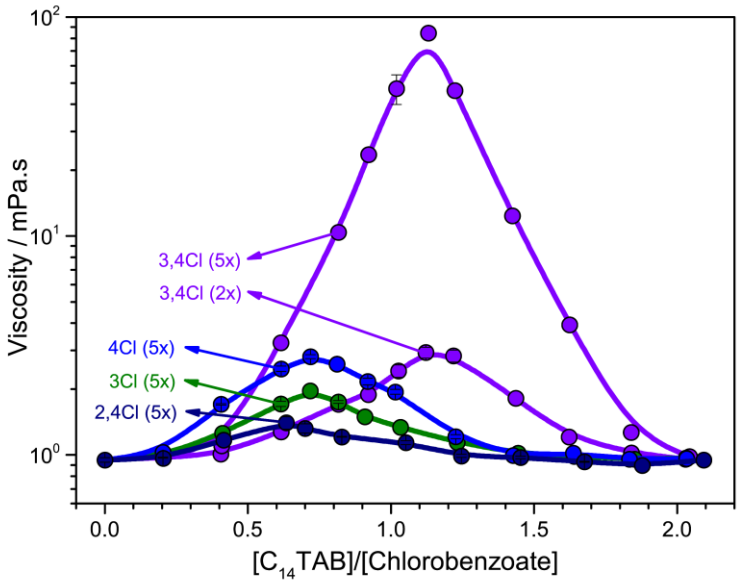

Figure 37. Viscosity as function of the ratio [C_{14}TAB]/[Chlorobenzoate] obtained at $25\ °C$. The chlorobenzoates are indicated by arrows in the curves and the indications $5x$ (or $2x$ for 3,4Cl) refers to the concentration multiplication factor in relation to the ITC experiments. The viscosities for C_{14}TAB, 4H, 2Cl, 2,3Cl and 2,6Cl remained similar to the water even multiplying the concentrations by a factor of $5x$ and, for clarity, they are now shown. The values were obtained from at least a duplicate and the lines are only guide for the eyes.

The sequence is essentially the one observed for the ΔH^o_{WLM}. Therefore, the premises about the correlation between ΔH^o_{WLM} and the number of molecules incorporated into the aggregates seems truthful, since the correlation between viscosity and size of wormlike micelles is valid in this concentration regime. However, the corresponding values of [C_{14}TAB]/[salt] for the maxima viscosity, in each case, are not the same as those observed for the minima of the enthalpograms (the enthalpograms as function of [C_{14}TAB]/[salt] ratio instead of [C_{14}TAB] can be seen in Figure A24). In all cases, the maxima values for the viscosity curves are slightly shifted to higher values of [C_{14}TAB]/[salt] relative to the minimum in the calorimetric curve. This is especially evident for C_{14}TAB with 3,4Cl where it was investigated in two concentrations, 2 and 5 times higher than the calorimetric experiments. Interestingly, for this anion, the ratio in which the maximum viscosity is reached is the same for the two concentrations used showing that there is no change on the solution concentration regime.

In order to investigate the reason for such non-coincidence of the values for [C_{14}TAB]/[anion], the apparent hydrodynamic radii of the aggregates were determined by using the DLS technique. The results are shown in Figure 38 and in this case, the concentration of C_{14}TAB and chlorobenzoate were increased twice when compared to the ones used in the calorimetric experiments. The distribution of the hydrodynamic radii and the correlation function obtained during the light scattering can be seen in Figure A25 for the 4Cl.

The Stockes-Einstein Equation was used to determine the apparent hydrodynamic radii of the aggregates formed by C_{14}TAB and chlorobenzoates. As wormlike micelles are not spherical, the hydrodynamic radii were strictly used to correlate qualitatively trends in the size of the aggregates with the curves obtained in ITC experiments.

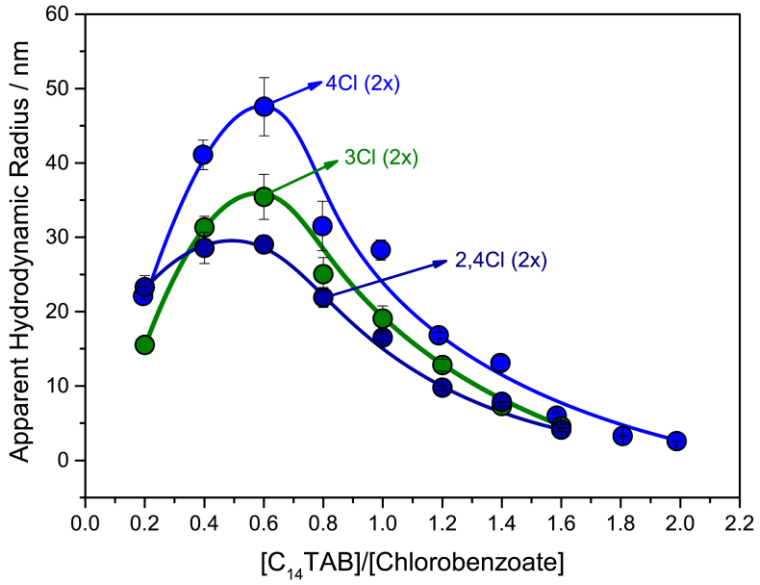

Figure 38. Apparent hydrodynamic radius of the aggregates as function of [C_{14}TAB]/[Chlorobenzoate] obtained at $25\ °C$. The chlorobenzoates are indicated by an arrow where the number means the position of the chlorine atom in the chlorobenzoate. The values were obtained from at least a duplicate and the lines are only guide for the eyes. $[Chlorobenzoate]_0 = 1.40\ mmol\ L^{-1}$.

The shape of the curves in Figure 38 was described in previous work for different combinations of C_{14}TAB and salicylate [154]. The maxima values for the apparent hydrodynamic radii are also shifted to higher values of [C_{14}TAB]/[chlorobenzoate] when

compared with the minimum of the enthalpogram. This means that for a fixed concentration of chlorobenzoate, beyond $[C_{14}TAB]/[chlorobenzoate]_{cc}$, the micelles keep growing up to their maxima length which do not coincide with the minimum of the thermogram. The progressive addition of $C_{14}TAB$ causes the redistribution of the components which leads to a higher number of shorter WLMs.

In the case of fluorescent molecules, the fractions of aromatic anions incorporated into the micelle and free in solution are commonly determined through time-resolved fluorescence spectroscopy, as proposed by Shikata and Morishima [184,185]. Additionally, based on this property, the mechanism of WLM formation in ITC experiments has been systematically investigated [68]. However, the derivatives of chlorobenzoates are not fluorescent. Alternatively, the different populations of aromatic anions can be determined by measuring the self-diffusion coefficient of the species in solution by ^1H NMR DOSY experiments. Such experiment was carried out with solutions of 4Cl and $C_{14}TAB$. The fraction of 4Cl incorporated into the aggregate, P_i, was determined through the Eq. 49.

$$P_i = \frac{D_{4Cl,i} - D^*_{4Cl}}{D^{C_{14}TAB}_{4Cl} - D^*_{4Cl}} \qquad \text{Eq. 49}$$

where $D_{4Cl,i}$ is the self-diffusion coefficient of 4Cl in a specific concentration ratio i; D^*_{4Cl} is the self-diffusion coefficient of 4Cl in pure water and $D^{C_{14}TAB}_{4Cl}$ is the self-diffusion coefficient of 4Cl assuming that it is totally incorporated into the $C_{14}TAB$ aggregate. The value measured for the self-diffusion coefficient of 4Cl in aqueous solution was $D^*_{4Cl} = 5.2\ 10^{-10}\ m^2\ s^{-1}$. $D^{C_{14}TAB}_{4Cl}$ was obtained at the condition in which $D_{4Cl,i}$ remained constant, even increasing the concentration of $C_{14}TAB$ (for $[C_{14}TAB]\ /[4Cl] > 1.4$). The value obtained for $D^{C_{14}TAB}_{4Cl}$was $0.72\ 10^{-10}\ m^2\ s^{-1}$.

The variation of the self-diffusion coefficient of the components for mixtures of $C_{14}TAB$ and 4Cl and the fraction of 4Cl incorporated into the aggregate are represented in Figure 39. The $C_{14}TAB$ and 4Cl concentration were increased two-fold compared to the ITC experiments. The parameters used for DOSY experiments can be seen in Table A2.

The values of the self-diffusion coefficient for the 4Cl, $D_{4Cl,i}^{C_{14}TAB}$, decreases as the concentration of C_{14}TAB increases and this is associated with the incorporation of part of 4Cl into the micelle. As it can be seen in the thermogram presented by Figure A24, the WLM formation occurs when $[C_{14}TAB]/[4Cl] = 0.26$. At this molar ratio, around 25% of the total 4Cl molecules were incorporated into the micellar environment to form the WLM. At the highest hydrodynamic radius ($[C_{14}TAB]/[4Cl] = 0.6$) around 60% of incorporation is observed, and finally, a fraction of 70% of the molecules of 4Cl are incorporated at the point of maximum viscosity. The further incorporation leads to the shortening of the WLM and hence, the increase of the self-diffusion coefficient of the aggregate.

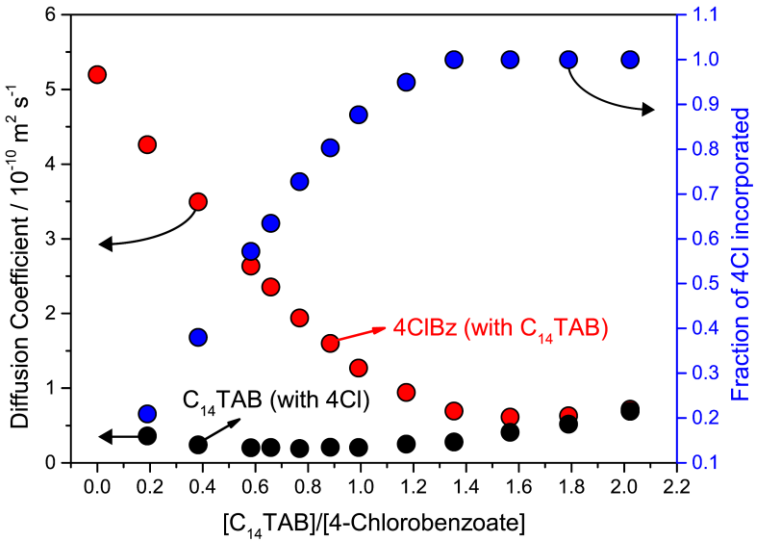

Figure 39. Self-diffusion coefficient of 4Cl in presence of C_{14}TAB (red circles), C_{14}TAB in presence of 4Cl (black circles) and fraction of 4Cl incorporated into the aggregate (blue circles) as function of the [C_{14}TAB]/[4Cl]. The C_{14}TAB and 4Cl concentration were increased two-fold compared to the ITC experiments. The temperature was maintained at $25\ °C$. The values were obtained from at least a duplicate.

Figure 40 shows the comparison of all the properties investigated and already discussed for the combination of C_{14}TAB and 4Cl. The comparison of all these properties is very

appropriate to correlate the energy released when WLM are formed, grow and become short, with the fraction of aromatic anion incorporated into the aggregate.

Images of Cryo-TEM for the solution containing C_{14}TAB and 4Cl at the critical molar ratio (black arrow of Figure 40) and at the maximum of the solution viscosity (blue arrow of Figure 40) are shown in Figure 41. The concentrations of C_{14}TAB and 4Cl were increased five times in relation with the calorimetric experiments.

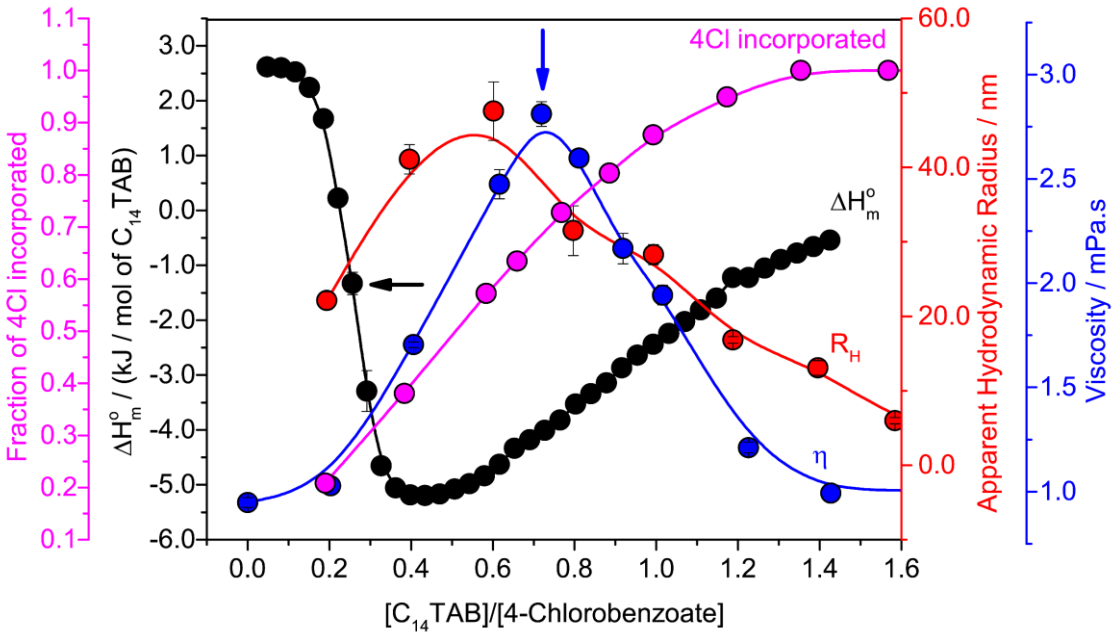

Figure 40. Variation of enthalpy in black, viscosity in blue, apparent hydrodynamic radius in red and the fraction of 4Cl molecules incorporated into the aggregate in pink as function of the ratio [C_{14}TAB]/[4Cl]. Each property is indicated in the graph and the axis is in the same color of the curve. The black and blue bold arrows indicate the [C_{14}TAB]/[4Cl] in which images of Cryo-TEM were obtained. The properties were obtained at 25 °C. The values were obtained from at least a duplicate and the lines are only guide for the eyes.

According to the pictures of Figure 41, both cases were observed WLM in solution. At [C_{14}TAB]/[chlorobenzoate]$_{cc}$, though the C_{14}TAB concentration is very low, the presence of WLM is clear, but the density of chains is low. Beyond [C_{14}TAB]/[anion]$_{cc}$, at the

maximum of the solution viscosity, more WLM are present and the images of WLM are clearer in comparison to the one obtained at $[C_{14}TAB]/[anion]_{cc}$.

Similar comparisons of Figure 40 for the other chlorobenzoates are shown in Appendix A (Figure A26 to Figure A28). The case for 3,4Cl is impressive and the maximum of solution viscosity is reached only when the $[C_{14}TAB]/[3,4Cl]$ is 12 times higher than the ratio in which WLM was formed according to ITC.

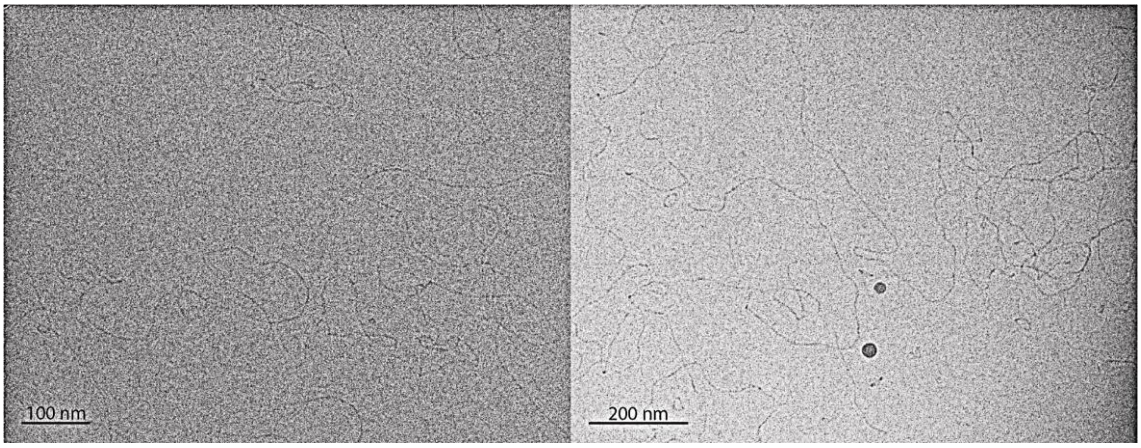

Figure 41. Cryogenic transmission electron microscopy of the solution containing $C_{14}TAB$ and 4Cl at the critical concentration ratio in which wormlike micelles are formed (left) according to the ITC experiments and at the maximum of the solution viscosity (right). The $C_{14}TAB$ and 4Cl concentration were increased 5 times in relation with the ITC experiments.

8.2. Partial conclusions

The intensity of the exothermic process observed when derivatives of chlorobenzoates are titrated with $C_{14}TAB$ in isothermal titration calorimetric experiments is a direct evidence of the affinity of the anion with the micellar environment. The embedding of the chlorobenzoate into the aggregate causes variation on the critical packing parameter, changing the morphology of the $C_{14}TAB$ aggregates when in presence of this series of chlorobenzoates, which leads to lower curvatures.

It was demonstrated that other parameters than the electrostatic interaction between the head of the surfactant and the carboxyl group of the chlorobenzoate need to be considered to explain the spontaneity of such process. The presence and position of the chlorine atoms in the aromatic ring critically influence the micellar aggregation. This was also evidenced by comparing the enthalpograms with the solution viscosity, apparent hydrodynamic radii of the aggregates and cryogenic transmission electron microscopy of the aggregates formed. If the chlorine atom is at the position 3 or/and 4 of the aromatic ring, the process of WLM formation is highly exothermic and cooperative. However, if the chlorine is at the position 2, the formation of the wormlike micelle is unfavorable, in agreement with previous results [186,187].

Interestingly, the DLS experiments have revealed that adding C_{14}TAB to a fixed concentration of chlorobenzoates, the wormlike micelles still grow beyond the critical point in which they are formed. Moreover, the [C_{14}TAB]/[chlorobenzoate] in which the viscosities of solutions reach the maxima values are shifted to higher values when compared with the minimum of the enthalpogram. For the case of C_{14}TAB and 4-chlorobenzoate, at the onset point of WLM formation, around 25% of the aromatic molecules are incorporated into the aggregates. However, the highest hydrodynamic radius is only observed when the fraction of 4-chlorobenzoate incorporated is about 50%, which agree with the Cryo-TEM pictures.

The magnitude of the energies and the critical concentrations of the surfactant and aromatic anion in which WLM are formed, grow and decrease can be precisely determined. This study demonstrated the high potential of ITC to investigate the affinity of chlorobenzoates to the micellar environment of cationic surfactant when small molecular variations are considered. One central aspect that can be drawn from this work is associated with the thermodynamic driven forces that result in wormlike micelles formation.

9. Role of F, Cl, Br and I in the wormlike micelle formation when combining C_{14}TAB with 4-halogenbenzoates [151]

9.1. Results and discussion

9.1.1. Low concentration regime

The calorimetric profile of WLM formation obtained from ITC is reasonably well understood. A lot of effort has been made by to fully characterize these systems using the ITC, always supported by other techniques such as DLS and Cryo-TEM [68,73,74,150,154,155]. In this study, we investigated the formation of WLM with C_{14}TAB and different 4-halogenbenzoates: 4-fluorobenzoate (4F), 4-chlorobenzoate (4Cl), 4-bromobenzoate (4Br) and 4-iodobenzoate (4I). The results were compared with that obtained for sodium benzoate (4H). Figure 42 shows the thermograms for the titration of 4-halogenbenzoates with either 10.0 (A) or $40.0\ mmol\ L^{-1}$ (B) of C_{14}TAB. The pH of all the solutions were fixed at 10.0 ± 0.1 to guarantee the deprotonated form of the 4-halogenbenzoic acid and that any energy variation was not related with the pH variation. The raw ITC data can be seen in Figure B1 to Figure B6.

The curves obtained with 10.0 mmol L^{-1} of C_{14}TAB are appropriated to investigate the formation, growth, and shortening of the chains of the aggregates for the anions with high affinity to the micellar environment. On the other hand, the curves with the titrant at $40.0\ mmol\ L^{-1}$ allow the investigation of the aggregation in which the incorporation of the anions into the micelle is not so favorable. The values for the variation of enthalpy and concentrations of C_{14}TAB associated with aggregation are not the same for the two surfactant concentrations. This is because for each injection, the whole variation of energy is measured. Therefore, endothermic processes, such as micellar breaking and

dehydration of the aromatic anion, and exothermic ones, associated with the interaction between surfactant and anion are simultaneously measured. If different surfactant concentrations are used in the titration, the variation of energy of the processes are different.

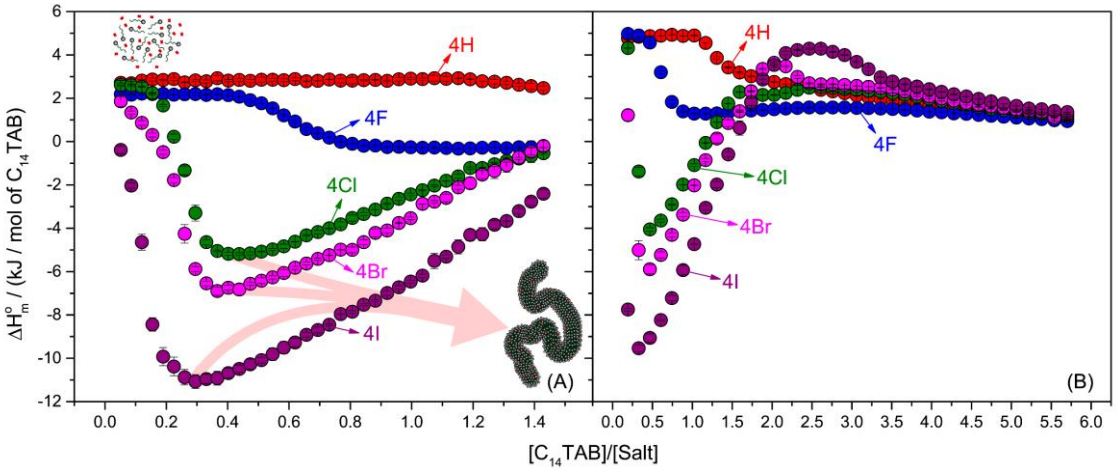

Figure 42. Variation of enthalpy per mol C_{14}TAB, ΔH^o_m, as function of the [C_{14}TAB]/[Salt] ratio using $10.0\,mmol\,L^{-1}$ (A) or $40.0\,mmol\,L^{-1}$ (B). The salts used were sodium benzoate (4H) or 4-halogenbenzoates (4F, 4Cl, 4Br, 4I) with concentration of $1.40\,mmol\,L^{-1}$ in the reaction cell. In (A) it is also represented unimers of surfactants and dissociated salts at the beginning of titration followed by the WLM aggregate formed at the minimum of the entalpogram of 4Br, 4Cl and 4I. Each curve is indicated by an arrow which specifies the salt used. The average values were obtained from at least a duplicate.

The thermogram for addition of C_{14}TAB in pure water (Figure B7) is associated with the micellar formation, in which the critical micelle concentration of the surfactant is observed at around $4.0\,mmol\,L^{-1}$ [146,154,179]. In presence of benzoate (4H), the micellar aggregation is observed at lower C_{14}TAB concentration (Figure 42B and Table 5) showing that more stable aggregates are formed. The stability is even higher when the micelles of C_{14}TAB are formed in presence of 4F, as the micellar aggregation is shifted to lower surfactant concentration. However, in all these cases, the variation of enthalpy is

relatively low in comparison with the titration of 4Cl, 4Br and 4I. The thermograms for these three aromatic anions are characteristic for WLM formation. A detailed description about the thermogram of WLM formation and the processes involved in the titration can be seen elsewhere [68,150,155] and also in section 4.2 of this thesis. It can be separated in three main regions (Figure B8): (i) at the beginning of the titration (a plateau is obtained, clearly observed for 4Cl in Figure 42A) the variation of enthalpy is small, and it is mainly associated with the demicellization process (of the C_{14}TAB micelles present in the solution of the syringe) and formation of ionic pairs; (ii) corresponding to the intense and cooperative exothermic process (for 4Cl, 4Br and 4I). It was demonstrated that, the titration of C_{14}TAB in a reaction cell containing enough sodium salicylate, the first aggregate formed (beyond the plateau) is the WLM [68] and this was the case observed for 4Cl, 4Br and 4I.; (iii) beyond the minimum of the enthalpogram, the anions remain embedded into the micelles, the aggregates grow to a maximum size and, then, the addition of more C_{14}TAB causes the decrease of the density of aromatic anions inserted into the micelles, leading to the shortening of the aggregates. In Figure 42B, a kind of shoulder for 4Cl, 4Br and 4I can be observed, indicating that in such C_{14}TAB concentration, endothermic processes overcome the exothermic processes. Beyond the shoulder, the curve trend to the base line (the variation of enthalpy goes to zero), indicating the end of the titration.

For all titrations, the standard molar enthalpy, ΔH_{ag}^{o}, Gibbs free energy, ΔG_{ag}^{o}, and entropy, $T\Delta S_{ag}^{o}$, together with the critical C_{14}TAB concentration for the aggregate formation for each organic salt were obtained using the thermogram presented in Figure 42B following the same methodology applied in the previous Chapter, Section 8.1, and they are showed in Table 5. The results are also presented in Figure 43, together with the results of the chlorobenzoate of the previous chapter (Chapter 8), as a plot of enthalpy as function of the entropy showing the enthalpy-entropy compensation [182] for the aggregation formation.

The enthalpogram for titration of C_{14}TAB in pure water can be used to compare the values for $[C_{14}TAB]_{cc}$ and ΔH_{ag}^{0} with the other cases. The variation of the free energy for micellization of C_{14}TAB in pure water is obtained directly from its CMC [188]. Therefore, based on the values of $[C_{14}TAB]_{cc}$, it can be concluded that the aggregates formed in

presence of all the studied anions are more stable relative to micelles containing only C_{14}TAB as it is possible to see in ΔG_{ag}^{o} values. However, only for the three aromatic anions (Cl, Br and I) in which WLM are formed, the contribution of ΔH_{WLM}^{o} to the variation of free energy is higher than for pure C_{14}TAB. The values for ΔH_{ag}^{o} depends not only on the specific interactions between the surfactant molecules and the anions at the micellar interface, but also on the fraction of C_{14}TAB and aromatic anion incorporated into the aggregate. In this sense, the partitioning of the anion in the aqueous phase and in the pseudo micellar phase must be considered. Part of the energy released may be associated with variations on the electronic density on the ring for the halogen atoms, affecting the cation-π interactions. The presence of the heteroatom affects the electronic cloud of the aromatic ring, influencing the ionization of the carboxyl group, as can be seen by the pK_a values of the 4-halogenbenzoic acids in Table 6. The higher is the atomic number of the halogen, the less favorable is the ionization of the acid. However, we infer that the most relevant contribution for WLM formation comes from the hydrophobic effect, which drives the anions from water to the micelle interface. The effect is much higher in the cases of 4Cl, 4Br and 4I, because the van der Waals volumes of then are significantly higher than the ones for hydrogen and fluorine.

Table 5. Standard molar enthalpy, ΔH_{ag}^{o},Gibbs free energy, ΔG_{ag}^{o}, and entropy, ΔS_{ag}^{o}, of aggregate formation and the critical C_{14}TAB concentration in $mmol\ L^{-1}$, $cc_{C_{14}TAB}$, and molar fraction, $x_{c_{14}TAB,cc}$, determined by the titration of C_{14}TAB $40.0\ mmol\ L^{-1}$ in a reaction cell containing water or organic salt $1.40\ mmol\ L^{-1}$.

Reaction cell	$cc_{C_{14}TAB}$ / $mmol\ L^{-1}$	$x_{c_{14}TAB,cc}$	ΔH_{ag}^{o} / kJ mol $^{-1}$	ΔG_{ag}^{o} / kJ mol $^{-1}$	$T\Delta S_{ag}^{o}$ / kJ mol $^{-1}$
Water	3.80	6.84 10^{-5}	-4.10	-40.89	36.79
4H	1.71	3.08 10^{-5}	-1.72	-44.30	42.58
4F	0.78	1.40 10^{-5}	-3.84	-47.64	43.80
4Cl	0.36	6.48 10^{-6}	-11.36	-50.94	39.58
4Br	0.33	5.94 10^{-6}	-13.80	-51.31	37.51
4I	0.17	3.06 10^{-6}	-17.71	-54.14	36.43

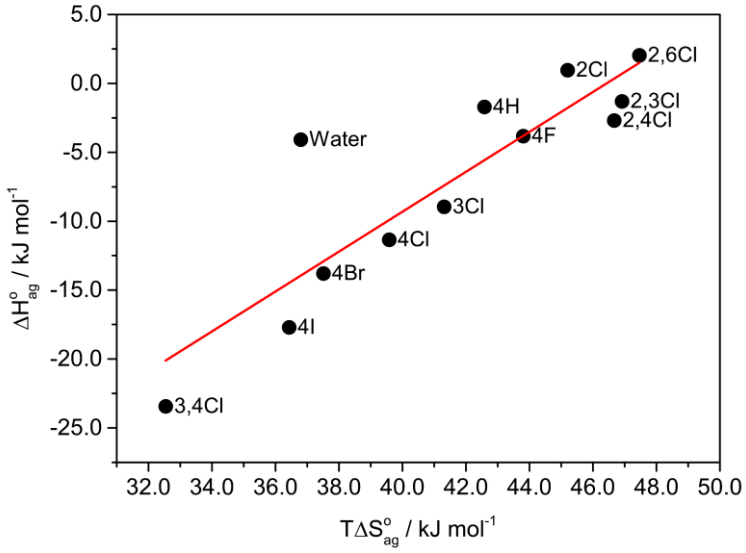

Figure 43. Standard molar enthalpy of aggregate formation (ΔH^o_{ag}) as function of standard molar entropy of aggregate formation ($T\Delta S^o_{ag}$) for all the organic salts investigated. It is also showed the results for the titration of C_{14}TAB in water. The line in red is a linear regression considering all data.

Table 6. pKa values of the benzoic acid derivatives and van der Waals volume of the atom at position 4 of the benzoic acid.

Element	pKa[a]	Van der Waals volume[b] / nm^3
H	4.20	2.3
F	4.03	4.2
Cl	4.05	7.1
Br	4.37	8.4
I	4.56	10.0

[a]determined in potentiometric titration; [b]obtained from ChemBioDraw Ultra 14.0

For a specific C_{14}TAB concentration, if the fraction of anions incorporated into the aggregate is higher, it is expected that longer WLM can be formed. Such aspect was investigated by measuring the viscosity of the solutions and the hydrodynamic radii of the aggregates. In Figure 44A are shown the curves for the variation of the viscosity of the solutions measured at the Newtonian region, as function of the [C_{14}TAB]/[4-

halogenbenzoate] ratio. For better accuracy, the concentrations of C_{14}TAB and 4-halogenbenzoates were increased 5 times relative to the ones used in the calorimetric experiments maintaining the same [C_{14}TAB]/[4-halogenbenzoate] ratio. In Figure 44B are shown the apparent hydrodynamic radii for the aggregates containing the 4Cl, 4Br and 4I as function of [C_{14}TAB]/[4-halogenbenzoate]. In order to obtain these results, the concentrations of the components were increased twice of that used in the calorimetric experiments.

Figure 44 clearly indicate the growth and the shortening of the WLM as the concentration of C_{14}TAB increases. The order of the maximum viscosity of the solutions is: 4I ≈ 20-fold 4Br and 4Br ≈ 5-fold 4Cl. Interestingly, the highest apparent hydrodynamic radii are practically the same for WLM formed with 4Cl, 4Br and 4I (Figure 44B). However, considering the high aspect radius of the WLM, the apparent hydrodynamic radius for WLM was used only to verify regions of growth and shortening of the aggregates and not the persistence length distribution of the WLMs.

The maxima values for viscosity and hydrodynamic radius do not coincide with the minimum of the curves of the thermograms (the comparative results for 4Cl, 4Br and 4I are shown in Figure 40, Figure B9, Figure B10, respectively). This trend was already observed for other WLM systems and it is explained by the fact that, by adding more C_{14}TAB, the anions remain incorporating into the aggregates even after the onset point for WLM formation [68,150,155]. For this reason, up to certain limit, the chains remain growing, but the magnitude of exothermic process decreases, once the large energy was released when the aggregate was formed. Beyond the maxima viscosities and hydrodynamic radii, the addition of more C_{14}TAB to a fixed salt concentration, makes the aggregate length decreases because the [salt] reduces. The density of incorporated anions per micelle decreases, leading to a higher number of shorter WLM.

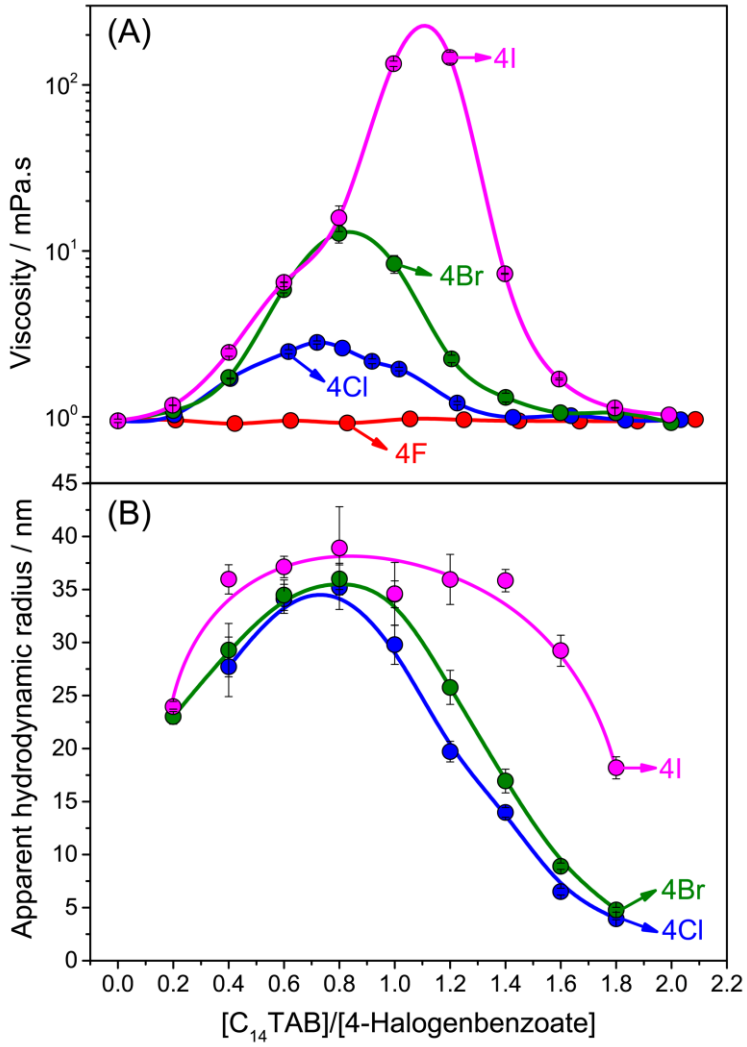

Figure 44. (A) Viscosity and (B) apparent hydrodynamic radius as function of the [C_{14}TAB]/[4-Halogenbenzoate] ratio obtained at $298\ K$. Each curve is indicated by an arrow which specifies the 4-halogenbenzoated used. The average values were obtained from at least a duplicate and the lines are only guide for the eyes.

Cryo-TEM images were acquired for solutions containing C_{14}TAB and 4F, 4Cl, 4Br or 4I and they are shown in Figure 45. Except for C_{14}TAB/4F, the samples were prepared using the two components in the concentrations in which the viscosities were maxima (Figure 44A). For 4F the Cryo-TEM images for C_{14}TAB/4F was obtained at [C_{14}TAB]/[4F] = 2.3.

Cryo-TEM images corroborated the indirect information obtained using other techniques that C_{14}TAB with 4F solution form only spherical micelles, whereas WLM were formed in the cases of 4Cl, 4Br and 4I. The size distribution of the aggregate in 4F

solution was obtained from the cryo-TEM images after counting at least 150 aggregates (Figure B11). The average radius was $2.9 \pm 0.3\, nm$ which is a little bigger than the micelles containing only C_{14}TAB [189]. Probably, this difference is associated with a small fraction of 4F incorporated into the micelle. There is a good correlation between the relative viscosity of the solutions for 4Cl, 4Br, and 4I and the correspondent Cryo-TEM images. The more viscous solutions, formed with 4I, presents larger density of WLM chains in comparison with the other systems.

By analyzing the result of ΔH_{ag}^{o}, the viscosity of the solutions and the Cryo-TEM images, it can be concluded that for a specific concentration of C_{14}TAB and 4-halogenbenzoate, larger number of 4I anions incorporates into the micellar environment relative to 4Br, 4Br relative to 4 Cl, and so on.

The partitioning of the anions between the micellar pseudo-phase and aqueous phase can be investigated using NMR, through the chemical shift of hydrogens of the aromatic anion or the self-diffusion coefficients of the species in solution. For such determination, experiments were carried out for combinations of C_{14}TAB together with 4F, 4Cl or 4Br. The experiments were not performed for 4I due to the broadening of the peak when pulsed gradient field was applied. The chemical shifts of ^{1}H nearby the COO^- and nearby the halogen atom of the aromatic anion as function of the [C_{14}TAB]/[4-Halogenbenzoate] can be seen in Figure B12. For the aromatic ^{1}H nearby the COO^- it was observed an increase in the chemical shift (downfield displacement). This is explained by the positioning of the aromatic anion at the micellar interface [190]. The surfactant and the aromatic anion are oppositely charged, so it can be expected that 4-halogenobenzoate molecules are incorporated into the micellar environment with the COO^- group and the aromatic ^{1}H nearby the COO^- pointing towards the aqueous phase. In this configuration, the ^{1}H nearby the halogen atom of the aromatic anion stays, on average, more immerse into the micelle environment suffering a upfield displacement.

The dependence of the self-diffusion coefficient of the C_{14}TAB and the 4-halogenbenzoate for 4F, 4Cl and 4Br as function of [C_{14}TAB]/[4-Halogenbenzoate] ratio is shown in Figure 46A. The fraction of the aromatic anion into the micellar environment was estimated by using the self-diffusion coefficient of the 4-halogenbenzoate in pure water and into the aggregate (Figure 46B) using the Eq. 49 of the previous Chapter. The

$D^{*}_{4-halogenbenzoate}$ measured for 4F, 4Cl and 4Br was $7.185 \cdot 10^{-10}$, $6.910 \cdot 10^{-10}$ and $6.731 \cdot 10^{-10}\ m^2 s^{-1}$, respectively, and the $D^{C_{14}TAB}_{4-halogenbenzoate}$ for 4F, 4Cl and 4Br, obtained from Figure 46A, where its respective self-diffusion coefficient stop to varies as the [C_{14}TAB] increases, are $2.02 \cdot 10^{-10}$, $1.50 \cdot 10^{-10}$ and $0.88 \cdot 10^{-10}\ m^2 s^{-1}$, respectively. The DOSY parameters used for each 4-halogenbenzoate can be seen in Table B1, Table B2 and Table B3 for 4F, 4Cl and 4Br, respectively.

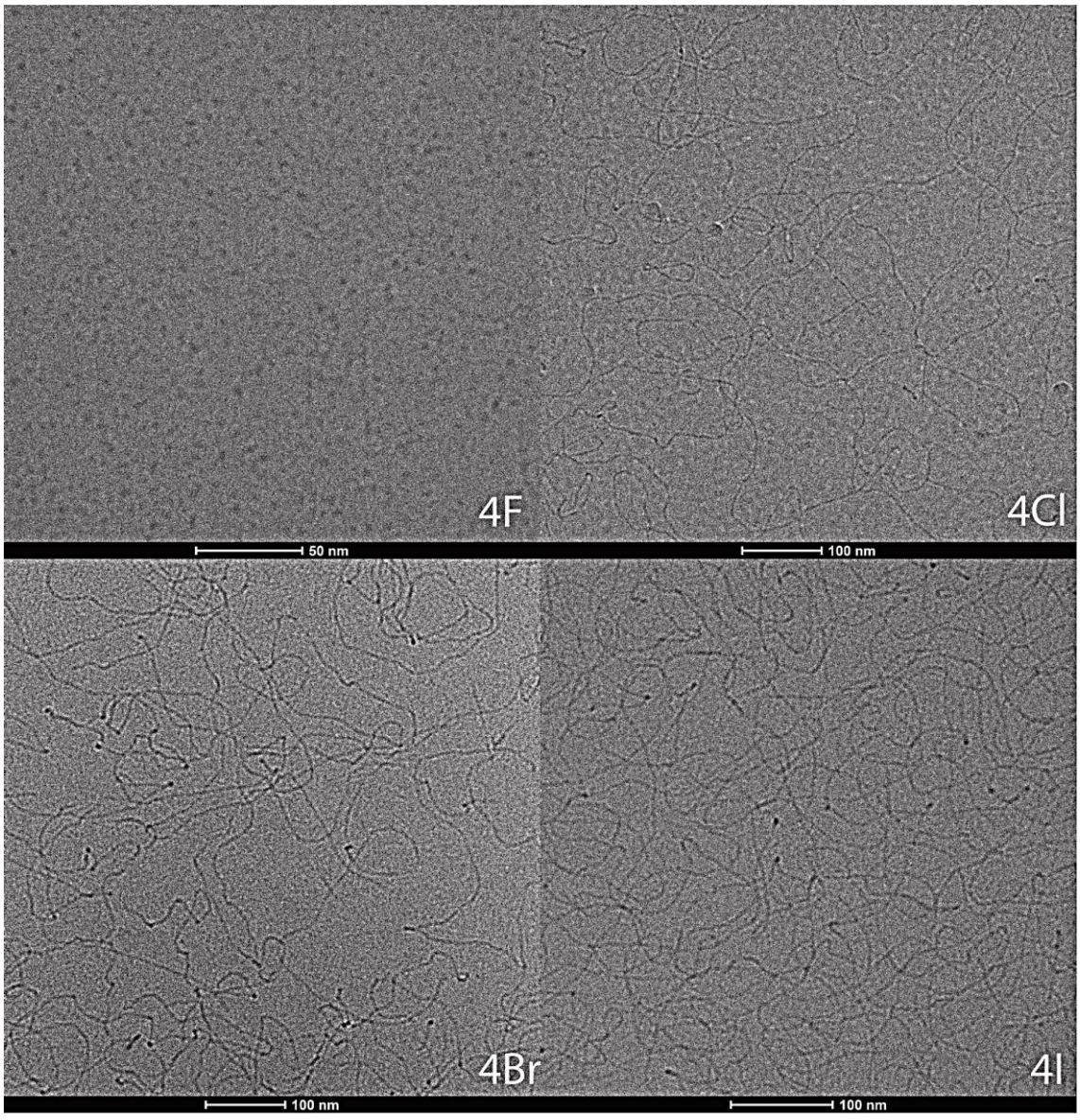

Figure 45. Cryo-TEM images obtained for all C_{14}TAB/4-halogenbenzoates studied. For 4Cl, 4Br and 4I, the images were obtained at the maximum of viscosity (Figure 44A) and for 4F at $[C_{14}TAB]/[4-halogenbenzoate] = 2.3$.

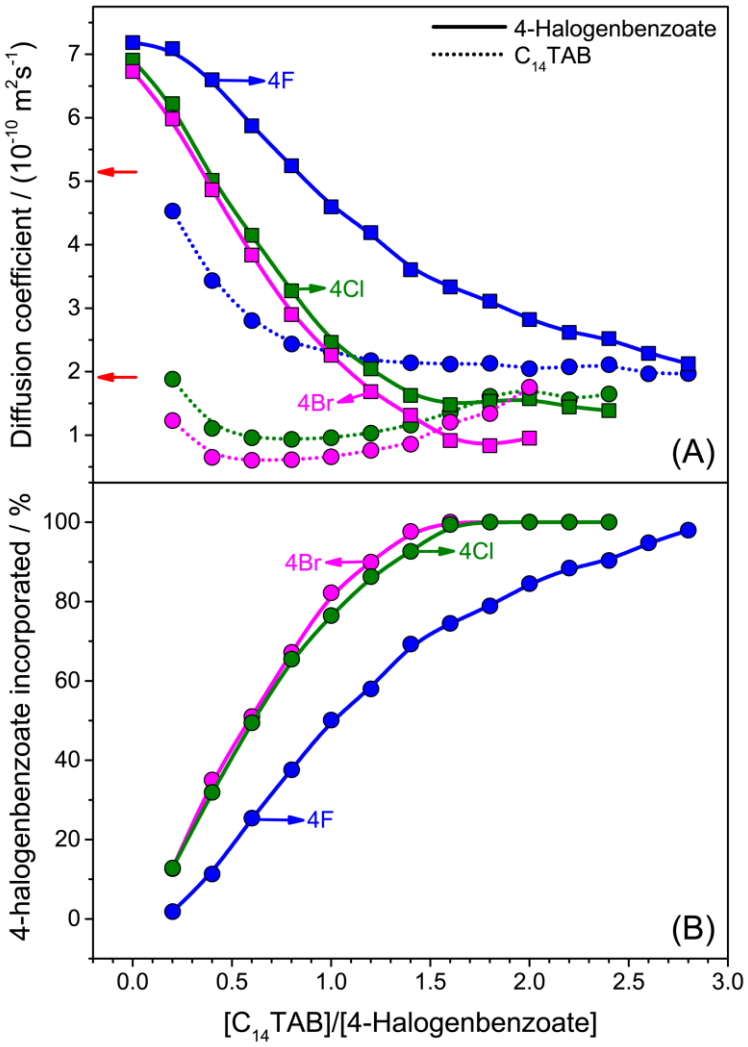

Figure 46. (A) ^{1}H Self-diffusion coefficient and (B) fraction of aromatic anion incorporated into the micelles, as function of the [C_{14}TAB]/[4-halogenbenzoate] ratio, obtained at $298\ K$. In (A), continuous and dashed lines correspond to the self-diffusion of 4-halogenbenzoate and C_{14}TAB, respectively. The self-diffusion coefficient for the unimers of C_{14}TAB and for the C_{14}TAB micelles (at $[C_{14}TAB] = 19.0\ mmol\ L^{-1}$) are indicated by red arrows in (A) and their values obtained experimentally and from [191] are 5.10 and $1.83\ 10^{-10}\ m^2\ s^{-1}$, respectively. The lines are only guide for the eyes.

Due to the incorporation into the aggregates, the self-diffusion coefficients of the aromatic anions decrease as [C_{14}TAB] increases. However, at around $[C_{14}TAB]/[4-halogenbenzoate] \approx 1.6$, light shoulders are observed for 4Cl and 4Br. The self-diffusion coefficient of C_{14}TAB also decreases, and for the combination with 4F, the

curve remains constant at $[C_{14}TAB]/[4-halogenbenzoate] \approx 0.9$, which is the same ratio in which the micelle is formed (see Figure 42B). The results for C_{14}TAB with 4Cl and 4Br are also in agreement with the previous results. The self-diffusion coefficients drop up to $[C_{14}TAB]/[4-halogenbenzoate] \approx 0.3 \sim 0.4$. Beyond this ratio, a flat minimum is observed until ≈ 1.0, and then, increasing again upon addition of more C_{14}TAB. The changes on the self-diffusion coefficient are consistent with the steps of WLM formation, growth and decrease.

An interesting aspect for 4Cl and 4Br is that in the region of the mentioned shoulder, the self-diffusion coefficient of the 4-halogenbenzoate is smaller than the correspondent values for the aggregates. A possible explanation for this is that the excess of C_{14}TAB in comparison to the 4-halogenbenzoate makes it thermodynamically favorable for simultaneous presence of aggregates containing only surfactants and WLM, resulting in an average with higher self-diffusion coefficient. This explanation was proposed by Mezzenga et al. in a system of reverse WLM [192].

Beside the limitation of the two-site model, at the [C_{14}TAB]/[4-halogenbenzoate] in which WLM are formed, only around 30% of the aromatic anion is incorporated into the micelle. Beyond this point, at the maxima viscosity of the solutions (Figure 44B), the level of incorporation reached $\approx 70\%$. Despite the differences in the viscosity of the solutions formed by C_{14}TAB and 4Cl and 4Br, according to Figure 46B, negligible variation on the fraction of incorporation of these two anions is observed. However, in range of concentration investigated, WLM formed with 4Br present lower self-diffusion coefficient (Figure 46A). The friction coefficient of a WLM chain, f, correlates with its contour length, $\bar{L}$, in a solution with viscosity η through Eq. 50 [193].

$$f = \frac{9\pi\eta}{4}\left(\frac{\pi}{6}\right)^{1/2}\bar{L}^{1/2} \qquad \text{Eq. 50}$$

Considering the Einstein equation, the self-diffusion coefficient of the WLM is $D_{WLM} = kT \;/\; f$, and then, $D_{WLM} \propto \bar{L}^{-1/2}$. Based on such relation and the self-diffusion

coefficients of Figure 46A, it can be estimate that WLM formed with 4Br are around 2.8 times longer than the ones formed with 4Cl.

9.1.2. High concentration regime

In semi-diluted and concentrated regimes, the chains of the WLM solutions entangle, forming viscoelastic solutions. The characteristic rheological diagram proposed by Rehage and Hoffmann, resulted from the combination of cationic surfactant and aromatic anions, was used for C_{14}TAB and the 4-halogenbenzoates [194]. For this, the concentration of C_{14}TAB was maintained at $60.0\ mmol\ L^{-1}$ varying the concentration of the 4-halogenbenzoates. The flow curves for the combination of the surfactant and the anions can be seen in Figure B13. From the flow curves, the plots of the zero-shear viscosity as a function of the ratio [anion]/[C_{14}TAB] were built as can be seen in Figure 47. It is important to draw attention to the fact that for low concentration, the results were expressed in terms of the ratio [surfactant]/[salt]. This is because in the ITC the surfactant concentration is continuously increasing in the cell reaction. However, for the rheological results in high concentration, the representation of the ratio as [salt]/[surfactant] is more usual.

In general, the tendency for the zero-shear viscosity was the same of that observed in the viscosity of the solution in dilute regime (Figure 44A). For the same [anion]/[C_{14}TAB] ratio, the higher is the atomic number of the halogen, more viscous are the solutions. However, as can be observed in Figure 47, two bumps are presented in the curve for 4I, with the minimum at [anion]/[C_{14}TAB] around 1.0. Around this point the viscosities of the solutions are lower than the correspondent solutions for 4Br and 4Cl. Interestingly, at the minimum, the ratio of the two components is ≈ 1.0. As pointed out by Rehage and Hoffmann [194], the minimum is observed in the region of charge neutrality of the WLM. Therefore, the low charge repulsion, enhances the contact points of the chains, leading to the formation of branched structures [80,195–197]. In such condition, the branches can slide along the micelles, creating an import mechanism for the stress relaxation, and thus lowering the viscosity. Possibly, in the range investigated, such

neutral condition is not reached for 4Br and 4Cl, due to the lower incorporation of these anions into the micelles. For this reason, the minimum is not observed.

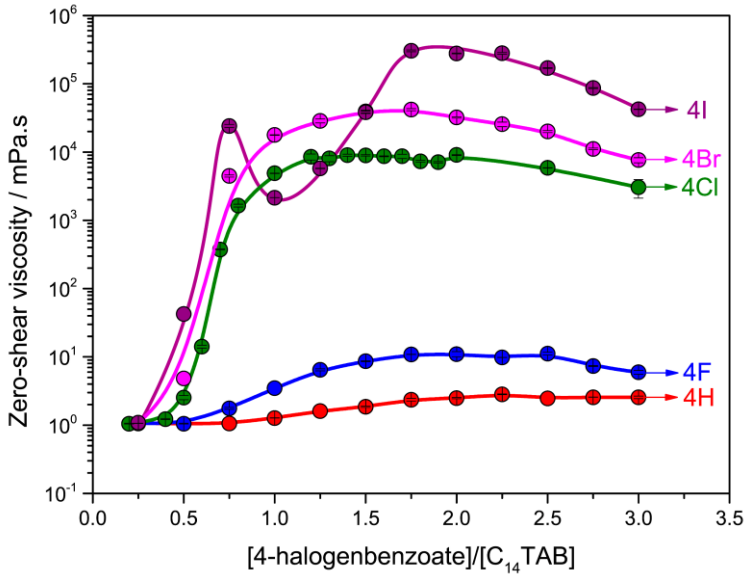

Figure 47. Zero-shear viscosity as function of the molar ratio [salt]/[C_{14}TAB] measured at $298\ K$, where the surfactant concentration was fixed at $60.0\ mmol\ L^{-1}$. The average values were obtained from at least a duplicate and the lines are only guide for the eyes.

In order to investigate this aspect, oscillatory rheology was conducted for the solutions of 4Cl, 4Br and 4I. Figure 48A presents the variation of G' and G'' as function of frequency, for samples containing C_{14}TAB $60.0\ mmol\ L^{-1}$ and 4I in different concentrations (plots for 4Cl and 4Br can be seen in Figure B14 and Figure B15, respectively). In addition, in Figure 48B are shown the Cole-Cole plots for 4I (the correspondent plots for 4Cl and 4Br can also be seen in Figure B16 and Figure B17, respectively).

In the concentration ratio where the 4I showed the decrease in viscosity, from 0.75 to 2.00, all the 4-halogenbenzoates fitted with the Maxwell model showed by Eq. 33 and Eq. 34. The Maxwellian behavior can also be verified in the Cole-Cole plots (Figure 48B), which relates the viscous with the elastic moduli by Eq. 38.

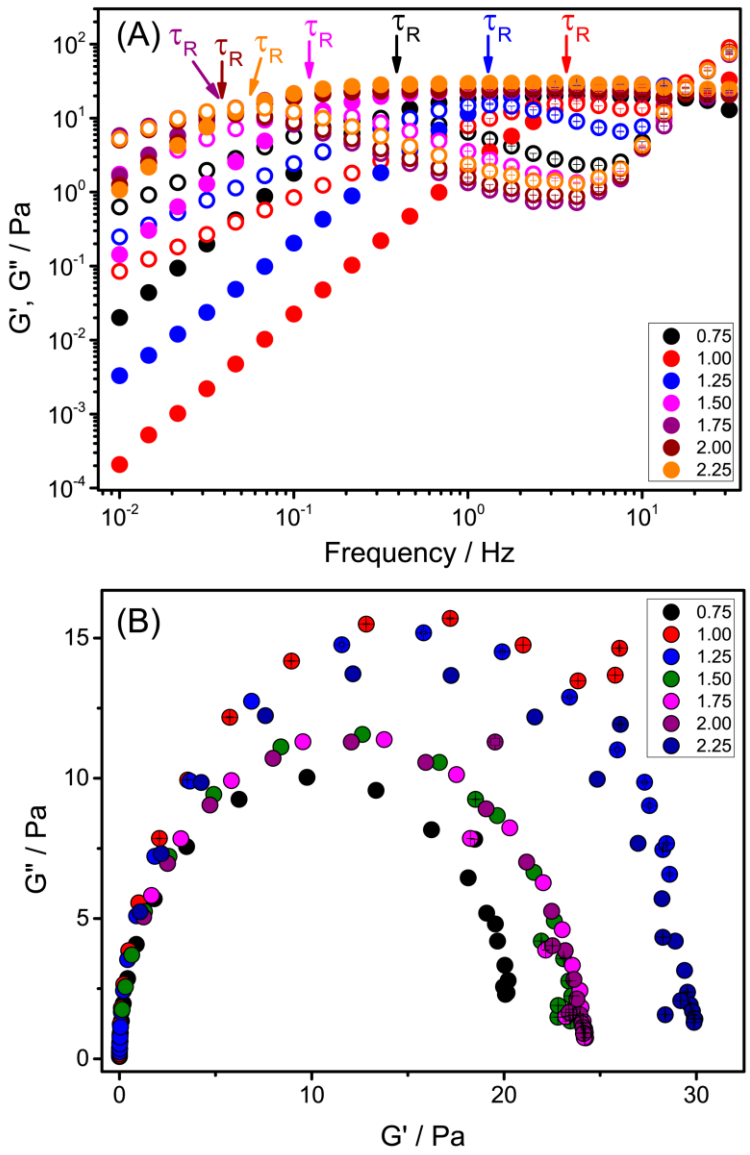

Figure 48. (A) Frequency sweep for the solutions of 4-iodobenzoate, closed symbols are for G' and open symbols for G'', and their (B) correspondent Cole-Cole plots. The legends refer to the ratio [4-halogenbenzoate]/[C_{14}TAB], in which [C_{14}TAB] was fixed at $60.0\ mmol\ L^{-1}$. Arrows in (A) indicate the relaxation time of each concentration. The experiments were carried out at $298\ K$ and the average values were obtained from at least a duplicate.

As can be observed, a quasi-perfect semi-circular trend characterizes the Maxwellian behavior. According to Cates [135], only one relaxation time $\tau_{rel.}$ is necessary to obtain a good fit, because the relaxation time of two processes, the reptation ($\tau_{rep.}$) and the

breaking-recombining ($\tau_{b.}$) contribute to $\tau_{rel.}$. For WLM in the investigated conditions, $\tau_{b.} \gg \tau_{rep.}$ and τ_R correlates with the two processes through the relation $\tau_{rel.} = \left(\tau_{b.} \cdot \tau_{rep.}\right)^{\frac{1}{2}}$ (Eq. 37). Therefore, such fast-breaking limit, where several breaking and recombination of the WLM transient chain occurs during the reptation time is the reason for a unique relaxation time required.

Using the Maxwell relations for G' and $G"$, $\tau_{rel.}$ is obtained from the inverse of the frequency at the cross point, when $G' = G"$. From parameters obtained from the rheological experiments in the linear viscoelastic regime, some characteristic lengths encountered in WLM (depicted in Figure 9) for each C_{14}TAB and aromatic anion system can be obtained.

The ratio between the contour length of WLM chain, $\bar{L}$, and the length of the segment between two entanglement points can be estimated through the relation appointed by Eq. 41. The plots of $\tau_{rel.}$ and $l_e/\bar{L}$ for WLM formed for 4Cl, 4Br and 4I, as a function of [4-halogenbenzoate]/[C_{14}TAB] are shown in Figure 49.

Based on the plots of Figure 49, some considerations about the internal structure of the WLM gel-like can be done. At $[4 - halogenbenzoate]/[C_{14}TAB] \approx 1$, the values for $\tau_{rel.}$ for 4I (Figure 49A) assume the lowest value, and this is possibly associated with the formation of the mentioned branched structure. The fast process of the sliding of the entanglements causes a fast relaxation of the applied stress, and the system becomes more liquid-like. Beyond this point, the relaxation time significantly increases, because the fraction of the aromatic anion in the Stern layer, more the fraction incorporated into the micellar palisade, make the WLM chains negatively charged. Therefore, the structure of the WLM changed from branched to entangled micelles and the process of sliding is lost. For 4Cl and 4Br, such branched structure is not formed and the variation of $\tau_{rel.}$ is in a narrower range. According to Figure 49B, at [4-halogenbenzoate]/[C_{14}TAB] = 0.75, $l_e/\bar{L}$ has the following trend: 4I < 4Br < 4Cl. This means that the density of entanglement points is higher for WLM formed with 4I. As already shown, this is because the formation of WLM is more intense with this anion.

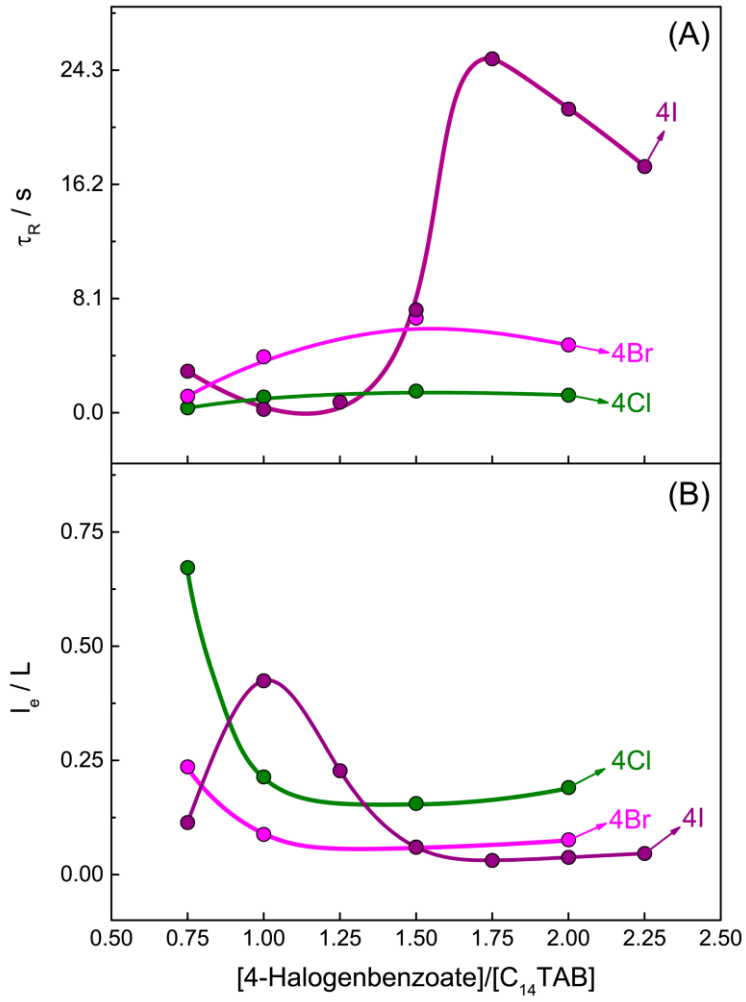

Figure 49. (A) Relaxation time and (B) $l_e/\bar{L}$ as function of the [4-halogenbenzoate]/[C_{14}TAB] for the 4Cl, 4Br and 4-iodobenzoate. The arrows in (A) indicate the color used for each 4-halogenzoate in the Figure. [C_{14}TAB] was fixed at $60.0\ mmol\ L^{-1}$. The average value was obtained from at least a duplicate and the lines are only guide for the eyes.

9.2. Partial conclusions

When the H atom at the position 4 of the aromatic ring in substituted by one halogen in benzoate, the incorporation of the anion into the micellar palisade of C_{14}TAB is more favorable. The variation of enthalpy and the critical concentration in which the aggregate is formed were determine in ITC experiments. It was observed that the higher is the atomic number of the halogen, the more energy is released during the micellar

aggregation, and the lower is the critical concentration of C_{14}TAB necessary to form the aggregate. One driven force for the embedding of the aromatic anion between the cationic heads of the surfactant is the cation-π interaction. Therefore, the substitution of H to the one halogen, can affect this interaction. Indeed, the values of pK_a for 4-halogenbenzoic acid increases from fluorine to iodine, indicating some influence of the halogen in the electronic cloud of the aromatic ring. However, the hydrophobic effect is another important component to drive the partitioning of the aromatic anion from the water phase to the micellar pseudo-phase. In this sense, the hydrophobic effect grows proportionally to the van der Waals volumes of the halogens ($F = 4.2$, $Cl = 7.1$, $Br = 8.4$ and $I = 10\ nm^3$). The high incorporation of the C_{14}TAB and 4-halogenbenzoate results in formation of wormlike micelles for 4-clorobenzoate, 4-bromobenzoate and mainly for 4-iodobenzoate, which is clearly characterized by Cryo-TEM. The thermograms obtained from titration of the 4-halogenbenzoates, with C_{14}TAB, were correlated with the formation, growth and shortening of the WLM. Such steps were also verified in the solution viscosities and the apparent hydrodynamic radii of the aggregates. By increasing the concentration of the two components the systems enter in the semi-dilute regime, characterized by the entanglements of the wormlike micelles chains. The gel-like characteristics were investigated by obtaining the rheograms in the linear and non-linear regimes. It was observed that in the case of 4-iodobenzoate, the high incorporation of the anion, result in the diagram described by Rehage and Hoffmann [194], in which two bumps are observed with a minimum viscosity at the ratio $1{:}\,1$ between the anion and the cationic surfactant. This is associated with the formation of wormlike micelles with branched structures. From the rheological results obtained in the linear regime, it was demonstrated that the systems follow the Maxwell model and the density of crosslinks is highest for 4-iodobenzoate. Wormlike micelle is a very flexible system, that can be tuned by changing components or their relative proportions. Therefore, the understand about the relevance of the molecular characteristics of the molecules that form the aggregate is central to design systems to fit for specific applications. In this sense, the present work contributes to the knowledge involving wormlike micelles.

10. Light-Triggered Rheological Changes in a System of Cationic Wormlike Micelles Formulated with a Photoacid Generator

In the first two chapters of the results and discussion, it was explored how the position and type of substituent in aromatic salts influence the formation of wormlike micelles formed with cationic surfactant. In the next two chapters, it will be explored how it is possible to formulate solutions containing wormlike micelles that are responsive to external stimuli. In this chapter, a pH responsive fluid composed of cationic surfactant C_{16}TAB or EHAC (C_{22}) with organic salt 1,2-dihydroxybenzene (DHB) will be presented and how it is possible to make it also responsive to the incidence of ultraviolet light through the addition of a photoacid generator.

10.1. Results and discussion

Figure 50 shows the molecules used in this study as well the concept behind the work. We combine $50.0\ mmol\ L^{-1}$ of the cationic surfactant C_{16}TAB with $50.0\ mmol\ L^{-1}$ of the organic acid DHB and $10.0\ mmol\ L^{-1}$ of the photoacid generator (PAG, diphenyliodonium-2-carboxylate). The black line corresponds to the zero-shear viscosity η_0 of the above solution at different pH. When this solution is irradiated with UV light, the PAG will be photolyzed by the reaction shown in Figure 50 and will thereby decompose into $10.0\ mmol\ L^{-1}$ each of benzoic acid (BA) and iodobenzene (IB) (UV-Vis spectra can be seen in Figure C1). In Figure 50, the red line corresponds to the η_0 at different pH of a solution containing $50.0\ mmol\ L^{-1}$ of CTAB and DHB + $10.0\ mmol\ L^{-1}$ of BA and IB. Conceptually, the red line is the rheology after UV irradiation. Thus, when the CTAB/DHB/PAG sample at $pH\ 7$ is exposed to UV light, the pH drops from 7 to about 3.5. Correspondingly, the viscosity increases almost 1000-fold, as shown by the

hypothetical path (blue points in Figure 50). Visual inspection also showed that the solution turned reddish, as can be noted from the vials in Figure 50. Note that the changes in viscosity, pH and color induced by UV light are irreversible. While the purpose of this Figure is to illustrate the concept, the curves in the graph correspond to actual data on our system, as shown below.

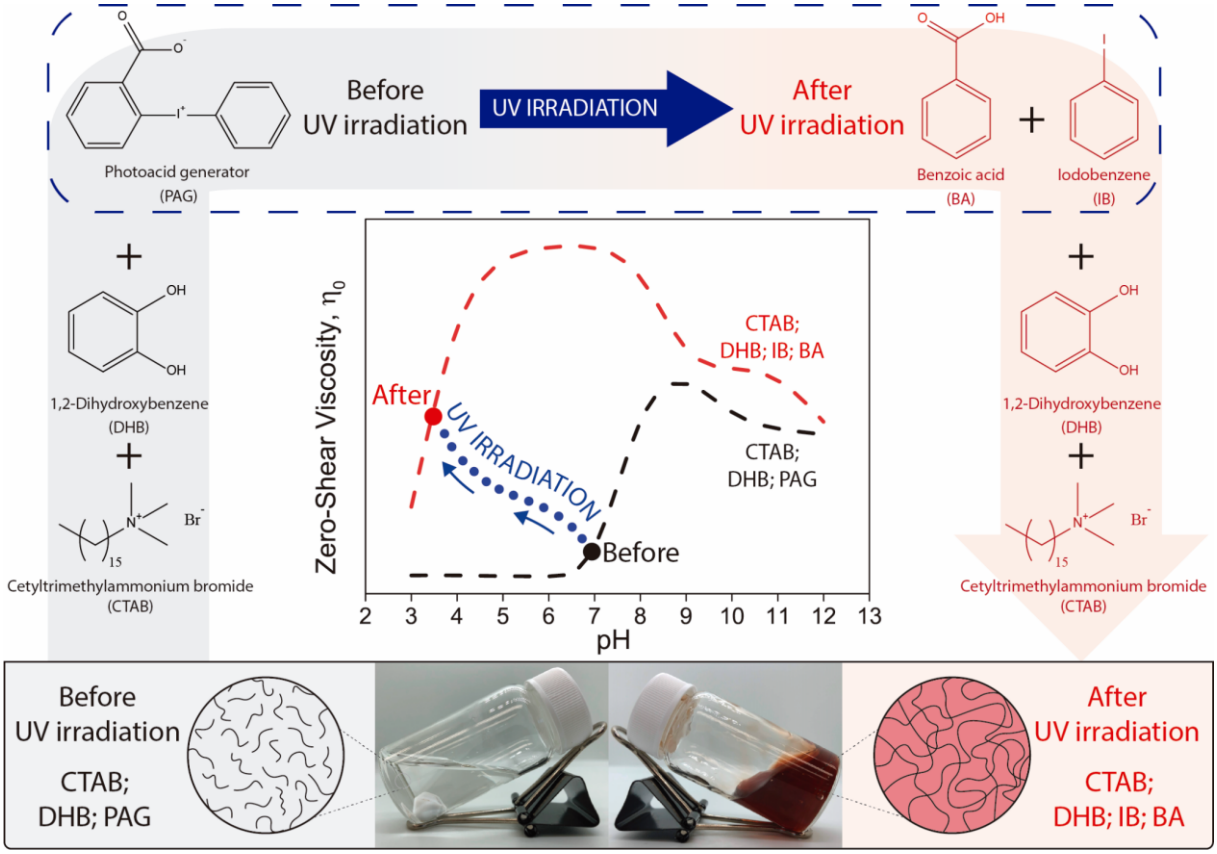

Figure 50. Schematic representation of the system and the concept behind the work. The center graph shows the zero-shear viscosity η_0 as a function of solution pH for two cases. The black line represents the solution containing CTAB, DHB and the PAG (structures in the top left). The red line represents the solution containing CTAB, DHB, IB and BA. As shown by the reaction on the right, IB and BA are the products formed by the UV-induced photolysis of the PAG. The blue line represents the change in η_0 and pH due to UV irradiation of the sample at $pH\ 7$. As the pH drops to ~ 3.5, the viscosity increases $1{,}000$-fold. The bottom panel shows visual evidence for this viscosity change: initially (left) the sample is colorless and has a viscosity close to water, whereas after UV irradiation, the sample is much more viscous and has a reddish color. The sample contains $[CTAB] = [DHB] = 50\ mmol\ L^{-1}$ and $[PAG] = 10.0\ mmol\ L^{-1}$.

Figure 51 shows rheological data (for η_0, from steady-shear rheology) for various combinations of CTAB ($50.0\ mmol\ L^{-1}$), DHB ($50.0\ mmol\ L^{-1}$), IB ($10.0\ mmol\ L^{-1}$) and BA ($10.0\ mmol\ L^{-1}$) from $pH\ 3$ to 12. All these data are for samples before any UV irradiation. Data for (i) CTAB + DHB and (ii) CTAB + DHB + BA + IB are grouped in Figure 51A. Data for (iii) CTAB + DHB + BA and (iv) CTAB + DHB + IB are in Figure 51B. The comparison of the viscosities for all the solutions investigated, without UV irradiation, can be seen in Figure C2 and the flow curves in Figure C3 up to Figure C7. In Figure 51A, the CTAB/DHB mixture shows a large increase in viscosity as the pH is increased above 7.0, with η_0 then peaking around a pH of 9.0 and then sharply decreasing. To explain this, we note that DHB has two pK_a values at 9.45 and 12.8. At low pH (< 7), DHB is fully protonated, and the neutral DHB interacts very weakly with CTAB molecules. With the first deprotonation of DHB (at $pH > 7$), DHB becomes mono-anionic and in this state, it strongly interacts with the cationic CTAB. The aromatic counterion of DHB embeds into the micellar palisade layer (due to its hydrophobicity) and such binding of the counterion strongly attenuates the micellar charge. This enables CTAB to form long WLMs, and the entanglement of these long chains drastically increases the solution viscosity. The drop in η_0 upon further pH increase is explained by the second DHB deprotonation. The dianionic DHB is less likely to remain embedded in CTAB micelles due to its high solubility in water — instead the DHB unbinds from the micelles. This has the effect of reducing the length of the WLMs and thereby reducing η_0.

The effect of IB or BA (photolysis products of the PAG) on the viscosity of CTAB/DHB was then investigated. IB is an uncharged hydrophobic molecule and it has negligible effect on η_0 apart from a small increase at high pH (Figure 51B). BA on the other hand is a weak organic acid with a pK_a of 4.2. Figure 51B shows that BA serves to increase η_0 over the pH range of 4 to 7. In this pH range, DHB is protonated, but BA becomes deprotonated and has low affinity for the micellar palisade [66,150]. Thus, BA induces WLMs of CTAB in this pH range. Surprisingly, the η_0 for the solution containing all four components (CTAB, DHB, BA, IB) is much higher than that with three out of the four components. This indicates an important synergistic enhancement of η_0 when both BA and IB are present. A possible explanation is that the presence of IB and BA changes the chemical potential of the DHB so as to favor its insertion into CTAB micelles. As the DHB is fully protonated in this pH range, the electrostatic interactions with CTAB are weak.

However, when BA and IB are both present, some of the BA and possibly also some DHB are apparently able to bind to CTAB and thereby induce WLM growth.

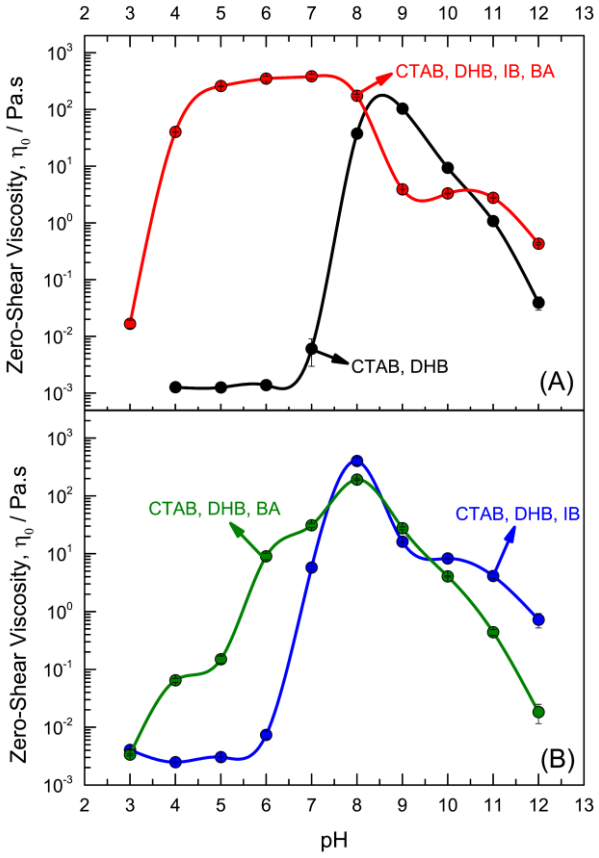

Figure 51. Zero-shear viscosity η_0 as function of solution pH for mixtures of CTAB, DHB, IB and BA (red line); CTAB and DHB (black line); CTAB, DHB and BA (green line); CTAB, DHB, IB (blue line). The following concentrations were used: $[CTAB] = [DHB] = 50.0\ mmol\ L^{-1}$ and $[IB] = [BA] = 10.0\ mmol\ L^{-1}$. The lines are only guide for the eyes and the values were obtained from at least a duplicate.

Having characterized all the scenarios without UV irradiation, we then added the PAG into the base solution of CTAB and DHB. Prior to UV exposure, the PAG has negligible influence on the CTAB/DHB rheology at pH up to 7 (Figure C8). We then took a sample of CTAB/DHB/PAG at an initial pH of 7.0 and irradiated it with UV light for a period of $30\ min$. A portion of the sample ($0.5\ mL$) was then removed and its rheology measured under steady shear. Irradiation was continued for the rest of the sample for another $30\ min$, then a sample was again removed for rheology, and the procedure was

repeated for additional intervals of time. In the absence of UV, the photolysis reaction stops, and thus, the rheology that is measured is characteristic of the UV irradiation time. We were thus able to generate the data shown in Figure 52A, which are for the viscosity η vs. shear-rate after different irradiation times. Over the first $90\ min$, η increases 10-fold, but the sample continues to show a Newtonian profile (constant η over the range of shear rates). With further irradiation, the rheology becomes noticeably shear-thinning, i.e., there is a decrease in η beyond a critical shear-rate. The zero-shear viscosity η_0 (i.e., the viscosity in the Newtonian plateau region) rises exponentially with irradiation time and it finally saturates after $390\ min$, as shown by the semilog plot in Figure 52B (a linear version of this plot, normalized by its initial viscosity, is shown below in Figure 54B). The final ratio of η_0 (after UV) to the η_0 (before UV) is more than 100.

In addition to rheology, we also monitored the solution pH at various times after UV irradiation. The combined data for η_0 and pH are mapped onto the plot in Figure 52C. This data clearly shows the initial (before UV) and final states of the sample. Initially, the sample contains CTAB, DHB and PAG, with its initial pH being 7 and its η_0 being low. UV causes the pH to drop and the η_0 to rise. Note that along with the pH drop, the photolysis products (BA and IB) are key to the rise in η_0, as discussed under Figure 51. After $390\ min$ of UV irradiation, the sample pH drops to about 3.5 and the final η_0 reached coincides with the η_0 expected for a mixture of CTAB, DHB, BA and IB at the same pH in the absence of UV. As an aside, UV caused the CTAB/DHB/PAG sample to transform from clear to a reddish color probably due to some photolysis by-product. In comparison the CTAB/DHB/BA/IB was colorless below pH 9.0. This shows that the compound giving color to the sample does not significantly affect its viscosity.

The effect of UV light on CTAB/DHB/PAG samples depends on the initial pH, as shown in Figure 53. Here, solutions at pH 7, 8, 9 and 10 were UV-irradiated and the drop in pH with time is plotted (the data in Figure 53A is normalized by the initial pH and replotted in Figure 53B). The pH decreases at the same rate in all cases over the first $75\ min$. Thereafter, there is a sharper decrease in pH when the initial pH is 7 (after a pH of 6.2 is reached). These data show that the initial pH of the sample should be carefully chosen to modulate the time-dependent rheology of the sample.

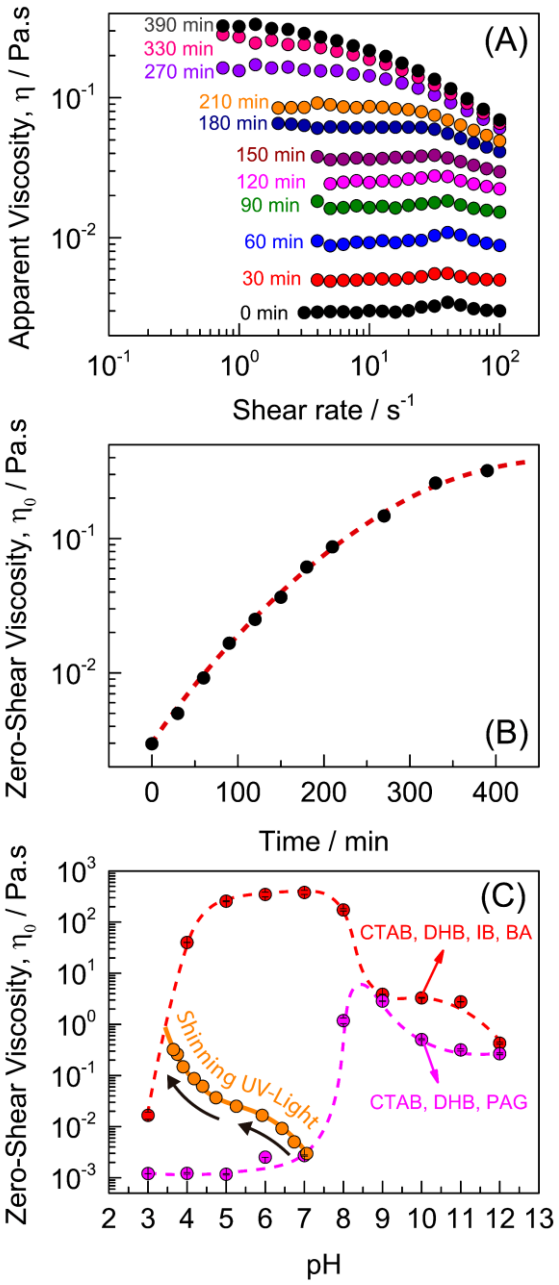

Figure 52. Effect of UV irradiation on the rheology of samples containing CTAB, DHB, and PAG. (A) Flow curves from steady-shear rheology (plots of viscosity η vs. shear-rate) of a sample with initial pH 7.0 at various UV irradiation times. (B) Zero-shear viscosity η_0 as function of irradiation time, extracted from the plots in (A). (C) Data for η_0 vs. pH for the UV-irradiated sample at various irradiation times. On this plot, data for η_0 vs. pH for a CTAB+DHB+PAG solution and for a CTAB+DHB+IB+BA solution are also plotted for comparison. The concentrations used are: $[CTAB] = [DHB] = 50.0\ mmol\ L^{-1}$ and $[PAG] = [IB] = [BA] = 10.0\ mmol\ L^{-1}$. The lines are only guide for the eyes and the values were obtained from at least a duplicate.

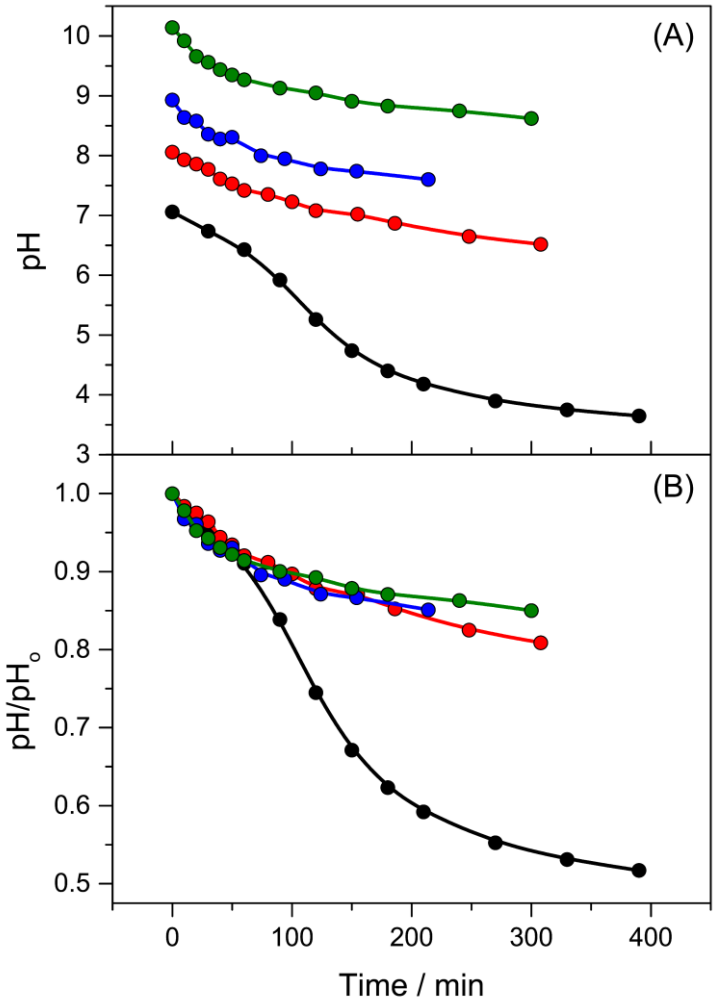

Figure 53. Solution pH as a function of UV irradiation time for the same CTAB/DHB/PAG sample starting at different initial pH. (A) Raw data; (B) Normalized data, where the pH is normalized by the initial pH (pH0). $[CTAB] = [DHB] = 50.0 mmol\ L^{-1}$ and $[PAG] = 10\ mmol\ L^{-1}$. The lines are only guide for the eyes.

In order to boost the response, we experimented with a different cationic surfactant. This surfactant, erucylbis(hydroxyethyl)methyl ammonium chloride (EHAC), has a C_{22} tail in comparison to the C_{16} tail in CTAB. Due to the longer tail, EHAC is a much stronger surfactant — for example, its critical micelle concentration is 50-fold lower than that of CTAB [107]. Results for a EHAC/DHB/PAG sample are compared to those for a CTAB/DHB/PAG one in Figure 54. In both cases, the samples are at $pH\ 7$ at $t = 0$ and thereafter they are irradiated with UV light. The viscosity rises and the pH decreases with time. For a ready comparison of the two surfactants, the data shown in Figure 54

are normalized by their values at $t = 0$ (the raw, un-normalized data are provided in Figure C9). The EHAC sample is $100 \times$ the viscosity of the CTAB sample at $t = 0$. Upon UV-irradiation, the viscosity and pH change faster for the EHAC sample. The highest η_0 is reached within $180\ min$ of irradiation, and this η_0 is $1000 \times$ the value at $t = 0$. For comparison, in the case of the CTAB sample, η_0 rises $100 \times$ the initial value and it does so in $390\ min$. With just $30\ min$ of UV, the pH decreased 0.5 units for both samples, but the corresponding rise in η_0 was 10-fold with EHAC vs. just 2-fold for CTAB. These results show that light-induced changes in properties depend on all the components present in the system, including the surfactant. Visual changes in the EHAC sample induced by UV light are shown in Figure C10 and Figure C11.

Oscillatory rheology was obtained to confirm the wormlike micelles structure in solution. Figure 55 shows the frequency sweep for the solutions containing CTAB + DHB and CTAB + DHB + PAG, both at pH 9.0 and $25\ °C$. As can be seem, both solutions present the results expected for solutions containing wormlike micelles [139], where in lower shear frequencies the solution behaves predominantly viscous (dissipation of the shear stress applied) with the $G" > G'$ and in higher frequencies, predominantly elastic, with the $G' > G"$. The inverse of the frequency where the $G' = G"$ is defined as the relaxation time $\tau_{rel.}$ [48], and as is showed in Figure 55, the addition of PAG into the CTAB + DHB solution decreases the relaxation time from 130.0 to $3.10\ s$. Additionally, the solutions do not behave as Maxwellian fluids once they did not follow the semicircular shape expected in the graph of $G' \times G"$ as can be seen in Figure C12. Responsiveness to UV light was also investigated by oscillatory rheology using EHAC + DHB + PAG system and similar trends of the Figure 55 was obtained and it can be seen in Figure C13.

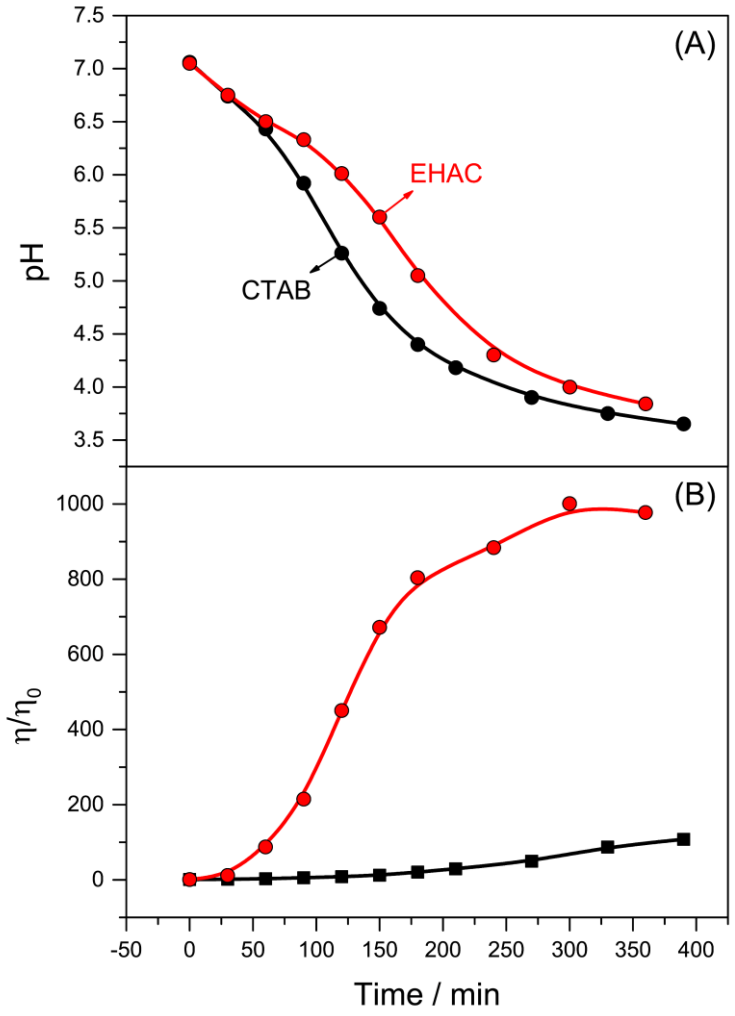

Figure 54. Solution pH (A) and zero-shear viscosity (B) as a function of UV irradiation time for a CTAB/DHB/PAG sample and an EHAC/DHB/PAG sample. Both samples start at a pH of 7. The viscosity data are normalized by its value at $t = 0$. $[CTAB] = [EHAC] = [DHB] = 50.0\ mmol\ L^{-1}$; $[PAG] = 10.0\ mmol\ L^{-1}$ for CTAB and $15.0\ mmol\ L^{-1}$ for EHAC. The lines are only guide for the eyes.

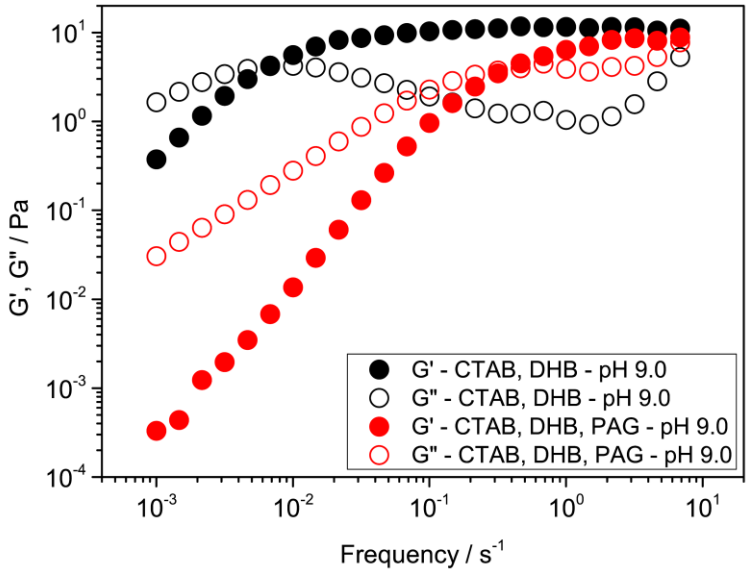

Figure 55. Elastic (G', filled symbols) and viscous (G'', empty symbols) moduli as functions of frequency for the solution containing CTAB + DHB and CTAB + DHB + PAG both at pH 9.0 and 25 °C. $[CTAB] = [DHB] = 50.0\ mmol\ L^{-1}$ and $[PAG] = 10.0\ mmol\ L^{-1}$.

10.2. Partial conclusions

We have devised a surfactant-based fluid whose rheology is sensitive to both pH and UV light. The components of the fluid are a cationic surfactant (CTAB), an aromatic compound (DHB) and a PAG (diphenyliodonium-2-carboxylate). The CTAB/DHB mixture is pH-responsive: its zero-shear viscosity η_0 increases by more than five orders of magnitude between a pH of 6 and 9. This rise in η_0 is due to the formation of WLMs, which are induced when one of the carboxylates on DHB is deprotonated. The addition of PAG to the CTAB/DHB mixture makes the fluid responsive to UV light. Upon UV irradiation, the PAG gets photolyzed into BA and IB and as a result, the solution pH drops from 7 to 3.5 and η_0 rises 100-fold. This viscosity-increase mirrors that seen with CTAB/DHB when BA and IB are both added. The extent of the viscosity-increase depends on the initial pH and the UV irradiation time. A change of surfactant from CTAB to EHAC considerably increases the maximum η_0 after irradiation (a net 1,000-fold rise over the η_0 before UV), and this higher η_0 is also reached in a shorter UV irradiation time (390 min for CTAB vs. 180 min for EHAC). Our study shows that PAGs are a powerful

class of molecules that can impart light-sensitivity to many kinds of fluids, and the use of PAGs in WLM systems is first reported herein.

11. Behavior of pH-responsive wormlike micelles in the presence of alkyl alcohols as cosurfactants

11.1. Results and discussion

As it was mentioned in the introductory part of this thesis (Chapter 1), the expected rheological behavior of diverting acidic fluid to be used in the acid stimulation stage in oil fields is relatively well known. When virgin, the acidic fluid must have low viscosity to facilitate the pumping and the incorporation of the fluid into the reservoir rock; in contact with the carbonaceous rock, the acidic fluid increases the pH and then the viscosity/viscoelasticity of the fluid so as to favor the divergence and, finally, with the continuous neutralization, the acidic fluid must decrease its viscosity so that it is recovered and does not damage the formation.

Some fluids are known to exhibit this behavior [2,11,26,28,198] and this Chapter will be aimed at fundamental research and the rheological response of an ideal fluid that has the expected behavior of a diverting acidic fluid. The fluid we chose to do this investigation is composed of C_{16}TAB and phthalic acid (PA) where we also investigated how the addition of linear alkyl alcohols as co-surfactants act on the viscosity of the system. The alcohols used were n-hexanol, n-octanol, n-decanol and n-dodecanol in different concentrations.

11.1.1. Influence of the pH and [Phthalic Acid]/[C_nTAB] ratio for the formation of WLM

Phthalic acid is an aromatic organic molecule with two acid groups subject to deprotonation (pK_a values are 2.9 and 5.5) [199]. As can be seen in Figure 56, If $pH <$

2.9, PA is the majority species in solution; if $2.9 < pH < 5.5$, P^- is the majority species in solution and if $pH > 5.5$, then, P^{2-} is majority. Due to this characteristic, PA and their deprotonated forms may present a great potential for pH responsive WLM formation depending on the species in solution. The fraction of the PA species in solution as function of the pH can be found elsewhere [199,200].

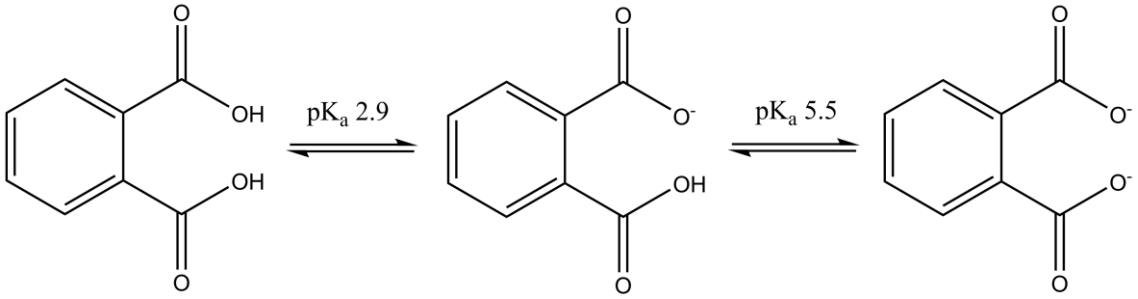

Figure 56. Molecular structures of PA and its charged species depending on the pH.

The ITC is a very interesting and sensible technique to investigate the aggregate formation and the variations in energy during this process. In this technique, a surfactant solution above its CMC can be titrated into a reaction cell containing a solution of the salt of interest. Throughout the titration, the chemical potentials of the molecules in the reaction cell can change, leading to a new interaction balance among the solvent, surfactant and salt molecules. These variations in molecular interactions are commonly followed by variations in temperature, as a result of adsorbed or released energy as heat, depending on the nature of the interactions and for each surfactant injection. The enthalpogram profile, which is obtained by enthalpy values as function of the molar ratio or concentration in the reaction cell, can provide information about the critical concentration and enthalpy for the aggregate formation and, in specific cases, can provide evidences for the form of the aggregates.

In this work, we have investigated the role of the solution pH for the WLM formation when titrating a solution containing $40.0\ mmol\ L^{-1}$ of C_{14}TAB in a solution containing $5.0\ mmol\ L^{-1}$ of PA in different pH and the results are shown in Figure 57. The raw data, without baseline correction, for each pH can be seen in Figure D1 up to Figure D8.

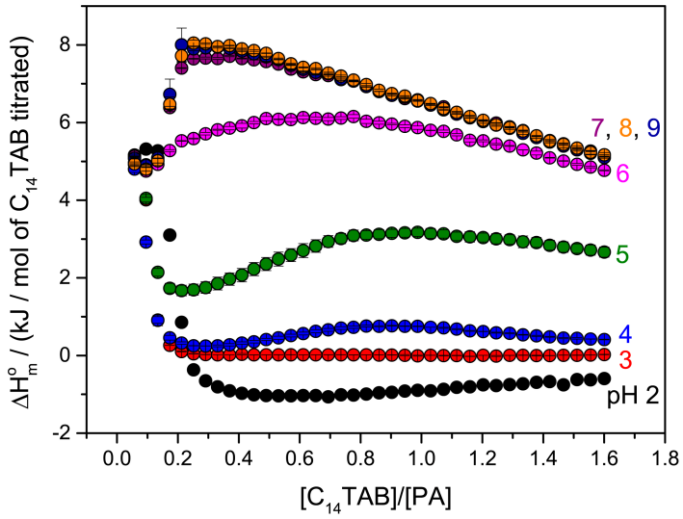

Figure 57. Molar enthalpy in kJ mol^{-1} as function of [C_{14}TAB]/[PA] ratio. $[C_{14}TAB]_0 = 40.0\ mmol\ L^{-1}$ and $[PA] = 5.0\ mmol\ L^{-1}$. The lines are only guide for the eyes and the values were obtained from at least a duplicate.

From Figure 57, it is possible to observe that the enthalpograms change considerably with the solution pH. In the conditions of the titration, it is reasonable to consider that the curves presented in Figure 57 have initial enthalpy values comparable among them. In addition, the curves can be separated in two major groups regarding the nature of the enthalpy. For pH values from 2 to 5, the aggregation processes are exothermic, whereas for pH from 6 to 9 the aggregation processes are endothermic.

For $pH\ 2$ and 3, which presented negative values of enthalpy at the minimum, the enthalpy increased ($pH\ 2$) or kept constant ($pH\ 3$) with further addition of C_{14}TAB. For pH 4 and 5, which presented a positive enthalpy at the minimum, the enthalpy increased again up to a local maximum and then decreased with further addition of C_{14}TAB. For pH 6 up to 9, the initial addition of C_{14}TAB increased the enthalpy (endothermic process) up to a maximum value and then the enthalpy decreased and for pH 7, 8 and 9, the enthalpograms have nearly the same profile.

Although the ITC is a very powerful technique to obtain thermodynamic parameters from a simple titration procedure, the interpretation of the different region of the

enthalpogram (enthalpy as function of the molar ratio) can require the correlation with other techniques. Our group has published a series of papers [68,150,151,155] identifying the enthalpogram profile for WLM formation and the interpretation according to the dynamic of the aggregate in the different regions of the enthalpogram. We proposed the enthalpogram interpretation forming the WLM with the classic sodium salicylate cosolute [68], investigated the enthalpogram profile using a series of aromatic cosolutes [155], studied the effect of the position and amount of the chlorine atom in the isomers of chlorobenzoate for the enthalpogram [150] and also studied the effect of the halogen atom size in the 4-halogenbenzoate for the formation of WLM using isothermal titration calorimetry [151].

Briefly speaking, when adding a surfactant solution, at concentration higher than its CMC, into a reaction cell containing a cosolute solution, the expected enthalpogram for WLM formation can present three main regions. The first region is associated with the rupture of the spherical micelles of the titrant solution and ionic pair formation between the free surfactants and cosolutes. This region is not always observed, depending on the hydrophobicity of the surfactant and on its affinity to the cosolute molecules. The second region, an intense exothermic process, where the surfactant concentration into the reaction cell is high enough for the formation and growth of the WLM. And finally, the third region, an endothermic process, where a redistribution of the cosolutes molecules present in the WLM aggregates is expected with a subsequently change in the aggregate length. The enthalpy of the exothermic process of the second region is the enthalpy of the WLM formation, ΔH^{o}_{WLM}, and the inflection point of this region is the critical concentration for the WLM formation, cc.

Essentially, to observe the whole curve or specific regions of the enthalpogram both concentrations, surfactant and cosolute, must be tuned. In the case of Figure 57, in order to observe the second and third region of the enthalpograms, it was not possible to observe the first region associated with the rupture of the C_{14}TAB spherical micelles. For $pH\ 2$, the PA is almost totally protonated and the interactions between the cationic surfactant C_{14}TAB and the PA is not so favorable to favor the formation of WLM, due to the absence of a negative charge, so as the enthalpogram observed has the profile of mixed micelle formation. For $pH\ 3$, where the PA species in solution are about half

protonated and half with one carboxyl group deprotonated, the enthalpogram profile did not presented the third expected region for the WLM formation. The increase in enthalpy after the local minimum and, then, even that a decrease in the cc is observed, only very short aggregates or mixed spherical micelles are expected. For $pH\ 4$ and 5, the enthalpogram observed is that expected for WLM formation. In these pH values, P^- is the majority in solution, so the Coulombic interactions between the P^- molecules and the C_{14}TAB are so strong that the entropic restrictions for P^- due to its incorporation into the aggregate interface is allowed, leading to the formation of WLM. In $pH\ 6$, the PA is almost completely deprotonated and its solubility in water is very high so as only spherical micelles with endothermic formation are observed. For $pH\ 7$ up to 9, the PA is totally deprotonated, assuming its P^{2-} form, and no molecular differences are observed among these pH so as the aggregate and enthalpogram expected is the same for all of them. Therefore, the driving force for the different forms of the aggregate and the enthalpogram obtained is associated with the PA specie in solution.

As it was seen, the pH can dictate either the WLM is going to be formed or not. In the case of the formation, a sharp increase in the solution viscosity can be expected. For the following experiments, C_{16}TAB was adopted in order to obtain results presenting changes in viscosity that are more evident than the ones expected for C_{14}TAB. In this sense, the solution viscosity of these systems was investigated in all pH range of responsiveness and [PA]/[C_{16}TAB] ratio for the aggregate formation fixing $[C_{16}TAB] = 100.0\ mmol\ L^{-1}$. The results can be seen in Figure 58 and all the flow curves can be seen in Figure D9 and Figure D10. From now on, all the results will be based on the cationic surfactant C_{16}TAB instead of C_{14}TAB because we would like to favor the formation of WLM and the use of a more hydrophobic surfactant is a common way to do so.

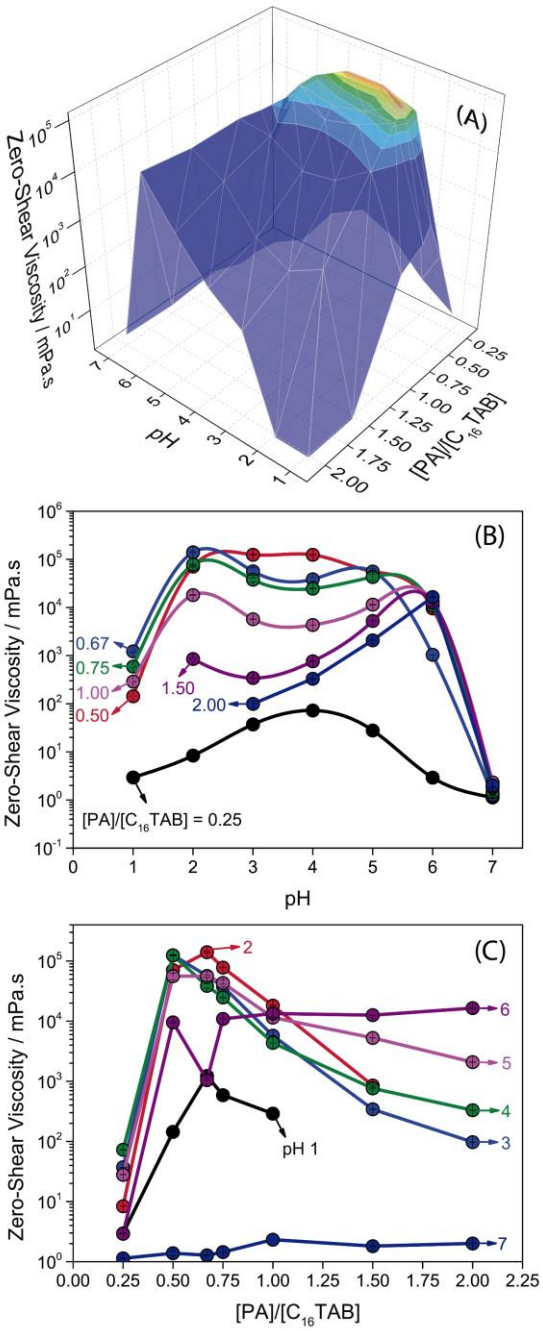

Figure 58. (A) Surface showing the influence of the solution pH and the [PA]/[C_{16}TAB] ratio for the zero-shear viscosity of the solution; (B) Zero-shear viscosity as function of the solution pH for the different [PA]/[C_{16}TAB]; (C) Zero-shear viscosity as function of the [PA]/[C_{16}TAB] in different solution pH. The lines are only guide for the eyes and the values were obtained from at least a duplicate.

The solutions were investigated in pH 1 to 7 and the ratio [PA]/[C_{16}TAB] from 0.25 to 2.00. The phase diagram, ratio as function of the solution pH, can be seen in Figure D11 and the phase separation was observed only for high [PA]/[C_{16}TAB] and low pH. For pH 1 the phase separation was observed for molar ratio higher than 1.50, whereas for pH 2, the phase separation occurred above ratio 2.00. In these pH values, both carboxyl groups of the PA are protonated and, as the Coulombic interaction with the surfactant is weak, its partition coefficient in water is high, and it precipitates because it reaches its maximum solubility in water. For all other pH and ratios, the solutions were stable at room temperature.

Both [PA]/[C_{16}TAB] ratio and solution pH are extremely important for the solution viscosity and Figure 58A shows a surface involving both variations. From Figure 58A it is possible to observe that the maximum of solution viscosity is in the range of pH 2 to 4 and ratio 0.50 to 0.75. Surfaces are interesting tools for qualitative and fast evaluation but not so friendly for quantitate assessment, then, the contour map of the surface are available in Figure D12 and also bidimensional graphs showing separately the influence of the solution pH or the [PA]/[C_{16}TAB] ratio for the solution viscosity in Figure 58B and Figure 58C, respectively.

Fixing the [PA]/[C_{16}TAB] ratio and varying the solution pH showed in Figure 58B, several remarks can be mentioned. For ratio 0.25 a different profile for the solution viscosity as function of the pH can be observed when compared to the other ratios. In this case, there is an excess of C_{16}TAB and increasing the pH, increases the solution viscosity little more than one order of magnitude comparing the pH 4, where the maximum is observed, to the pH 1 and then the solution viscosity decreases again to water-like viscosity. The gain in the viscosity in this pH range occurs due to the PA that are partially deprotonated and according to fraction of species in solution of PA as function of the solution pH, the PA with one carboxyl deprotonated has its maximum exactly at this pH.

For ratios with higher PA concentration, the profile is different from that observed for 0.25 but very similar among them. In pH 1, the solution viscosity is already two orders of magnitude higher than water. Increasing to pH 2, the solution viscosity increases more than five orders of magnitude where a maximum of viscosity is observed in some pH. Increasing the pH from pH 2 to 6, the viscosity decreases a little in pH 3, 4 and 5

and then increases again in $pH\ 6$. After this pH, the solution viscosity decreases in four orders of magnitude reaching values comparable to water.

The increase in the solution viscosity in these ratios occurred due to the formation of the wormlike micelles and a possible explanation for the maximum of the solution viscosity in $pH\ 2$ and 6 is that the high concentration of PA and C_{16}TAB changed the pK_a of the PA to favor the coulombic interactions between the PA and C_{16}TAB and hence the formation of WLM, decreasing the first pK_a and increasing the second one.

Still in Figure 58, it is worth noting that for ratios ≥ 0.50 and fixing the solution pH, the increase of the ratio makes the solution less viscous which is better visualized in Figure 58C. In Figure 58C is possible to observe that the increase of the [PA]/[C_{16}TAB] enhances the viscosity up to ratios of about 0.50 and after that, the solution viscosity drops, except for the $pH\ 7$ which changed a little the solution viscosity with the solution pH. After the maximum in the solution viscosity for ratio 0.50, the decrease with the pH is lower as higher is the pH up to $pH\ 6$, where no decrease is observed in the solution viscosity with the addition of PA.

To investigate the reversibility of the system, the solution of ratio $[PA]/[C_{16}TAB] = 0.50$ was cycled between $pH\ 1$ and $2\ 8$ times and the flow curves, together with the zero-shear viscosity in each cycle can be seen in Figure 59.

In general, the viscosities of the solutions with $pH\ 2$ are higher than the one observed in $pH\ 1$. However, the viscosity in $pH\ 1$ becomes considerable higher throughout the cycles, whereas the opposite is observed in $pH\ 2$. To change the pH from 1 to 2, or from 2 to 1, small aliquots containing HCl or NaOH were added to the solution. The WLM solution were prepared in a concentrated regime, so aliquots of acid or base were very concentrated as well. In this process of adjustment of pH, several Cl and Na^+ ions were also added, which change drastically the ionic strength of the solution. As it is already known, WLM formed by cationic surfactant and anionic salts present different responses depending on the ionic strength. Other studies involving cationic surfactants and PA showed a better reversibility than that observed in Figure 59 [201] but this occurred because their systems had a lower concentration than the one presented herein, so the

changes in pH requires a small concentration of acid or base and, consequently, a lower ionic strength variation.

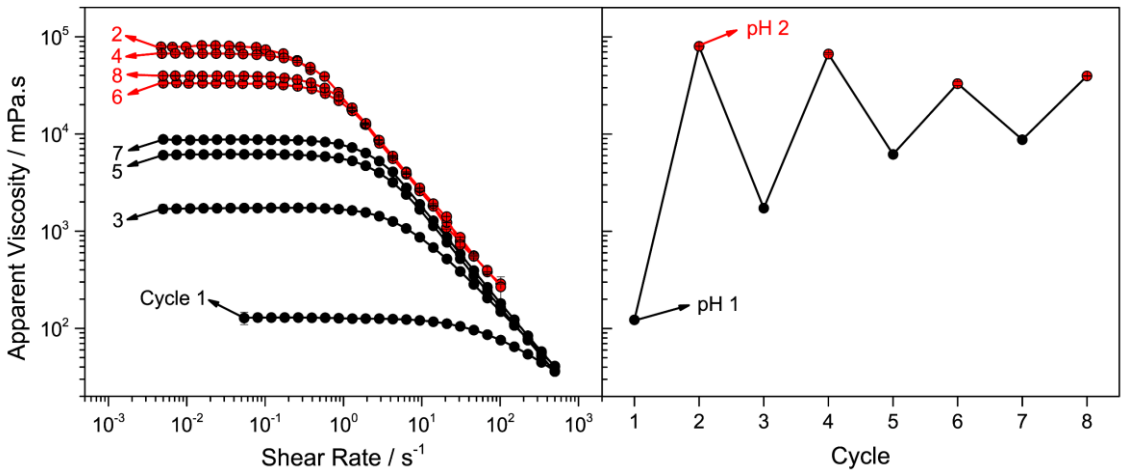

Figure 59. (A) Flow curve and (B) zero-shear viscosity over 8 pH cycling between pH 1 and 2 for the solution $[PA]/[C_{16}TAB] = 0.5$, with $[C_{16}TAB] = 100.0\ mmol\ L^{-1}$. Red curves and red squares are for pH 2 and black curves and black squares are for pH 1. The lines are only guide for the eyes and the values were obtained from at least a duplicate

Cryo-TEM images were obtained for $[PA]/[C_{16}TAB] = 0.50$, with $[C_{16}TAB] = 20.0\ mmol\ L^{-1}$, in pH 1, 3, 5 and 7 and they can be seen in Figure 60.

For pH 1 and 7 it was observed spherical micelles and for pH 3 and 5, wormlike micelles. Differently from what was observed in Figure 58 where WLM is already perceived in pH 1 due to the increase in the solution viscosity, in pH 1 cryo-TEM images were observed only spherical micelles due to the lower concentration of PA and C_{16}TAB even that the ratio is the same. We also investigated the solution viscosity in the concentrations very close of that used for cryo-TEM, using $50.0\ mmol\ L^{-1}$ of C_{16}TAB, with the same ratio, and it can be seen in Figure D13 together with the flow curves in Figure D14. The results show that, in pH 1 a decrease from 100.0 to $50.0\ mmol\ L^{-1}$ in C_{16}TAB concentration, in ratio 0.50, decreased in more than 2 orders of magnitude the solution viscosity, reaching almost the water-like viscosity. So, it is expected that in

$20\ mmol\ L^{-1}$ of C_{16}TAB and ratio 0.50, only spherical micelles are observed in $pH\ 1$ as it was observed from cryo-TEM images.

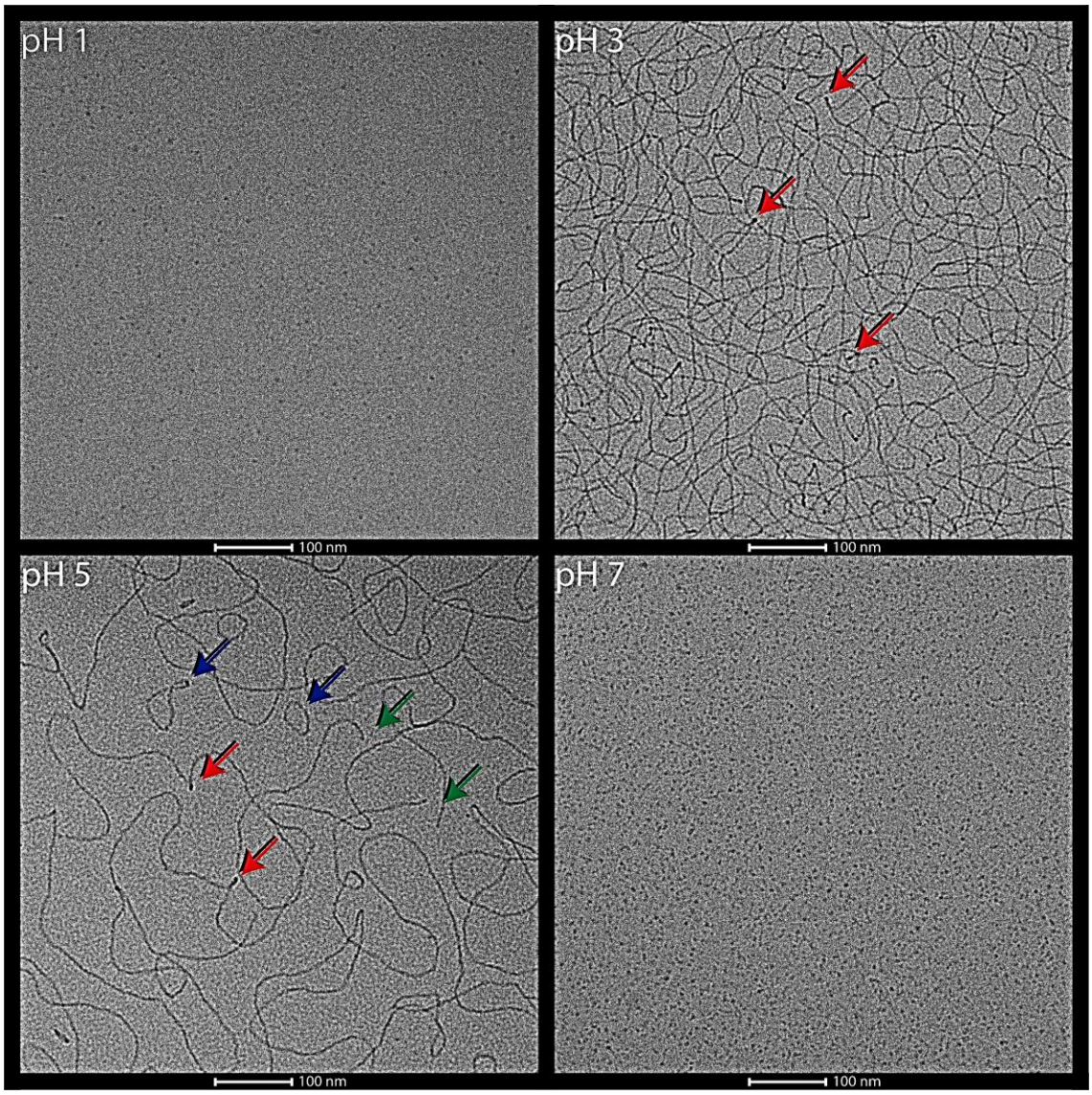

Figure 60. Cryo-TEM for $[PA]/[C_{16}TAB] = 0.5$ with $[C_{16}TAB] = 20.0\ mmol\ L^{-1}$ in $pH\ 1$, 3, 5 and 7. Red, blue and green arrows are torsion points, closed rings and endcaps of the WLMs.

The diameter of the spherical micelles observed in $pH\ 1$ and 7 has comparable sizes considering the uncertainty, $7.2 \pm 1{,}0$ and 5.8 ± 0.5 nm, respectively. For the count, at least 100 micelles were taken into account and the images considered, together with

the diameter distribution, can be seen in Figure D15 up to Figure D18. In both pH values, the diameter is similar to the one expected for spherical micelles of C_{16}TAB [202] and shows that the presence of the PA did not influence the radius of the aggregate in these pH.

For $pH\ 3$ and 5, where WLM are observed, the entanglement density is clearly different. For $pH\ 3$, a much more crowded solution is observed with several torsion points in the WLM chains while for $pH\ 5$ the WLM are relatively spaced where torsion points are also observed and also closed-ring micelles and endcaps. Even though some endcaps were observed, it was not possible to estimate any WLM contour length because no WLM was fully visualized within the detector window.

11.1.2. Addition of n-alcohols

N-alcohols with long alkyl chain is known to have surface activity and can act as co-surfactants [203,204]. The addition of these molecules in systems containing aggregates can deeply interfere in the structure and the dynamic of the aggregate formed. In this section, we studied the influence of n-alcohols such as 1-hexanol, 1-octanol, 1-decanol and 1-dodecanol in the solution containing $[PA]/[C_{16}TAB] = 0.50$ fixing $[C_{16}TAB] = 100.0\ mmol\ L^{-1}$ and all range of pH responsiveness.

To begin with, we have investigated the phase diagram for all the alcohols varying the alcohol concentration up to $20.0\ mmol\ L^{-1}$ as function of the solution pH. The results for decanol and dodecanol can be seen in Figure 61.

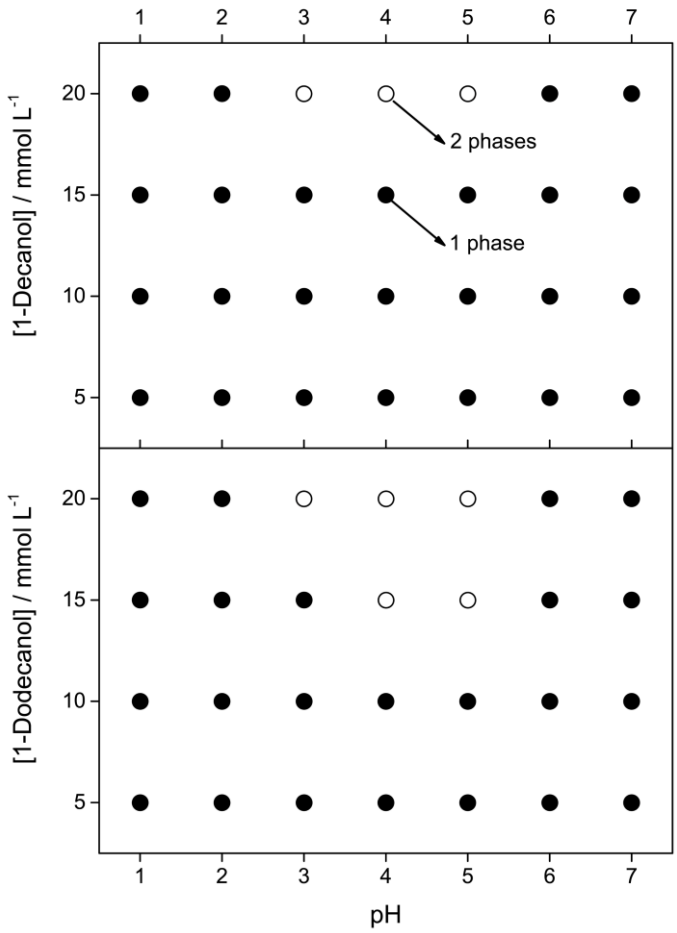

Figure 61. Phase diagrams for the solutions containing $[PA]/[C_{16}TAB] = 0.5$ with $[C_{16}TAB] = 100.0\ mmol\ L^{-1}$ and different concentration of 1-decanol or 1-dodecanol as function of the solution pH.

For hexanol and octanol, the alcohol was totally soluble until $20.0\ mmol\ L^{-1}$, but for decanol and dodecanol a phase separation was observed in higher concentration of alcohols and intermediate pH. For decanol, the phase separation occurred only with the addition of $20.0\ mmol\ L^{-1}$ of alcohol in the pH values of 3, 4 and 5. For dodecanol, the phase separation occurred in a lower concentration of alcohol, with $15.0\ mmol\ L^{-1}$ in pH values of 4 and 5, and with $20.0\ mmol\ L^{-1}$ in the pH values of 3, 4 and 5.

As the alkyl chain of the alcohols added is relatively long and all of them are totally insoluble in water, the solubilization of these alcohols in this system can only occur with the incorporation of the alcohol into the surface of the aggregate with the OH group orientated to the aqueous phase. This incorporation deeply changes the structure of the

aggregate formed and, in some cases, depending on the pH can promote the phase separation.

To investigate the role of the alcohols in the WLM chain, we also studied these solutions with rheology using the fluid $[PA]/[C_{16}TAB] = 0.50$, with $[C_{16}TAB] = 100.0\, mmol\, L^{-1}$. The zero-shear viscosity as function of the solution pH for all the alcohols investigated in the different concentration can be seen in Figure 62. The flow curves, 3D surfaces and contour maps can also be seen from Figure D19 to Figure D22.

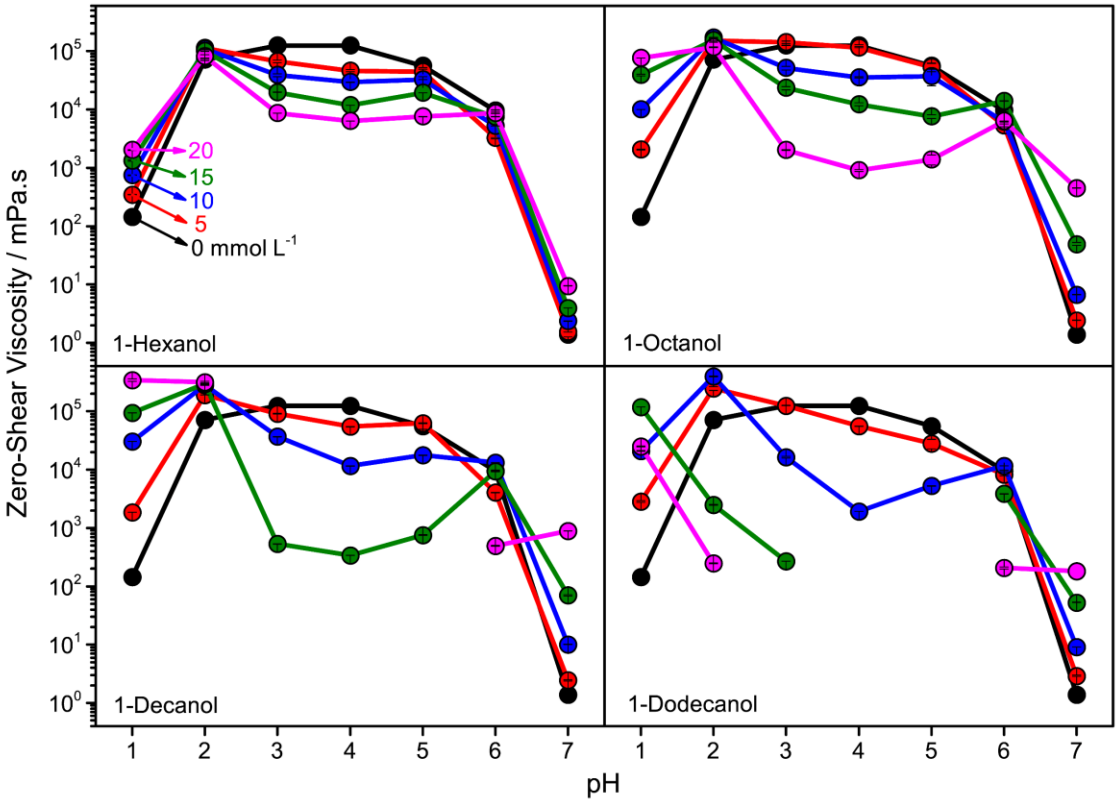

Figure 62. Zero-shear viscosity as function of the pH for the solutions containing $[PA]/[C_{16}TAB] = 0.50$, with $[C_{16}TAB] = 100.0\, mmol\, L^{-1}$, and different concentrations of the alcohols 1-hexanol, 1-octanol, 1-decanol and 1-dodecanol. The arrows in the curves of the 1-hexanol indicate the alcohol concentration and the colors scheme are the same for the other alcohols. The lines are only guide for the eyes and the values were obtained from at least a duplicate.

As can be seen, the presence of the alcohol deeply interferes in the viscosity of the solution, depending on the identity of the alcohol, concentration of the alcohol and the pH. With the alcohol incorporation into the WLM body, the dynamic of the WLM change and the intermolecular interactions occurring in the interface of the WLM, which changes the CPP and hence length of the aggregates. So, depending on the alcohol, concentration and pH, the viscosity changes both by the WLM length and by the change in the relaxation dynamic of the WLM. Unfortunately, it was not possible to obtain the results of oscillatory rheology in time to be included in the thesis due to the COVID-19 stoppage, but these data will be in the scientific article that we intend to submit with these data.

The viscosity of the solution varied with the addition of the alcohol. As higher the alkyl chain, higher the interference for the same alcohol concentration. For the extremes pH, 1 and 7, the addition of the alcohol increased the solution viscosity and for intermediate pHs, 3, 4 and 5, the solution viscosity decreased with the addition of the alcohol.

For $pH\ 1$, the predominant form of the PA is with the two carboxyl group protonated, which does not interact properly with the cationic surfactants due to the absence of a negative charge. Because of that, any addition of alcohol can change the CPP, increasing the aggregate length and the viscosity of the solution. As longer the alkyl chain of the alcohol and higher the alcohol concentration, more pronounced is this effect and higher is the solution viscosity. For the intermediate pH, 3, 4 and 5, P^- is the major specie in solution, so due to the intense Coulombic forces between the P^- and the surfactant molecules, it is expected a high incorporation of the salt in the interface of the aggregate. In this scenario, the alcohol molecules are also incorporated into the interface of the aggregate which is highly populated, and they can compete spatially with the molecules present in this crowded environment. As a consequence, the mean distance between the PA and the surfactant molecules can be increased, changing the surfactant CPP and the aggregate length and, hence, the solution viscosity. The longer the alcohol alkyl chain or the higher the alcohol concentration, the higher is the intensity of this aspect. And, finally, for $pH\ 7$ the P^{2-} is the main specie in solution which is very soluble in water and barely is incorporated into the WLM structure. The interface of the

aggregate is poorly populated by the P^{2-} and then the addition of the alcohol molecules into water increases the CPP, so its length and the viscosity of the solution.

In Figure D25, Figure D26 and Figure D27, it is also possible to find graphs of the influence of the alcohol concentration in different pH values for each alcohol used, the influence of the pH for the different alcohols used fixing the alcohol concentration and the influence of the identity of the alcohol used in the solution viscosity in the different solution pH fixing the alcohol concentration. They are essentially the same data plotted in different forms to help identify and interpret different trends.

11.2. Partial conclusions

Fluids containing wormlike micelles composed of C_{16}TAB and phthalic acid are responsive to pH and have the ideal rheological profile expected for a diverting acid fluid: when virgin (low pH), the fluid has low viscosity; with neutralization the fluid has a large increase in viscosity and, after a certain point of neutralization, its viscosity reduces again close to the water viscosity. In the case of the fluid presented in this study, this viscosity modulation is associated with the different pK_a that the phthalic acid molecule presents. At pH below the first pK_a or above the second pK_a, the phthalic acid molecule is fully protonated and deprotonated, respectively. In these forms, the interactions with the cationic surfactant are not as effective, making their partitioning in the micelle environment not high and the formation of wormlike micelles and increased viscosity is not favored. When the pH is between the two pK_a of phthalic acid, the majority form of phthalic acid in solution is the monoanionic and, due to the strong interactions with the cationic surfactant and its partitioning in the micellar environment, wormlike micelles with long contour length are induced giving the solution a high viscosity.

The addition of linear alkyl alcohols to the solution containing C_{16}TAB and phthalic acid can greatly change the viscosity and viscoelasticity of the solution depending on the pH. At pH below the first pK_a and above the second pK_a of the phthalic acid, the addition of alcohols caused an increase in the viscosity of the solution and the larger the size of the

alcohol chain, the greater the resulting viscosity. For pH intermediate to the two pK_a of phthalic acid, a decrease in viscosity was observed and, the higher the alcohol chain of alcohol, the lower the viscosity.

12. Static acid dissolution of carbonate outcrops investigated by time domain Nuclear Magnetic Resonance and X-ray tomography

12.1. Results and discussion

In addition to the rheological properties of a diverting acidic fluid (Chapter 11), the reactivity of the acidic fluid with carbonaceous rock is also another fundamental parameter for a successful acid stimulation step as discussed in Chapter 1. Thus, in this Chapter, it was investigated the acid reactivity of different carbonaceous rocks against aqueous solution of hydrochloric acid and acetic acid.

12.1.1. Acid dissolution

The carbonate samples and their reactivities were studied following the methodology described in materials and methods, section 7.7.3. The photographs of the plugs of each carbonate before the reaction can be seen in Figure E7 and the images of the same outcrops during the four dissolution cycles can be accompanied from Figure E8 to Figure E11. The figures show that the higher the time of dissolution, the more damaged the sample seems to be, indicating the progress of the chemical reaction. The corresponding mass loss as a function of time due to the acid dissolution is presented in Figure 63.

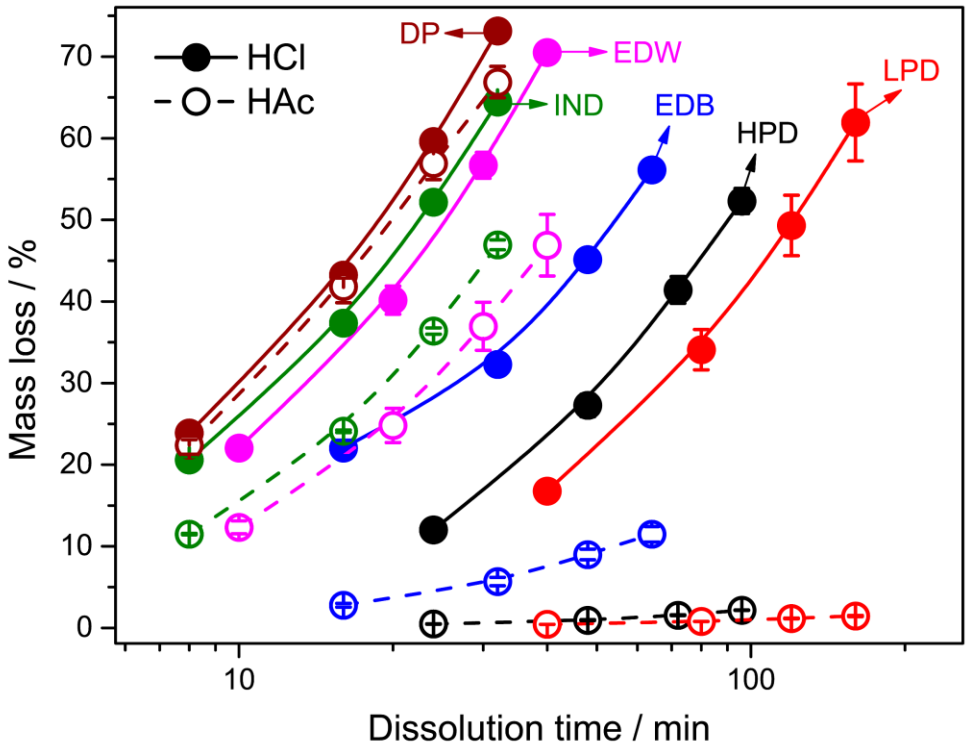

Figure 63. Percentage of mass loss as a function of the reaction time for each carbonate outcrops and both acid dissolution processes (HCl and HAc). Full symbols and continuous lines are for the results obtained in HCl and empty symbols and dashed lines are for HAc. The color scheme is represented by the arrows and the respective abbreviations for each carbonate rock. The lines are only guide for the eyes and the bar errors are mean deviations obtained for sets of three experiments.

Figure 63 can be separated into two major groups. As can be seen, there is a group of samples where the reactivity is very similar for both acids, *i.e.* the mass loss and time dependence seem to be very comparable for HCl and HAc. For this first group (group 1), we can cite DP (wine symbols), EDW (pink symbols) and IND (green symbols). In this case, the mass loss due to the dissolution in HCl solution are slightly higher than the ones for HAc, which is expected, since the HCl is a stronger acid than the organic acid, HAc.

On the other hand, the mass loss of the second group (group 2) depends strongly on the acid used. That is the case for EDB (blue symbols), HPD (black symbols) and LPD (red symbols). In Figure 63, it is possible to see that these carbonate rocks barely react with

HAc, whereas a considerable mass loss is noted when reacting with HCl, even though the percentages are still lower than the ones observed in group one.

It is very well known that petrophysical properties of carbonate rocks are very important for the kinetic aspects of a reaction with organic and inorganic acids. In this sense, we tried to correlate the results presented in Figure 63 with the permeabilities and porosities of the respective samples. These properties are summarized in Table 7, sorted by permeability, from the highest to the lowest. The morphologies of each sample can be also discussed by observing the microscopic images of thin sections, which are presented in Appendix E (Figure E12 to Figure E16).

Table 7. Permeability and porosity of each carbonate. The data is presented from the highest to the lowest permeability. The reaction group is also presented.

Carbonate rock type	Group	Permeability / mD	Porosity / %
HPD	2	468.00	14.90
EDB	2	268.00	35.30
IND	1	216.49	15.90
DP	1	97.73	25.60
LPD	2	9.74	10.60
EDW	1	0.63	17.10

A good combination of permeability and porosity, *i.e.* higher values of both properties to favor the reaction advance, could be the key to explain the results observed in Figure 63. However, no easy correlations between the trends presented in Figure 63 and Table 7 can be made. For example, HPD and EDB present the highest values of permeability and both are from the reaction group 2 where a low reactivity can be seen, depending on the acid used. In addition to that, EDW is the less permeable carbonate rock and even though it reaches one of the highest reaction rates. Porosity cannot be used to explain the trend in Figure 63 as well, since no correlations between the mass loss and the porosities values can be made. These observations are evidences that, although the morphology of the rock is relevant for the reaction with acid solutions, in the case of

static reaction the chemical composition can be more relevant. To investigate such aspect, X-ray fluorescence was carried out and the atomic compositions of the carbonates before acid dissolution are presented in Figure 64.

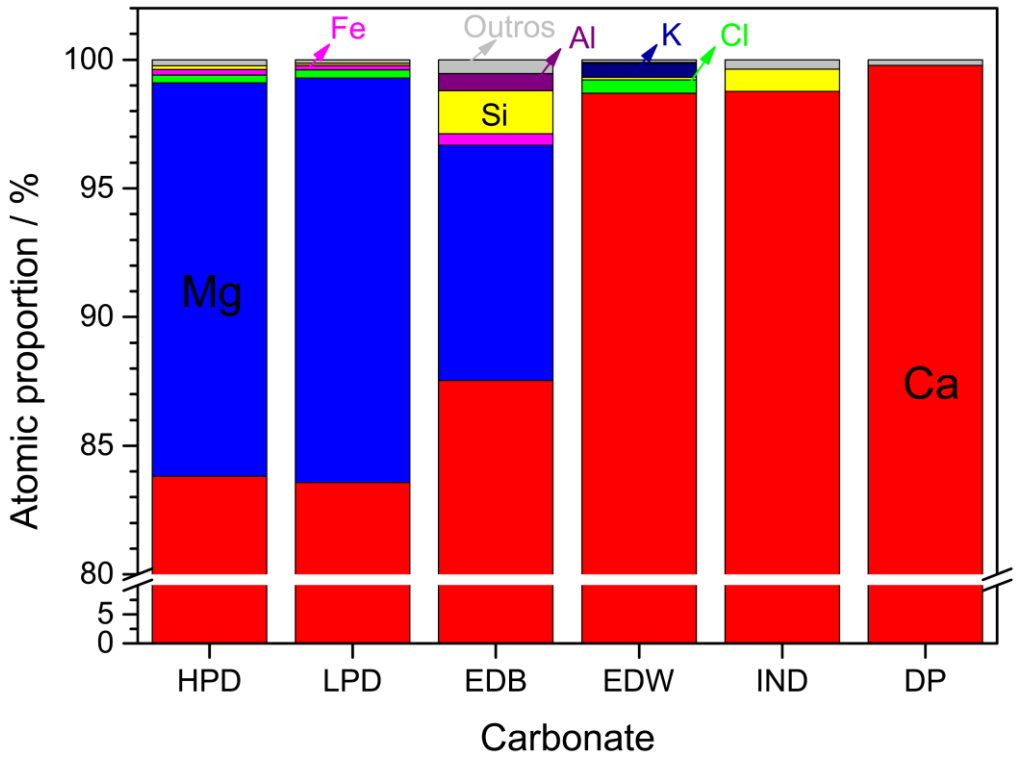

Figure 64. Atomic composition of carbonate outcrops obtained by X-ray fluorescence. Only the components with weight percentage higher than 0.1% are presented separately. Red is for calcium, blue for magnesium, yellow for silicon, purple for aluminum, dark blue for potassium, green for chlorine, pink for iron and grey is for all other elements.

Although the mass loss and the petrophysical properties are not very comparable, a good correlation can be established between the mass loss and the chemical composition (see Figure 64). HPD, LPD and EDB, the carbonate rocks from group 2 with low reactivity, present in their composition a high content of Mg. Interestingly, the higher the Mg content in composition, the lowest the mass loss observed. The dolomites presented about 15% of Mg and the lowest reaction rates followed by EDB, which is composed by about 10% of Mg. On the other hand, DP, EDW and IND do not present

significant amount of Mg in their compositions and the acid dissolution for their plugs occur normally when using both acids.

It is worth to mention that the influence of Mg^{2+} in solution was investigated. The hypothesis was that the Mg^{2+} ions released into the solution, due to the reaction between the carbonate rocks from group 2 and the acid solution, could possibly slow the progress of the reaction. To investigate that, acid solutions were prepared containing different amounts of $MgCl_2$ and the acid dissolution experiments were carried out following the same procedure. No considerable differences were noted when comparing the results of mass loss in the presence or absence of the $MgCl_2$, indicating that low reactivity for some samples depends on the nature of the carbonate rocks.

The acid used for the dissolution process also plays an important role on the mass loss results. This can be easily noted when observing the surfaces of the carbonate plugs used for the dissolution experiments (see Figure E7 to Figure E11). When comparing plugs from the same outcrop that underwent acid dissolution in HCl or HAc it is possible to observe that, depending on the acid used, the impact on the carbonate surfaces are very different. Irregular surfaces are formed for HPD and LPD, when reacting with HCl; however, practically no modifications were observed on these matrices when reacting with HAc. The remarkable cases are presented in Figure 65, where photographs of DP, EDW and EDB are presented after the first and fourth cycles for HCl and HAc solutions.

When comparing cycles 1 and 4, it can be noted that EDB samples submerged into HCl solution suffered a very uniform dissolution where the samples decreased in size radially, whereas the outcrops submerged into HAc apparently did not change considerably. Interesting, EDW and DP samples with HCl suffered a similar radial reduction in size with small grooves on the surface; however, when reacting with HAc, the original size is basically preserved, although a very irregular surface was formed with small pores on the entire outcrop. In addition to that, noticeable modifications on the coloration of the EDW and DP, depending on the acid used, being the DP the most evident example of this statement. IND samples followed a similar behavior, though it is hard to describe that due to the silicon domains that are practicable insoluble. Summarizing, samples from group 1 (DP, EDW and IND) suffer a reduction in size with

HCl and an irregular surface is formed with HAc and samples from group 2 (HDP, LDP and EDB) also suffer the radial reduction with HCl, but HAc is not strong enough to cause any modification.

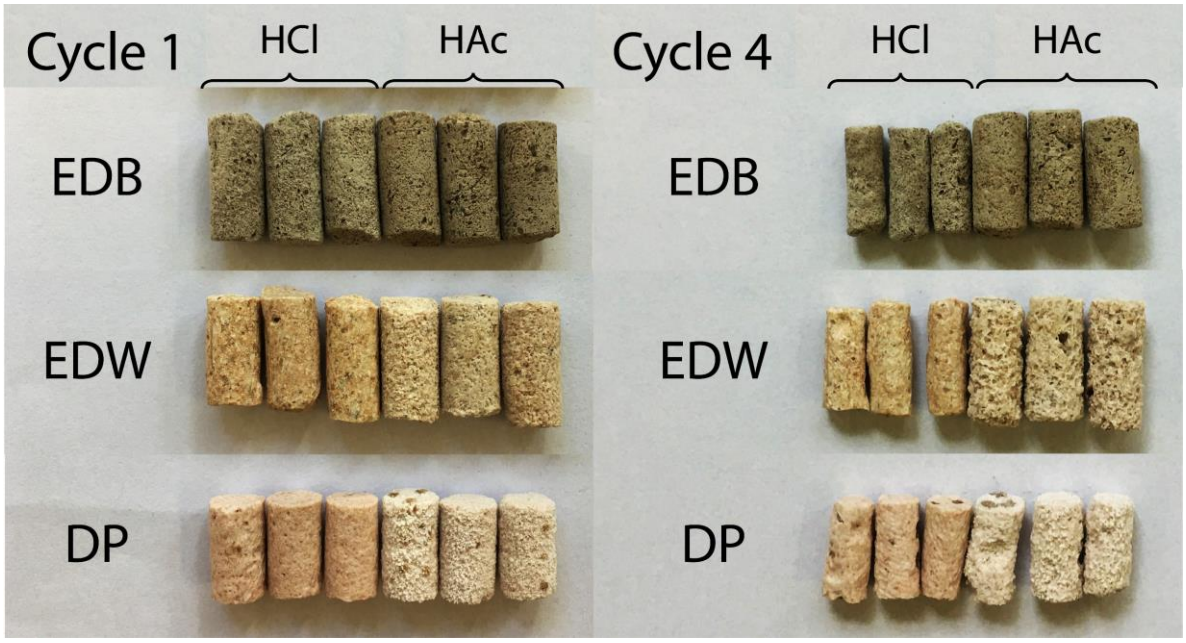

Figure 65. Pictures of the carbonates after first cycle (left) and fourth cycle (right) of acid dissolution for EDB, EDW and DP using carbonate triplicates. The three plugs on the left were reacted in HCl solution and the three on the right with HAc.

It suggests these different patterns of dissolutions may be driven by different mechanisms, depending on the acid used. HCl is a strong acid, which means that when in solution all the molecules go through ionization, forming an equivalent of H^+ and Cl^-. In this case, carbonate rocks suffer a regular dissolution because the H^+ ions are always available and in contact with the entire surface of the plugs. On the other hand, HAc is a weak acid presenting a small value of dissociation constant, *i.e.* it only ionizes partially when in solution. In this case, H^+ ions are less available in this case, so the protonated form of the molecule is more likely to collide with the surface of the carbonate plugs, slowing the reaction rate and occurring in specific points of the surface [205]. Consequently, plugs submerged into HAc solution present an irregular aspect with

several small pores on the surface, though their original dimensions are practically preserved.

12.1.2. NMR experiments

The theory for time domain NMR (TD–NMR) for porous media can be found elsewhere [206,207] and it is described that the transverse relaxation time determined for fluids within the pores can be related as in Eq. 51 [208].

$$\left(\frac{1}{T_2}\right)_{total} = \left(\frac{1}{T_2}\right)_{bulk} + \rho_2 \frac{S}{V} \qquad \text{Eq. 51}$$

where the first term on the left side of Eq. 51 refers to the bulk relaxation rate and the second the surface relaxation rate, ρ_2 is the surface relaxivity, and S and V are, respectively, the surface and volume of the pores where the water molecules are confined. Normally, the V/S ratio is associated with pore size.

In many cases, the surface relaxation rate is much higher than the bulk relaxation rate, so that the bulk contribution can be disregarded. However, in the case of the macropores in carbonate rocks, the pore sizes can be large enough to make bulk and surface relaxation rates similar, making it difficult to distinguish bulk and surface relaxations.

The outcrops used herein were very small, so the ratio between the outer pores (pores near the external surface) and the pores in the interior of these samples are very relevant. When investigating larger samples, most of the incorporated water can be found in the interior of the carbonate rocks, so that the fraction of water incorporated into outer pores is not very relevant. However, for the smaller outcrops, water molecules on the outer pores becomes important, since they represent a major portion of the incorporated water. In addition, due to the intense acid dissolution, in some of the cases listed so far, this ratio changes considerably. Since in this work the static

reaction has been investigated, the main variations occur predominantly on the external surface.

As mentioned, for these experiments, water must be incorporated into the pores of the carbonate rocks and it was done during each acid dissolution interval between the quarters of t_{50}. For each cycle, the described procedure was repeated and the amount of water incorporated was determined by gravimetry. In order to keep the outer pores filled or partially filled with water, the excess water on the external surface after saturation was removed in a process of rolling the sample over an aluminum sheet. Figure E17 presents the data of the amount of water incorporated as a function of the experimental cycle for each carbonate outcrop. Invariably, the amount of water slightly increases with the dissolution cycles.

For the group with a higher dissolution rate (DP, EDW and IND), a higher absorption of water was observed for the samples treated with HAc, probably due to formation of several pores on the surface, as discussed so far. For the other group (HPD, LPD and EDB), no considerable difference on the trends, depending on the acid, can be noted.

Following, the distributions of relaxation times for the carbonate rocks, for the different dissolution cycles when using both acids will be presented. The remarkable cases, DP and EDW, were chosen to be presented in Figure 66 and, besides these two, EDB is also presented as an example of a carbonate outcrop that did not suffered severe variations due to the acid dissolution. The other carbonates were also investigated, and the distributions of relaxation time can be found in Appendix E in Figure E18.

EDB samples are from the group of low reactivity. When reacting with HCl, it was reported a low reaction rate and, apparently, the outcrops only suffer a reduction in size radially. As a result, the relaxation time distribution does not present any considerable variations during the experimental cycles. When reacting with HAc, no considerable variations could be seen in any case.

When EDW is treated with HCl, no considerable difference can be seen even at the fourth cycle, reinforcing the idea that the outcrops were radially affected. However, treating with HAc leads to the appearance of a second population at the region of higher relaxation time values. More than that, the relative intensity of this second population

increases after each cycle of acid dissolution. As can be seen in Figure 66, outer pores are being formed and enlarged on the surface of EDW samples, which explains the existence of this second population.

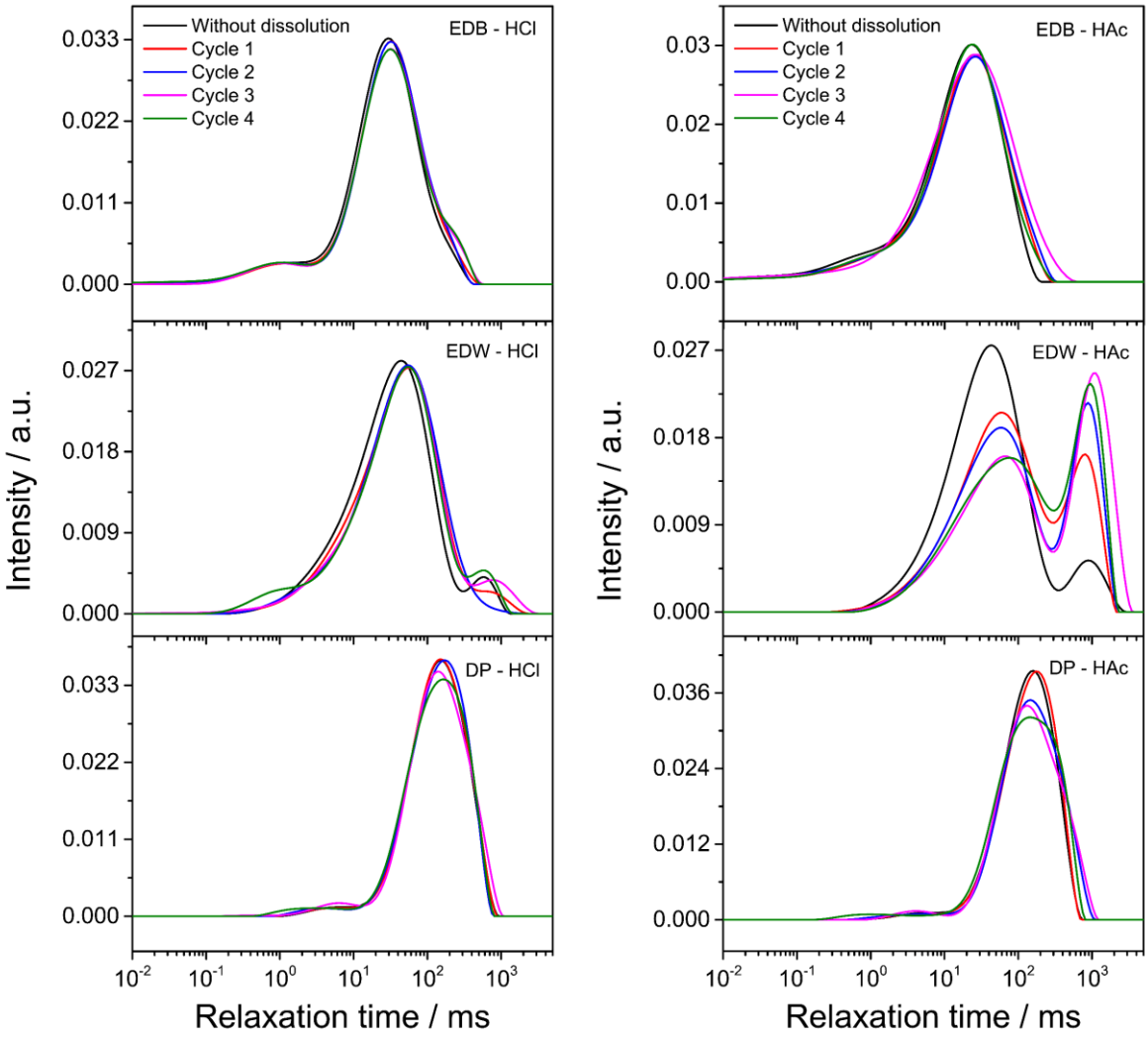

Figure 66. Transverse relaxation time distribution (T_2) after progressive cycles of acid dissolution. On the left are presented the results obtained in HCl solution and on the right are presented the results obtained in HAc. From the top to the bottom, the carbonates presented are EDB, EDW and DP.

At last, DP samples present a very interesting profile. Although a small shoulder in the relaxation time distribution is formed when treated with HAc, no considerable variation

is observed for both acids. Whether just Figure 66 is observed, it seems that DP behaves similarly to EDB samples. However, it worth to mention that besides its high reactivity (Figure 63), the surface of DP outcrops is very altered during the cycles of reaction (Figure 65).

Regarding this difference in behavior of DP and EDW samples, when reacting with HAc, it could be explained by the disparity in their permeability (see Table 7), which is about 100 times higher for DP in comparison to EDW. Hence, this could be an evidence that the HAc could penetrate deeper into the DP than it could be possible for EDW. However, this can be related only to the distribution of the pore size of each rock (which is narrow for DP).

12.1.3. Micro-CT experiments

To investigate whether is occurring variations in the inner pores or not, X-ray micro–computed tomography was carried out. Images were obtained before the reaction and after a time which corresponds to half of t_{50}. By these experiments, we intended to map the whole outcrops during the acid dissolution, better describing the variations that occur on the surface and inside the carbonate rocks.

Figure 67 presents the heat maps and the distribution of distance between the treated surface and the original surface for EDB, EDW and DP samples. A similar scheme for the other carbonates can be found in Figure E19. This information was obtained through the images of micro-CT before and after the acid dissolution for each acid (see Figure E20). The heat maps in Figure 67 show how effective was the acid dissolution on the sample surfaces. The color scale ranges from blue, for regions where the surface did not suffer variations up to the red, for regions that suffered intense variations. As already discussed, outcrops treated with HCl are more likely to suffer intense acid dissolutions and this can be seen in Figure 67. However, when treated with HAc, the acid dissolution depends on the chemical composition of the carbonate. For EDB, which presents Mg in its composition, it barely reacts, and then no considerable variations can be noted. The profile observed in this case agrees with the relaxation time distribution, presented in

Figure 66. For EDW, it is possible to notice a homogeneous dissolution for both HCl and HAc. Some specific points on the surface suffered more intense variations than other regions, creating and enlarging specific pores, as also discussed for the NMR data. For DP, although visually the samples seemed very different after treated with either HCl or HAc (regarding irregularities on the surface and coloration of the samples), no remarkable differences were observed when comparing samples throughout the dissolution cycles by using NMR and micro-CT.

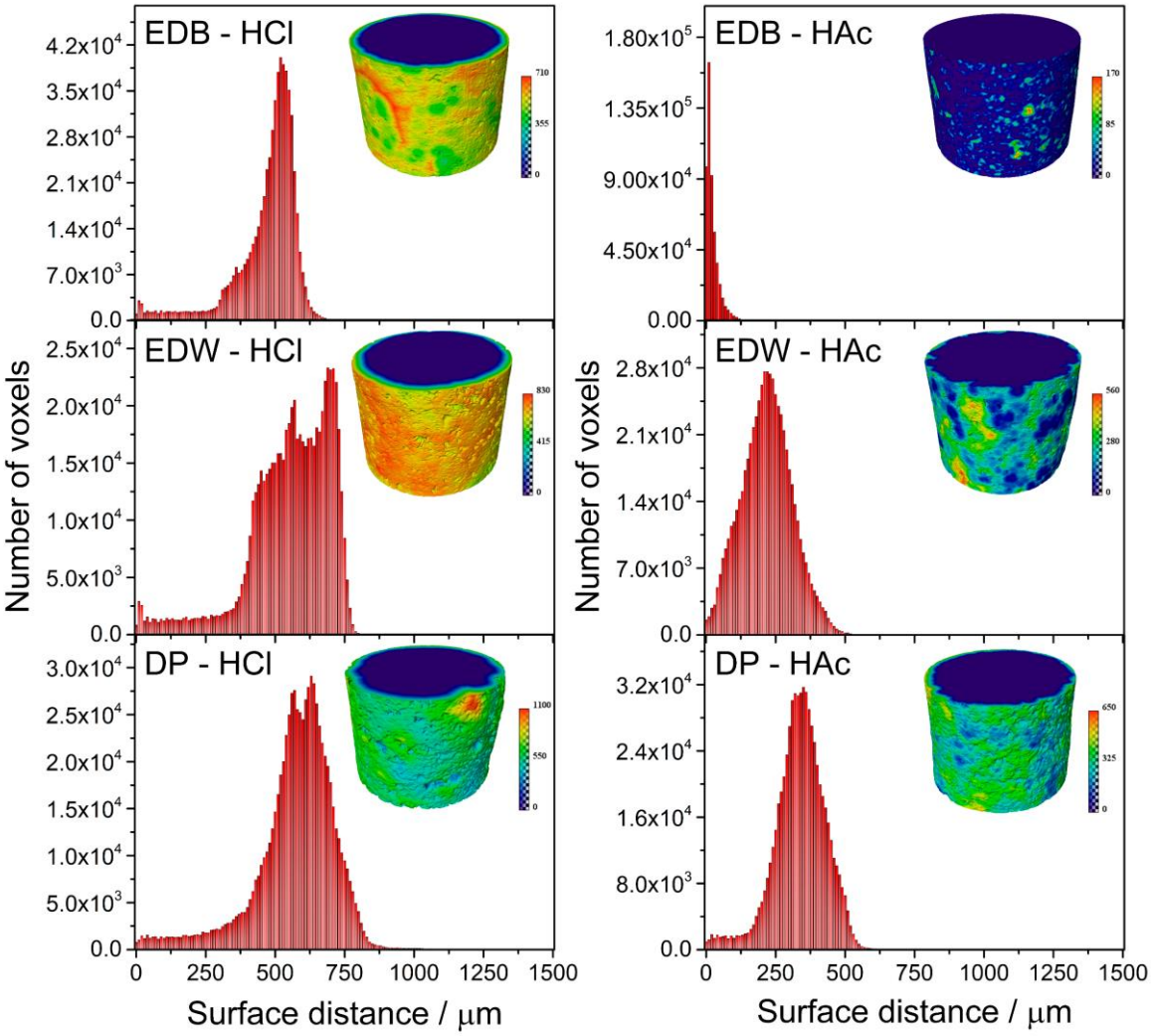

Figure 67. Heat map and points of distance between the treated surface and the original ones. On the left are presented data obtained treating the samples with HCl and on the right with HAc. From top to bottom are presented the results for EDB, EDW and DP outcrops.

Additionally, by using micro-CT, it was estimated the surface deformation due to the acid dissolution. For that, the volume and area of the surface were measured, and the respective radius values were calculated by using Eq. 45 and Eq. 46. Deformation parameter d was also calculated using Eq. 47, which is shown in Table 8

Table 8. Deformation parameter (d) calculated for samples before and after the acid dissolution in HCl and HAc.

	HCl solution		HAc solution	
Rock	d before dissolution	d after dissolution	d before dissolution	d after Dissolution
HPD	0.16	0.26	0.20	0.21
LPD	0.02	0.15	0.02	0.26
EDB	0.02	0.10	0.01	0.12
DP	0.12	0.14	0.06	0.27
EDW	0.09	0.03	0.03	0.32
IND	0.07	0.05	0.07	0.40

It is possible to observe that parameter d, even before dissolution, is different from zero and this reflects the presence of outer pores on the surface. The difference observed for parameter d before and after acidic dissolution is explained by the irregular surfaces created. Using the strongest acid HCl for dissolution, only the carbonates that showed greater reactivity (HPD, LPD and EDB) had an increase in the deformation parameter d, causing their surfaces to become more irregular. In the case of dissolution with the weaker organic acid HAc, an increase in surface deformation was observed for practically all carbonate plugs, especially those that did not have Mg in their composition, that is, those with greater reactivity.

12.2. Partial conclusions

The reactivity between a carbonate rock and an acid solution depends on many factors, such as petrophysical features, chemical composition, as well as concentration and strength of the acids. It was not possible to establish a good correlation between petrophysical features (porosity and permeability) and acid dissolution rate. However, it was identified two different sample groups regarding the dissolution rate. One of them presented higher dissolution rates (DP, EDW and IND) and the other one presented lower dissolution rate (HDP, LPD and EDB). Additionally, the difference on the dissolution rates when using HCl or HAc solutions is very pronounced in the case of the second group. From these observations, we conclude that the high Mg content present in group 2 samples (obtained by X-ray fluorescence) is mandatory for the reactivity.

The dissolution profiles obtained after the dissolution processes are different for each group and for each acid. When reacting with HCl, samples have their size decreased almost homogeneously and radially, regardless which group they come from. When reacting with HAc, group 1 samples present different patterns, where a very irregular surface is formed. This was explained by the difference in mechanism of reaction, which depends on the availability of H^+ in solution. These different patterns were investigated by ^{1}H-NMR and micro-CT, which showed good correlation. The static acid dissolution affects majorly the surface of the carbonate rocks. ^{1}H-NMR and micro-CT demonstrate that, according to procedures employed, the dissolution occurs mainly on the surface of the carbonate samples, with no significant effects on the internal pores.

13. Evaluation of a new formulation based on viscoelastic surfactant for acid stimulation in carbonates

All the rheological and flow results obtained for QuoVadis were collected in collaboration with students Renato Nunes de Souza and Matheus da Silva Barbosa. In this Chapter, I will present in a general way the progress of the different generations of QuoVadis, but a more detailed description for QuoVadis G2, will be addressed in the master's dissertation of Matheus da Silva Barbosa which is planned to be defended in the first half of 2021. So, I would like to thank Matheus da Silva da Barbosa for allowing me to use some of the rheological and flow results of QuoVadis G2 so that I could do this approach.

Commercially available diverting acid fluids were studied in this Chapter to elaborate an easy, reproducible and reliable methodology. Although it was found very interesting profiles and results for the commercial diverting fluids, VES 1 and VES 2, they are not the main focus of this Chapter. The main idea is to study the feasibility to create an economically favorable fluid which can be versatile to attend different demands, regarding the different properties that can be relevant for a diverting acid solution. This goal justifies the existence of different QuoVadis generations (diverting acid fluid developed and characterized during the project), which can be easily manipulated to be applied for different purposes, as it will be discussed throughout this Chapter.

13.1. Results and discussion

13.1.1. Methodology for rheological characterization of diverting acid fluids

VES fluids are based on surfactant aggregates and, since they are maintained by intermolecular interactions, variations in the environment can cause severe changes in the microstructure of the aggregates, leading to different rheological responses. In this sense, the wellbore properties, such as its composition, pressure, temperature, and a few parameters adopted for the matrix acidizing certainly influence on the diverting fluid responses. In order to standardize the experiments, minimize experimental errors and generate reproductible and reliable data, an experimental methodology was adopted.

The increase of the carbonate permeabilities during the matrix acidizing process occurs due to interconnection of the inner pores caused by the reaction between the H^+ ions of the fluid and the carbonate rocks. In this case, H^+ reacts with the calcium carbonate, generating CO_2, in which its solubility strongly depends on the pressure, calcium ions and water, as demonstrated in Eq. 52 [209].

$$2\,H^+_{(aq)} + CaCO_{3(s)} \rightleftharpoons CO_{2(g)} + Ca^{2+}_{(aq)} + H_2O_{(l)} \qquad \text{Eq. 52}$$

Based on that, calcium carbonate should be used to elaborate an adequate methodology to study these acid fluids. However, the concentration of H^+ in the diverting fluids are quite high leading to intense reaction, as described in Eq. 52. In this case, for each mol of $CaCO_3$ consumed by the HCl, is formed a mol of CO_2. In the reservoir, which is found a few kilometers under sea (for offshore reservoirs), the pressure may be high enough to keep the CO_2 gas solubilized, whereas for the conditions adopted in the lab, an intense release of CO_2 as a gas is almost inevitable during the neutralization in the laboratory fume hood. The gas released combined with the

interfacial activity of the surfactant molecules can form a very stable viscoelastic foam. Because of that, the rheology investigation would be compromised to this foam instead of the rheological property of the acid fluid itself.

Some studies demonstrate that Ca^{2+} plays an important role for the rheological response of VES [210–213]; therefore, an alternative for the neutralization procedure was using $Ca(OH)_2$ instead of $CaCO_3$, as its neutralization reaction is demonstrated in Eq. 53.

$$2\,H^{+}_{(aq)} + Ca(OH)_{2_{(s)}} \rightleftharpoons Ca^{2+}_{(aq)} + 2\,H_2O_{(l)} \qquad \text{Eq. 53}$$

When comparing Eq. 52 and Eq. 53, two main differences can be noted. When reacting with $Ca(OH)_2$ instead of $CaCO_3$, no CO_2 is formed and no gas is released during the process; also, 2 mols of water molecules is formed in products, whereas only one mol of water molecule is formed with $CaCO_3$. When calculating the variation in volume due to the formation of the double of water molecules it leads to variation in the final concentration lower than $3\ vol\%$, which is even less relevant than experimental errors of around 5%, for example. In addition, the quantity of Ca^{2+} ions formed in both reactions is the same, demonstrating that the ionic strength is approximately the same, which should not cause significantly difference on the results. Showed that, we conclude that working with $Ca(OH)_2$ is more interesting for being easier and more reliable. To prove that this neutralization procedure is valid, rheological experiments were performed with samples neutralized with both $CaCO_3$ and $Ca(OH)_2$. The results are compared in Figure 68, where the flow curves for VES 1 submitted to a reaction with either $CaCO_3$ or $Ca(OH)_2$ is presented. In addition, the zero-shear viscosity as a function of the percentage of neutralization is also presented.

Regardless what was used to spend the acid concentration in VES 1, a profile of non-Newtonian fluid was obtained. Specifically, the flow curves presented in Figure 68 correspond to pseudoplastic fluids, where the viscosity does not suffer any variation at low shear rate values and, then, decreases as function of the shear rate. The first region is commonly described as a Newtonian Plateau and the second as a shear thinning region. The latter case clearly refers to the decreasing in viscosity, where the structures

present in the fluid are no longer able to resist to the flow occurring an alignment to the shear field [23]. The point where occurs a transition of regions characterizes a critical shear rate. Interestingly, it is possible to be noted that the higher the viscosity of the solution, the lower the shear rate where this transition occurs, indication a relation between these two properties. This statement can be exemplified by comparing non-neutralized VES 1 and the 60% neutralized (with $CaCO_3$) VES 1, which present zero shear viscosities of 17 and $689\ mPa\ s$, respectively, and present critical shear rate values of 200 and $10\ s^{-1}$, approximately.

WLM solutions are very well known for presenting pseudoplastic properties, and the increasing in viscosity is typically related with the formation of longer aggregates or even with the entanglement of the structures of the WLM. Apparently, when advancing in the percentage of neutralization, *i.e.* decreasing the H^+ concentration and increasing the Ca^{2+} concentration, the formation of longer WLM is favored leading to a more viscous system. This behavior occurs up to certain limit, where, in this case, a phase separation occurs due to the neutralization procedure and the solution loses its viscosity, which is severely decreased. This response indicates how VES 1 is applicable for diverting systems.

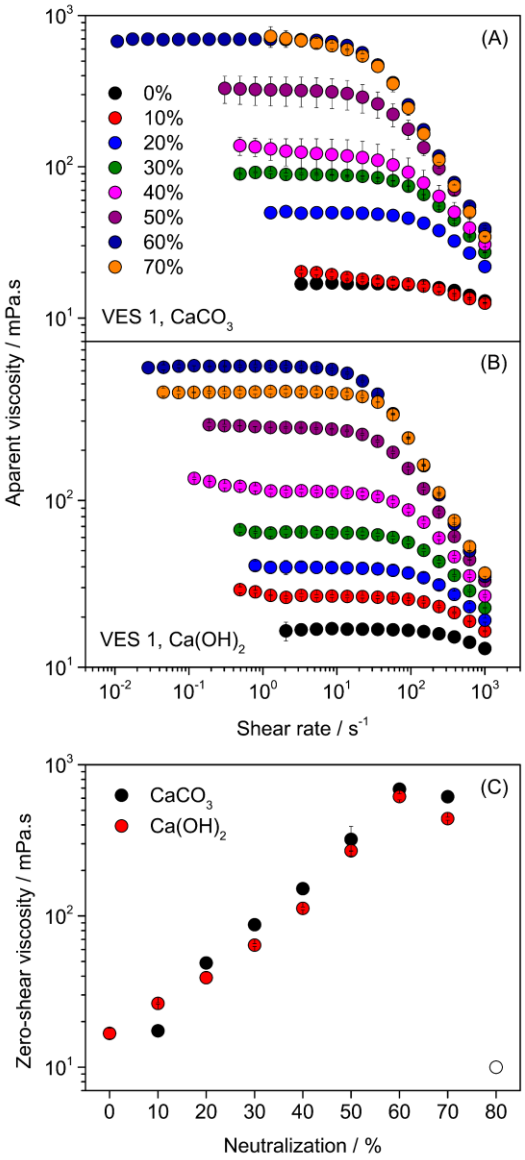

Figure 68. (A) Flow curves, presenting the viscosity as function of the shear rate for acid VES 1 neutralized with $CaCO_3$ and (B) with $Ca(OH)_2$. (C) Zero-shear viscosity as function acid neutralization with $CaCO_3$ and $Ca(OH)_2$. Experiments were performed at $25\ °C$ and atmospheric pressure. Open symbols in (C) represent phase separation of the fluid in 80% of neutralization both with $CaCO_3$ and $Ca(OH)_2$ and its viscosity value is only illustrative.

More interesting than that, Figure 68C shows how similar are the zero shear viscosities (calculated by the slope of a stress *versus* shear rate graph [125,214] in the Newtonian region for VES 1 when reacted with either $CaCO_3$ or $Ca(OH)_2$). The curves presented are practically the same. Therefore, since no differences can be noted in both scenarios and,

as discussed before the calcium hydroxide is way easier to work with, it was established that it will be used for further investigations.

Another argument could be mentioned to question the validity of the proposed methodology. In the case of higher pressures, CO_2 would possibly be a soluble product, so we decided to investigate what would be the influence of pressure on these rheological measurements. In addition to that, although liquid fluids are barely compressible, the pressure effect on responsive WLM still is an open subject. In this sense, Figure 69 shows a comparison of flow curves obtained for VES 1 60% neutralized with $Ca(OH)_2$ using a pressurizing cell under atmospheric pressure and using the pressurizing cell under $35\ bar$ (pressurized with CO_2 gas).

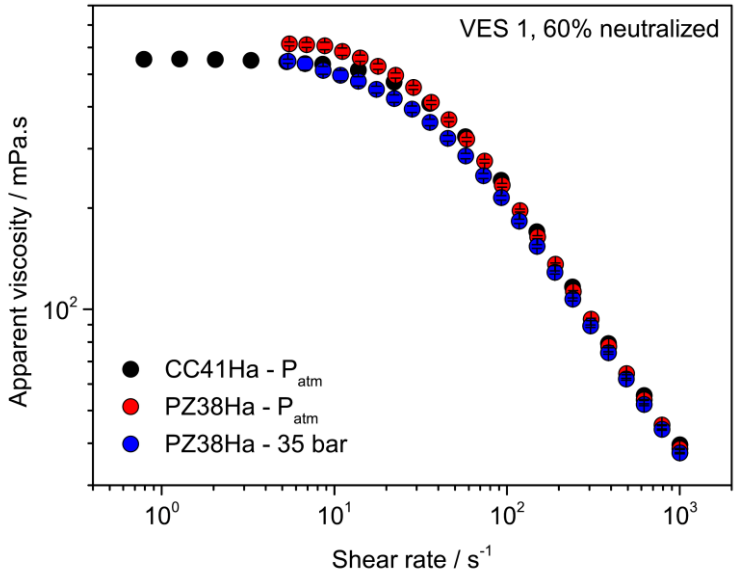

Figure 69. Flow curves, viscosity as a function of the shear rate, for VES 1 60% neutralized at $25\ °C$. CC41Ha and PZ38Ha means the cylindric concentric geometry and pressure cell (which can operate under pressure or not). Black and red circles were done under atmosphere pressure (open system) and the blue under $35\ bar$ of CO_2.

By observing Figure 69, it is possible to affirm two important features. First, the rheological data are very reproductible regardless the geometry used, although for PZ38Ha the experiments started in shear rate values which are slightly higher than the

ones for CC41Ha. Second, pressurizing VES 1 up to $35\ bar$ with CO_2 does not lead to any considerable change in the rheological response. This is an evidence that the WLM structures present in VES 1 are not pressure responsive, at least under these conditions. On the other hand, when monitoring viscosity and pressure values as function of the time for a closed system that was pressurized with CO_2 at $35\ bar$ and, then, had the gas flow interrupted, it was observed a drop in both properties. For a two hours interval it was observed a drop of 14% and 3% in viscosity and pressure, respectively. The drop in pressure as function of time indicates that the CO_2 is being solubilized into the solution, which leads to a decrease in pH explained the variation in viscosity. The related information can be observed in Figure F1.

Combining the results and discussions presented in this session, we assume that the methodology proposed to investigate diverting acid solutions by neutralizing with $Ca(OH)_2$, instead of $CaCO_3$, and under atmospheric pressure instead of higher pressures to simulate the wellbore conditions at mild conditions of pressure, is an adequate procedure, which will be adopted throughout the rest of the discussions.

13.1.2. Rheological characterization

Diverting phenomena in matrix acidizing is totally related to the rheological properties of the fluids used for this purpose; therefore, its characterization is relevant to design fluids that can respond accordingly. Zero-shear viscosity is suitable to characterize VES systems since its investigation allows to be understood which profile of behavior which fluid can adopt. However, due to high pumping pressures and small pores and pathways in which the fluid is submitted to, in the real scenario, diverting acid fluids are acting on the carbonate rocks under high shear rate values. This is the importance of the whole flow curves, where information about the apparent viscosity in any shear rate value can be obtained and compared among different systems. In this sense, Figure 70 presents a study carried out with VES 1 and VES 2, where the apparent viscosity obtained at the Newtonian region (zero-shear viscosity), at $10\ s^{-1}$ and $100\ s^{-1}$, as a function of the neutralization percentage is presented. This Figure was created with the data obtained

by the flow curves of each system, which can be found in the Appendix F, Figure F2 and Figure F3 for VES 1 and VES 2, respectively.

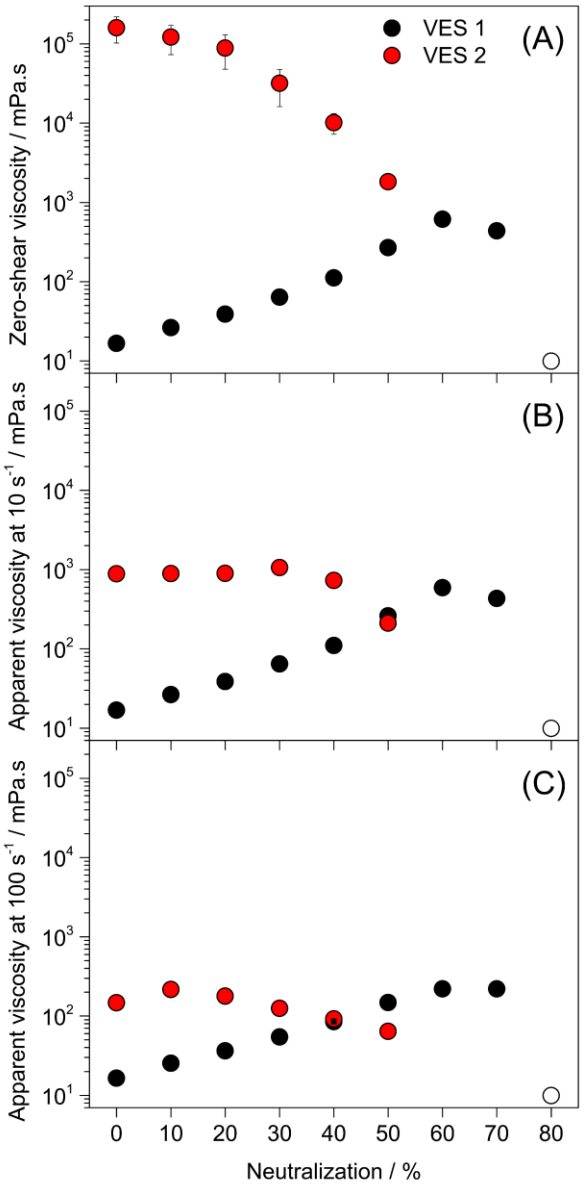

Figure 70. Apparent viscosity as function of the neutralization percentage obtained at zero-shear, 10 and 100 s^{-1}, in this order from top to the bottom. Black and red circles are for VES 1 and 2, respectively. Open symbols represent the neutralization where the fluid phase separated, and their values are only illustrative.

As shown in Figure 70, the increase in the shear rate decreases the apparent viscosity at the same neutralization. As demonstrated before, in Figure 68C and by the flow curves

of VES 2 (Figure F2), VES systems are pseudoplastic fluids. From a certain point is correct to say that the higher the shear rate, the lower the viscosity, explaining the difference among the apparent viscosity range in y axis of Figure 70. In addition, regardless the shear rate and the type of fluid, VES 1 or 2, a remarkable variation of the viscosity as function of the neutralization percentage is noted, which should be expected, once during the reaction the concentrations of H^+ and Ca^{2+} is continuously changed and both species are known for being important triggers to WLM responses applied to diverting acid fluids [198,215,216]. The variations in rheological properties originates from the WLM structural variations; therefore, the presence of Ca^{2+} and the decrease in H^+ concentration lead to a quick response of the WLM, and consequently, a variation in the viscosity. The possibility to has their properties tuned depending on the environment assures the WLM to be well applied for matrix acidizing and diverting phenomena [28,217]. For VES systems, these variations are typically related to an increase in contour length or other parameters, such as surface charge or aggregates composition of the WLM [218]. However, the profile obtained for both fluids are quite different, suggesting these two commercially available fluids are based on different mechanisms or operating proposals.

Low viscosity values are noted for VES 1 at low neutralization percentage range, which is continuously increased when the reaction steps forward. Though it happens up to a certain point, where a maximum viscosity value is reached. Following, the viscosity slightly decreases and then a total drop occurs, in this case, caused by the phase separation. Regardless whether the phase separation is observed or not, the described profile is well known for diverting fluid, which is observed for the three shear rates evaluated. On the other hand, VES 2 surprisingly presented a whole different behavior. For this case, the initial viscosity is considerably high, reaching values of $160{,}000\ mPa\ s$ at zero-shear viscosity, whereas this values for VES 1 at the same condition is around $20\ mPa\ s$. More than that, differently from what was observed for VES 1, the viscosity for VES 2 just decreases as a function of the neutralization percentage. To be more precise, it goes through a maximum at 10 and 30% of neutralization for 10 and $100\ s^{-1}$, respectively, though the increase in viscosity is still irrelevant when compared to the profile observed for VES 1. These observations demonstrate how different strategies

may be adopted to promote diverting phenomena in matrix acidizing; however, based on these rheological information, it is not possible to point which fluid has a better performance in the wellbore, since complex considerations must be taken into account.

However, a few implications of these profiles can be briefly discussed. Low initial viscosity is preferred when pumping the fluid, since it requires low energy to do so. Also, an expanded range of neutralization can be useful, *i.e.* depending on the kinetic of the reaction, reaching a higher neutralization percentage gives more time for the fluid to penetrates deeper into the carbonate rocks. These are characteristics noted for VES 1. For VES 2, the higher viscosity can be very efficient to block pathways, by changing the local permeability, and favoring the diverting process.

As both commercially available fluids are often used in matrix acidizing, it was decided to formulate our own acid diverting solution, QuoVadis, which was designed to attend both strategies with its different generations. In this sense, Figure 71 shows the zero-shear viscosity and the apparent viscosities at 10 and $100\,s^{-1}$ for the different generations of QuoVadis.

First, it will be discussed the profiles observed at zero-shear viscosity, once the interpretation depends only on the systems investigated and is not related to flow effects. The differences and particularities observed for 10 and $100\,s^{-1}$ will be discussed next. As the first generation, QuoVadis G1 behaves similarly to that observed for VES 1. It presents low viscosity at the beginning, goes through a maximum and a drop in the viscosity is observed after that. The second generation present the same trend for the viscosity, although the reached values of viscosity are superior throughout the range of neutralization. In addition to that, G2 present a wider range of efficiency, since the drop in the viscosity is only observed for neutralizations higher than 80% (50% is observed for G1). The third generation is the more complex and interesting version of the QuoVadis, *e.g.* depending on its composition (represented by A, B and C) the fluid can perform similarly to VES 1 or similarly to VES 2. QuoVadis G3 A works in the same way as the VES 2, presenting a very high viscosity even prior to any neutralization procedure. The viscosity of pure fluid is the highest presented and it only decreases as a function of the advancing reaction. In addition, this formulation presented the phase separation at the lowest neutralization percentage among QuoVadis formulations,

which was 50%. However, changing its composition to B, it is obtained a fluid performing like a VES 1 or G1 and G2, but the viscosity is higher than the ones observed for the mentioned cases. G3 C also present the same trend, increasing the viscosity up to a maximum, although its initial viscosity is comparable to the viscosity of G2, which does not correspond to classical behavior of acid diverting fluids as they use to present low initial viscosity to be easily pumped into the wellbore.

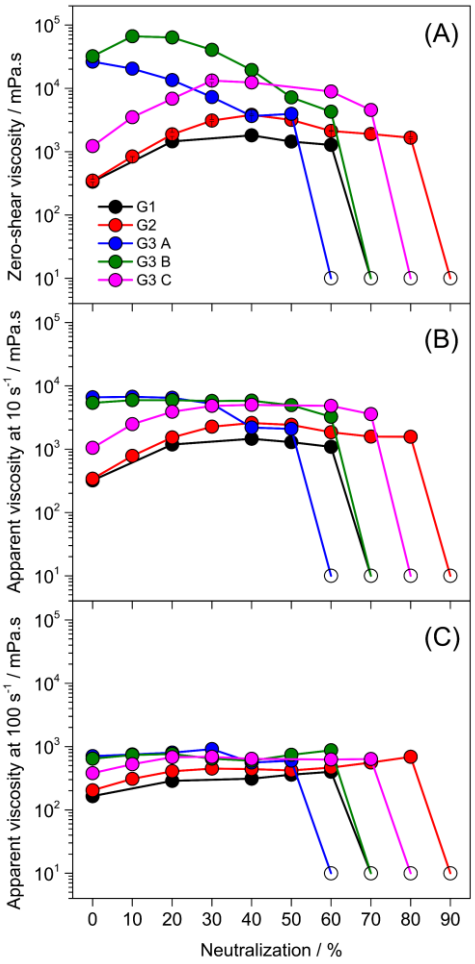

Figure 71. Apparent viscosity as function of the neutralization percentage obtained at zero-shear, 10 and $100\ s^{-1}$, in this order from top to the bottom for the different generations of the acid fluid QuoVadis. Black circles are for G1, red for G2, blue for G3 A, green for G3 B and pink for G3 C. Open symbols represent the neutralization where the fluid phase separated, and their values are only illustrative.

When increasing the shear rate (10 and $100\ s^{-1}$) interesting points are evidenced. For example, G1, G2 and G3 C presented a second increase in its viscosity after passing through a maximum. It is already known that increasing the shear rate excessively, fluids goes from a steady flow region to a turbulent flow. In this case, an increasing in torque applied to keep the shear rate increasing is observed, and the rising viscosity in high shear is considered as artefact. This is the main reason, to investigate the rheological behavior for these systems up to $100\ s^{-1}$, as can be seen in Figure F2 up to Figure F5 in Appendix F, this effect occurs for some cases when shear rate is higher than $100\ s^{-1}$. In this sense, the increase in the viscosity observed in these results presented in Figure 71 can be related to intrinsic characteristics of the fluid.

Summarizing, QuoVadis formulations seem to be very relevant since their performance for diverting solutions can be tuned by changing their compositions, which makes the proposed fluid very versatile with powerful viscosity responses.

13.1.3. Important features for diverting fluids

It was shown so far that diverting systems can present different behaviors regarding their viscosity variation as a function of the neutralization percentage and shear rates. Due to these possibilities, we have developed a fluid to be applied to such purposes, the diverting system QuoVadis, which was already presented as well. Since diverting phenomenon depends on several parameters, such as carbonate rocks characteristics, the reaction rate between the acid and the matrix, viscosity of the fluid and its dependence to temperature, ionic strength, pressure and others, it can be very challenging to point an ideal diverting system. However, regarding the rheological properties, it is possible to identify five parameters that are very relevant for the matrix acidizing and the diverting phenomenon. These characteristics and their respective importance will be listed to further compare how these different profiles can directly affect the oil recovery process. It is worth to mention that QuoVadis and its different formulations were thought based on these five characteristics which will be described as follows.

I) The viscosity of the pure acid fluid prior to any neutralization ($\eta_{0\%}$). The lower the viscosity, the lesser is the energy required to pump the fluid into the wellbore. In addition to that, following the Darcy's law (Eq. 54), the carbonate matrix, which is a porous media, is easily penetrated by less viscous fluids, reaching a significative portion of the reservoir. Thus, a low initial viscosity is important for the beginning of the process.

II) Maximum viscosity (η_{max}) and the neutralization value when it occurs. Also based on the Darcy's law, it is predictable that viscous fluids should cause a decrease in local permeability, essentially causing the diverting phenomenon, thus the higher the maximum viscosity, the better for the process. However, it is important to control the neutralization range where it occurs. It is not adequate reaching a maximum viscosity at very low neutralization percentage, because the advance of the fluid into the carbonate porous media should not be promptly interrupted, neither it can occurs in very high neutralization percentage, because the excessive reaction could damage the wellbore surroundings.

III) The increment in the viscosity ($\eta_{max}/\eta_{0\%}$). Essentially, it is a relation between points I and II, though it is still a very relevant point to be discussed. Considering the increment in the viscosity as ratio between the maximum viscosity and the initial viscosity, it would be required a fluid with a very low $\eta_{0\%}$ and very high η_{max} in order to reach a great increment. As both properties are desired, the increment is good parameter to be pursued. For example, a fluid can present very low viscosity at the beginning, but whether its viscosity will be increased or not is crucial to its performance. Also, a fluid can be very viscous at the maxima, but whether its initial viscosity is very elevated the matrix acidizing procedure is compromised.

IV) Efficiency range (ER), or the neutralization range where the fluid remains highly viscous. Once the fluid increases its viscosity promoting the diverting phenomenon, avoid a precipitated drop in the viscosity is important to extend the performance of the fluid, increasing the area affected by the stimulation process. For this parameter, it was obtained an average viscosity value for each diverting fluid and the efficiency range was determined for neutralization percentages that correspond to those viscosity values higher than the average.

V) Neutralization percentage where the fluid presents the lowest viscosity or occurs the phase separation after neutralization. After the pathways had been created, the main intention is having the oil going through these wormholes to increase the oil/gas production. Therefore, it must occur a drop in the viscosity of the diverting fluid in order to increase the local permeability again, allow the oil recovery and, also, do not damage the reservoir.

An illustrative profile for the variations of viscosity as a function of the neutralization percentage for an ideal fluid is presented in Figure F6. It is worth mentioning that the Figure is not based in any model, it only reflects the properties discussed above. These five listed points were extracted from the data presented so far for VES 1, VES 2, QuoVadis G1, G2, G3 A, G3 B and G3 C. They are presented in Appendix F by Table F1 up to Table F3, for zero-shear viscosity, $10\ s^{-1}$ and $100\ s^{-1}$, respectively.

VES 1 is the diverting fluid with the lowest $\eta_{0\%}$ followed by QuoVadis G1 and G2, which are fluids that presents a similar profile. The highest viscosity (η_{max}) is reached by QuoVadis G3 and any other formulation of QuoVadis reaches higher values than the commercially available fluid. The increment in viscosity is more relevant for VES 1, however this is due to its very low initial viscosity. In this sense, QuoVadis G2 also presented a relevant increment in viscosity, though its η_{max} is almost four times higher than η_{max} found for VES 1. In addition to that, QuoVadis G2 also presented a broad efficiency range (from 30 up to 60%) and its viscosity only drops in very high percentage of neutralization (80%). Based on these trends, we conclude that QuoVadis G2 is the most suitable formulation to eventually be applied for matrix acidizing; therefore, it was decided to procedure the investigations with QuoVadis G2.

13.1.4. Core-flooding experiments

At last, as a proof of concept, core-flooding experiments were performed where QuoVadis G1, G2 and G3 C were pumped into carbonates and the pressure difference as function of the porous volume injected to keep the flow was monitored. The porous volume is the fraction of the total volume of carbonate rock which is considered empty,

prior to the reactive flow. For that, it was used Indian Limestone outcrops presenting different petrophysical properties, as they can be found in Table 3. Results obtained by core flooding experiments can be found in Figure 72 and in Figure F8. It is worth mentioning that, although few graphs present low porous volume prior to the QuoVadis injection, the experiment were only performed after previous stabilization obtained when pumping a brine into the core.

Since the experiments were performed with a constant flow rate (q), the pressure differential (∇P) varies mainly with the fluid viscosity and with the local permeability of the carbonate rock, as can be seen in Eq. 54 (Darcy's law).

$$q = -\frac{kA}{\eta L}\nabla P \qquad \text{Eq. 54}$$

Where k is the carbonate permeability, η is the viscosity of the pumped fluid, and A and L the cross-sectional area and length of the carbonate plug.

In this sense, profiles obtained in Figure 72 can be qualitatively discussed in terms of the viscosity and petrophysical variations during the process. Brine is firstly injected to saturate the carbonate plugs until the stabilization is reached. Regardless the generation of the QuoVadis fluid used for the experiment it is observed a remarkable increase in pressure differential right after the injection of the fluid, characterized by the transition from black line (brine) to red line (QuoVadis). Proceeding, a very noisy signal can be noted for every experiment performed. This pattern is observed up to the point where the pressure differential approaches the zero and, then, the brine is injected again but this time in order to clean the carbonate rock and interrupt the reaction.

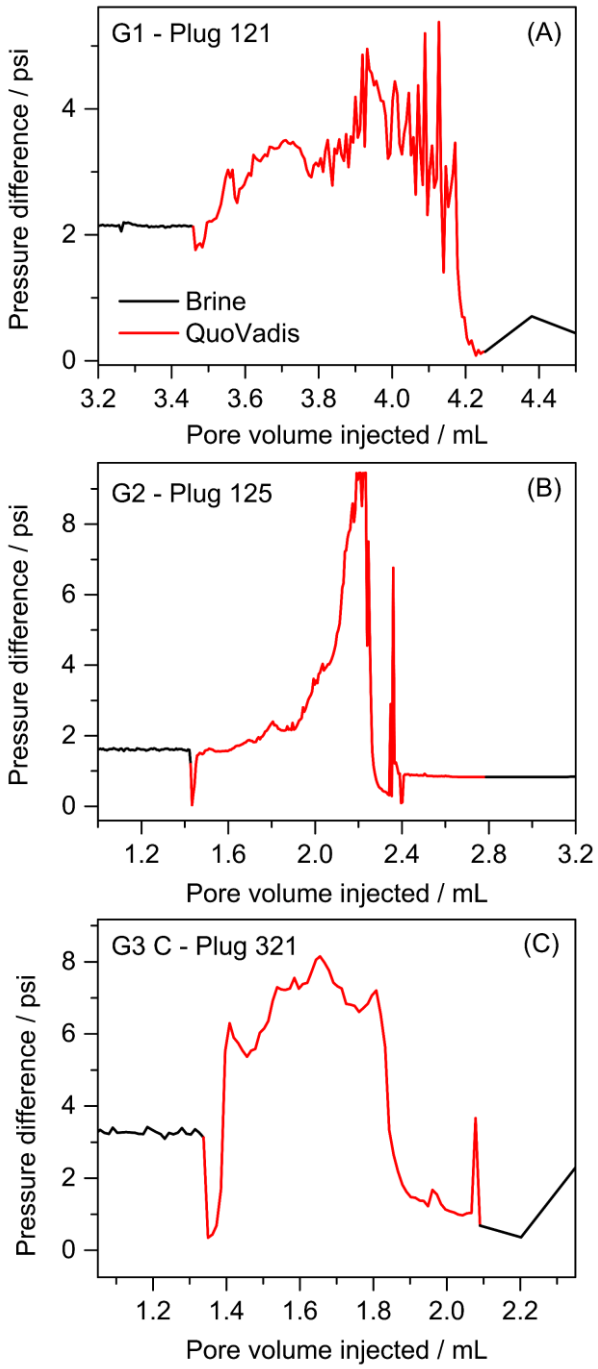

Figure 72. Pressure difference as function of the pore volume injected in core-flooding experiments. Top to bottom is presented results obtained for the injection of QuoVadis G1, G2 and G3 C. The plugs used for the experiments were 121, 125 and 321, respectively (petrophysical properties are found in Table 3). Black lines are for brine injection and red lines are for QuoVadis injection.

The first increase can be related to the fact that the initial viscosity of the diverting fluid is considerable higher than the brine viscosity (see Figure 71 for QuoVadis η_0) and the first steps of the reaction between the acid and the carbonate, which increases even more the viscosity of the pumped fluid. At this point, the fluid incorporates into the matrix, filling the pores, once filled with brine, and at the same time increasing the permeability due to the reaction. When step forwarding in the reaction, diverting phenomena start to occurs, which is evidenced by the noise signal mentioned before, and alternative pathways are formed adjacent to the main pathway of the wormhole. Finally, since the fluid is passing through the carbonate plug, there is a moment where the bottom of carbonate is reached and now, the fluid can easily be pumped, and differential pressure drops up to zero. In every case, it takes approximately 1.0 porous volume to the fluid pass through the plug.

It is challenging to compare the performance of each fluid, since the carbonate rocks can be very heterogenous. For the experiments presented in Figure 72, samples used presented very similar porosities values; however, permeabilities were 275, 394 and $98\ mD$ (see Table 3) for the fluids G1, G2 and G3 C, respectively. Therefore, it was performed similar experiments using several carbonate rocks (all samples were Indian Limestone and their properties are presented in Table 3) and three different QuoVadis generations (G1, G2 and G3 C), where it was obtained the maximum increase in differential pressure (dP_{max}/dP_i) and their respective mean deviation. The core flooding results for these experiments can be found in Figure F8. The results obtained were 1.44 $\pm$ 0.54, 2.61 $\pm$ 0.66 and 2.85 $\pm$ 0.36 for G1, G2 and G3 C, respectively. The increase in pressure differential is relevant to indicate diverting ability potential and, in this case, G3 generation seems to be the most suitable fluid.

After the experiment carried out with Indian Limestone 122 (see results in Figure F8), the carbonate plug were taken to obtain images of the wormhole formed due to the reaction between the carbonate and HCl present in QuoVadis G1 acid fluid. Figure 73 present four images obtained by rotating the cylinder in its coaxial axis for each $90°$ of rotation, by using NMR technique.

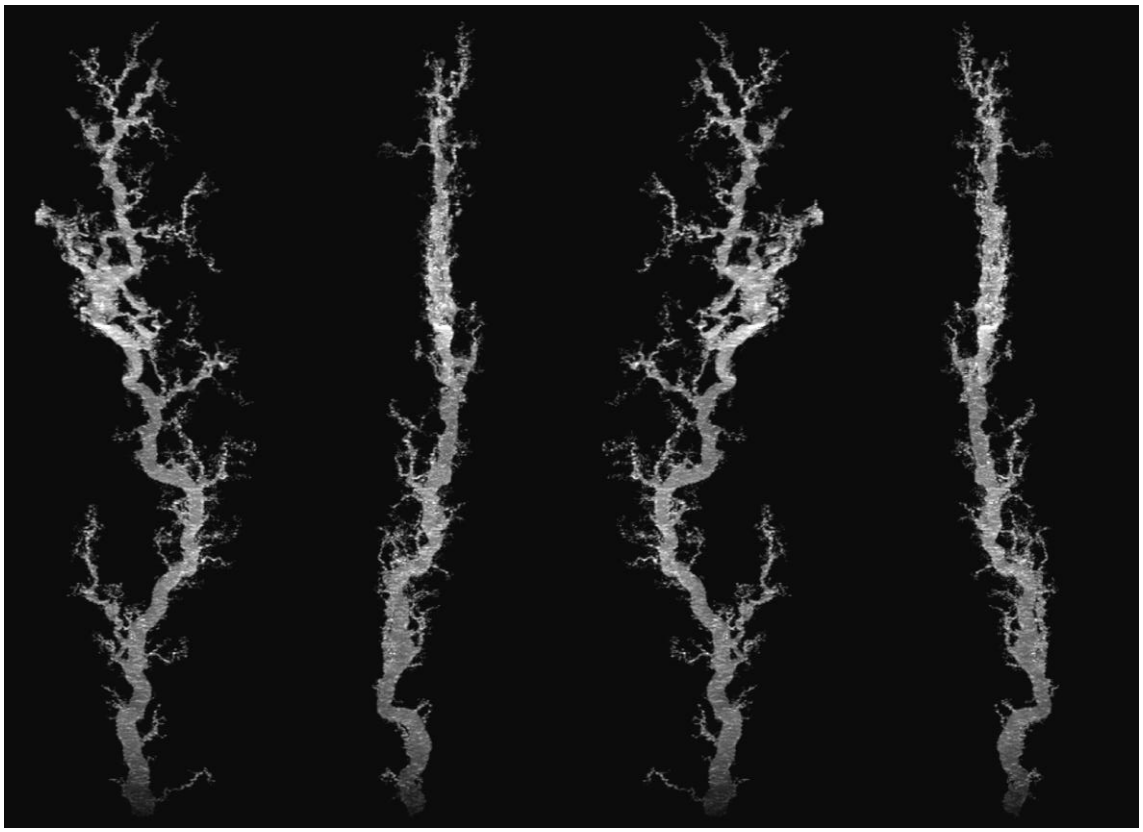

Figure 73. Wormhole formed in Indian Limestone plug (122) after core flooding experiments where QuoVadis G1 was injected. The four images correspond to the same cylinder, which was rotated in its own coaxial axis for each $90°$.

As can be seen in Figure 73, QuoVadis G1 is suitable to promote diverting phenomenon in carbonate rocks. The result obtained demonstrates the formation of dominant wormhole, where a main pathway is formed with limited diameter throughout the plug and smaller adjacent pathways were also formed.

13.2. Partial conclusions

The use of diverting acid fluids in the stimulation of carbonaceous wells brings numerous benefits to the stimulation process, enabling and increasing the return on the investment of enhanced oil recovery. In this work, a methodology was proposed to investigate the rheological properties of diverting acid fluids based on VES, evaluating

the effect of neutralizing the system with $Ca(OH)_2$ and $CaCO_3$ and the rheological response of the fluid with the CO_2 pressurization, with the purpose of simulating an environment similar to that found in carbonaceous wells. The neutralization with $Ca(OH)_2$, bypasses experimental limitations and sources of error, such as the formation of viscoelastic foam. It was possible to characterize rheological properties of the commercial VES, evaluating changes in the apparent viscosity of the fluid upon different percentage of neutralization. Such protocol was then used to investigate the rheological properties of a new diverting acid fluids, named QuoVadis. In a certain percentage of neutralization, QuoVadis showed pseudoplastic behavior, attributed to long micellar aggregates (wormlike micelles), triggered by pH changes. QuoVadis was then tested in core-flooding experiments and the results obtained have demonstrated the efficiency of QuoVadis to produce divergence, presenting high values of dP_{max}/dP_i. The formation of a desirable wormhole, with a main channel and limited diameter with several lateral ramifications (vascularization) was obtained. Therefore, it can be concluded that all generations of QuoVadis have shown excellent rheological responses upon different neutralization degrees.

14. Conclusions

The addition of halogen atoms in the aromatic benzoate ring favors the formation of WLM with C_{14}TAB and the favoring is directly associated with the substitution positions and the halogen atom used. The substitution position in ascending order of favoring is given by ortho < meta < para and, the larger the size of the halogen atom, the greater the favoring of WLM formation under the same conditions. In high concentration regimes, additional stress relaxation mechanisms, which imply in lower solution viscosity, were observed for 4-iodobenzoate, an organic salt with greater hydrophobicity within the investigated 4-halogenbenzoate series.

Fluids containing quaternary amino surfactants with phthalic acid or 1,2-dihydroxybenzene are responsive to pH changes and can modulate their viscosity according to the pH of the solution. In the investigated conditions, the change in pH by one unit was sufficient to observe a viscosity gain greater than 10-thousand times in some conditions. The addition of photoacid generator in the fluid containing 1,2-dihydroxybenzene made the fluid also responsive to UV light and a viscosity gain of more than one thousand times was observed by irradiating the sample for $300\ min$ of UV and using EHAC surfactant.

In the process of acid stimulation in oil producing wells, several parameters are important to have an excellent stimulation step and one of them is the reactivity of the acid fluid used with the reservoir rock. Among the investigated carbonates, hydrochloric acid showed greater reactivity than acetic acid and the rate of reactivity and the acid dissolution pattern of the rock surface depends on the petrophysical, elementary and crystallographic nature of the carbonate. Rocks that contained magnesium in their compositions significantly reduced the reaction rate, especially in cases with HAc.

Finally, the rheological and flow properties of diverting acidic fluids were investigated and a divergent acidic fluid named QuoVadis was developed, which presented the necessary rheological and flow properties for a divergent acidic fluid. Currently in its third generation, the fluid has three formulation options that are G3 A, B and C, which expands its applicability to different types of oil producing wells.

15. References

[1] P. Nejat, F. Jomehzadeh, M.M. Taheri, M. Gohari, M.Z. Abd. Majid, A global review of energy consumption, CO 2 emissions and policy in the residential sector (with an overview of the top ten CO 2 emitting countries), Renew. Sustain. Energy Rev. 43 (2015) 843–862. https://doi.org/10.1016/j.rser.2014.11.066.

[2] L. Zhao, X. Chen, H. Zou, P. Liu, C. Liang, N. Zhang, N. Li, Z. Luo, J. Du, A review of diverting agents for reservoir stimulation, J. Pet. Sci. Eng. 187 (2020) 106734. https://doi.org/10.1016/j.petrol.2019.106734.

[3] D. McDuff, C.E. Shuchart, S. Jackson, D. Postl, J.S. Brown, Understanding Wormholes in Carbonates: Unprecedented Experimental Scale and 3-D Visualization, in: SPE Annu. Tech. Conf. Exhib., Society of Petroleum Engineers, 2010: pp. 1–9. https://doi.org/10.2118/134379-MS.

[4] M. Zoveidavianpoor, A. Samsuri, S.R. Shadizadeh, Well Stimulation in Carbonate Reservoirs: The Needs and Superiority of Hydraulic Fracturing, Energy Sources, Part A Recover. Util. Environ. Eff. 35 (2013) 92–98. https://doi.org/10.1080/15567036.2011.644389.

[5] A.P. Teles, A.C. Machado, A. Pepin, N. Bize-Forest, R.T. Lopes, I. Lima, Analysis of subterranean Pre-salt carbonate reservoir by X-ray computed microtomography, J. Pet. Sci. Eng. 144 (2016) 113–120. https://doi.org/10.1016/j.petrol.2016.03.008.

[6] R. Barati, J.-T. Liang, A review of fracturing fluid systems used for hydraulic fracturing of oil and gas wells, J. Appl. Polym. Sci. 131 (2014) n/a-n/a. https://doi.org/10.1002/app.40735.

[7] T. Wang, J. Xiao, L. Wang, A. Ma, M. Tian, C. Wang, Synthesis of gemini ammonium sulfobetaine and its proppant suspension and gel-breaking mechanisms, RSC Adv. 10 (2020) 7879–7886. https://doi.org/10.1039/D0RA00211A.

[8] M. Pournik, L. Li, B.T. Smith, H.A. Nasr-El-Din, Effect of Acid Spending on Etching

and Acid-Fracture Conductivity, SPE Prod. Oper. 28 (2013) 46–54. https://doi.org/10.2118/136217-PA.

[9] P.F. Sullivan, M.K.R. Panga, V. Lafitte, Applications of Wormlike Micelles in the Oilfield Industry, in: RSC Soft Matter, Royal Society of Chemistry, Cambridge, 2017: pp. 330–352. https://doi.org/10.1039/9781782629788-00330.

[10] B. Guo, X. Liu, X. Tan, Acidizing, in: Pet. Prod. Eng., Elsevier, 2017: pp. 367–387. https://doi.org/10.1016/B978-0-12-809374-0.00013-1.

[11] A.T. Jardim Neto, C.A.M. Silva, R.S. Torres, R.L. Farias, F.G.M. Prata, L.A.M. Souza, A.Z.I. Pereira, A. Calderon, E.F. Sandes, Self-Diverting Acid for Effective Carbonate Stimulation Offshore Brazil: A Successful History, in: SPE Eur. Form. Damage Conf. Exhib., Society of Petroleum Engineers, 2013: pp. 85–97. https://doi.org/10.2118/165089-MS.

[12] P. Maheshwari, R.R. Ratnakar, N. Kalia, V. Balakotaiah, 3-D simulation and analysis of reactive dissolution and wormhole formation in carbonate rocks, Chem. Eng. Sci. 90 (2013) 258–274. https://doi.org/10.1016/j.ces.2012.12.032.

[13] C.N. Fredd, M.L. Hoefner, H.S. Fogler, Microemulsion Applications in Carbonate Reservoir Stimulation, in: Prop. Uses Microemulsions, InTech, 2017: p. 13. https://doi.org/10.5772/65973.

[14] M. Mahmoud, H. Nasr-El-Din, Challenges During Shallow and Deep Carbonate Reservoirs Stimulation, J. Energy Resour. Technol. 137 (2015) 1–8. https://doi.org/10.1115/1.4028230.

[15] A.F. Ibrahim, H. Nasr-El-Din, J. de Paulo, C. Ewbank, O.C.C. Poltronieri, Evaluation of New Viscoelastic Surfactant Systems in High-Temperatures Carbonates Acidizing, in: SPE Annu. Tech. Conf. Exhib., Society of Petroleum Engineers, 2018: pp. 1–20. https://doi.org/10.2118/191606-MS.

[16] C.N. Fredd, H.S. Fogler, Optimum Conditions for Wormhole Formation in Carbonate Porous Media: Influence of Transport and Reaction, SPE J. 4 (1999) 196–205. https://doi.org/10.2118/56995-PA.

[17] B. Bazin, From Matrix Acidizing to Acid Fracturing: a Laboratory Evaluation of Acid/Rock Interactions, in: Proc. Abu Dhabi Int. Pet. Exhib. Conf., Society of Petroleum Engineers, 1998: pp. 11–14. https://doi.org/10.2523/49491-MS.

[18] J.W. Morse, R.S. Arvidson, The dissolution kinetics of major sedimentary carbonate minerals, Earth-Science Rev. 58 (2002) 51–84. https://doi.org/10.1016/S0012-8252(01)00083-6.

[19] S.L. Brantley, Kinetics of Mineral Dissolution, in: Kinet. Water-Rock Interact., Springer New York, New York, NY, 2008: pp. 151–210. https://doi.org/10.1007/978-0-387-73563-4_5.

[20] L. Järvinen, J. Leiro, F. Bjondahl, C. Carletti, T. Lundin, K. Gunnelius, J.-H. Smått, O. Eklund, Characterisation of dolomites before and after reactivity measurement with HCl solution, Surf. Interface Anal. 47 (2015) 284–294. https://doi.org/10.1002/sia.5715.

[21] H.W. Rauch, W.B. White, Dissolution kinetics of carbonate rocks: 1. Effects of lithology on dissolution rate, Water Resour. Res. 13 (1977) 381–394. https://doi.org/w.

[22] O.S. Pokrovsky, S. V. Golubev, J. Schott, A. Castillo, Calcite, dolomite and magnesite dissolution kinetics in aqueous solutions at acid to circumneutral pH, 25 to 150 °C and 1 to 55 atm pCO2: New constraints on CO2 sequestration in sedimentary basins, Chem. Geol. 265 (2009) 20–32. https://doi.org/10.1016/j.chemgeo.2009.01.013.

[23] A.A. Garrouch, A.R. Jennings, A contemporary approach to carbonate matrix acidizing, J. Pet. Sci. Eng. 158 (2017) 129–143. https://doi.org/10.1016/j.petrol.2017.08.045.

[24] R. Ratnakar, N. Kalia, V. Balakotaiah, Carbonate Matrix Acidizing with Gelled Acids: An Experiment-Based Modeling Study, in: SPE Int. Prod. Oper. Conf. Exhib., Society of Petroleum Engineers, 2012: pp. 207–222. https://doi.org/10.2118/154936-MS.

[25] H.A. Nasr-El-Din, A.M. Al-Mohammed, A. Al-Aamri, O.A. Al-Fuwaires, Reaction of

Gelled Acids With Calcite, SPE Prod. Oper. 23 (2008) 353–361. https://doi.org/10.2118/103979-PA.

[26] A.I. Rabie, A.M. Gomaa, H.A. Nasr-El-Din, HCl/Formic In-Situ-Gelled Acids as Diverting Agents for Carbonate Acidizing, SPE Prod. Oper. 27 (2012) 170–184. https://doi.org/10.2118/140138-PA.

[27] M. Amro, Extended Matrix Acidizing Using Polymer-Acid Solutions, in: Proc. SPE Tech. Symp. Saudi Arab. Sect., Society of Petroleum Engineers, 2006: pp. 1–9. https://doi.org/10.2523/106360-MS.

[28] M. Liu, S. Zhang, J. Mou, F. Zhou, Y. Shi, Diverting mechanism of viscoelastic surfactant-based self-diverting acid and its simulation, J. Pet. Sci. Eng. 105 (2013) 91–99. https://doi.org/10.1016/j.petrol.2013.03.001.

[29] E. Sabadini, R. Rodrigues, Oil Field Exploration: Worm Micelle Applications, in: Encycl. Surf. Colloid Sci. Third Ed., Taylor & Francis, 2016: pp. 5002–5010. https://doi.org/10.1081/E-ESCS3-120051435.

[30] N. Liu, M. Liu, Simulation and analysis of wormhole propagation by VES acid in carbonate acidizing, J. Pet. Sci. Eng. 138 (2016) 57–65. https://doi.org/10.1016/j.petrol.2015.12.011.

[31] C. Frank, Q. Qi, F. Wayne, A Novel Self-Diverting-Acid Developed for Matrix Stimulation of Carbonate Reservoirs, in: Proc. SPE Int. Symp. Oilf. Chem., Society of Petroleum Engineers, 2001: pp. 477–482. https://doi.org/10.2523/65033-MS.

[32] D. Myers, Surfactant Science and Technology, 3rd ed., John Wiley & Sons, Inc., Hoboken, NJ, USA, 2005. https://doi.org/10.1002/047174607X.

[33] T. Cosgrove, Colloid Science, Blackwell Publishing Ltd., Oxford, UK, 2005. https://doi.org/10.1002/9781444305395.

[34] M.J. Rosen, J.T. Kunjappu, Surfactants and Interfacial Phenomena, John Wiley & Sons, Inc., Hoboken, NJ, USA, 2012. https://doi.org/10.1002/9781118228920.

[35] D.F. Evans, H. Wennerstrom, The Colloidal Domain, 2nd ed., Wiley-VCH, 1999.

[36] T.F. Tadros, Applied Surfactants, Wiley, 2005.

https://doi.org/10.1002/3527604812.

[37] T. Tadros, Encyclopedia of Colloid and Interface Science, n.d.

[38] I.N. Levine, Physical Chemistry, 6th ed., McGraw-Hill Education, 2008. https://doi.org/10.1039/c1cs15191f.

[39] P. Atkins, J. de Paula, Physical chemistry, 6th ed., McGraw-Hill Education, 2008. http://scholar.google.com/scholar?hl=en&btnG=Search&q=intitle:No+Title#0.

[40] N.B. Vargaftik, B.N. Volkov, L.D. Voljak, International Tables of the Surface Tension of Water, J. Phys. Chem. Ref. Data. 12 (1983) 817–820. https://doi.org/10.1063/1.555688.

[41] J.W. McBain, H.E. Martin, XCII.—Studies of the constitution of soap solutions: the alkalinity and degree of hydrolysis of soap solutions, J. Chem. Soc., Trans. 105 (1914) 957–977. https://doi.org/10.1039/CT9140500957.

[42] B. Vincent, McBain and the centenary of the micelle, Adv. Colloid Interface Sci. 203 (2014) 51–54. https://doi.org/10.1016/j.cis.2013.11.012.

[43] E.C. Lingafelter, Aqueous Solutions of Paraffin-Chain Salts., Chem. Rev. 44 (1949) 135–140. https://doi.org/10.1021/cr60137a009.

[44] J.N. Israelachvili, D.J. Mitchell, B.W. Ninham, Theory of self-assembly of hydrocarbon amphiphiles into micelles and bilayers, J. Chem. Soc. Faraday Trans. 2. 72 (1976) 1525. https://doi.org/10.1039/f29767201525.

[45] J.N. Israelachvili, S. Marcelja, R.G. Horn, J.N. Israelachvili, Physical principles of membrane organization, Q. Rev. Biophys. 13 (1980) 121–200. https://doi.org/10.1017/S0033583500001645.

[46] J. Israelachvili, Intermolecular and Surface Forces, Elsevier, 2011. https://doi.org/10.1016/C2009-0-21560-1.

[47] X. Li, P. Wang, X. Hou, F. Wang, H. Zhao, B. Zhou, H. Zhang, H. Yang, W. Kang, Effects of sodium chloride on rheological behaviour of the gemini-like surfactants, Soft Matter. 16 (2020) 4024–4031. https://doi.org/10.1039/D0SM00243G.

[48] C.A. Dreiss, Wormlike micelles: where do we stand? Recent developments, linear rheology and scattering techniques, Soft Matter. 3 (2007) 956. https://doi.org/10.1039/b705775j.

[49] C.A. Dreiss, Y. Feng, Wormlike Micelles, Royal Society of Chemistry, Cambridge, 2017. https://doi.org/10.1039/9781782629788.

[50] S. Ezrahi, E. Tuval, A. Aserin, Properties, main applications and perspectives of worm micelles, Adv. Colloid Interface Sci. 128–130 (2006) 77–102. https://doi.org/10.1016/j.cis.2006.11.017.

[51] W. Kang, P. Wang, H. Fan, H. Yang, C. Dai, X. Yin, Y. Zhao, S. Guo, A pH-responsive wormlike micellar system of a noncovalent interaction-based surfactant with a tunable molecular structure, Soft Matter. 13 (2017) 1182–1189. https://doi.org/10.1039/C6SM02655A.

[52] L. Matthews, Ż. Przybyłowicz, S.E. Rogers, P. Bartlett, A.J. Johnson, R. Sochon, W.H. Briscoe, The curious case of SDS self-assembly in glycerol: Formation of a lamellar gel, J. Colloid Interface Sci. 572 (2020) 384–395. https://doi.org/10.1016/j.jcis.2020.03.102.

[53] Y. Hu, L. Ge, J. Han, R. Guo, Concentration and temperature induced dual-responsive wormlike micelle to hydrogel transition in ionic liquid-type surfactant [C 16 imC 9]Br aqueous solution without additives, Soft Matter. 11 (2015) 5624–5631. https://doi.org/10.1039/C5SM01084E.

[54] M. Zhao, M. Gao, C. Dai, C. Zou, Z. Yang, X. Wu, Y. Liu, Y. Wu, S. Fang, W. Lv, Investigation of Novel Triple-Responsive Wormlike Micelles, Langmuir. 33 (2017) 4319–4327. https://doi.org/10.1021/acs.langmuir.7b01011.

[55] X.-L. Wei, C.-H. Han, P.-P. Geng, X.-X. Chen, Y. Guo, J. Liu, D.-Z. Sun, J.-H. Zhang, M.-J. Yu, Thermo-responsive properties driven by hydrogen bonding in aqueous cationic gemini surfactant systems, Soft Matter. 12 (2016) 1558–1566. https://doi.org/10.1039/C5SM02247A.

[56] N. Dharaiya, U. Patel, D. Ray, V.K. Aswal, N. V. Sastry, P. Bahadur, Different pH triggered aggregate morphologies in sodium oleate–cationic surfactants mixed

systems, New J. Chem. (2017). https://doi.org/10.1039/C6NJ03871A.

[57] Y. Feng, Z. Chu, pH-Tunable wormlike micelles based on an ultra-long-chain “pseudo” gemini surfactant, Soft Matter. 11 (2015) 4614–4620. https://doi.org/10.1039/C5SM00677E.

[58] M.F. Torres, J.M. González, M.R. Rojas, A.J. Müller, A.E. Sáez, D. Löf, K. Schillén, Effect of ionic strength on the rheological behavior of aqueous cetyltrimethylammonium p-toluene sulfonate solutions, J. Colloid Interface Sci. 307 (2007) 221–228. https://doi.org/10.1016/j.jcis.2006.11.002.

[59] C. Oelschlaeger, P. Suwita, N. Willenbacher, Effect of Counterion Binding Efficiency on Structure and Dynamics of Wormlike Micelles, Langmuir. 26 (2010) 7045–7053. https://doi.org/10.1021/la9043705.

[60] C. Oelschlaeger, N. Willenbacher, Rheological properties of aqueous solutions of cetylpyridinium chloride in the presence of sodium chlorate, Rheol. Acta. 50 (2011) 655–660. https://doi.org/10.1007/s00397-011-0548-z.

[61] P. Somasundaran, Encyclopedia of Surface and Colloid Science, 3rd ed., CRC Press, 2015.

[62] T. Lu, L. Xia, X. Wang, A. Wang, T. Zhang, A Dually Effective Inorganic Salt at Inducing Obvious Viscoelastic Behavior of both Cationic and Anionic Surfactant Solutions, Langmuir. 27 (2011) 9815–9822. https://doi.org/10.1021/la2018709.

[63] H.-M. Chang, C.-Y. Lin, S.-H. Tung, Correlations between temperature-dependent rheology and electrostatic interactions in reverse wormlike micelles induced by inorganic salts, Soft Matter. 16 (2020) 3505–3513. https://doi.org/10.1039/C9SM02508A.

[64] salar Afra, H. Samouei, P. Truong, H. Nasr-El-Din, Micellar Growth and Network Formation in Acidic Solutions of a Sulfobetaine Zwitterionic Surfactant Triggered by an Inorganic Salt, Soft Matter. (2020). https://doi.org/10.1039/d0sm00399a.

[65] Y.-Q. Nan, J.-X. Liu, S.-S. Zhang, D.-J. Chen, Q.-X. Ye, C. Yuan, L.-S. Hao, Photo-responsive wormlike micellar systems based on mixed cationic/anionic

surfactants and mixed photo-sensitive additives, Colloids Surfaces A Physicochem. Eng. Asp. 572 (2020) 124988. https://doi.org/10.1016/j.colsurfa.2020.124988.

[66] T.H. Ito, P.C.M.L. Miranda, N.H. Morgon, G. Heerdt, C.A. Dreiss, E. Sabadini, Molecular Variations in Aromatic Cosolutes: Critical Role in the Rheology of Cationic Wormlike Micelles, Langmuir. 30 (2014) 11535–11542. https://doi.org/10.1021/la502649j.

[67] H. Lu, Q. Shi, B. Wang, Z. Huang, Spherical-to-wormlike micelle transition in a pseudogemini surfactant system with two types of effective pH-responsive groups, Colloids Surfaces A Physicochem. Eng. Asp. 494 (2016) 74–80. https://doi.org/10.1016/j.colsurfa.2016.01.014.

[68] R.N. de Souza, M.Z. Jora, L.G.T.A. Duarte, K.J. Clinckspoor, T.D.Z. Atvars, E. Sabadini, A new interpretation of the mechanism of wormlike micelle formation involving a cationic surfactant and salicylate, J. Colloid Interface Sci. 552 (2019) 794–800. https://doi.org/10.1016/j.jcis.2019.05.025.

[69] X.F. Geng, X.Q. Hu, X.C. Jia, L.J. Luo, Effects of sodium salicylate on the microstructure of a novel zwitterionic gemini surfactant and its rheological responses, Colloid Polym. Sci. 292 (2014) 915–921. https://doi.org/10.1007/s00396-013-3137-0.

[70] M.I. Alkschbirs, A.M. Percebom, W. Loh, H. Westfahl, M.B. Cardoso, E. Sabadini, Effects of some anions of the Hofmeister series on the rheology of cetyltrimethylammonium-salicylate wormlike micelles, Colloids Surfaces A Physicochem. Eng. Asp. 470 (2015) 1–7. https://doi.org/10.1016/j.colsurfa.2015.01.052.

[71] C. Manohar, U.R.K. Rao, B.S. Valaulikar, R.M. Lyer, On the origin of viscoelasticity in micellar solutions of cetyltrimethylammonium bromide and sodium salicylate, J. Chem. Soc. Chem. Commun. (1986) 379. https://doi.org/10.1039/c39860000379.

[72] A. Shukla, H. Rehage, Zeta Potentials and Debye Screening Lengths of Aqueous,

Viscoelastic Surfactant Solutions (Cetyltrimethylammonium Bromide/Sodium Salicylate System), Langmuir. 24 (2008) 8507–8513. https://doi.org/10.1021/la800816e.

[73] K.J. Clinckspoor, L.L. Jorge, H. Hoffmann, E. Sabadini, Rheological and calorimetric study of alkyltrimethylammonium bromide-sodium salicylate wormlike micelles in aqueous binary systems, J. Colloid Interface Sci. 515 (2018) 198–207. https://doi.org/10.1016/j.jcis.2018.01.024.

[74] B. Šarac, G. Mériguet, B. Ancian, M. Bešter-Rogač, Salicylate Isomer-Specific Effect on the Micellization of Dodecyltrimethylammonium Chloride: Large Effects from Small Changes, Langmuir. 29 (2013) 4460–4469. https://doi.org/10.1021/la400161n.

[75] V. Hartmann, R. Cressely, Influence of sodium salicylate on the rheological behaviour of an aqueous CTAB solution, Colloids Surfaces A Physicochem. Eng. Asp. 121 (1997) 151–162. https://doi.org/10.1016/S0927-7757(96)03773-9.

[76] A.S. Mahadevi, G.N. Sastry, Cation−π Interaction: Its Role and Relevance in Chemistry, Biology, and Material Science, Chem. Rev. 113 (2013) 2100–2138. https://doi.org/10.1021/cr300222d.

[77] C.D. Umeasiegbu, V. Balakotaiah, R. Krishnamoorti, pH-Induced Re-entrant Microstructural Transitions in Cationic Surfactant–Hydrotrope Mixtures, Langmuir. 32 (2016) 655–663. https://doi.org/10.1021/acs.langmuir.5b02211.

[78] T. van Vliet, H. Lyklema, 6 Rheology, in: Fundam. Interface Colloid Sci. Vol. IV, 2005: pp. 6.1-6.88. https://doi.org/10.1016/S1874-5679(05)80024-8.

[79] B. Kronberg, K. Holmberg, B. Lindman, An Introduction to the Rheology of Polymer and Surfactant Solutions, in: Surf. Chem. Surfactants Polym., John Wiley & Sons, Ltd, Chichester, UK, 2014: pp. 361–376. https://doi.org/10.1002/9781118695968.ch19.

[80] F. Lequeux, S.J. Candau, Dynamical Properties of Wormlike Micelles, in: 1994: pp. 51–62. https://doi.org/10.1021/bk-1994-0578.ch003.

[81] M.E. Cates, S.M. Fielding, Rheology of giant micelles, 2006. https://doi.org/10.1080/00018730601082029.

[82] H. Rehage, H. Hoffmann, Viscoelastic surfactant solutions: model systems for rheological research, Mol. Phys. 74 (1991) 933–973. https://doi.org/10.1080/00268979100102721.

[83] F. Lequeux, Reptation of Connected Worm, Europhys. Lett. 19 (1992) 675–681. https://doi.org/10.1209/0295-5075/19/8/003.

[84] Y. Kim, P. Dalhaimer, D.A. Christian, D.E. Discher, Polymeric worm micelles as nano-carriers for drug delivery, Nanotechnology. 16 (2005) S484–S491. https://doi.org/10.1088/0957-4484/16/7/024.

[85] P. Wang, W. Kang, H. Yang, X. Yin, Y. Zhao, Z. Zhu, X. Zhang, pH-Responsive wormlike micelles based on microstructural transition in a C 22 -tailed cationic surfactant–aromatic dibasic acid system, RSC Adv. 7 (2017) 37699–37705. https://doi.org/10.1039/C7RA07000D.

[86] Y. Lin, X. Han, J. Huang, H. Fu, C. Yu, A facile route to design pH-responsive viscoelastic wormlike micelles: Smart use of hydrotropes, J. Colloid Interface Sci. 330 (2009) 449–455. https://doi.org/10.1016/j.jcis.2008.10.071.

[87] Z. Lin, A. Mateo, Y. Zheng, E. Kesselman, E. Pancallo, D. Hart, Y. Talmon, T. Davis, S. L., J. Zakin, Comparison of drag reduction, rheology, microstructure and stress-induced precipitation of dilute cationic surfactant solutions with odd and even alkyl chains, Rheol. Acta. 41 (2002) 483–492. https://doi.org/10.1007/s00397-002-0235-1.

[88] B. Lu, X. Li, L.E. Scriven, H.T. Davis, Y. Talmon, J.L. Zakin, Effect of Chemical Structure on Viscoelasticity and Extensional Viscosity of Drag-Reducing Cationic Surfactant Solutions, Langmuir. 14 (1998) 8–16. https://doi.org/10.1021/la970630n.

[89] Y. Zhang, J. Schmidt, Y. Talmon, J.L. Zakin, Co-solvent effects on drag reduction, rheological properties and micelle microstructures of cationic surfactants, J. Colloid Interface Sci. 286 (2005) 696–709.

https://doi.org/10.1016/j.jcis.2005.01.055.

[90] L.D. Rhein, M. Schlossman, A. O'Lenick, P. Somasundaran, Surfactants in Personal Care Products and Decorative Cosmetics, 3rd ed., CRC Press, 2007.

[91] M. Rieger, L.D. Rhein, Surfactants in Cosmetics, CRC Press, 1997.

[92] P. Mukerjee, Size distribution of small and large micelles. Multiple equilibrium analysis, J. Phys. Chem. 76 (1972) 565–570. https://doi.org/10.1021/j100648a019.

[93] Y. Mylonas, G. Staikos, M. Ullner, Chain conformation and intermolecular interaction of partially neutralized poly(acrylic acid) in dilute aqueous solutions, Polymer (Guildf). 40 (1999) 6841–6847. https://doi.org/10.1016/S0032-3861(98)00861-1.

[94] Z. Chu, C. a Dreiss, Y. Feng, Smart wormlike micelles, Chem. Soc. Rev. 42 (2013) 7174. https://doi.org/10.1039/c3cs35490c.

[95] Y. Feng, Z. Chu, C.A. Dreiss, Smart Wormlike Micelles, Springer Berlin Heidelberg, Berlin, Heidelberg, 2015. https://doi.org/10.1007/978-3-662-45950-8.

[96] C. Dai, Q. Yang, M. Gao, M. Zhao, J. Jiang, The mechanism difference between CO 2 and pH stimuli for a dual responsive wormlike micellar system, Phys. Chem. Chem. Phys. 20 (2018) 19900–19905. https://doi.org/10.1039/C8CP02107D.

[97] J. Jiang, Q. Xu, G. Wang, Z. Cui, Light and CO 2 /N 2 dual stimuli-responsive wormlike micelles based on a zwitterionic surfactant and an azobenzene surfactant, Soft Matter. 14 (2018) 773–779. https://doi.org/10.1039/C7SM02064C.

[98] S.C. Sharma, L.K. Shrestha, K. Tsuchiya, K. Sakai, H. Sakai, M. Abe, Viscoelastic Wormlike Micelles of Long Polyoxyethylene Chain Phytosterol with Lipophilic Nonionic Surfactant in Aqueous Solution, J. Phys. Chem. B. 113 (2009) 3043–3050. https://doi.org/10.1021/jp8102244.

[99] G.C. Kalur, B.D. Frounfelker, B.H. Cipriano, A.I. Norman, S.R. Raghavan, Viscosity Increase with Temperature in Cationic Surfactant Solutions Due to the Growth of

Wormlike Micelles, Langmuir. 21 (2005) 10998–11004. https://doi.org/10.1021/la052069w.

[100] T. Wolff, C.S. Emming, T. a Suck, G. Von Buenau, Photorheological effects in micellar solutions containing anthracene derivatives: a rheological and static low angle light scattering study, J. Phys. Chem. 93 (1989) 4894–4898. https://doi.org/10.1021/j100349a043.

[101] N. Müller, T. Wolff, G. von Bünau, Light-induced viscosity changes of aqueous solutions containing 9-substituted anthracenes solubilized in cetyltrimethylammonium micelles, J. Photochem. 24 (1984) 37–43. https://doi.org/10.1016/0047-2670(84)80004-0.

[102] N. Rincón-Londoño, A. Tavera-Vázquez, C. Garza, N. Esturau-Escofet, A. Kozina, R. Castillo, Structural Changes in Wormlike Micelles on the Incorporation of Small Photoswitchable Molecules, J. Phys. Chem. B. 123 (2019) 9481–9490. https://doi.org/10.1021/acs.jpcb.9b07276.

[103] H. Shi, Y. Wang, B. Fang, Y. Talmon, W. Ge, S.R. Raghavan, J.L. Zakin, Light-Responsive Threadlike Micelles as Drag Reducing Fluids with Enhanced Heat-Transfer Capabilities, Langmuir. 27 (2011) 5806–5813. https://doi.org/10.1021/la200080w.

[104] S. Geng, Y. Wang, L. Wang, T. Kouyama, T. Gotoh, S. Wada, J.-Y. Wang, A Light-Responsive Self-Assembly Formed by a Cationic Azobenzene Derivative and SDS as a Drug Delivery System, Sci. Rep. 7 (2017) 39202. https://doi.org/10.1038/srep39202.

[105] R. Kumar, S.R. Raghavan, Photogelling fluids based on light-activated growth of zwitterionic wormlike micelles, Soft Matter. 5 (2009) 797–803. https://doi.org/10.1039/B809452G.

[106] A. Matsumura, K. Sakai, H. Sakai, M. Abe, Photoinduced Increase in Surfactant Solution Viscosity Using Azobenzene Dicarboxylate for Molecular Switching, J. Oleo Sci. 60 (2011) 203–207. https://doi.org/10.5650/jos.60.203.

[107] H. Oh, A.M. Ketner, R. Heymann, E. Kesselman, D. Danino, D.E. Falvey, S.R.

Raghavan, A simple route to fluids with photo-switchable viscosities based on a reversible transition between vesicles and wormlike micelles, Soft Matter. 9 (2013) 5025. https://doi.org/10.1039/c3sm00070b.

[108] Z. Chen, D. Xie, B. Song, C. Li, X. Pei, R. Li, Worm-like micelles constructed by “pseudo” tetrameric surfactants containing azobenzene groups, J. Mol. Liq. 155 (2020) 113847. https://doi.org/10.1016/j.molliq.2020.113847.

[109] B. Song, Y. Hu, J. Zhao, A single-component photo-responsive fluid based on a gemini surfactant with an azobenzene spacer, J. Colloid Interface Sci. 333 (2009) 820–822. https://doi.org/10.1016/j.jcis.2009.02.030.

[110] A.M. Ketner, R. Kumar, T.S. Davies, P.W. Elder, S.R. Raghavan, A Simple Class of Photorheological Fluids: Surfactant Solutions with Viscosity Tunable by Light, J. Am. Chem. Soc. 129 (2007) 1553–1559. https://doi.org/10.1021/ja065053g.

[111] S. Aikawa, R.G. Shrestha, T. Ohmori, Y. Fukukita, Y. Tezuka, T. Endo, K. Torigoe, K. Tsuchiya, K. Sakamoto, K. Sakai, M. Abe, H. Sakai, Photorheological Response of Aqueous Wormlike Micelles with Photocleavable Surfactant, Langmuir. 29 (2013) 5668–5676. https://doi.org/10.1021/la4001939.

[112] R. Kumar, A.M. Ketner, S.R. Raghavan, Nonaqueous Photorheological Fluids Based on Light-Responsive Reverse Wormlike Micelles, Langmuir. 26 (2010) 5405–5411. https://doi.org/10.1021/la903834q.

[113] W. Kang, Y. Zhao, P. Wang, Z. Li, X. Hou, Z. Huang, H. Yang, Rheological behavior and mechanism of pH-responsive wormlike micelle variations induced by isomers of phthalic acid, Soft Matter. 14 (2018) 4445–4452. https://doi.org/10.1039/C8SM00467F.

[114] G. Verma, V.K. Aswal, P. Hassan, pH-Responsive self-assembly in an aqueous mixture of surfactant and hydrophobic amino acid mimic, Soft Matter. 5 (2009) 2919. https://doi.org/10.1039/b900891h.

[115] L. Rose J., B.V.R. Tata, V.K. Aswal, P.A. Hassan, Y. Talmon, L. Sreejith, pH-switchable structural evolution in aqueous surfactant-aromatic dibasic acid system, Eur. Phys. J. E. 38 (2015) 4. https://doi.org/10.1140/epje/i2015-15004-9.

[116] H. Lu, Q. Shi, Z. Huang, PH-responsive anionic wormlike micelle based on sodium oleate induced by NaCl, J. Phys. Chem. B. 118 (2014) 12511–12517. https://doi.org/10.1021/jp506809m.

[117] X. Liu, Z. Huang, Y. Ma, C. Zheng, H. Lu, Preparation of CO 2 responsive wormlike micelles and the effect of hydrogen bond on the strength of the network, J. Dispers. Sci. Technol. 39 (2018) 77–82. https://doi.org/10.1080/01932691.2017.1296364.

[118] H. Maeda, R. Kakehashi, Effects of protonation on the thermodynamic properties of alkyl dimethylamine oxides, Adv. Colloid Interface Sci. 88 (2000) 275–293. https://doi.org/10.1016/S0001-8686(00)00048-8.

[119] Y. Zhang, P. An, X. Liu, A “worm”-containing viscoelastic fluid based on single amine oxide surfactant with an unsaturated C 22 -tail, RSC Adv. 5 (2015) 19135–19144. https://doi.org/10.1039/C4RA16772D.

[120] B. Wang, L. Liu, C. Zheng, H. Lu, pH and temperature-responsive wormlike micelles formed by single amine oxide surfactant, J. Dispers. Sci. Technol. 39 (2018) 539–547. https://doi.org/10.1080/01932691.2017.1334212.

[121] Z. Chu, Y. Feng, pH-switchable wormlike micelles, Chem. Commun. 46 (2010) 9028. https://doi.org/10.1039/c0cc02415e.

[122] X. Wu, Y. Huang, S. Fang, C. Dai, H. Li, Z. Xu, M. Zhao, CO2-responsive smart wormlike micelles based on monomer and “pseudo” gemini surfactant, J. Ind. Eng. Chem. (2017). https://doi.org/10.1016/j.jiec.2017.11.021.

[123] G. Zhao, X. Wu, R. Luan, S. Azizullah, H. Fan, C. Dai, CO2-controllable smart nanostructured fluids in a pseudo Gemini surfactant system, J. Mol. Liq. 274 (2019) 133–139. https://doi.org/10.1016/j.molliq.2018.10.144.

[124] Y. Zhang, Z. Chu, C.A. Dreiss, Y. Wang, C. Fei, Y. Feng, Smart wormlike micelles switched by CO2 and air, Soft Matter. 9 (2013) 6217. https://doi.org/10.1039/c3sm50913c.

[125] A. Introduction, J.W. Goodwin, R.W. Hughes, A. Introduction, Rheology for

Chemists, 2nd ed., Royal Society of Chemistry, Cambridge, 2008. https://doi.org/10.1039/9781847558046.

[126] A.Y. Malkin, A.I. Isayev, Rheology: Concepts, Methods, and Applications, 3rd ed., ChemTec Publishing, 2017.

[127] T.F. Tadros, Rheology of Dispersions, n.d.

[128] C.W. Macosko, RHEOLOGY Principles , Measurements and Applications, n.d.

[129] K.J. Clinckspoor, Estudo estrutural, termodinâmico e cinético sobre a formação e interações de micelas gigantes em sistemas aquosos binários, UNICAMP, 2019.

[130] E.C. Bingham, Rheology. I. The nature of fluid flow, J. Chem. Educ. 6 (1929) 1113. https://doi.org/10.1021/ed006p1113.

[131] B. Dong, J. Zhang, L. Zheng, S. Wang, X. Li, T. Inoue, Salt-induced viscoelastic wormlike micelles formed in surface active ionic liquid aqueous solution, J. Colloid Interface Sci. 319 (2008) 338–343. https://doi.org/10.1016/j.jcis.2007.11.040.

[132] O. Manero, F. Bautista, J.F.A. Soltero, J.E. Puig, Dynamics of worm-like micelles: The Cox-Merz rule, J. Nonnewton. Fluid Mech. 106 (2002) 1–15. https://doi.org/10.1016/S0377-0257(02)00082-4.

[133] J. Zhang, A. Ping, Y. Liu, L. Li, Q. Li, X. Wei, Structural changes in a cationic surfactant-water mixtures, Phys. Chem. Liq. 53 (2015) 706–716. https://doi.org/10.1080/00319104.2015.1033418.

[134] I. a. Kadoma, C. Ylitalo, J.W. van Egmond, Structural transitions in wormlike micelles, Rheol. Acta. 36 (1997) 1–12. https://doi.org/10.1007/BF00366719.

[135] M.E. Cates, Reptation of living polymers: dynamics of entangled polymers in the presence of reversible chain-scission reactions, Macromolecules. 20 (1987) 2289–2296. https://doi.org/10.1021/ma00175a038.

[136] J.F. Berret, J. Appell, G. Porte, Linear rheology of entangled wormlike micelles, Langmuir. 9 (1993) 2851–2854. https://doi.org/10.1021/la00035a021.

[137] B.F. García, S. Saraji, A new insight into the dependence of relaxation time on

frequency in viscoelastic surfactant solutions: From experimental to modeling study, J. Colloid Interface Sci. 517 (2018) 265–277. https://doi.org/10.1016/j.jcis.2018.01.078.

[138] H. Lu, M. Yuan, B. Fang, J. Wang, Y. Guo, Wormlike Micelles in Mixed Amino Acid-Based Anionic Surfactant and Zwitterionic Surfactant Systems, J. Surfactants Deterg. 18 (2015) 589–596. https://doi.org/10.1007/s11743-015-1683-9.

[139] M.E. Cates, S.J. Candau, Statics and dynamics of worm-like surfactant micelles, J. Phys. Condens. Matter. 2 (1990) 6869–6892. https://doi.org/10.1088/0953-8984/2/33/001.

[140] M.A. Calabrese, S.A. Rogers, R.P. Murphy, N.J. Wagner, The rheology and microstructure of branched micelles under shear, J. Rheol. (N. Y. N. Y). 59 (2015) 1299–1328. https://doi.org/10.1122/1.4929486.

[141] S. Khandavalli, J. Hendricks, C. Clasen, J.P. Rothstein, A comparison of linear and branched wormlike micelles using large amplitude oscillatory shear and orthogonal superposition rheology, J. Rheol. (N. Y. N. Y). 60 (2016) 1331–1346. https://doi.org/10.1122/1.4965435.

[142] M.E. Helgeson, T.K. Hodgdon, E.W. Kaler, N.J. Wagner, A systematic study of equilibrium structure, thermodynamics, and rheology of aqueous CTAB/NaNO3 wormlike micelles, J. Colloid Interface Sci. 349 (2010) 1–12. https://doi.org/10.1016/j.jcis.2010.05.045.

[143] S.A. Rogers, M.A. Calabrese, N.J. Wagner, Rheology of branched wormlike micelles, Curr. Opin. Colloid Interface Sci. 19 (2014) 530–535. https://doi.org/10.1016/j.cocis.2014.10.006.

[144] A.L. Kwiatkowski, V.S. Molchanov, A.I. Kuklin, O.E. Philippova, Opposite effect of salt on branched wormlike surfactant micelles with and without embedded polymer, J. Mol. Liq. 311 (2020) 113301. https://doi.org/10.1016/j.molliq.2020.113301.

[145] J. Lah, M. Bešter-Rogač, T.-M. Perger, G. Vesnaver, Energetics in Correlation with Structural Features: The Case of Micellization, J. Phys. Chem. B. 110 (2006)

23279–23291. https://doi.org/10.1021/jp062796f.

[146] W. Loh, C. Brinatti, K.C. Tam, Use of isothermal titration calorimetry to study surfactant aggregation in colloidal systems, Biochim. Biophys. Acta - Gen. Subj. 1860 (2016) 999–1016. https://doi.org/10.1016/j.bbagen.2015.10.003.

[147] G. Bai, A. Lopes, M. Bastos, Thermodynamics of micellization of alkylimidazolium surfactants in aqueous solution, J. Chem. Thermodyn. 40 (2008) 1509–1516. https://doi.org/10.1016/j.jct.2008.05.016.

[148] K. Bouchemal, F. Agnely, A. Koffi, M. Djabourov, G. Ponchel, What can isothermal titration microcalorimetry experiments tell us about the self-organization of surfactants into micelles?, J. Mol. Recognit. 23 (2009) 335–342. https://doi.org/10.1002/jmr.998.

[149] D. Fu, X. Gao, J. Wang, Y. Xie, F. Yang, X. Sui, P. Li, B. Huang, X. Zhang, K. Kan, Micellization, surface activities and thermodynamics study of dialkylpyridinium [C 16 pymC n][Br] (n = 1–4) in aqueous solutions, J. Dispers. Sci. Technol. 0 (2020) 1–11. https://doi.org/10.1080/01932691.2019.1710528.

[150] M.Z. Jora, R. nunes de Souza, T.M. Barbosa, C.F. Tormena, E. Sabadini, Probing the Formation of Wormlike Micelles Formed by Cationic Surfactant with Chlorobenzoate Derivatives, Langmuir. 35 (2019) 17046–17053. https://doi.org/10.1021/acs.langmuir.9b02173.

[151] M.Z. Jora, R.N. de Souza, E. Sabadini, Role of F, Cl, Br and I in the wormlike micelles formation when combining C14TAB with 4-halogenbenzoates, J. Mol. Liq. 315 (2020) 113744. https://doi.org/10.1016/j.molliq.2020.113744.

[152] J. Liu, B. Dong, D. Sun, X. Wei, S. Wang, L. Zheng, Enthalpy measurements for the formation of salt-induced wormlike micelles using isothermal titration microcalorimetry, Colloids Surfaces A Physicochem. Eng. Asp. 380 (2011) 308–313. https://doi.org/10.1016/j.colsurfa.2011.03.019.

[153] A. Kroflič, B. Sˇarac, J. Cerkovnik, M. Bešter-Rogač, Hydrophobicity of counterions as a driving force in the self-assembly process: Dodecyltrimethylammonium chloride and parabens, Colloids Surfaces A Physicochem. Eng. Asp. 460 (2014)

108–117. https://doi.org/10.1016/j.colsurfa.2014.02.002.

[154] T.H. Ito, R.K. Rodrigues, W. Loh, E. Sabadini, Calorimetric and Light Scattering Investigations of the Transition from Spherical to Wormlike Micelles of C 14 TAB Triggered by Salicylate, Langmuir. 31 (2015) 6020–6026. https://doi.org/10.1021/acs.langmuir.5b01027.

[155] T.H. Ito, K.J. Clinckspoor, R.N. De Souza, E. Sabadini, The thermal signature of wormlike micelles, J. Chem. Thermodyn. 94 (2016) 61–66. https://doi.org/10.1016/j.jct.2015.10.021.

[156] E. Sabadini, K.J. Clinckspoor, Chapter 11. New Insights into the Formation of Wormlike Micelles: Kinetics and Thermodynamics, in: C.A. Dreiss, Y. Feng (Eds.), Wormlike Micelles, 1st ed., Royal Society of Chemistry, Cambridge, 2017: pp. 298–329. https://doi.org/10.1039/9781782629788-00298.

[157] E.J. Creatto, F. Ceccacci, G. Mancini, E. Sabadini, Effect of the Hydrophobic Tail of a Chiral Surfactant on the Chirality of Aggregates and on the Formation of Wormlike Micelles, Langmuir. 34 (2018) 13288–13295. https://doi.org/10.1021/acs.langmuir.8b02556.

[158] M. Medeiros, X. Marcos, A.A. Velasco-Medina, S. Perez-Casas, J. Gracia-Fadrique, Micellization and adsorption modeling of single and mixed nonionic surfactants, Colloids Surfaces A Physicochem. Eng. Asp. 556 (2018) 81–92. https://doi.org/10.1016/j.colsurfa.2018.08.005.

[159] M. Uchman, S. Pispas, L. Kováčik, M. Štěpánek, Morphologically Tunable Coassembly of Double Hydrophilic Block Polyelectrolyte with Oppositely Charged Fluorosurfactant, Macromolecules. 47 (2014) 7081–7090. https://doi.org/10.1021/ma500622a.

[160] H.-J. Lee, H. Kim, D. Park, K.S. Jin, J.W. Chang, H.-Y. Lee, Mechanism for Transition of Reverse Cylindrical Micelles to Spherical Micelles Induced by Diverse Alcohols, Langmuir. 36 (2020) 8174–8183. https://doi.org/10.1021/acs.langmuir.0c01246.

[161] N. Zhang, R. Qi, H. Li, B. Guan, Y. Liu, Y. Han, Y. Wang, Interaction of phospholipid vesicles with gemini surfactants of different lysine spacer lengths, Soft Matter. 15

(2019) 9458–9467. https://doi.org/10.1039/C9SM02040C.

[162] C. Sofroniou, I. Chazapi, E. Leontidis, Binding of lanthanide salts to zwitterionic phospholipid micelles, J. Colloid Interface Sci. 557 (2019) 568–579. https://doi.org/10.1016/j.jcis.2019.09.048.

[163] N. Zhang, R. Qi, Y. Chen, X. Ji, Y. Han, Y. Wang, Partition of Glutamic Acid-Based Single-Chain and Gemini Amphiphiles into Phospholipid Membranes, Langmuir. 34 (2018) 13652–13661. https://doi.org/10.1021/acs.langmuir.8b02627.

[164] R. Domínguez, A. Rodríguez, A. Maestre, I. Robina, M.L. Moyá, Synthesis and physicochemical characterization of alkanedyil-α-ω-bis(dimethyldodecylammonium) bromide, 12-s-12,2Br -, surfactants with s=7, 9, 11 in aqueous medium, J. Colloid Interface Sci. 386 (2012) 228–239. https://doi.org/10.1016/j.jcis.2012.06.089.

[165] K. Łudzik, S. Woloszczuk, W. Zając, M. Jazdzewska, A. Rogachev, A.I. Kuklin, A. Zawisza, M. Jóźwiak, Can the Isothermal Calorimetric Curve Shapes Suggest the Structural Changes in Micellar Aggregates?, Int. J. Mol. Sci. 21 (2020) 5828. https://doi.org/10.3390/ijms21165828.

[166] L. Feng, D. Xie, B. Song, J. Zhang, X. Pei, Z. Cui, Aggregate evolution in aqueous solutions of a Gemini surfactant derived from dehydroabietic acid, Soft Matter. 14 (2018) 1210–1218. https://doi.org/10.1039/C7SM02173A.

[167] R. Wang, H. Yan, W. Ma, Y. Li, Complex formation between cationic gemini surfactant and sodium carboxymethylcellulose in the absence and presence of organic salt, Colloids Surfaces A Physicochem. Eng. Asp. 509 (2016) 293–300. https://doi.org/10.1016/j.colsurfa.2016.09.023.

[168] R. Wang, M. Tian, Y. Wang, Coacervation and aggregate transitions of a cationic ammonium gemini surfactant with sodium benzoate in aqueous solution, Soft Matter. 10 (2014) 1705–1713. https://doi.org/10.1039/c3sm52819g.

[169] D. Wang, K. Ou, Z. Yang, M. Lin, Z. Dong, Thermodynamic insights and molecular environments into catanionic surfactant systems: Influence of chain length and molar ratio, J. Colloid Interface Sci. 548 (2019) 77–87.

https://doi.org/10.1016/j.jcis.2019.04.023.

[170] M. Tian, L. Zhu, D. Yu, Y. Wang, S. Sun, Y. Wang, Aggregate Transitions in Mixtures of Anionic Sulfonate Gemini Surfactant with Cationic Ammonium Single-Chain Surfactant, J. Phys. Chem. B. 117 (2013) 433–440. https://doi.org/10.1021/jp310065y.

[171] N. V. Sastry, D.K. Singh, Surfactant and Gelation Properties of Acetylsalicylate Based Room Temperature Ionic Liquid in Aqueous Media, Langmuir. 32 (2016) 10000–10016. https://doi.org/10.1021/acs.langmuir.6b02074.

[172] G.G. Singh, G.G. Singh, T.S. Kang, Micellization Behavior of Surface Active Ionic Liquids Having Aromatic Counterions in Aqueous Media, J. Phys. Chem. B. 120 (2016) 1092–1105. https://doi.org/10.1021/acs.jpcb.5b09688.

[173] M.D. Pelta, G.A. Morris, M.J. Stchedroff, S.J. Hammond, A one-shot sequence for high-resolution diffusion-ordered spectroscopy, Magn. Reson. Chem. 40 (2002) S147–S152. https://doi.org/10.1002/mrc.1107.

[174] A. Botana, J.A. Aguilar, M. Nilsson, G.A. Morris, J-modulation effects in DOSY experiments and their suppression: The Oneshot45 experiment, J. Magn. Reson. 208 (2011) 270–278. https://doi.org/10.1016/j.jmr.2010.11.012.

[175] M. Nilsson, The DOSY Toolbox: A new tool for processing PFG NMR diffusion data, J. Magn. Reson. 200 (2009) 296–302. https://doi.org/10.1016/j.jmr.2009.07.022.

[176] Recommended Practices for Core Analysis RB 40, 2nd ed., 1998.

[177] H.Y.H. Carr, E.M.E. Purcell, Effects of Diffusion on Free Precession in Nuclear Magnetic Resonance Experiments, Phys. Rev. 94 (1954) 630–638. https://doi.org/10.1103/PhysRev.94.630.

[178] S. Meiboom, D. Gill, Modified Spin-Echo Method for Measuring Nuclear Relaxation Times, Rev. Sci. Instrum. 29 (1958) 688. https://doi.org/10.1063/1.1716296.

[179] E. Fuguet, C. Ràfols, M. Rosés, E. Bosch, Critical micelle concentration of surfactants in aqueous buffered and unbuffered systems, Anal. Chim. Acta. 548

(2005) 95–100. https://doi.org/10.1016/j.aca.2005.05.069.

[180] A. Parker, W. Fieber, Viscoelasticity of anionic wormlike micelles: effects of ionic strength and small hydrophobic molecules, Soft Matter. 9 (2013) 1203–1213. https://doi.org/10.1039/C2SM27078A.

[181] J. Oremusová, Micellization of Alkyl Trimethyl Ammonium Bromides in Aqueous Solutions–Part 1: Critical Micelle Concentration (CMC) and Ionization Degree, Tenside Surfactants Deterg. 49 (2012) 231–240. https://doi.org/10.3139/113.110187.

[182] C. Jolicoeur, P.R. Philip, Enthalpy–Entropy Compensation for Micellization and Other Hydrophobic Interactions in Aqueous Solutions, Can. J. Chem. 52 (1974) 1834–1839. https://doi.org/10.1139/v74-262.

[183] B.C. Smith, L.C. Chou, J.L. Zakin, Measurement of the orientational binding of counterions by nuclear magnetic resonance measurements to predict drag reduction in cationic surfactant micelle solutions, J. Rheol. (N. Y. N. Y). 38 (1994) 73–83. https://doi.org/10.1122/1.550496.

[184] T. Shikata, Y. Morishima, Microdynamic Behavior in Threadlike Micelles, Langmuir. 12 (1996) 5307–5311. https://doi.org/10.1021/la9603481.

[185] T. Shikata, S. Imai, Y. Morishima, Molecular Motions in Threadlike Micelles, Langmuir. 13 (1997) 5229–5234. https://doi.org/10.1021/la962028n.

[186] B. Lu, X. Li, L.E. Scriven, H.T. Davis, Y. Talmon, J.L. Zakin, Effect of Chemical Structure on Viscoelasticity and Extensional Viscosity of Drag-Reducing Cationic Surfactant Solutions, Langmuir. 14 (1998) 8–16. https://doi.org/10.1021/la970630n.

[187] S. Gravsholt, Viscoelasticity in highly dilute aqueous solutions of pure cationic detergents, J. Colloid Interface Sci. 57 (1976) 575–577. https://doi.org/10.1016/0021-9797(76)90236-8.

[188] M.F. Emėrson, A. Holtzer, On the Ionic Strength Dependence of Micelle Number, J. Phys. Chem. 69 (1965) 3718–3721. https://doi.org/10.1021/j100895a010.

[189] N. Gorski, J. Kalus, Temperature Dependence of the Sizes of Tetradecyltrimethylammonium Bromide Micelles in Aqueous Solutions, Langmuir. 17 (2001) 4211–4215. https://doi.org/10.1021/la0017882.

[190] K. Bijma, M.J. Blandamer, J.B.F.N. Engberts, Effect of Counterions and Headgroup Hydrophobicity on Properties of Micelles Formed by Alkylpyridinium Surfactants. 2. Microcalorimetry, Langmuir. 14 (1998) 79–83. https://doi.org/10.1021/la970216n.

[191] A.A. Shahir, M. Rashidi-Alavijeh, S. Javadian, J. Kakemam, A. Yousefi, Molecular interaction of Congo Red with conventional and cationic gemini surfactants, Fluid Phase Equilib. 305 (2011) 219–226. https://doi.org/10.1016/j.fluid.2011.04.004.

[192] I. Martiel, L. Sagalowicz, R. Mezzenga, Viscoelasticity and Interface Bending Properties of Lecithin Reverse Wormlike Micelles Studied by Diffusive Wave Spectroscopy in Hydrophobic Environment, Langmuir. 30 (2014) 10751–10759. https://doi.org/10.1021/la502748e.

[193] H. Yamakawa, M. Fujii, Translational Friction Coefficient of Wormlike Chains, Macromolecules. 6 (1973) 407–415. https://doi.org/10.1021/ma60033a018.

[194] H. Rehage, H. Hoffmann, Rheological properties of viscoelastic surfactant systems, J. Phys. Chem. 92 (1988) 4712–4719. https://doi.org/10.1021/j100327a031.

[195] A. Khatory, F. Lequeux, F. Kern, S.J. Candau, Linear and nonlinear viscoelasticity of semidilute solutions of wormlike micelles at high salt content, Langmuir. 9 (1993) 1456–1464. https://doi.org/10.1021/la00030a005.

[196] F. Lequeux, Reptation of Connected Wormlike Micelles, Europhys. Lett. 19 (1992) 675–681. https://doi.org/10.1209/0295-5075/19/8/003.

[197] Z. Lin, Branched Worm-like Micelles and Their Networks, Langmuir. 12 (1996) 1729–1737. https://doi.org/10.1021/la950570q.

[198] G.T. Bulgakova, R.Y. Kharisov, A. V. Pestrikov, A.R. Sharifullin, Experimental study of a viscoelastic surfactant-based in situ self-diverting acid system: Results and

interpretation, Energy and Fuels. 28 (2014) 1674–1685. https://doi.org/10.1021/ef4019542.

[199] Z. Yan, C. Dai, M. Zhao, Y. Li, M. Du, D. Peng, Study of pH-responsive surface active ionic liquids: the formation of spherical and wormlike micelles, Colloid Polym. Sci. 293 (2015) 1759–1766. https://doi.org/10.1007/s00396-015-3552-5.

[200] C. Zheng, H. Lu, L. Wang, Z. Huang, The pH and temperature dual-responsive micelle transition in the mixture of hydrotrope potassium phthalic acid and quaternary ammonium surfactants cetyltrimethylammonium bromide, J. Dispers. Sci. Technol. 38 (2017) 1330–1335. https://doi.org/10.1080/01932691.2016.1236268.

[201] W. Kang, Y. Zhao, P. Wang, Z. Li, X. Hou, Z. Huang, H. Yang, Rheological behavior and mechanism of pH-responsive wormlike micelle variations induced by isomers of phthalic acid, Soft Matter. 14 (2018) 4445–4452. https://doi.org/10.1039/C8SM00467F.

[202] R. Dorshow, J. Briggs, C.A. Bunton, D.F. Nicoli, Dynamic light scattering from cetyltrimethylammonium bromide micelles. Intermicellar interactions at low ionic strengths, J. Phys. Chem. 86 (1982) 2388–2395. https://doi.org/10.1021/j100210a028.

[203] T. Schmutzler, T. Schindler, M. Schmiele, M. Appavou, S. Lages, A. Kriele, R. Gilles, T. Unruh, The influence of n- hexanol on the morphology and composition of CTAB micelles, Colloids Surfaces A Physicochem. Eng. Asp. 543 (2018) 56–63. https://doi.org/10.1016/j.colsurfa.2017.12.039.

[204] Z. Mitrinova, S. Tcholakova, N. Denkov, Control of surfactant solution rheology using medium-chain cosurfactants, Colloids Surfaces A Physicochem. Eng. Asp. 537 (2018) 173–184. https://doi.org/10.1016/j.colsurfa.2017.10.018.

[205] M. Buijse, P. de Boer, B. Breukel, G. Burgos, Organic Acids in Carbonate Acidizing, SPE Prod. Facil. 19 (2004) 128–134. https://doi.org/10.2118/82211-PA.

[206] F.R. Branco, N.A. Gil, NMR study of carbonates wettability, J. Pet. Sci. Eng. 157 (2017) 288–294. https://doi.org/10.1016/j.petrol.2017.06.023.

[207] B. Kenyon, S. Land, Nuclear Magnetic Resonance Imaging — Technology for the 21st Century, Oilf. Rev. (1995) 19–33.

[208] K.R. Brownstein, C.E. Tarr, Importance of classical diffusion in NMR studies of water in biological cells, Phys. Rev. A. 19 (1979) 2446–2453. https://doi.org/10.1103/PhysRevA.19.2446.

[209] A.A. Garrouch, A.R. Jennings, A contemporary approach to carbonate matrix acidizing, J. Pet. Sci. Eng. 158 (2017) 129–143. https://doi.org/10.1016/j.petrol.2017.08.045.

[210] A.F. Ibrahim, H. Nasr-el-din, J. De Paulo, C. Ewbank, Evaluation of New Viscoelastic Surfactant Systems in High-Temperatures Carbonates Acidizing, Soc. Pet. Eng. (2018) 1–20. https://doi.org/https://doi.org/10.2118/191606-MS.

[211] W. Al-Sadat, M.S. Nasser, F. Chang, H.A. Nasr-El-Din, I.A. Hussein, Laboratory evaluation of the effects of additives and pH on the thermorheological behavior of a viscoelastic zwitterionic surfactant used in acid stimulation, J. Pet. Sci. Eng. 122 (2014) 458–467. https://doi.org/10.1016/j.petrol.2014.08.006.

[212] W. Al-Sadat, M.S. Nasser, F. Chang, H.A. Nasr-El-Din, I.A. Hussein, Rheology of a viscoelastic zwitterionic surfactant used in acid stimulation: Effects of surfactant and electrolyte concentration, J. Pet. Sci. Eng. 124 (2014) 341–349. https://doi.org/10.1016/j.petrol.2014.09.014.

[213] J.S. Pedersen, L. Cannavacciuolo, P. Schurtenberger, Giant Micelles. Properties and Applications, 1st ed., CRC Press, 2007. https://doi.org/10.1201/9781420007121.

[214] G. Schramm, A Practical Approach to Rheology and Rheometry, (n.d.).

[215] W. Al-Sadat, M.S. Nasser, F. Chang, H.A. Nasr-El-Din, I.A. Hussein, Rheology of a viscoelastic zwitterionic surfactant used in acid stimulation: Effects of surfactant and electrolyte concentration, J. Pet. Sci. Eng. 124 (2014) 341–349. https://doi.org/10.1016/j.petrol.2014.09.014.

[216] L. Qiu, Y. Shen, C. Wang, pH- and KCl-induced formation of worm-like micelle

viscoelastic fluids based on a simple tertiary amine surfactant, J. Pet. Sci. Eng. 162 (2018) 158–165. https://doi.org/10.1016/j.petrol.2017.12.037.

[217] S. Kefi, J. Lee, T. Pope, P. Sullivan, E. Nelson, A. Hernandez, T. Olsen, M. Parlar, B. Powers, A. Roy, Expanding applications for viscoelastic surfactants, Oilf. Rev. 16 (2004) 10–23.

[218] A. V. Sangwai, R. Sureshkumar, Coarse-Grained Molecular Dynamics Simulations of the Sphere to Rod Transition in Surfactant Micelles, Langmuir. 27 (2011) 6628–6638. https://doi.org/10.1021/la2006315.

[219] M.M. Davis, H.B. Hetzer, Relative strengths of forty aromatic carboxylic acids in benzene at 25-degrees-C, J. Res. Natl. Bur. Stand. (1934). 60 (1958) 569. https://doi.org/10.6028/jres.060.057.

Appendix A Probing the formation of wormlike micelles formed by cationic surfactant with chlorobenzoate derivatives

Table A1. pK_a of the different chlorobenzoic acids studied. Values for the 2-chlorobenzoic acid, 3-chlorobenzoic acid and 3,4-dichlorobenzoic acid were obtained from reference [219].

Compound	pK_a
2,6-dichlorobenzoic acid	1.82
2,3-dichlorobenzoic acid	2.41
2,4-dichlorobenzoic acid	2.76
2-chlorobenzoic acid	2.92
3,4-dichlorobenzoic acid	3.64
3-chlorobenzoic acid	3.8
4-chlorobenzoic acid	4.05
Benzoic acid	4.2

Table A2. Values of diffusion delay (Δ) and diffusion-encoding gradient pulse width (δ) used for self-diffusion measurement specified for each solution of different [C_{14}TAB]/[4Cl] ratio.

$[C_{14}TAB]/[4-Chlorobenzoate]$	$\Delta\ /\ ms$	$\delta\ /\ \mu s$
0.20	120	1400
0.40	120	1400
0.60	100	1600
0.70	120	1600
0.80	100	1800
0.90	120	1800
1.00	120	2000
1.20	120	2000
1.40	120	2300
1.60	120	2200
1.80	120	2300
2.00	120	2400

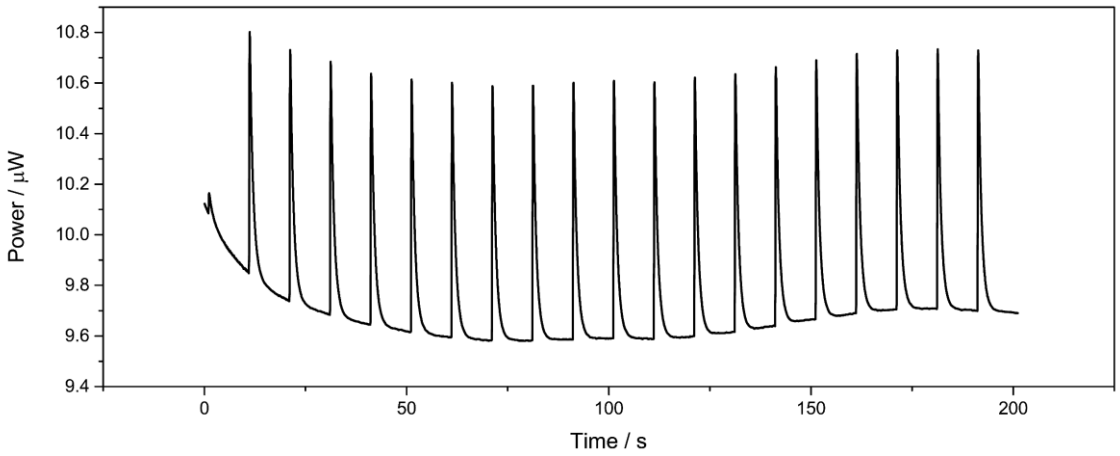

Figure A1. Differential electric power in μW as function of time for the titration of C_{14}TAB $10.0\ mmol\ L^{-1}$ in a reaction cell containing water, both solutions at pH 10.0 ± 0.1.

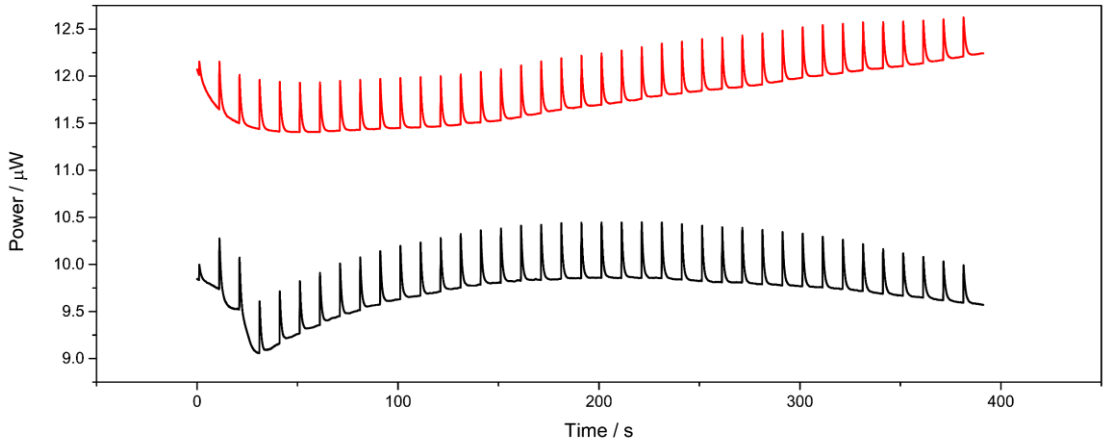

Figure A2. Differential electric power in μW as function of time for two titrations of C_{14}TAB $10.0\ mmol\ L^{-1}$ in a reaction cell containing sodium benzoate $1.40\ mmol\ L^{-1}$, both solutions at pH 10.0 ± 0.1.

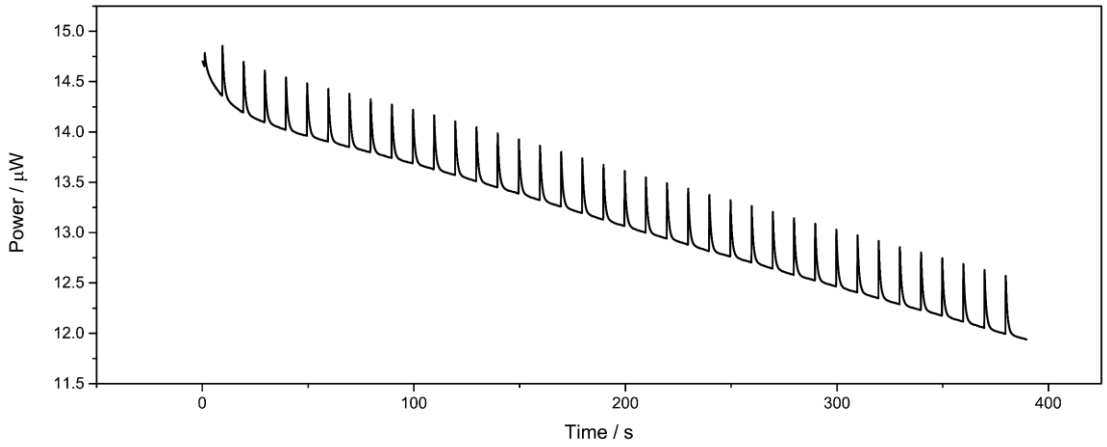

Figure A3. Differential electric power in μW as function of time for the titration of C_{14}TAB $10.0\ mmol\ L^{-1}$ in a reaction cell containing 2-chlorobenzoate $1.40\ mmol\ L^{-1}$, both solutions at pH 10.0 ± 0.1.

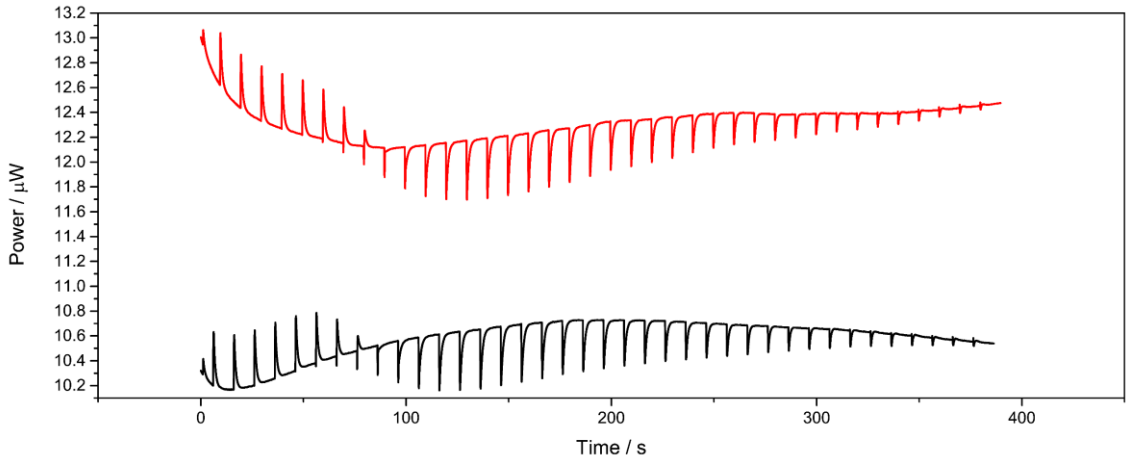

Figure A4. Differential electric power in μW as function of time for two titrations of C_{14}TAB $10.0\ mmol\ L^{-1}$ in a reaction cell containing 3-chlorobenzoate $1.40\ mmol\ L^{-1}$, both solutions at pH 10.0 ± 0.1.

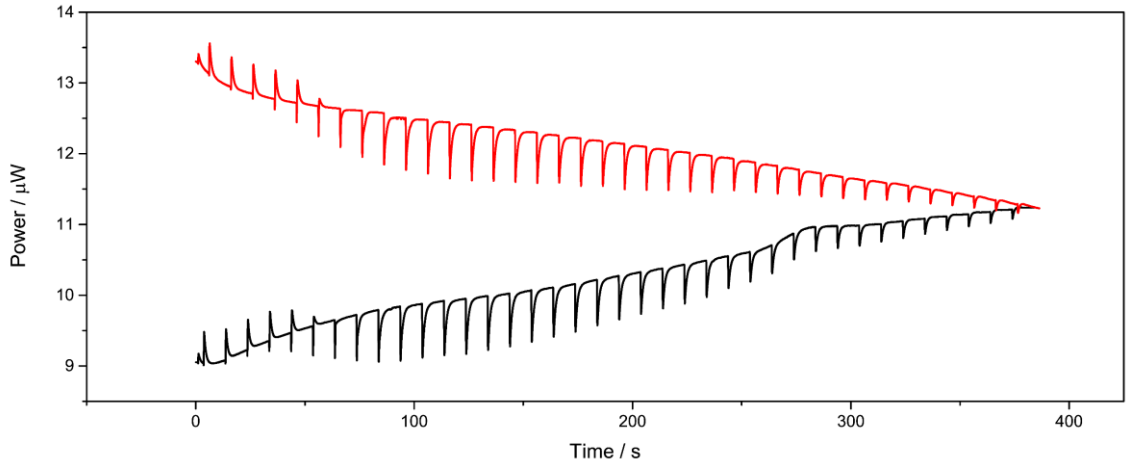

Figure A5. Differential electric power in μW as function of time for two titrations of C_{14}TAB $10.0\ mmol\ L^{-1}$ in a reaction cell containing 4-chlorobenzoate $1.40\ mmol\ L^{-1}$, both solutions at pH 10.0 ± 0.1.

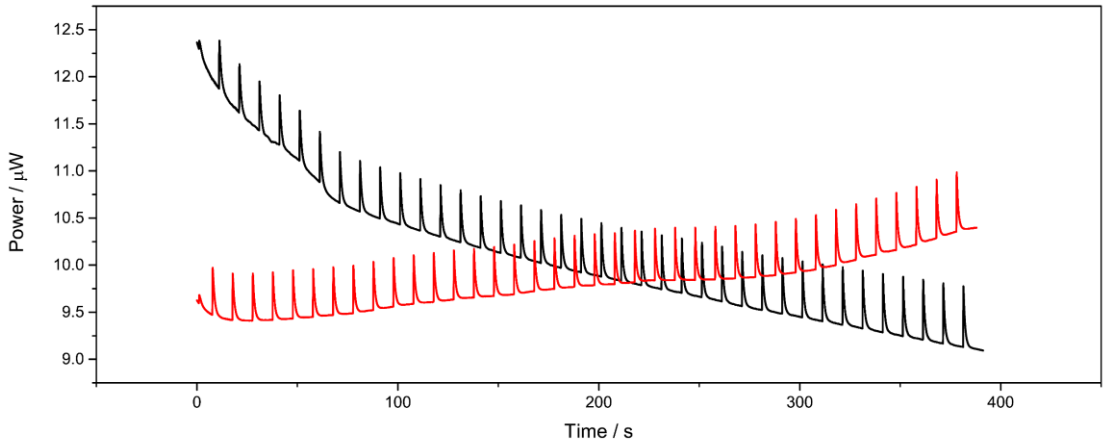

Figure A6. Differential electric power in μW as function of time for two titrations of $C_{14}TAB$ $10.0\ mmol\ L^{-1}$ in a reaction cell containing 2,6-dichlorobenzoate $1.40\ mmol\ L^{-1}$, both solutions at pH 10.0 ± 0.1.

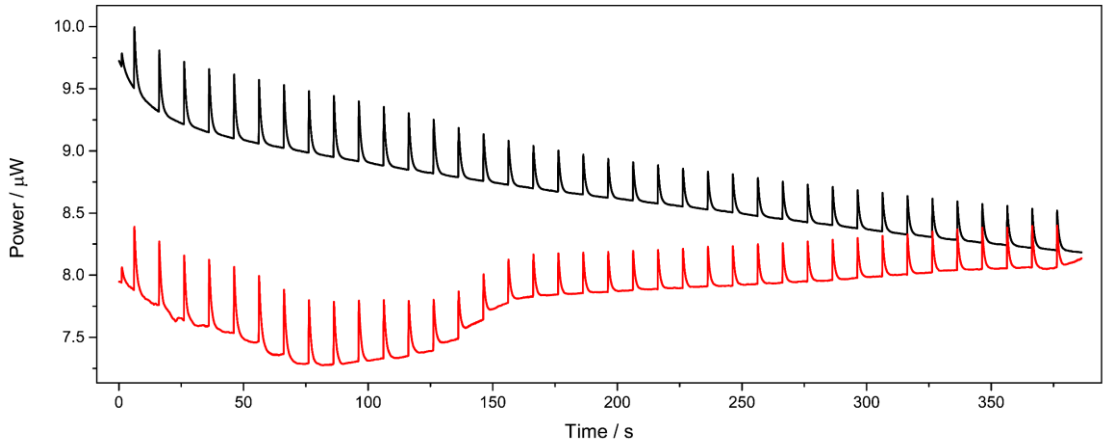

Figure A7. Differential electric power in μW as function of time for two titrations of $C_{14}TAB$ $10.0\ mmol\ L^{-1}$ in a reaction cell containing 2,3-dichlorobenzoate $1.40\ mmol\ L^{-1}$, both solutions at pH 10.0 ± 0.1.

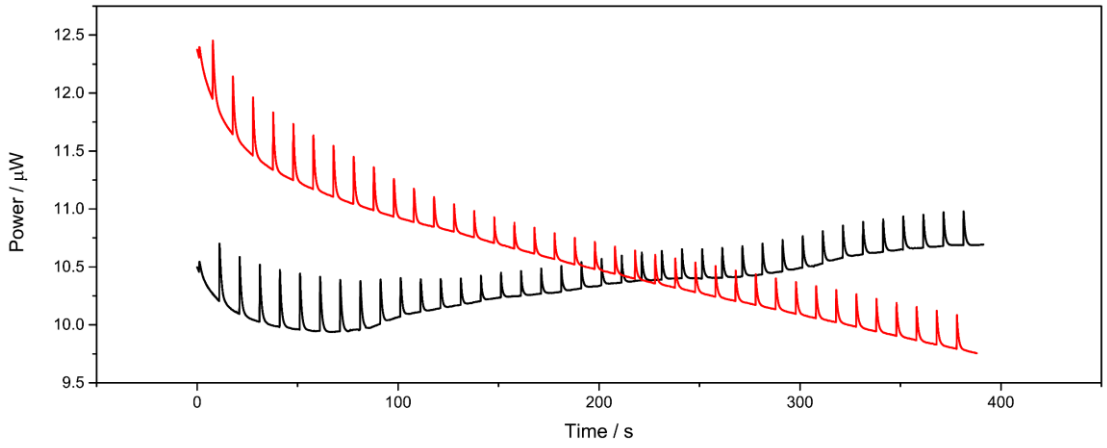

Figure A8. Differential electric power in μW as function of time for two titrations of $C_{14}TAB$ $10.0\ mmol\ L^{-1}$ in a reaction cell containing 2,4-dichlorobenzoate $1.40\ mmol\ L^{-1}$, both solutions at pH 10.0 ± 0.1.

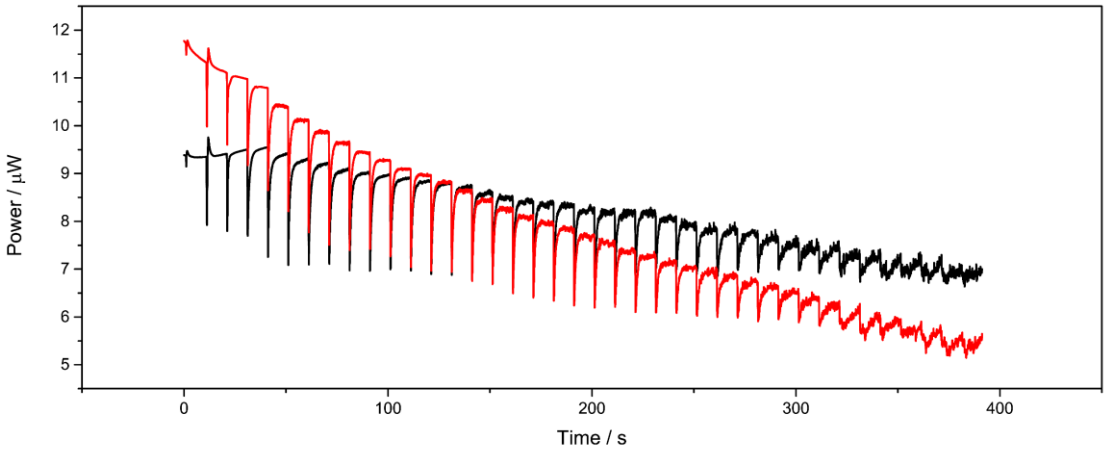

Figure A9. Differential electric power in μW as function of time for two titrations of $C_{14}TAB$ $10.0\ mmol\ L^{-1}$ in a reaction cell containing 3,4-dichlorobenzoate $1.40\ mmol\ L^{-1}$, both solutions at pH 10.0 ± 0.1.

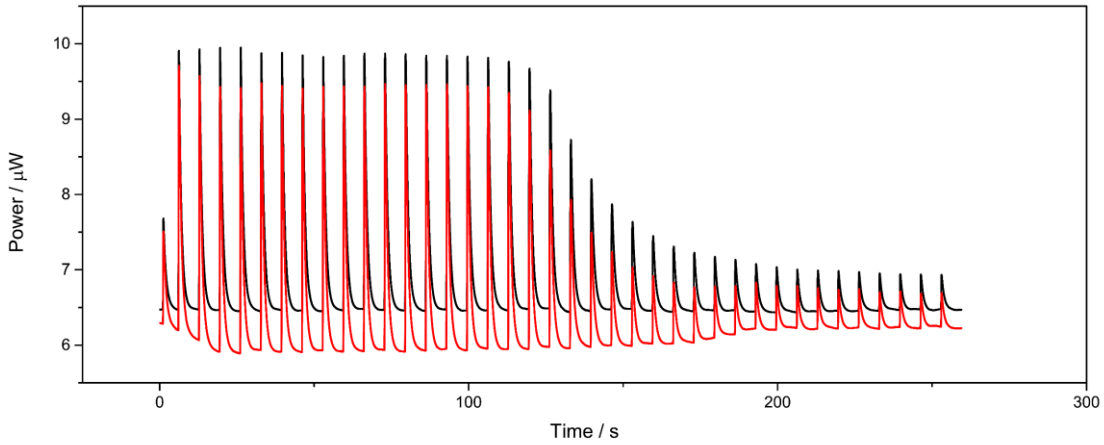

Figure A10. Differential electric power in μW as function of time for two titrations of C_{14}TAB $40.0\ mmol\ L^{-1}$ in a reaction cell containing water, both solutions at pH 10.0 ± 0.1.

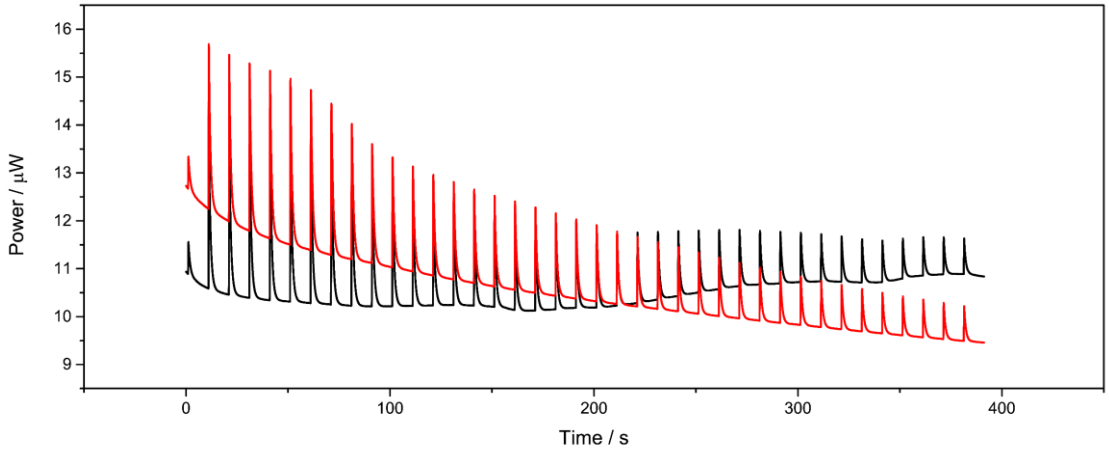

Figure A11. Differential electric power in μW as function of time for two titrations of C_{14}TAB $40.0\ mmol\ L^{-1}$ in a reaction cell containing sodium benzoate $1.40\ mmol\ L^{-1}$, both solutions at pH 10.0 ± 0.1.

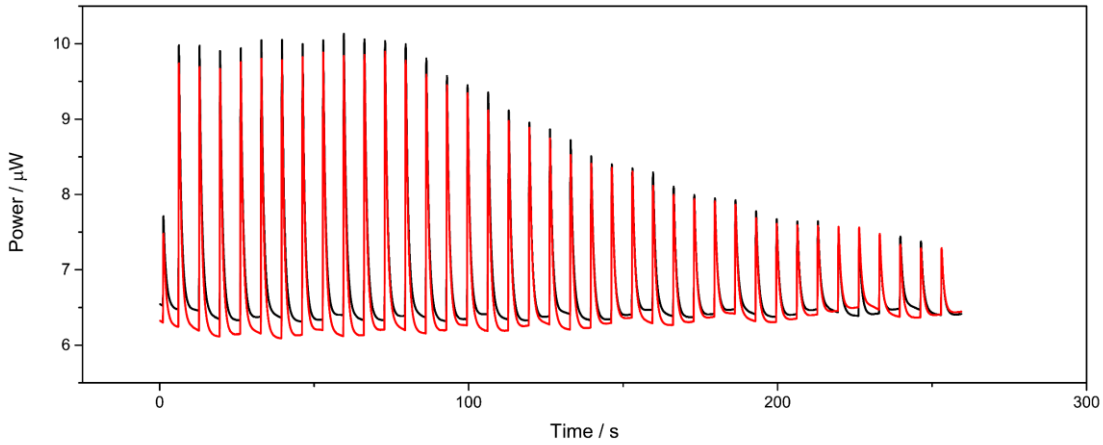

Figure A12. Differential electric power in μW as function of time for two titrations of C_{14}TAB $40.0\ mmol\ L^{-1}$ in a reaction cell containing 2-chlorobenzoate $1.40\ mmol\ L^{-1}$, both solutions at pH 10.0 ± 0.1.

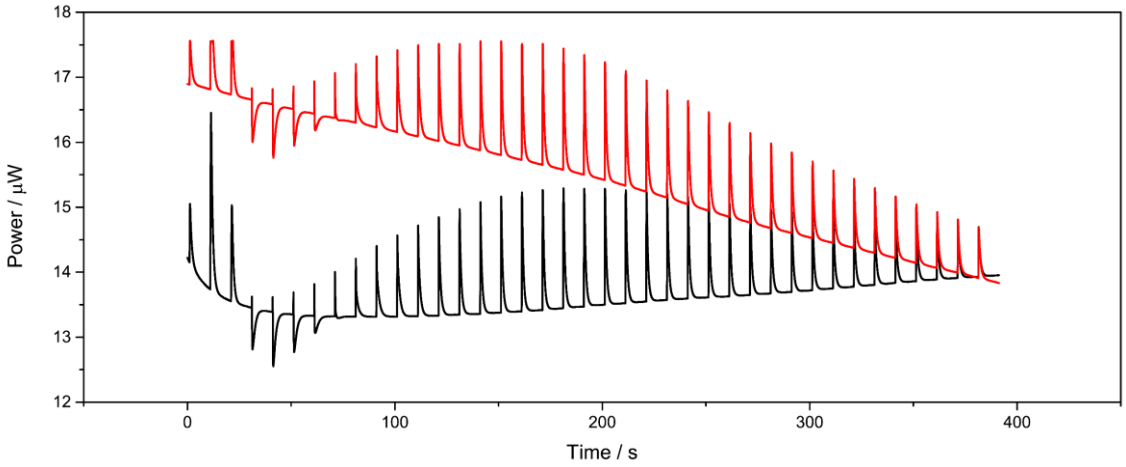

Figure A13. Differential electric power in μW as function of time for two titrations of C_{14}TAB $40.0\ mmol\ L^{-1}$ in a reaction cell containing 3-chlorobenzoate $1.40\ mmol\ L^{-1}$, both solutions at pH 10.0 ± 0.1.

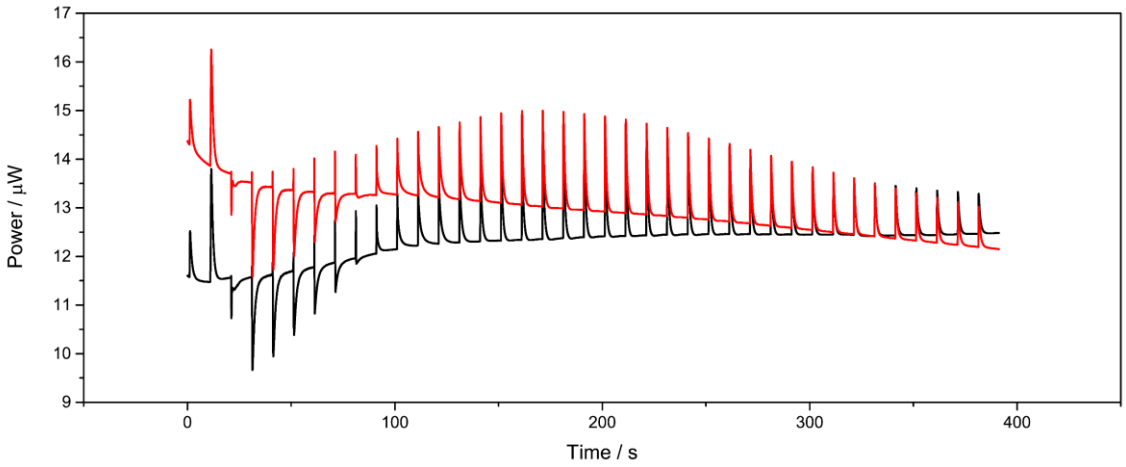

Figure A14. Differential electric power in μW as function of time for two titrations of C_{14}TAB $40.0\ mmol\ L^{-1}$ in a reaction cell containing 4-chlorobenzoate $1.40\ mmol\ L^{-1}$, both solutions at pH 10.0 ± 0.1.

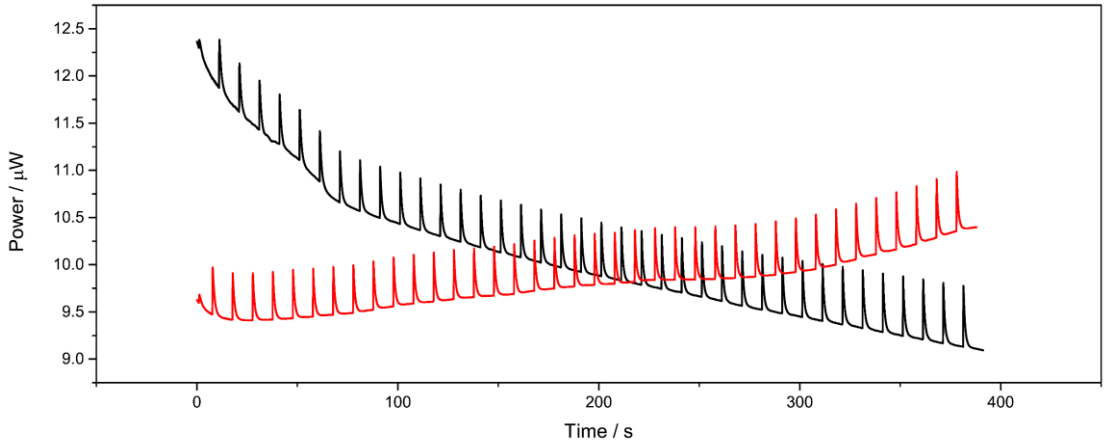

Figure A15. Differential electric power in μW as function of time for two titrations of C_{14}TAB $40.0\ mmol\ L^{-1}$ in a reaction cell containing 2,6-dichlorobenzoate $1.40\ mmol\ L^{-1}$, both solutions at pH 10.0 ± 0.1.

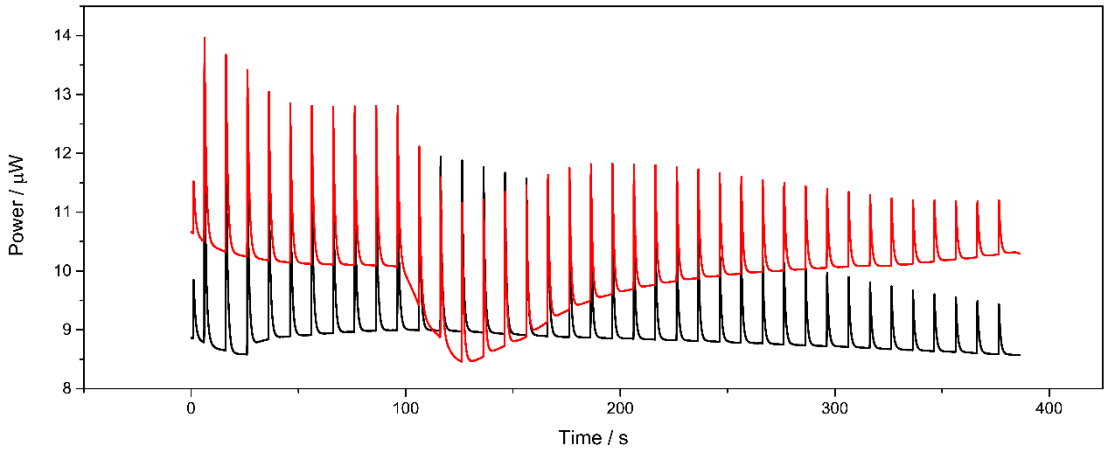

Figure A16. Differential electric power in μW as function of time for two titrations of C_{14}TAB $40.0\ mmol\ L^{-1}$ in a reaction cell containing 2,3-dichlorobenzoate $1.40\ mmol\ L^{-1}$, both solutions at pH 10.0 ± 0.1.

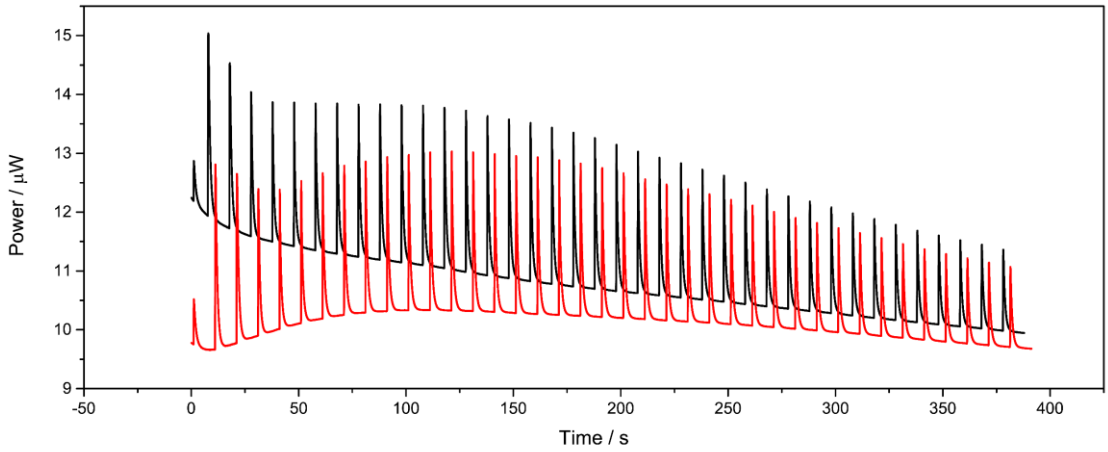

Figure A17. Differential electric power in μW as function of time for two titrations of C_{14}TAB $40.0\ mmol\ L^{-1}$ in a reaction cell containing 2,4-dichlorobenzoate $1.40\ mmol\ L^{-1}$, both solutions at pH 10.0 ± 0.1.

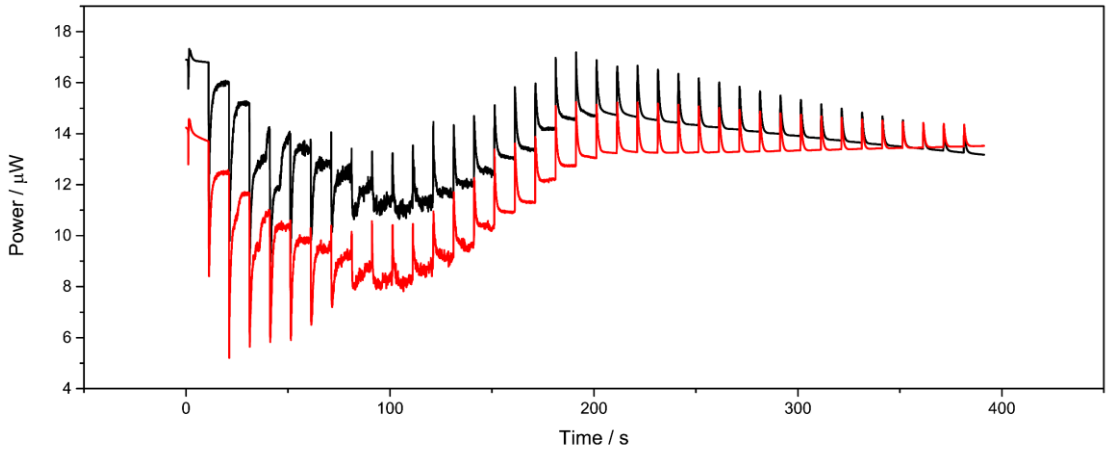

Figure A18. Differential electric power in μW as function of time for two titrations of $C_{14}TAB$ $40.0\ mmol\ L^{-1}$ in a reaction cell containing 3,4-dichlorobenzoate $1.40\ mmol\ L^{-1}$, both solutions at pH 10.0 ± 0.1.

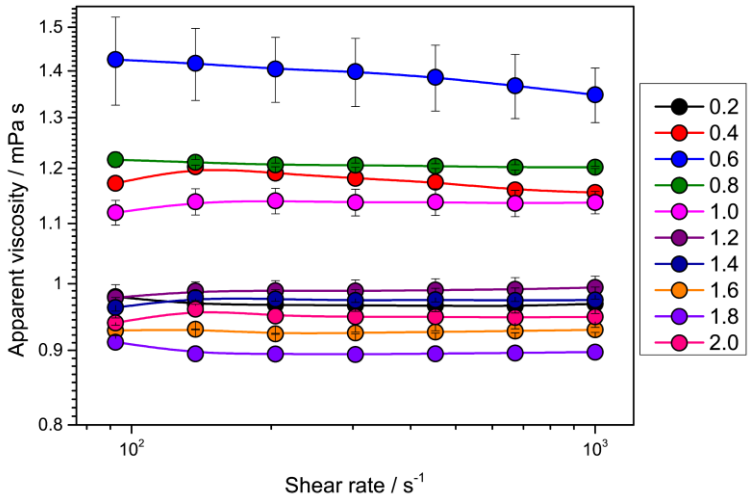

Figure A19. Flow curve for the solutions containing $C_{14}TAB$ and 2,4-dichlorobenzoate $5x$ at 25 $°C$ and pH 10 ± 0.1. The numbers in the legend represents the ratio [$C_{14}TAB$]/[salt] fixing the salt concentration at $1.4\ mmol\ L^{-1}$.

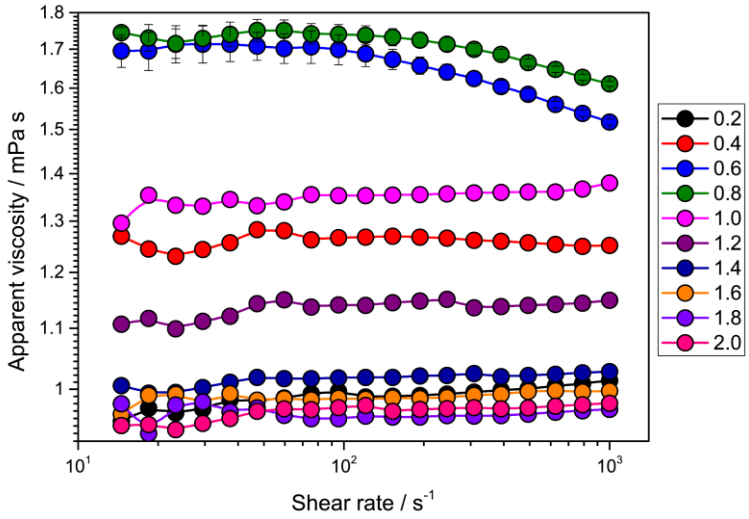

Figure A20. Flow curve for the solutions containing C_{14}TAB and 3-chlorobenzoate $5x$ at $25\ °C$ and pH 10 ± 0.1. The numbers in the legend represents the ratio [C_{14}TAB]/[salt] fixing the salt concentration at $1.4\ mmol\ L^{-1}$.

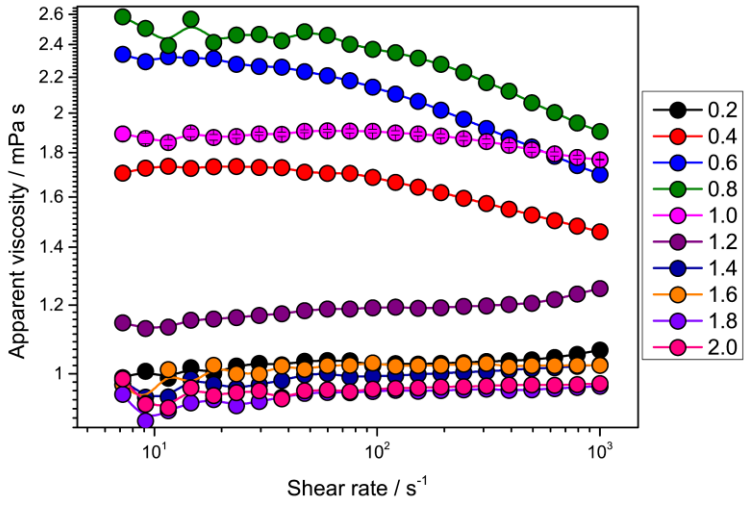

Figure A21. Flow curve for the solutions containing C_{14}TAB and 4-chlorobenzoate $5x$ at $25\ °C$ and pH 10 ± 0.1. The numbers in the legend represents the ratio [C_{14}TAB]/[salt] fixing the salt concentration at $1.4\ mmol\ L^{-1}$.

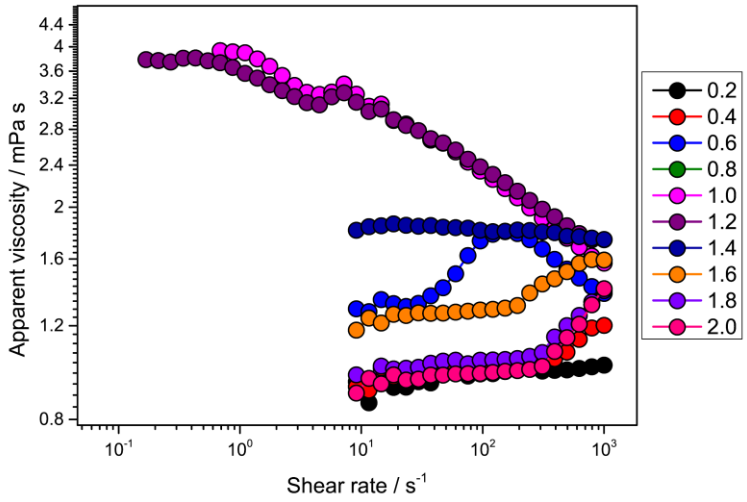

Figure A22. Flow curve for the solutions containing C_{14}TAB and 3,4-dichlorobenzoate $2x$ at 25 °C and pH 10 ± 0.1. The numbers in the legend represents the ratio [C_{14}TAB]/[salt] fixing the salt concentration at $1.4\ mmol\ L^{-1}$.

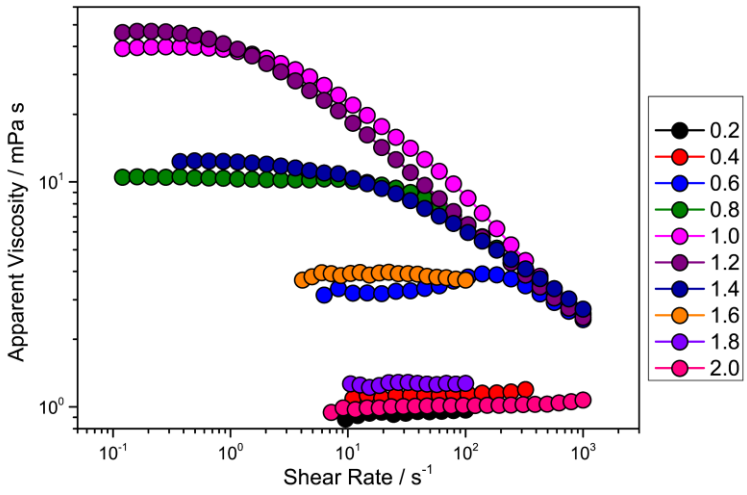

Figure A23. Flow curve for the solutions containing C_{14}TAB and 3,4-dichlorobenzoate $5x$ at 25 °C and pH 10 ± 0.1. The numbers in the legend represents the ratio [C_{14}TAB]/[salt] fixing the salt concentration at $1.4\ mmol\ L^{-1}$.

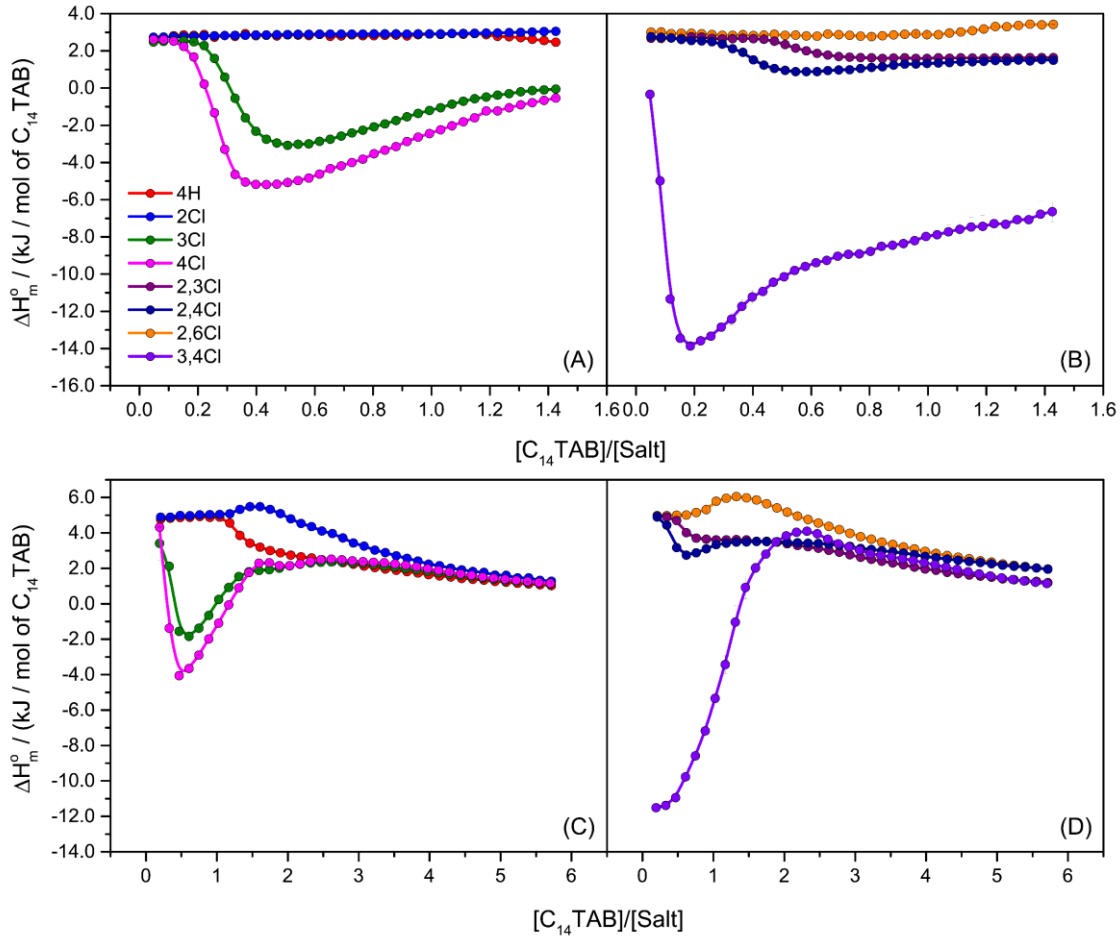

Figure A24. Enthalpy in kJ per mol of $C_{14}TAB$ as a function of the $[C_{14}TAB]/[salt]$ ratio in the reaction cell. $1.40\ mmol\ L^{-1}$ of salt was fixed in the reaction cell and (A, B) $10.0\ mmol\ L^{-1}$ or (C, D) $40.0\ mmol\ L^{-1}$ of $C_{14}TAB$ in the syringe. In (A) and (C) are shown the salts without and with one substitution in the aromatic ring and in (B) and (D) with two substitutions. 4H refers to sodium benzoate and the others to chlorobenzoates where the numbers refer to the substitution position of the chlorine atom in the aromatic ring. Values have been obtained from at least duplicated and the lines are only guide for the eyes.

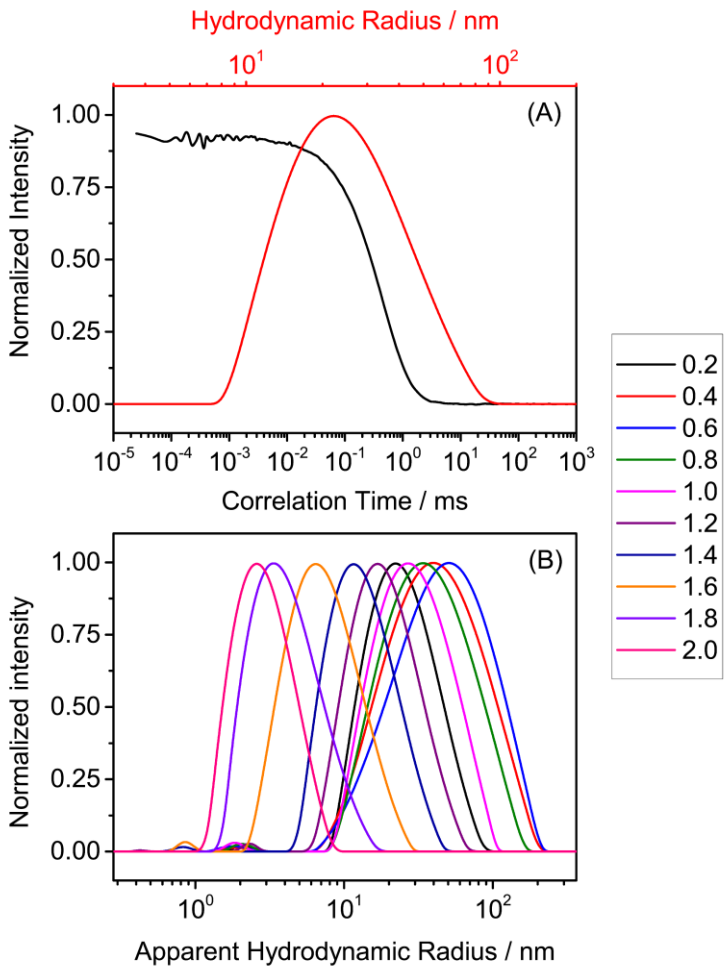

Figure A25. (A) Correlation function and hydrodynamic radius distribution for the solution containing 4Cl and C_{14}TAB with $[C_{14}TAB]/[4Cl] = 0.2$. (B) hydrodynamic radius distribution for the different [C_{14}TAB]/[4Cl] ratios.

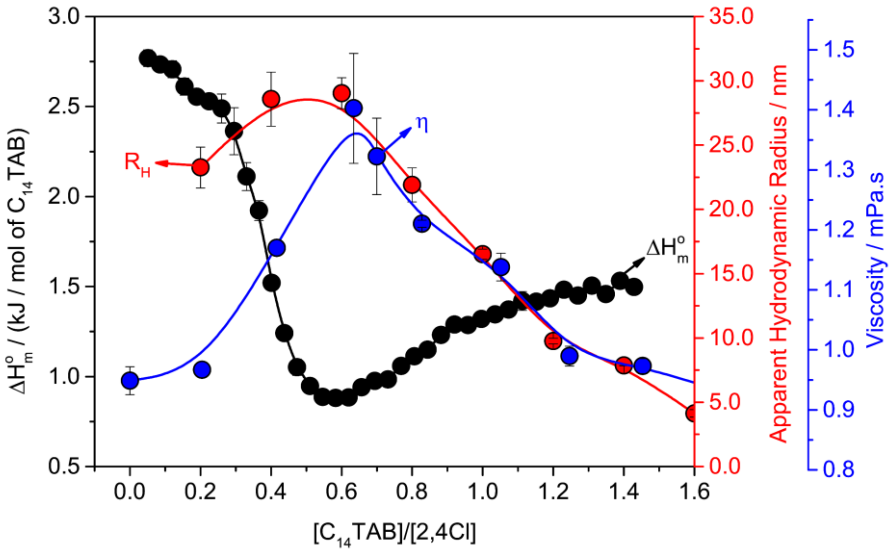

Figure A26. Variation of enthalpy, viscosity of the solutions, and the apparent hydrodynamic radius, as function of the ratio [C_{14}TAB]/[2,4Cl]. Each property is indicated by an arrow in the graph and the axis is in the same color of the curve. The temperature was maintained at $25\ °C$. The values were obtained from at least a duplicate and the curves are only guide for the eyes.

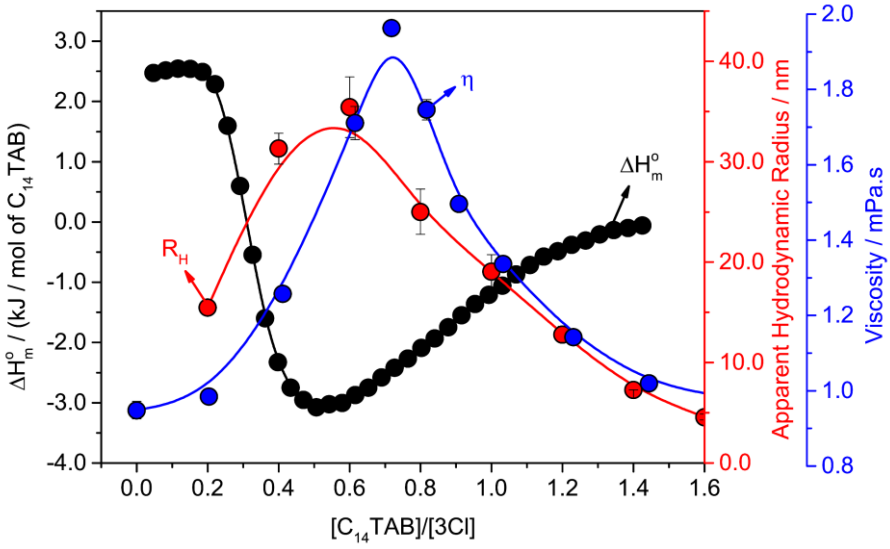

Figure A27. Variation of enthalpy, viscosity of the solutions, and the apparent hydrodynamic radius, as function of the ratio [C_{14}TAB]/[3Cl]. Each property is indicated by an arrow in the graph and the axis is in the same color of the curve. The temperature was maintained at $25\ °C$. The values were obtained from at least a duplicate and the curves are only guide for the eyes.

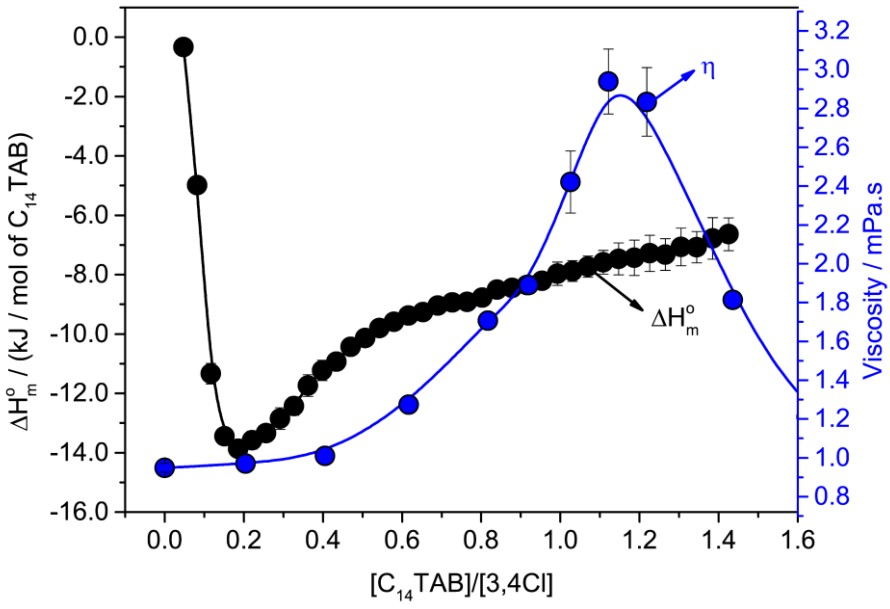

Figure A28. Variation of enthalpy and viscosity of the solutionsas function of the ratio [C_{14}TAB]/[3,4Cl]. Each property is indicated by an arrow in the graph and the axis is in the same color of the curve. The temperature was maintained at $25\ °C$. The values were obtained from at least a duplicate and the curves are only guide for the eyes.

Appendix B Role of F, Cl, Br and I in the wormlike micelle formation when combining C_{14}TAB with 4-halogenbenzoates

Table B1. Values of diffusion-encoding gradient pulse width (δ) and diffusion delay (Δ) used for DOSY experiments for each [C_{14}TAB]/[4-fluorobenzoate] ratio.

$[C_{14}TAB]/[4F]$	Δ / ms	δ / μs
0.0	1,000	150
0.2	1,000	180
0.4	1,000	185
0.6	1,100	200
0.8	1,200	200
1.0	1,200	200
1.2	1,200	200
1.4	1,200	200
1.6	1,400	200
1.8	1,400	200
2.0	1,400	200
2.2	1,400	200
2.4	1,400	200
2.6	1,400	200
2.8	1,400	200

Table B2. Values of diffusion-encoding gradient pulse width (δ) and diffusion delay (Δ) used for DOSY experiments for each [C_{14}TAB]/[4-chlorobenzoate] ratio. The 4-chlorobenzoate and C_{14}TAB self-diffusion were obtained in different set of parameters depending on the concentration.

	4Cl self-diffusion		$C_{14}TAB$ self-diffusion	
$[C_{14}TAB]/[4\mathrm{Cl}]$	$\Delta\ /\ ms$	$\delta\ /\ \mu s$	$\Delta\ /\ ms$	$\delta\ /\ \mu s$
0.0	1,000	120		
0.2	1,000	200	1,600	200
0.4	1,000	200	1,700	200
0.6	1,100	200	2,100	200
0.8	1,300	200	2,200	200
1.0	1,300	200	2,200	200
1.2	1,300	200	2,200	200
1.4	1,800	200	1,800	200
1.6	1,800	200	1,800	200
1.8	1,800	200	1,800	200
2.0	1,800	200	1,800	200
2.2	1,800	200	1,800	200
2.4	1,800	200	1,800	200

Table B3. Values of diffusion-encoding gradient pulse width (δ) and diffusion delay (Δ) used for DOSY experiments for each [C_{14}TAB]/[4-bromobenzoate] ratio. The 4-bromobenzoate and C_{14}TAB self-diffusion were obtained in different set of parameters depending on the concentration.

	4Br self-diffusion		$C_{14}TAB$ self-diffusion	
$[C_{14}TAB]/[4\mathrm{Br}]$	$\Delta\ /\ ms$	$\delta\ /\ \mu s$	$\Delta\ /\ ms$	$\delta\ /\ \mu s$
0.0	1,000	120		
0.2	1,000	200	1,800	200
0.4	1,000	200	2,100	200
0.6	1,100	200	2,400	210
0.8	1,200	200	2,200	200
1.0	1,300	200	2,300	200
1.2	1,400	200	2,300	200
1.4	1,800	220	2,400	210
1.6	1,900	200	1,900	200
1.8	1,900	200	1,900	200
2.0	2,000	220	2,000	220

Table S4. Values of blot time, blot force, blot wait, blot total and drain time on the sample preparation for the cryo-TEM analysis for each sample.

Sample	Blot time / s	Blot force	Blot wait / s	Blot total	Drain Time / s
4F	3.0	-5.0	0	1.0	0
4Cl	2.5	-5.0	10.0	1.0	30.0
4Br	2.0	-5.0	20.0	1.0	30.0
4I	2.5	-5.0	0.0	2.0	30.0

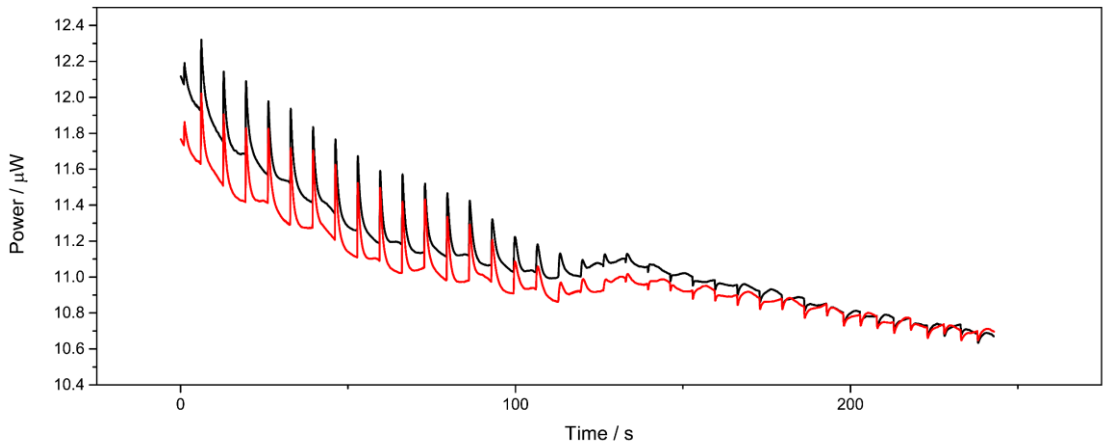

Figure B1. Differential electric power in μW as function of time for two titrations of C_{14}TAB $10.0\ mmol\ L^{-1}$ in a reaction cell containing 4-fluorobenzoate $1.40\ mmol\ L^{-1}$, both solutions at pH 10.0 ± 0.1.

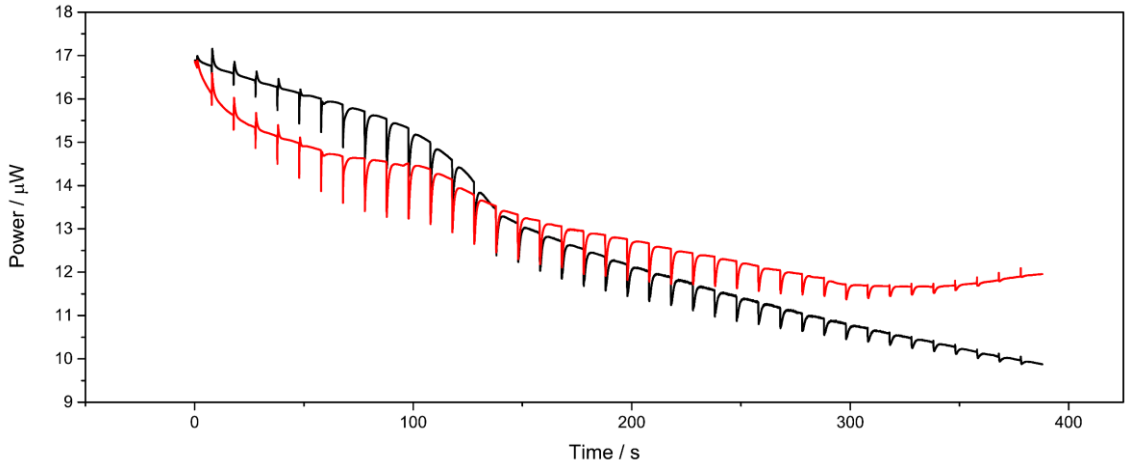

Figure B2. Differential electric power in μW as function of time for two titrations of C_{14}TAB $10.0\ mmol\ L^{-1}$ in a reaction cell containing 4-bromobenzoate $1.40\ mmol\ L^{-1}$, both solutions at pH 10.0 ± 0.1.

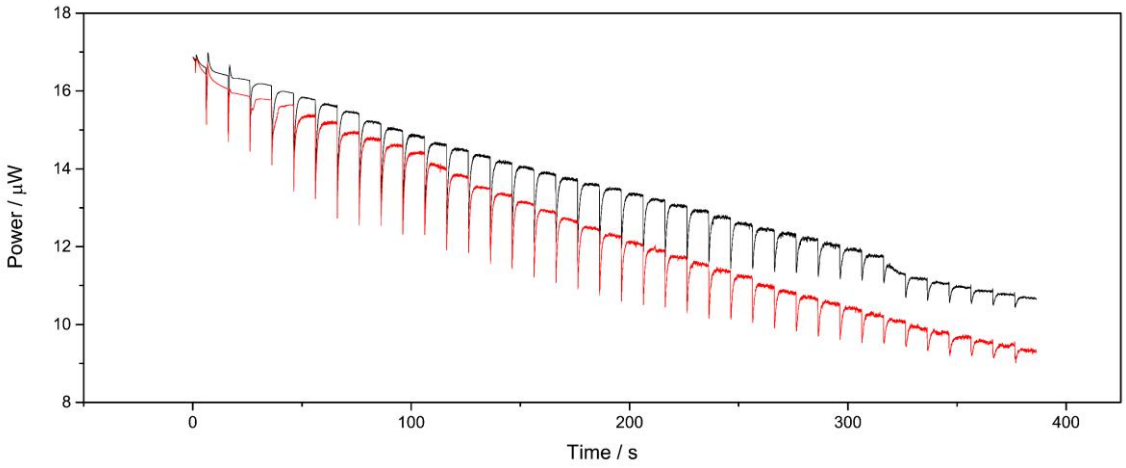

Figure B3. Differential electric power in μW as function of time for two titrations of $C_{14}TAB$ $10.0\ mmol\ L^{-1}$ in a reaction cell containing 4-iodobenzoate $1.40\ mmol\ L^{-1}$, both solutions at pH 10.0 ± 0.1.

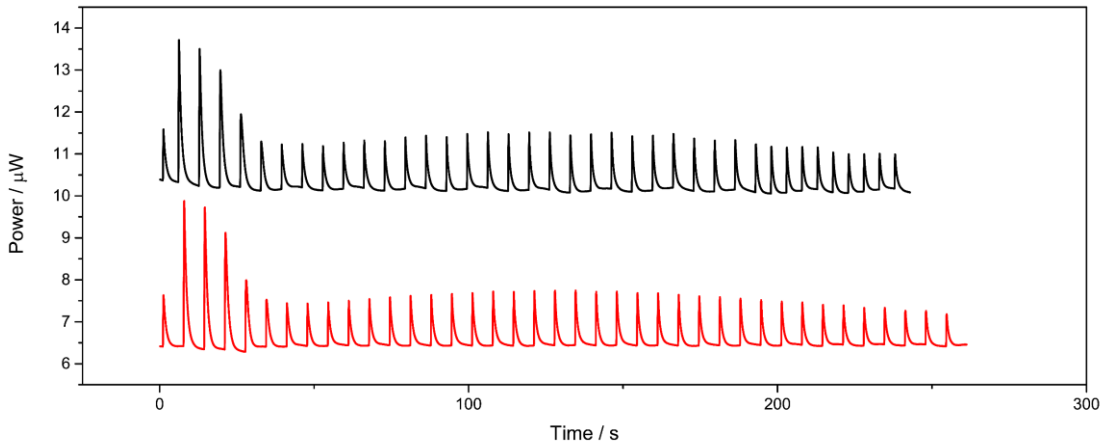

Figure B4. Differential electric power in μW as function of time for two titrations of $C_{14}TAB$ $40.0\ mmol\ L^{-1}$ in a reaction cell containing 4-fluorobenzoate $1.40\ mmol\ L^{-1}$, both solutions at pH 10.0 ± 0.1.

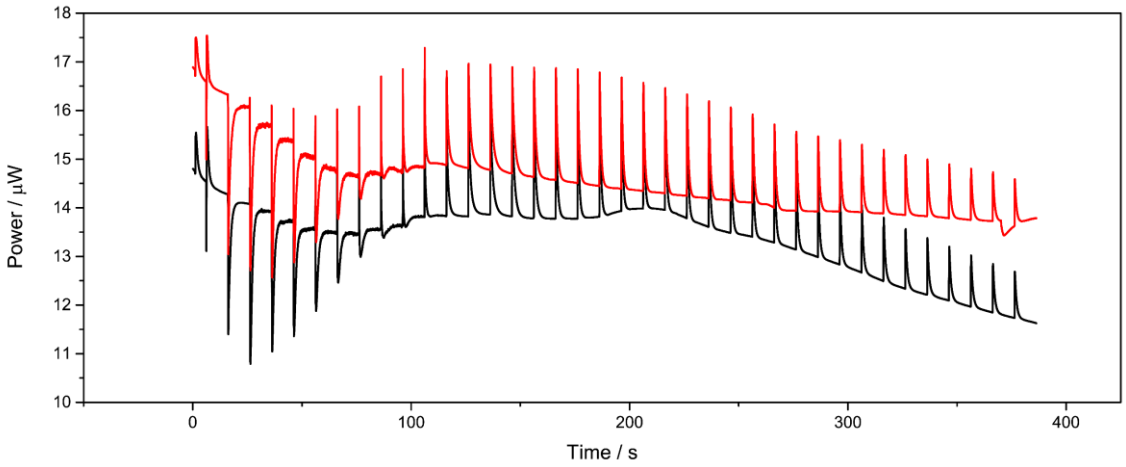

Figure B5. Differential electric power in μW as function of time for two titrations of C_{14}TAB $40.0\ mmol\ L^{-1}$ in a reaction cell containing 4-bromobenzoate $1.40\ mmol\ L^{-1}$, both solutions at pH 10.0 ± 0.1.

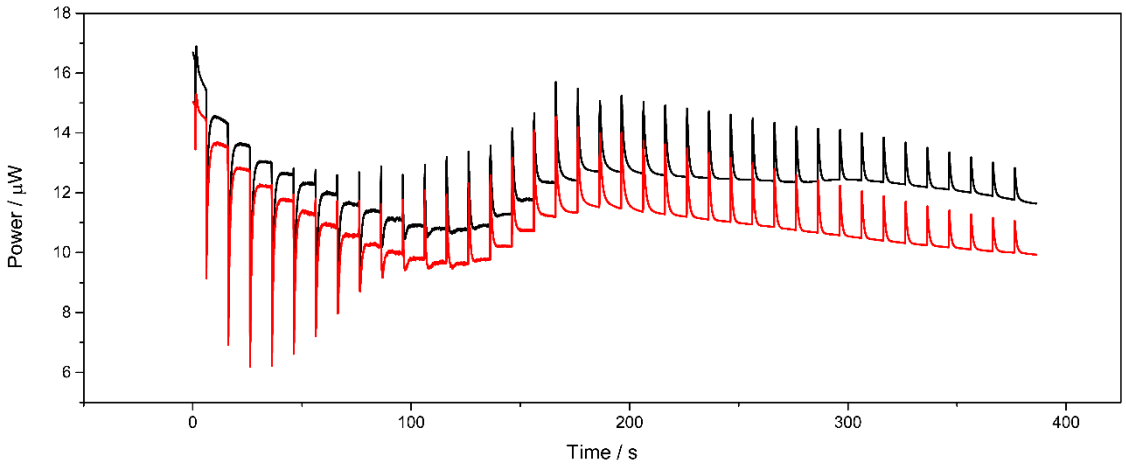

Figure B6. Differential electric power in μW as function of time for two titrations of C_{14}TAB $40.0\ mmol\ L^{-1}$ in a reaction cell containing 4-iodobenzoate $1.40\ mmol\ L^{-1}$, both solutions at pH 10.0 ± 0.1.

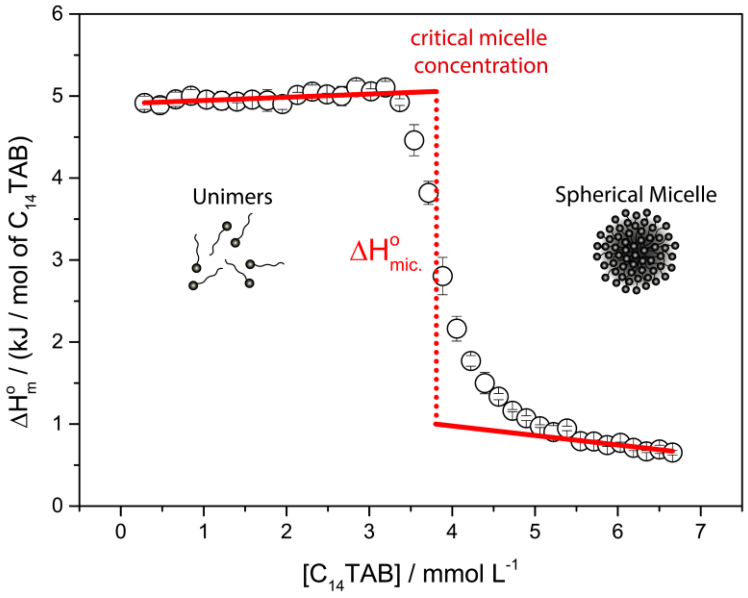

Figure B7. Variation of enthalpy per mol of injectant (C_{14}TAB) as function of C_{14}TAB concentration at $298\,K$ using a $40.0\,mmol\,L^{-1}$ C_{14}TAB as titrant solution. The red dashed line represents the critical micelle concentration, concentration where unimers in solution aggregates to form the spherical micelles, and how the enthalpy of micellization is calculated.

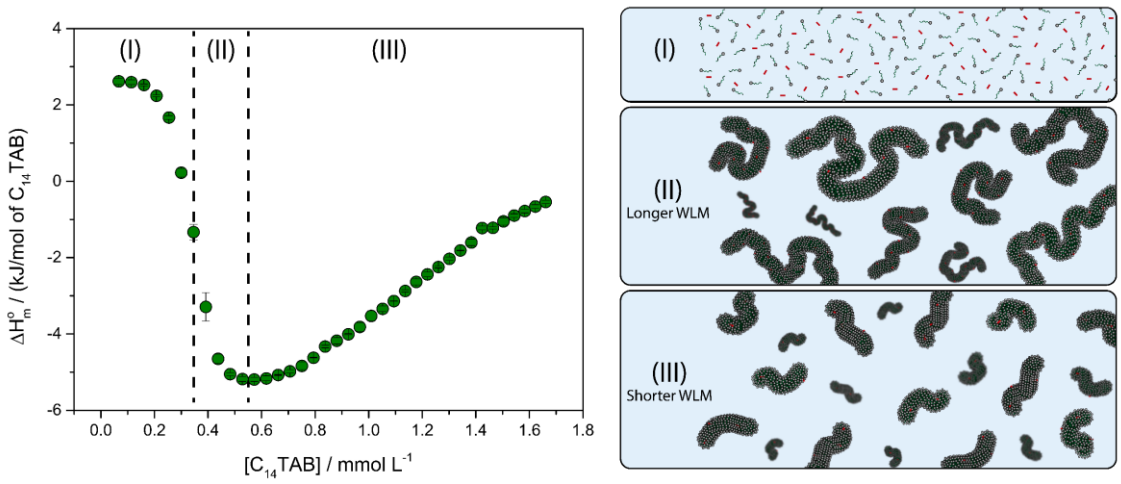

Figure B8. Enthalpy as function of the C_{14}TAB titrated for 4Cl highlighting the three regions of the thermogram. (I) Breakage of the spherical micelle when the C_{14}TAB is titrated and only unimers is expected in the reaction cell; (II) formation and growth of the wormlike micelles; (III) Shrinkage of the WLM up to the point where only spherical micelle is expected in the reaction cell with the titration of further C_{14}TAB. $[4Cl] = 1.40\,mmol\,L^{-1}$ and $[C14TAB] = 10.0\,mmol\,L^{-1}$, both at pH 10.0 ± 0.1.

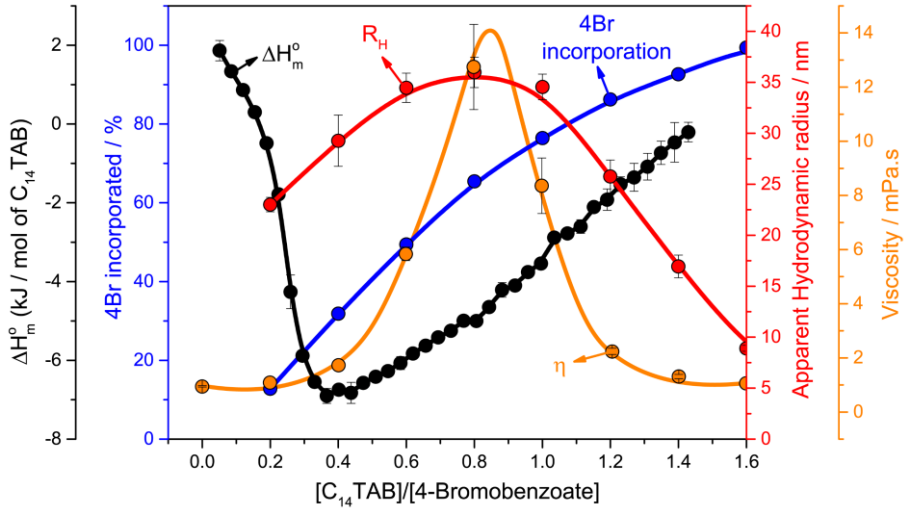

Figure B9. Enthalpy, ΔH_m^o, viscosity, η, apparent hydrodynamic radius, R_H, and percentage of 4-bromobenzoate incorporated as function of the $[C_{14}TAB]/[4-bromobenzoate]$ ratio. Each curve is indicated by an arrow which specifies the property and the lines are only guide for the eyes. The average values were obtained from at least a duplicate.

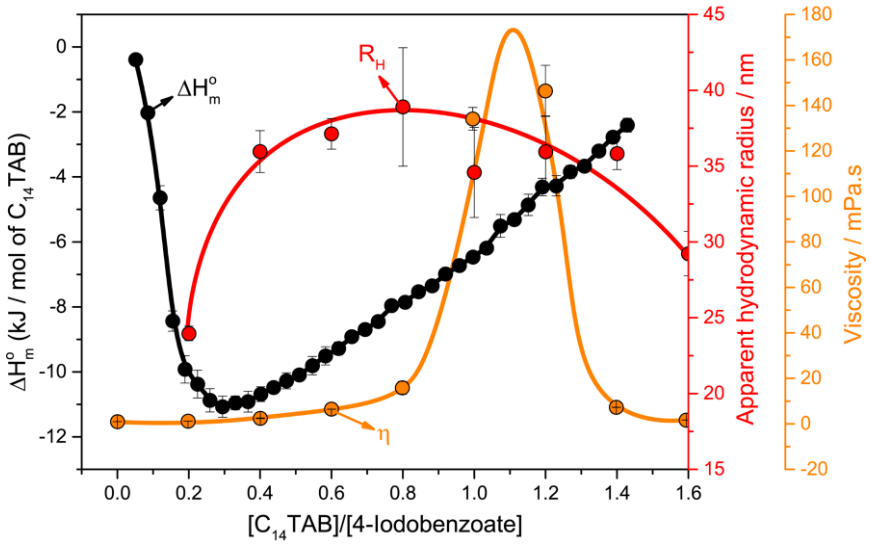

Figure B10. Enthalpy, ΔH_m^o, viscosity, η, and apparent hydrodynamic radius, R_H, as function of the $[C_{14}TAB]/[4-iodobenzoate]$ ratio. Each curve is indicated by an arrow which specifies the property and the lines are only guide for the eyes. The average values were obtained from at least a duplicate.

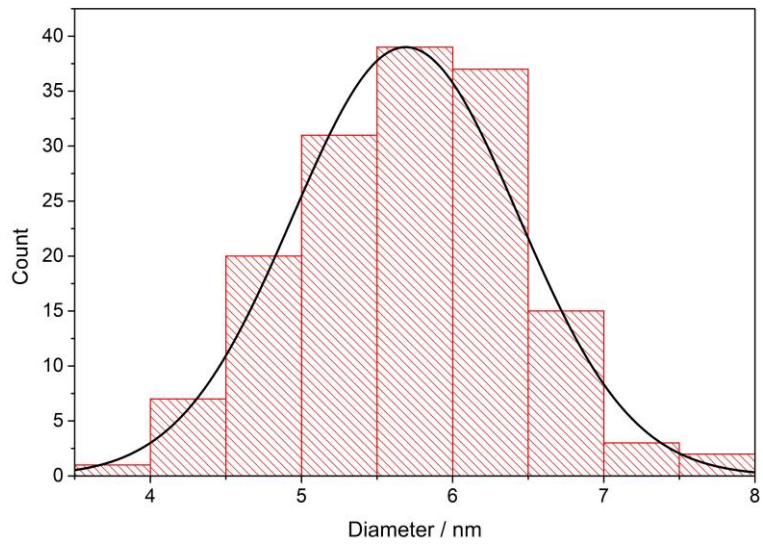

Figure B11. Count of aggregates as function of the aggregate diameter for $[C_{14}TAB]/[4F] = 2.32$. At least 150 aggregate were considered.

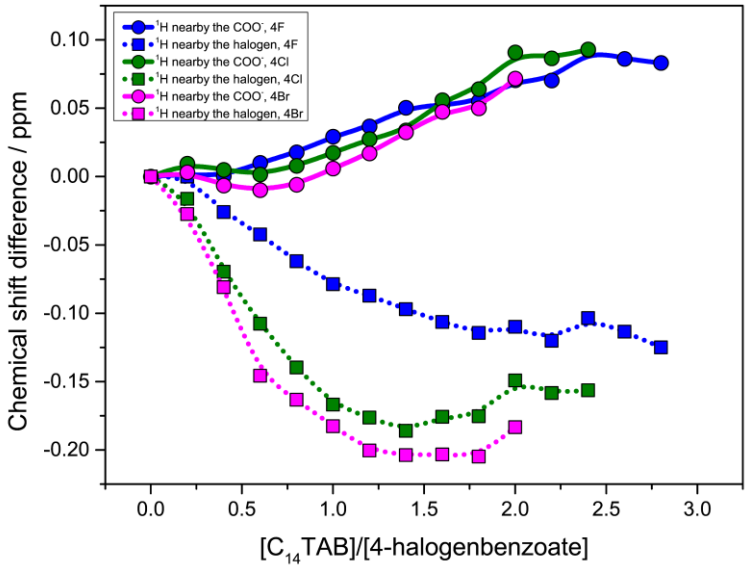

Figure B12. Chemical shift difference in ppm as function of the $[C_{14}TAB]/[4-Halogenbenzoate]$ ratio. The $[C_{14}TAB]$ and $[4-halogenbenzoate]$ were increased 2 times in relation to the calorimetric experiments. Aromatic hydrogens nearby the carboxyl group are indicated by continuous line and the aromatic hydrogens nearby the halogen atom are indicated by dotted lines.

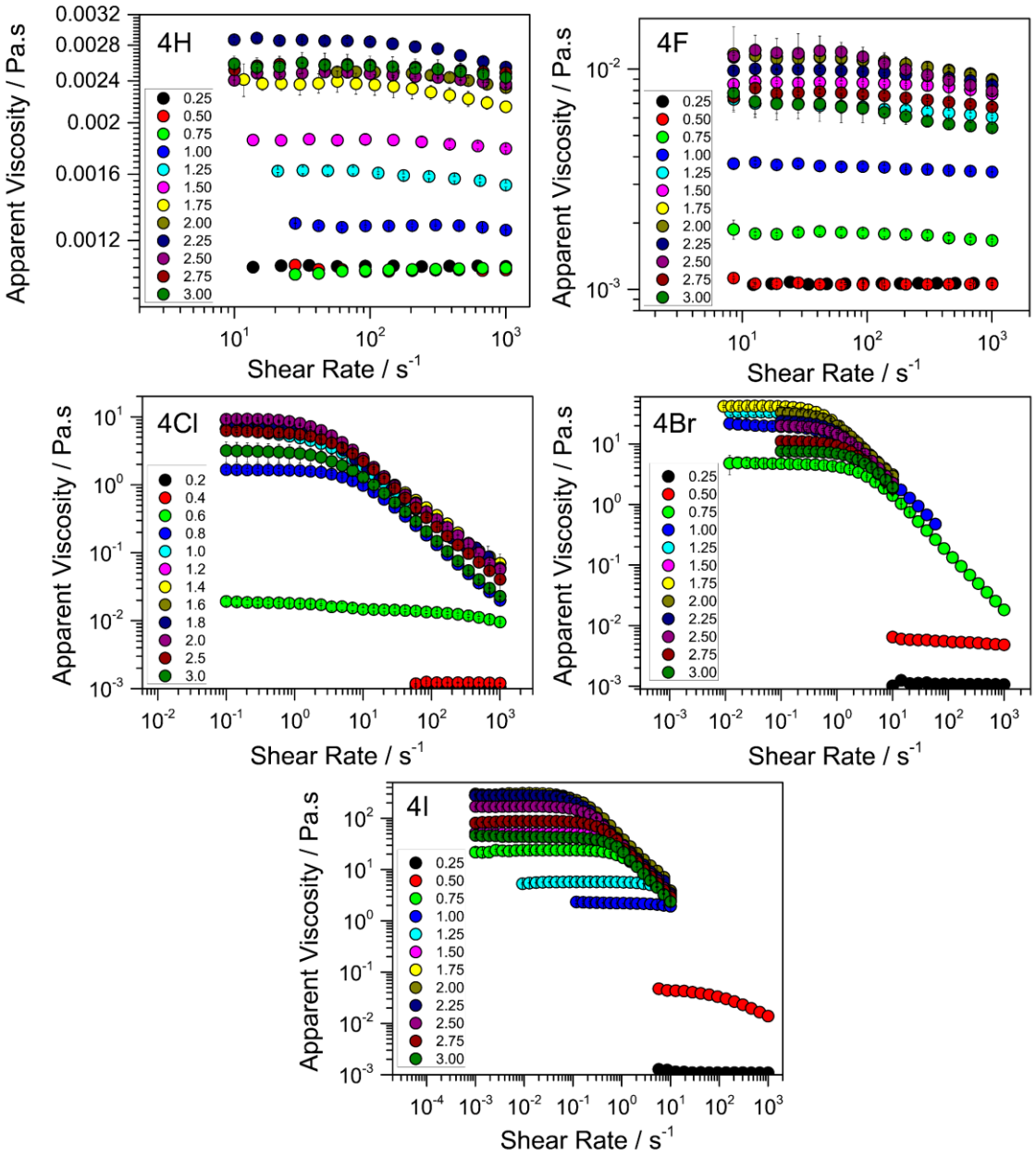

Figure B13. Flow curves of the solutions containing C_{14}TAB and 4-halogenbenzoate. The 4-halogenbenzoate of each graph is indicated at the up-right corner. The legend in each graph indicates the [4-halogenbenzoate]/[C_{14}TAB] ratio. [C_{14}TAB] concentration was fixed at $60.0\ mmol\ L^{-1}$. The average values were obtained from at least a duplicate.

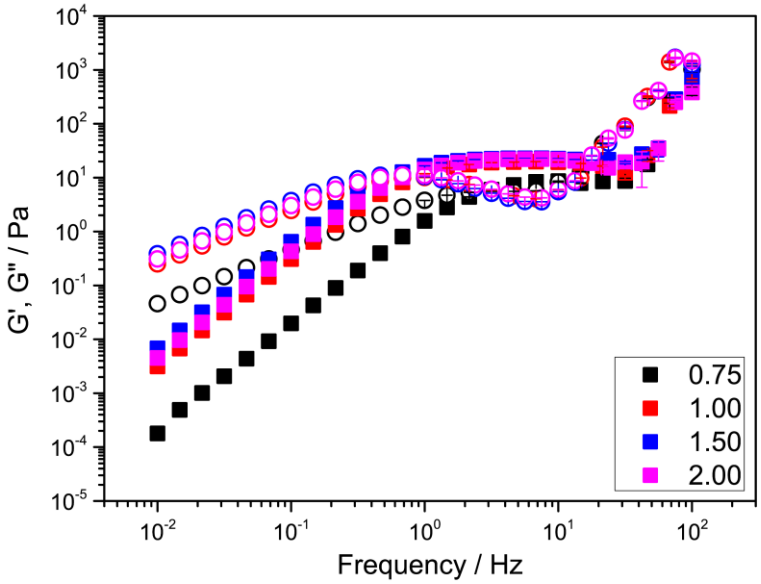

Figure B14. Mechanical frequency sweep for the solutions of 4-chlorobenzoate. Filled symbols refers to the G' and open symbols to the $G"$. The legend refers to the ratio [4-chlorobenzoate]/[C_{14}TAB]. The average values were obtained from at least a duplicate. [C_{14}TAB] was fixed at $60.0\ mmol\ L^{-1}$.

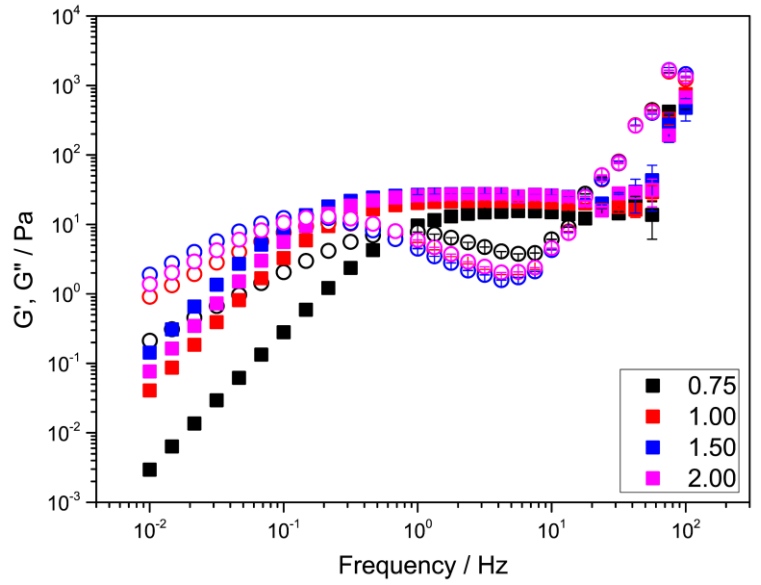

Figure B15. Mechanical frequency sweep for the solutions of 4-bromobenzoate. Filled symbols refers to the G' and open symbols to the $G"$. The legend refers to the ratio [4-bromobenzoate]/[C_{14}TAB]. The average values were obtained from at least a duplicate. [C_{14}TAB] was fixed at $60.0\ mmol\ L^{-1}$.

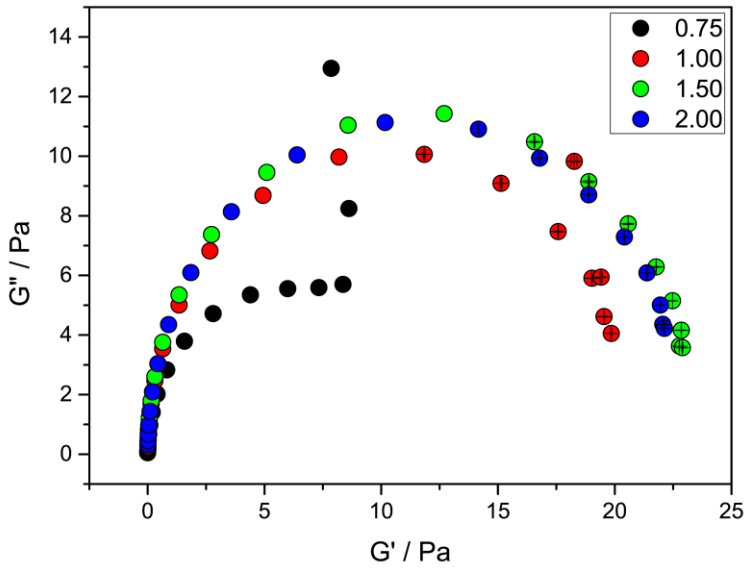

Figure B16. Cole-Cole plot for the solutions of 4-chlorobenzoate. The legend refers to the ratio [4-halogenbenzoate]/[C_{14}TAB]. The average values were obtained from at least a duplicate. [C_{14}TAB] was fixed at $60.0\ mmol\ L^{-1}$.

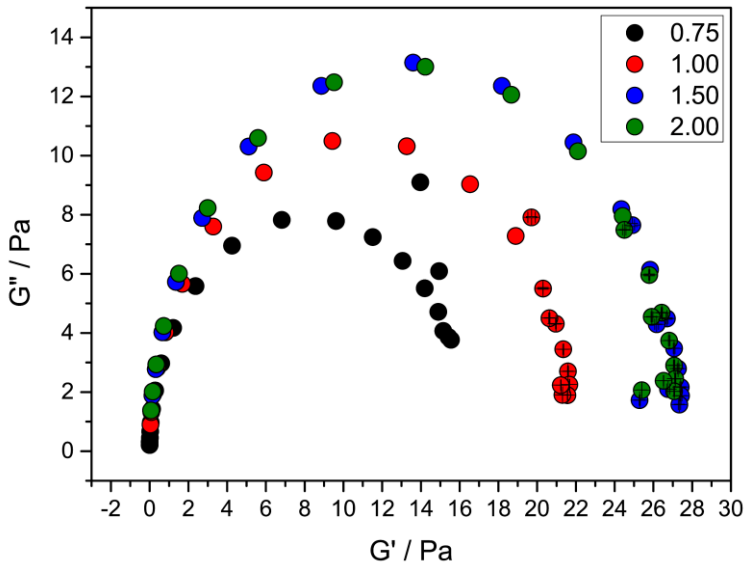

Figure B17. Cole-Cole plot for the solutions of 4-bromobenzoate. The legend refers to the ratio [4-halogenbenzoate]/[C_{14}TAB]. The average values were obtained from at least a duplicate. [C_{14}TAB] was fixed at $60.0\ mmol\ L^{-1}$.

Appendix C Light-Triggered Rheological Changes in a System of Cationic Wormlike Micelles Formulated with a Photoacid Generator

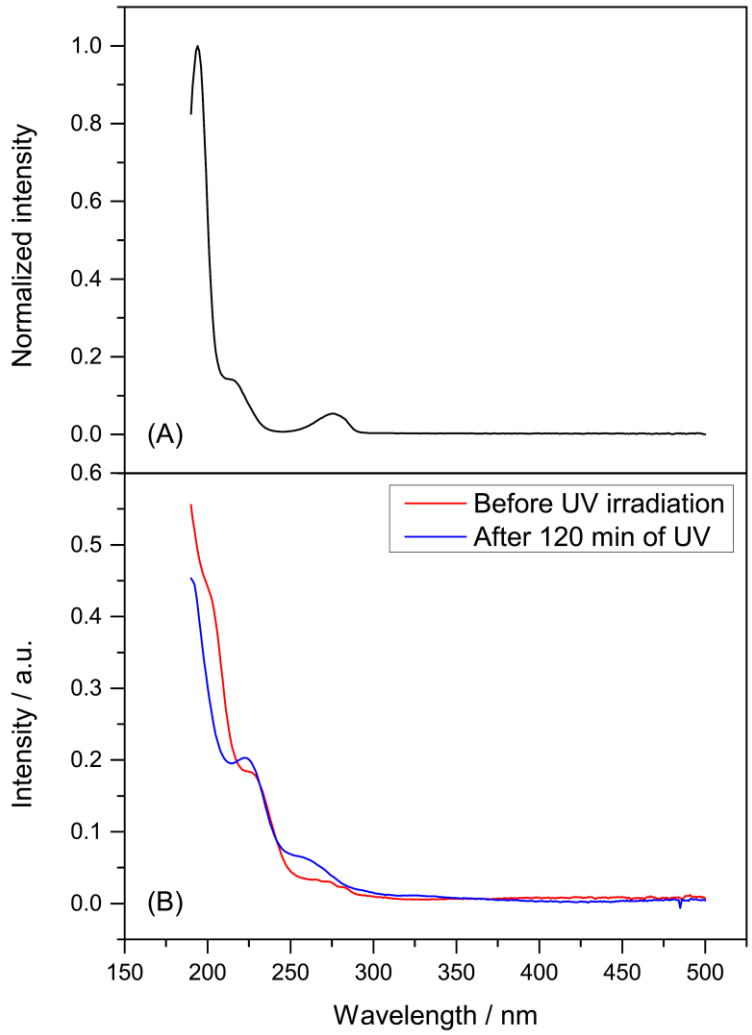

Figure C1. UV spectra of (A) DHB and (B) PAG aqueous solution at pH 7.0. PAG spectra were obtained before and after UV irradiation of 120 min.

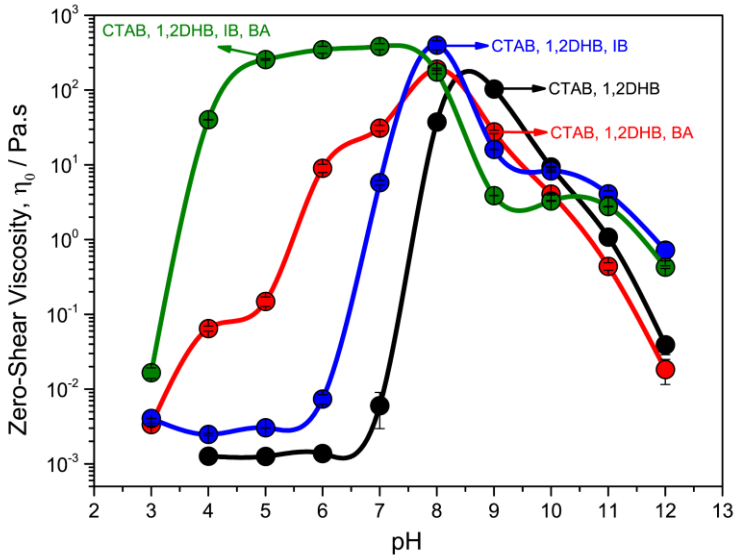

Figure C2. Zero-shear viscosity in Pa s as function of solution pH without irradiation considering the initial and final scenario of irradiation and the influence of each photolysis products in the solution viscosity. The lines are only guide for the eyes. $[CTAB] = [DHB] = 50\ mmol\ L^{-1}$ and $[IB] = [BA] = 10\ mmol\ L^{-1}$ and the average values were obtained from at least a duplicate.

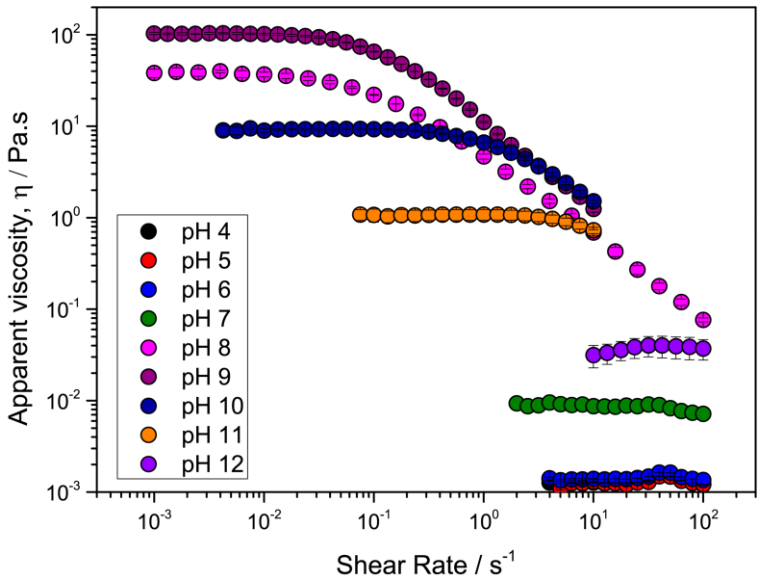

Figure C3. Apparent viscosity as function of shear rate for the solution containing CTAB/DHB in different pH. $[CTAB] = [DHB] = 50.0\ mmol\ L^{-1}$. Values were obtained from at least a duplicate.

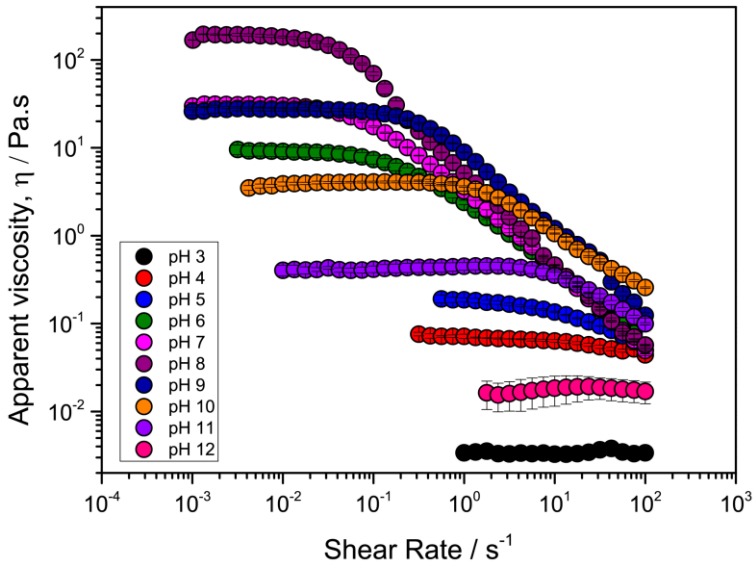

Figure C4. Apparent viscosity as function of shear rate for the solution containing CTAB/DHB/BA in different pH. $[CTAB] = [DHB] = 50.0\ mmol\ L^{-1}$, $[BA] = 10.0\ mmol\ L^{-1}$. Values were obtained from at least a duplicate.

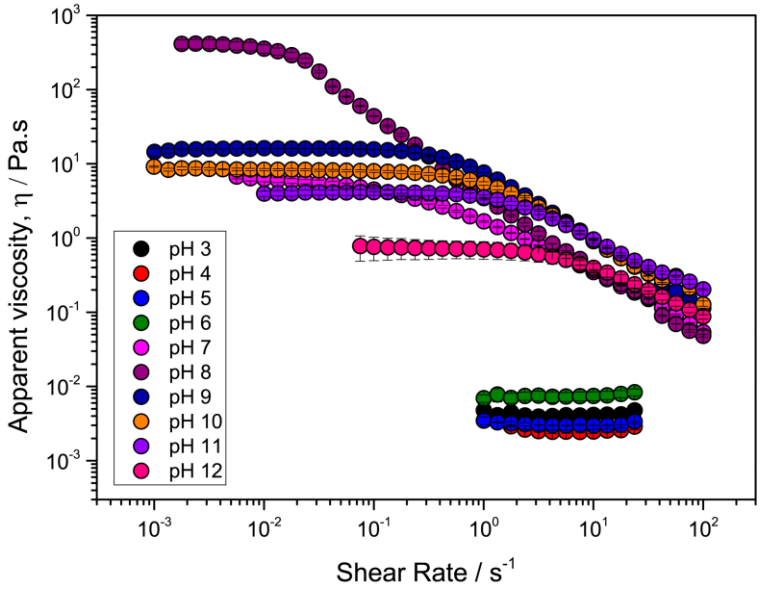

Figure C5. Apparent viscosity as function of shear rate for the solution containing CTAB/DHB/IB in different pH. $[CTAB] = [DHB] = 50.0\ mmol\ L^{-1}$, $[IB] = 10.0\ mmol\ L^{-1}$. Values were obtained from at least a duplicate.

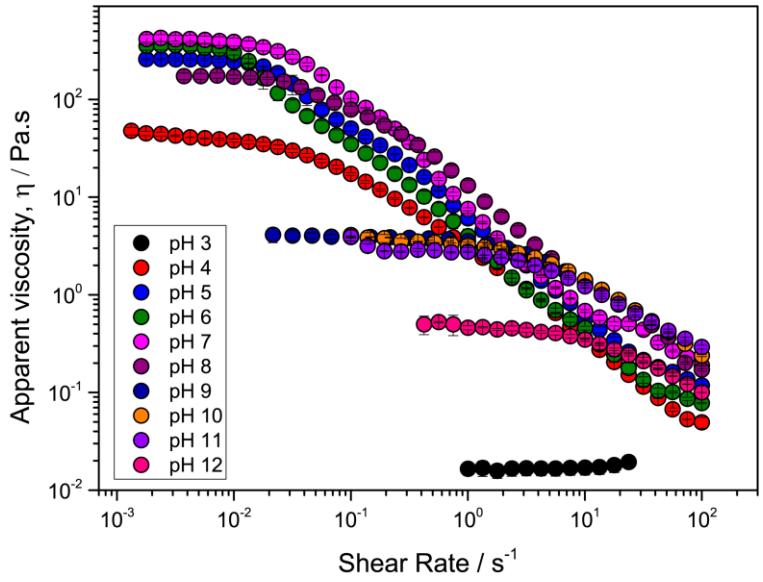

Figure C6. Apparent viscosity as function of shear rate for the solution containing CTAB/DHB/BA/IB in different pH. $[CTAB] = [DHB] = 50.0\ mmol\ L^{-1}$, $[BA] = [IB] = 10.0\ mmol\ L^{-1}$. Values were obtained from at least a duplicate.

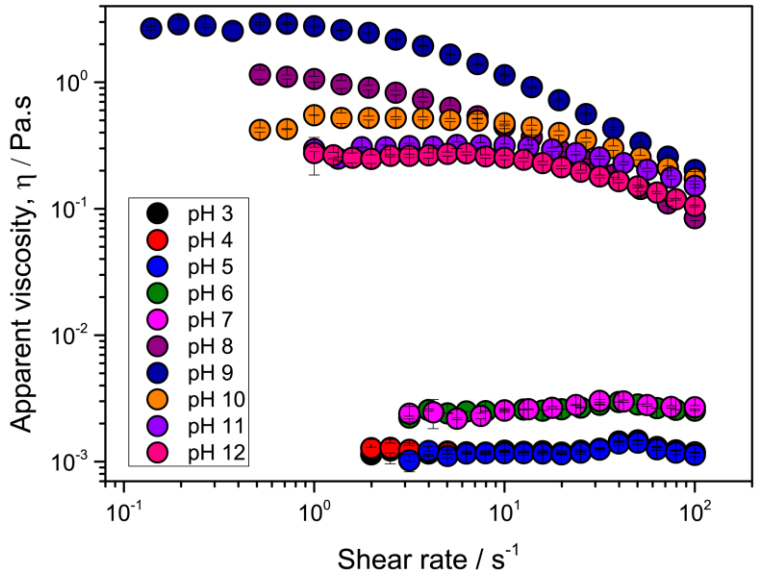

Figure C7. Apparent viscosity as function of shear rate for the solution containing CTAB/DHB/PAG in different pH. $[CTAB] = [DHB] = 50.0\ mmol\ L^{-1}$, $[PAG] = 10.0\ mmol\ L^{-1}$. Values were obtained from at least a duplicate.

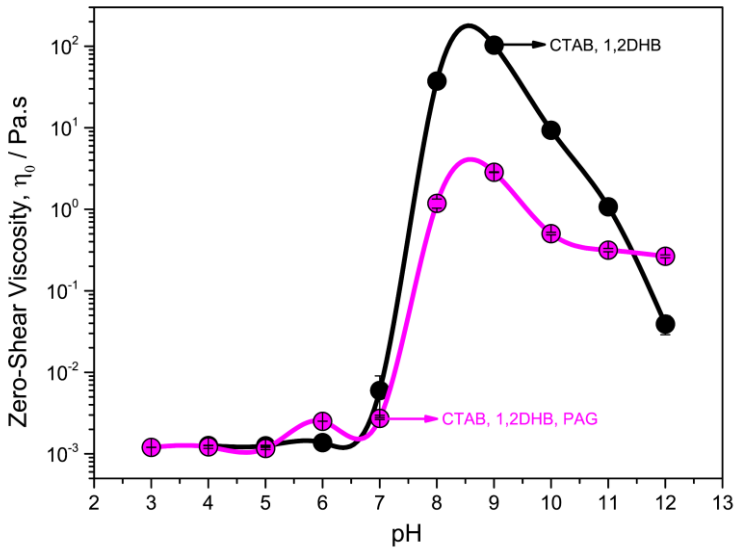

Figure C8. Influence of the PAG in the solution viscosity of CTAB/DHB in different pHs. $[CTAB] = [DHB] = 50\ mmol\ L^{-1}$ and $[PAG] = 10\ mmol\ L^{-1}$. The lines are only guide for the eyes and the values were obtained from at least a duplicate.

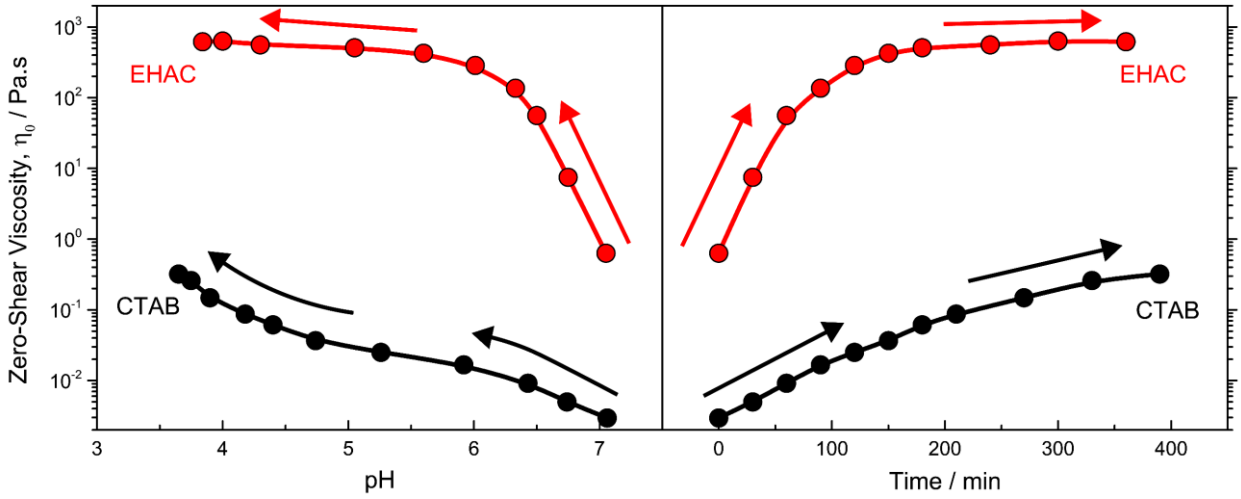

Figure C9. Zero-shear viscosity of the solution containing CTAB or EHAC, DHB and PAG as function of pH and UV irradiation time. $[CTAB] = [EHAC] = [DHB] = 50\ mmol\ L^{-1}$. $[PAG]_o = 10\ mmol\ L^{-1}$ for CTAB solutions and $[PAG]_0 = 15\ mmol\ L^{-1}$ for the EHAC solutions.

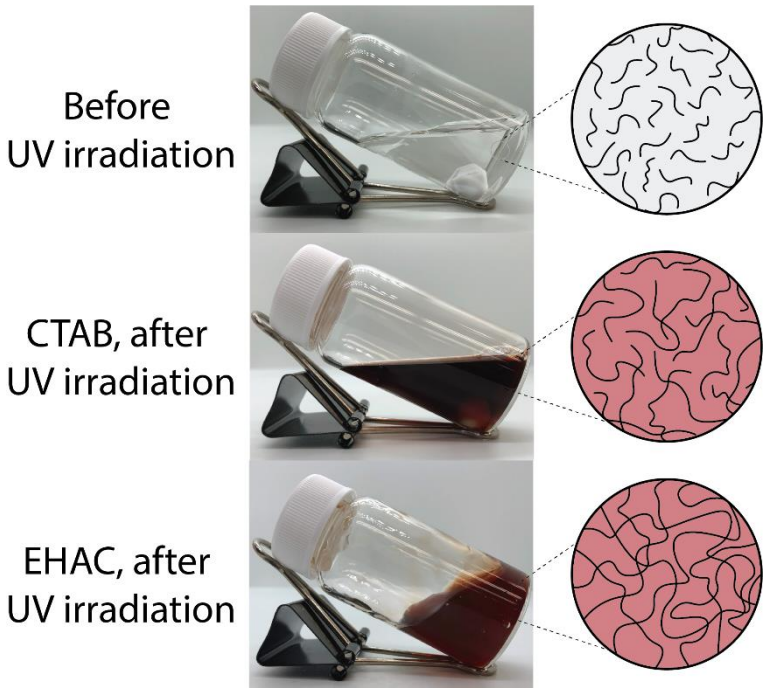

Figure C10. Changes on the solution appearance before and after UV irradiation. The solution contains CTAB or EHAC, DHB and PAG with initial pH 7.0 ± 0.1. $[CTAB] = [EHAC] = [DHB] = 50\ mmol\ L^{-1}$. $[PAG]_o = 10\ mmol\ L^{-1}$ for CTAB and $[PAG]_o = 15\ mmol\ L^{-1}$ for EHAC.

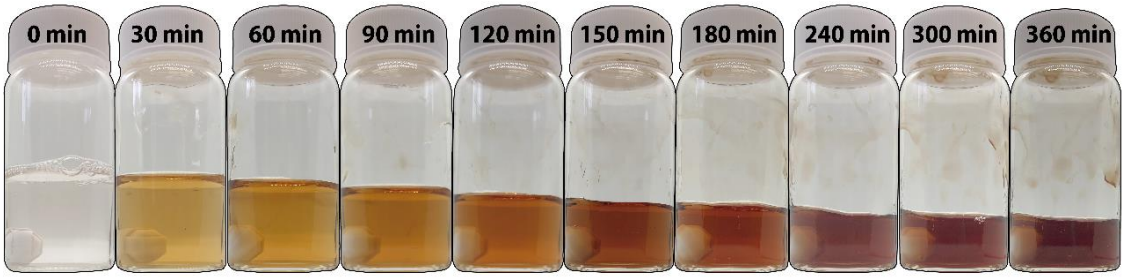

Figure C11. Changes on the solution appearance after shinning UV light with different times. The solution contains EHAC, DHB and PAG with initial pH 7.0 ± 0.1. $[EHAC] = [DHB] = 50\ mmol\ L^{-1}$ and $[PAG]_o = 15\ mmol\ L^{-1}$. The decrease in the volume of the solution occurs by sampling $0.50\ mL$ for the rheological analysis at each UV irradiation time.

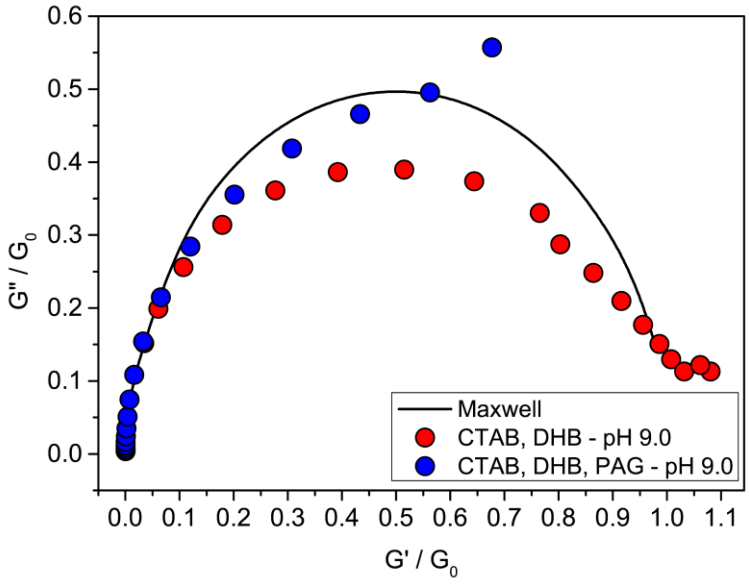

Figure C12. Cole-Cole plot for the solutions containing CTAB + DHB (red circles) and CTAB + DHB + PAG (blue circles) at $pH\ 9.0$ without UV irradiation. The continuous black line is the result expected for a Maxwellian fluid. $[CTAB] = [DHB] = 50\ mmol\ L^{-1}$ and $[PAG] = 10\ mmol\ L^{-1}$.

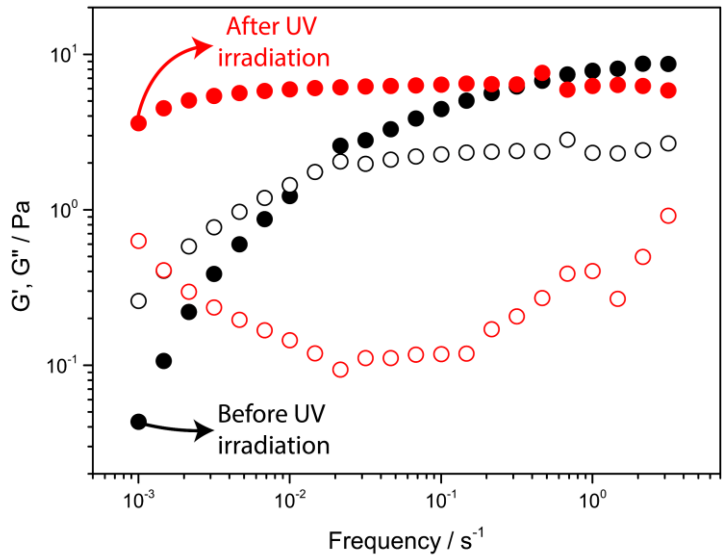

Figure C13. Elastic (*G*′, filled symbols) and viscous (*G*″, empty symbols) moduli as functions of frequency for a solution containing EHAC, DHB and PAG before (black symbols) and after (red symbols) UV irradiation for $2\ h$. The initial and final pH were 7.5 and 4.0. [EHAC] = [DHB] = $50.0\ mmol\ L^{-1}$ and [PAG] = $10.0\ mmol\ L^{-1}$.

Appendix D Behavior of pH-responsive wormlike micelles in the presence of alkyl alcohols as cosurfactants

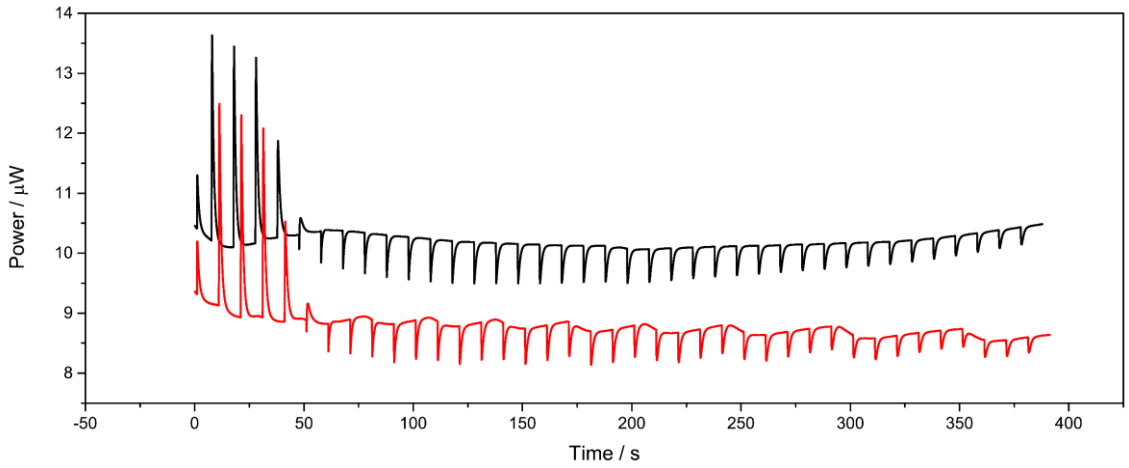

Figure D1. Differential electric power in μW as function of time for two titrations of $C_{14}TAB$ $40.0\ mmol\ L^{-1}$ in a reaction cell containing phthalic acid $5.0\ mmol\ L^{-1}$ at pH 2.0 ± 0.1.

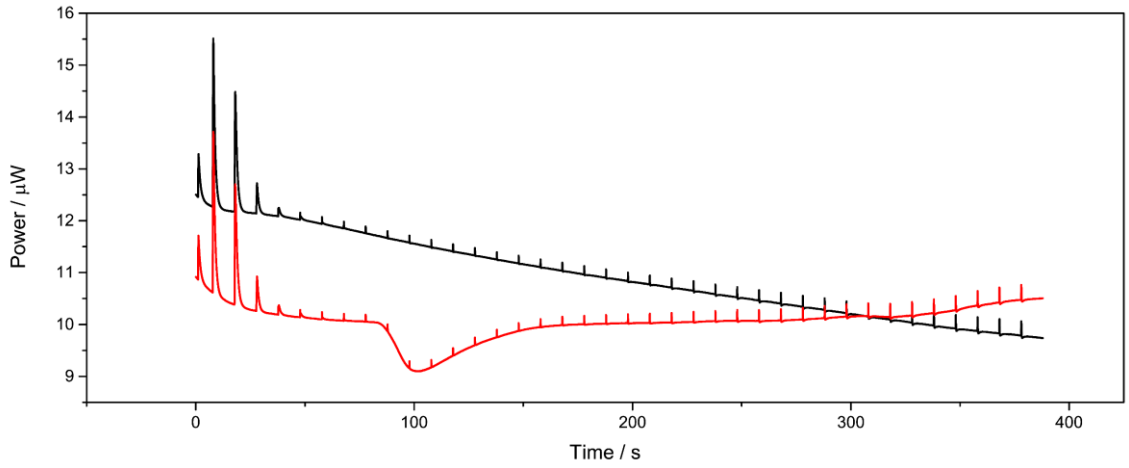

Figure D2. Differential electric power in μW as function of time for two titrations of $C_{14}TAB$ $40.0\ mmol\ L^{-1}$ in a reaction cell containing phthalic acid $5.0\ mmol\ L^{-1}$ at pH 3.0 ± 0.1.

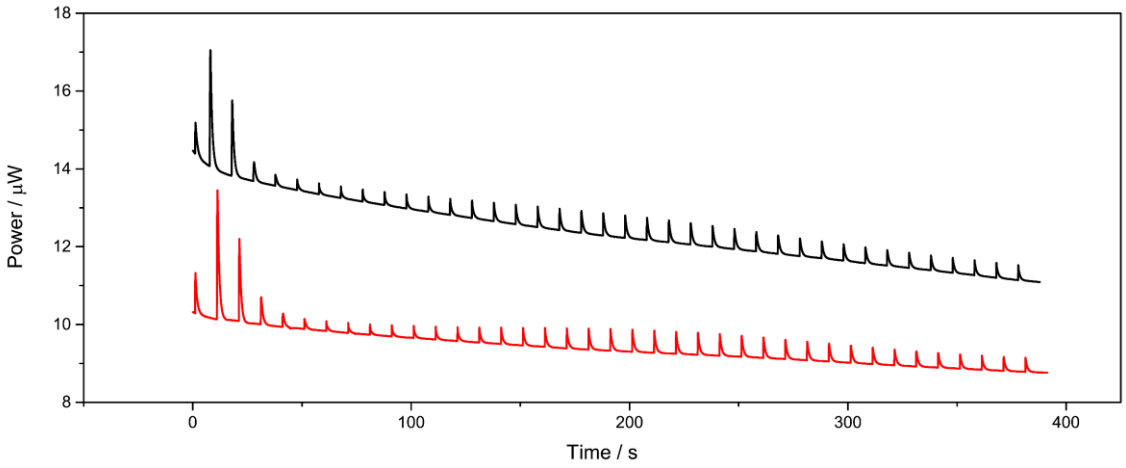

Figure D3. Differential electric power in μW as function of time for two titrations of C_{14}TAB $40.0\ mmol\ L^{-1}$ in a reaction cell containing phthalic acid $5.0\ mmol\ L^{-1}$ at pH 4.0 ± 0.1.

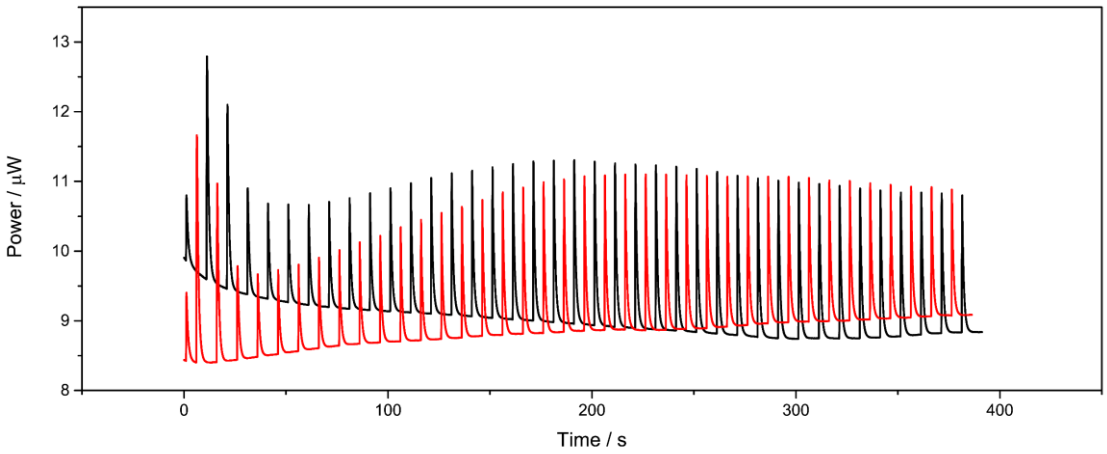

Figure D4. Differential electric power in μW as function of time for two titrations of C_{14}TAB $40.0\ mmol\ L^{-1}$ in a reaction cell containing phthalic acid $5.0\ mmol\ L^{-1}$ at pH 5.0 ± 0.1.

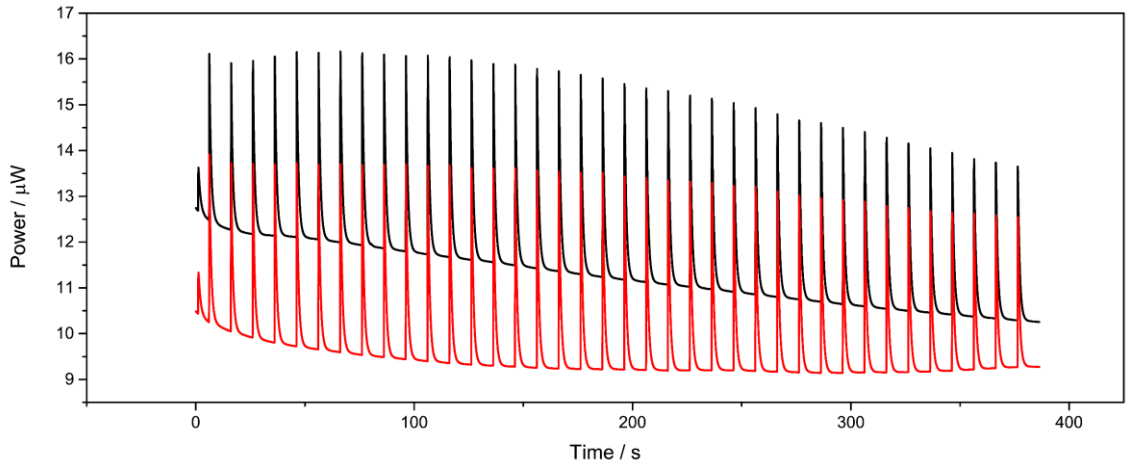

Figure D5. Differential electric power in μW as function of time for two titrations of C_{14}TAB $40.0\ mmol\ L^{-1}$ in a reaction cell containing phthalic acid $5.0\ mmol\ L^{-1}$ at pH 6.0 ± 0.1.

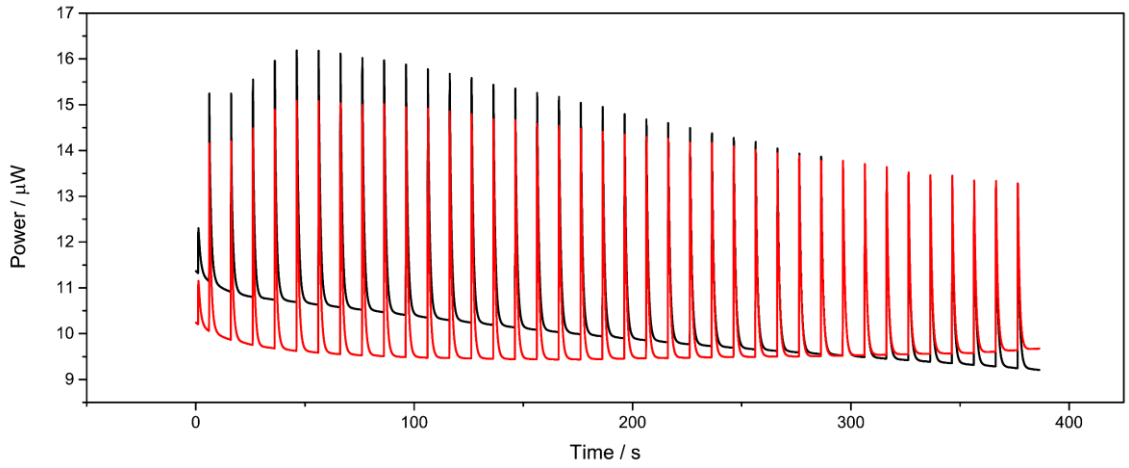

Figure D6. Differential electric power in μW as function of time for two titrations of C_{14}TAB $40.0\ mmol\ L^{-1}$ in a reaction cell containing phthalic acid $5.0\ mmol\ L^{-1}$ at pH 7.0 ± 0.1.

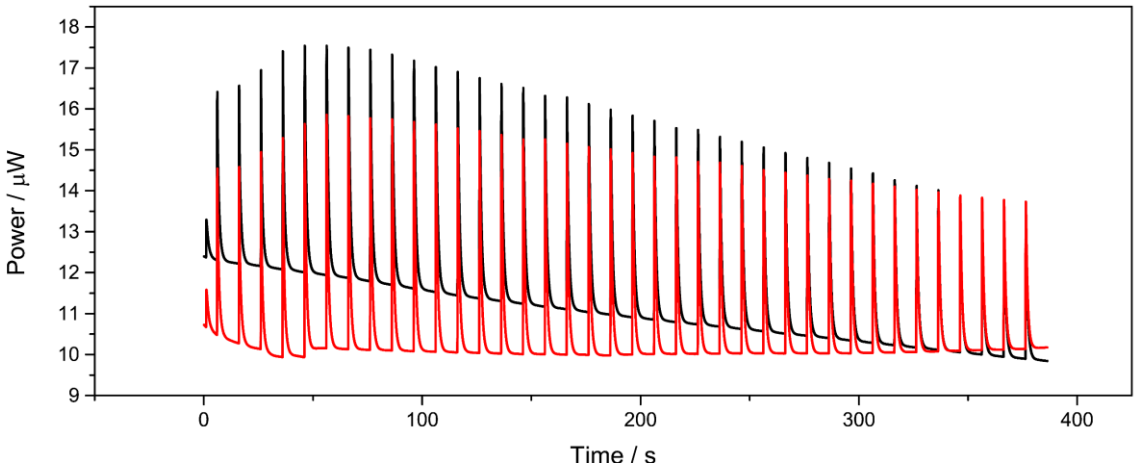

Figure D7. Differential electric power in μW as function of time for two titrations of C_{14}TAB $40.0\ mmol\ L^{-1}$ in a reaction cell containing phthalic acid $5.0\ mmol\ L^{-1}$ at pH 8.0 ± 0.1.

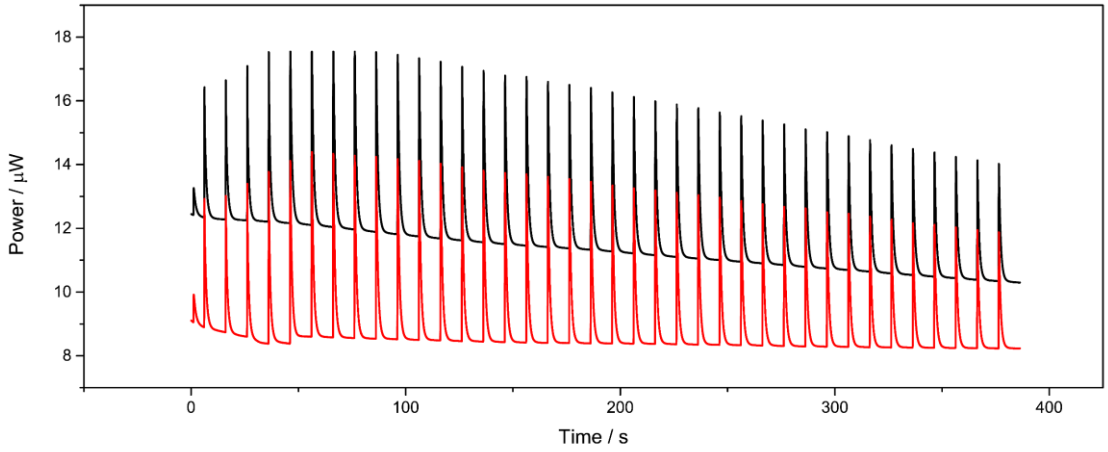

Figure D8. Differential electric power in μW as function of time for two titrations of C_{14}TAB $40.0\ mmol\ L^{-1}$ in a reaction cell containing phthalic acid $5.0\ mmol\ L^{-1}$ at pH 9.0 ± 0.1.

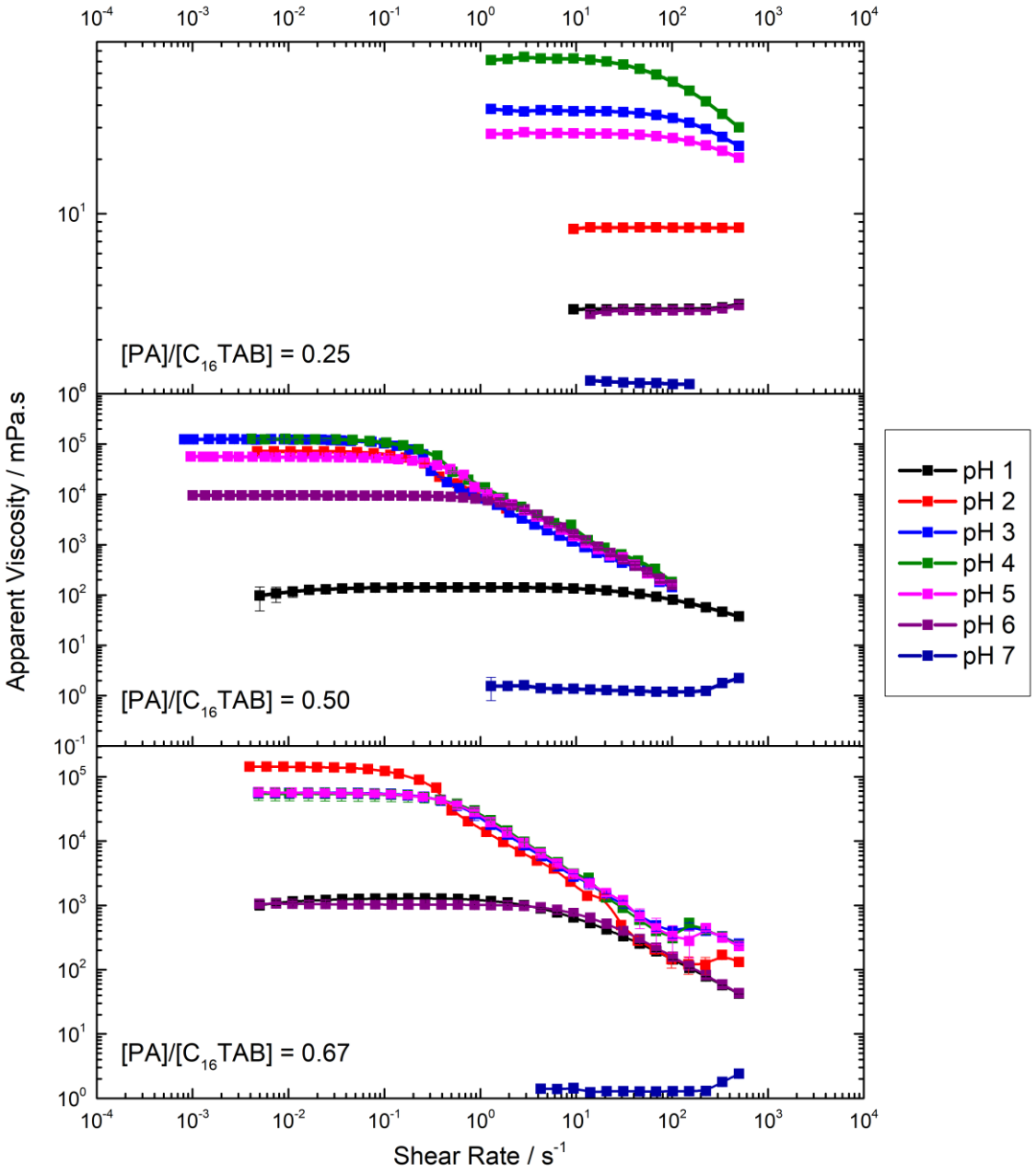

Figure D9. Flow curves for the solutions containing phthalic acid and C16TAB in different proportions fixing $[C_{16}TAB] = 100.0\ mmol\ L^{-1}$ in different solution pH. The lines are only guide for the eyes and the values were obtained from at least a duplicate

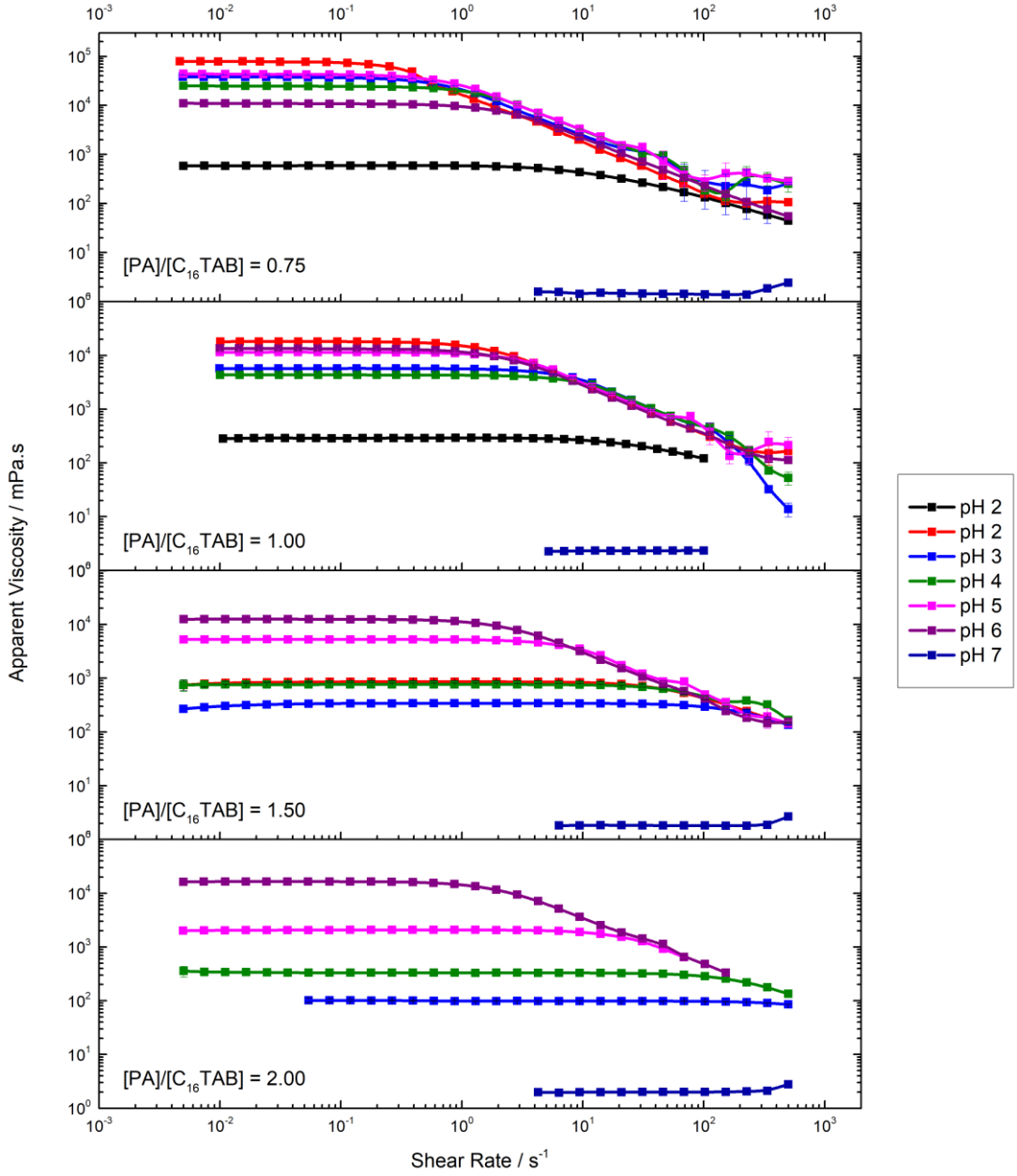

Figure D10. Flow curves for the solutions containing phthalic acid and C_{16}TAB in different proportions fixing $[C_{16}TAB] = 100.0\ mmol\ L^{-1}$ in different solution pH. The lines are only guide for the eyes and the values were obtained from at least a duplicate.

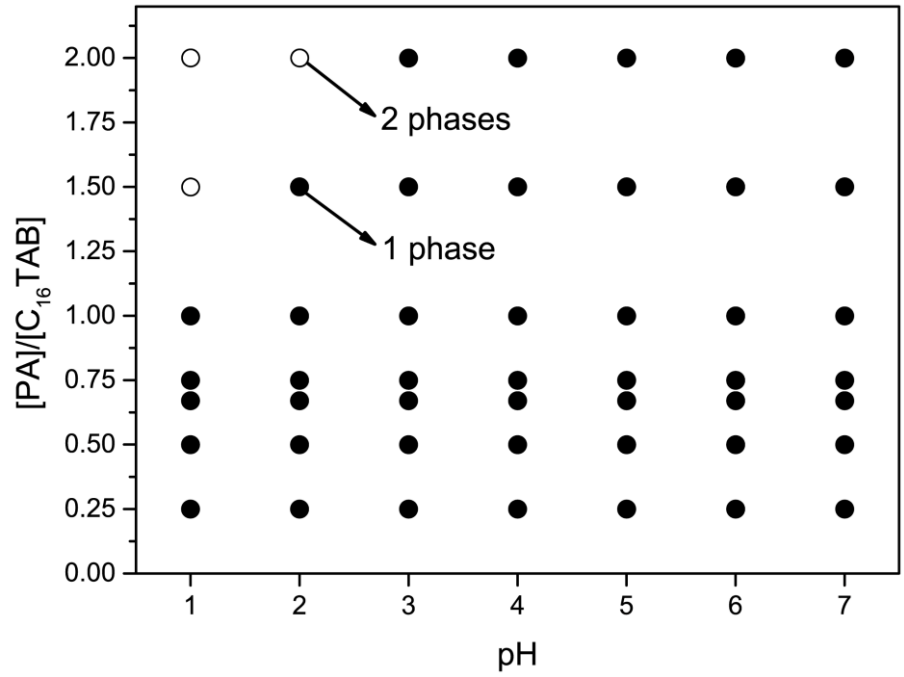

Figure D11. Phase diagram for the solution containing phthalic acid and C_{16}TAB in different proportions and solution pH. C_{16}TAB was fixed at $100.0\ mmol\ L^{-1}$.

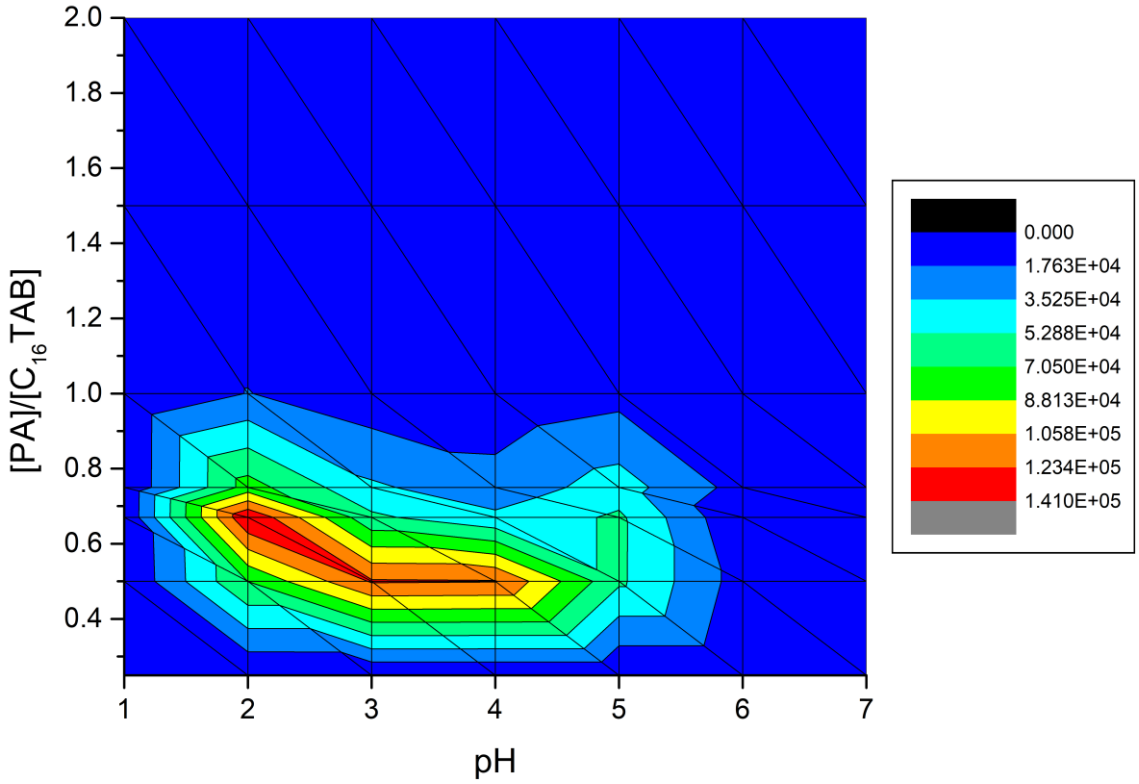

Figure D12. Contour map showing the influence of the [PA]/[C_{16}TAB] ratio and the solution pH for the solution viscosity. The [C_{16}TAB] was fixed at $100.0\ mmol\ L^{-1}$ and the values were obtained from at least a duplicate.

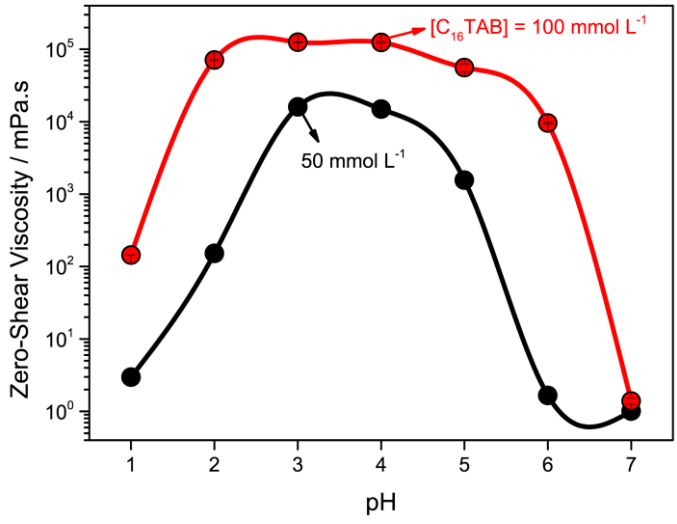

Figure D13. Zero-shear viscosity as function of the solution pH for [PA]/[C_{16}TAB] = 0.5 with $[C_{16}TAB] = 100.0\ mmol\ L^{-1}$ and $50.0\ mmol\ L^{-1}$. The lines are only guide for the eyes and the values were obtained from at least a duplicate.

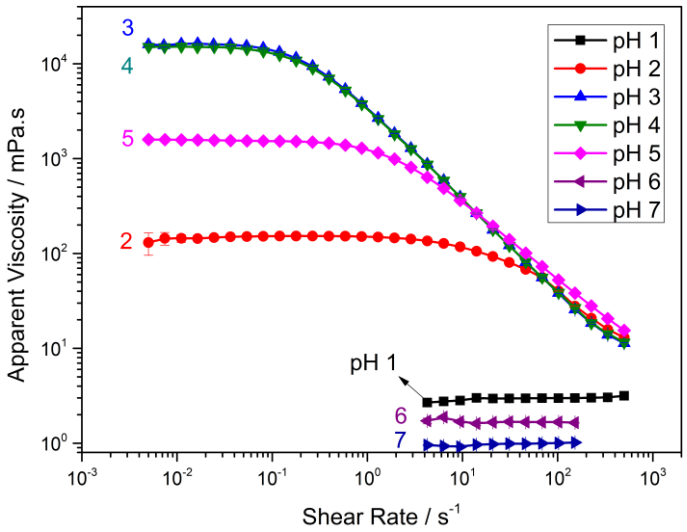

Figure D14. Flow curves for the solutions containing phthalic acid and C_{16}TAB in different solution pH fixing $[C_{16}TAB] = 50.0\ mmol\ L^{-1}$. The lines are only guide for the eyes and the values were obtained from at least a duplicate.

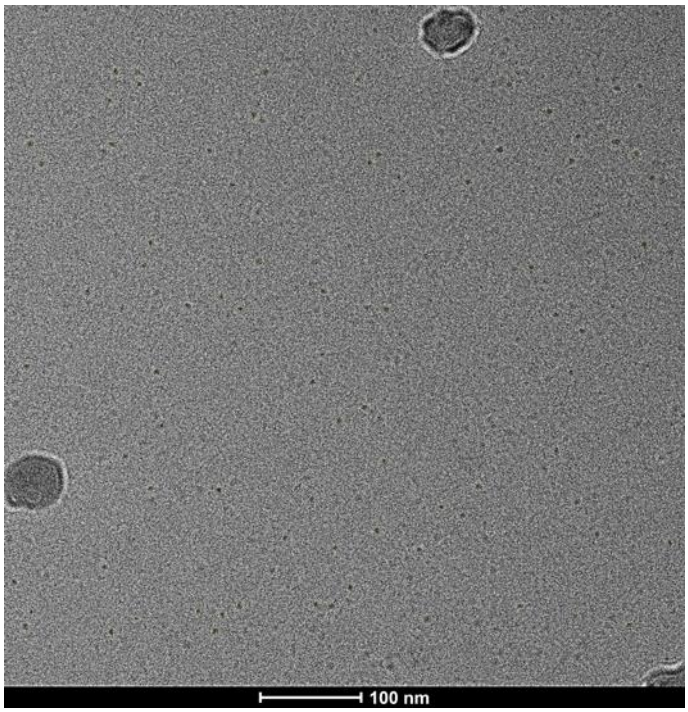

Figure D15. CRYO-TEM image of the solution containing $[PA]/[C_{16}TAB] = 0.5$ with $[C_{16}TAB] = 20.0\ mmol\ L^{-1}$ in pH 1.

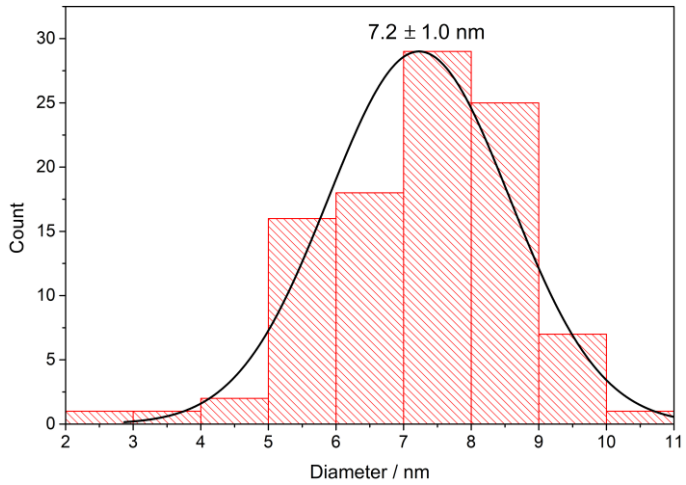

Figure D16. Diameter distribution of the micelle visualized in CRYO-TEM image of the solution containing $[PA]/[C_{16}TAB] = 0.5$ with $[C_{16}TAB] = 20.0\, mmol\, L^{-1}$ in pH 1. 100 micelles were counted.

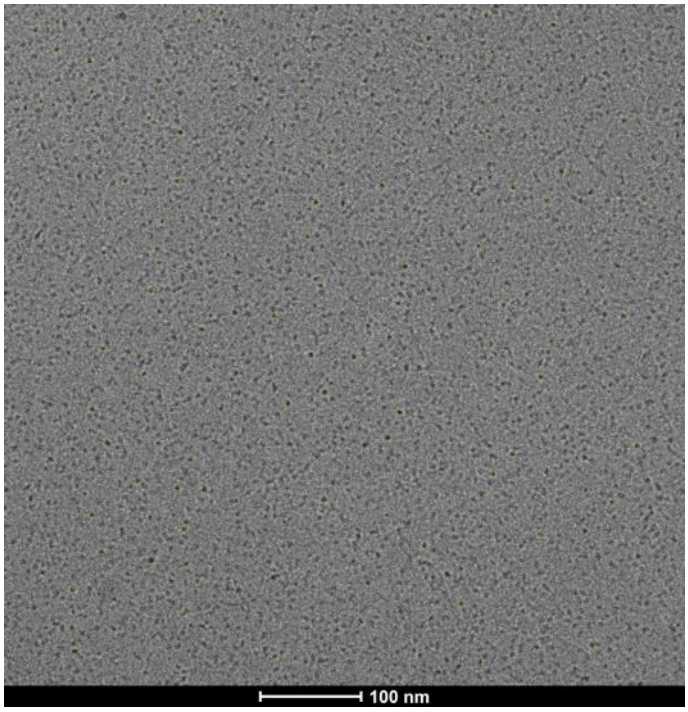

Figure D17. CRYO-TEM image of the solution containing $[PA]/[C_{16}TAB] = 0.5$ with $[C_{16}TAB] = 20.0\, mmol\, L^{-1}$ in pH 7.

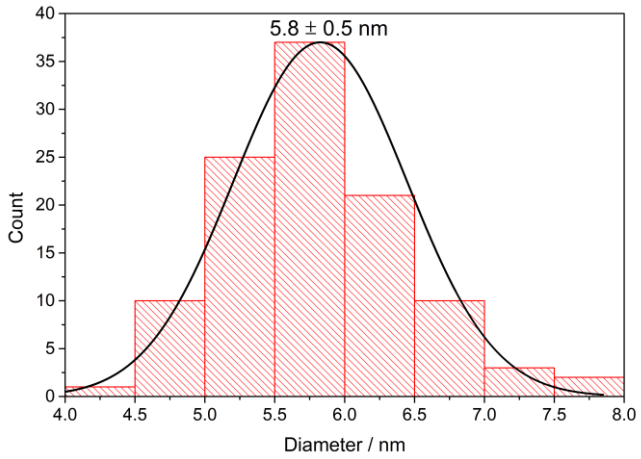

Figure D18. Diameter distribution of the micelle visualized in CRYO-TEM image of the solution containing $[PA]/[C_{16}TAB] = 0.5$ with $[C_{16}TAB] = 20.0\, mmol\, L^{-1}$ in pH 7. 109 micelles were counted.

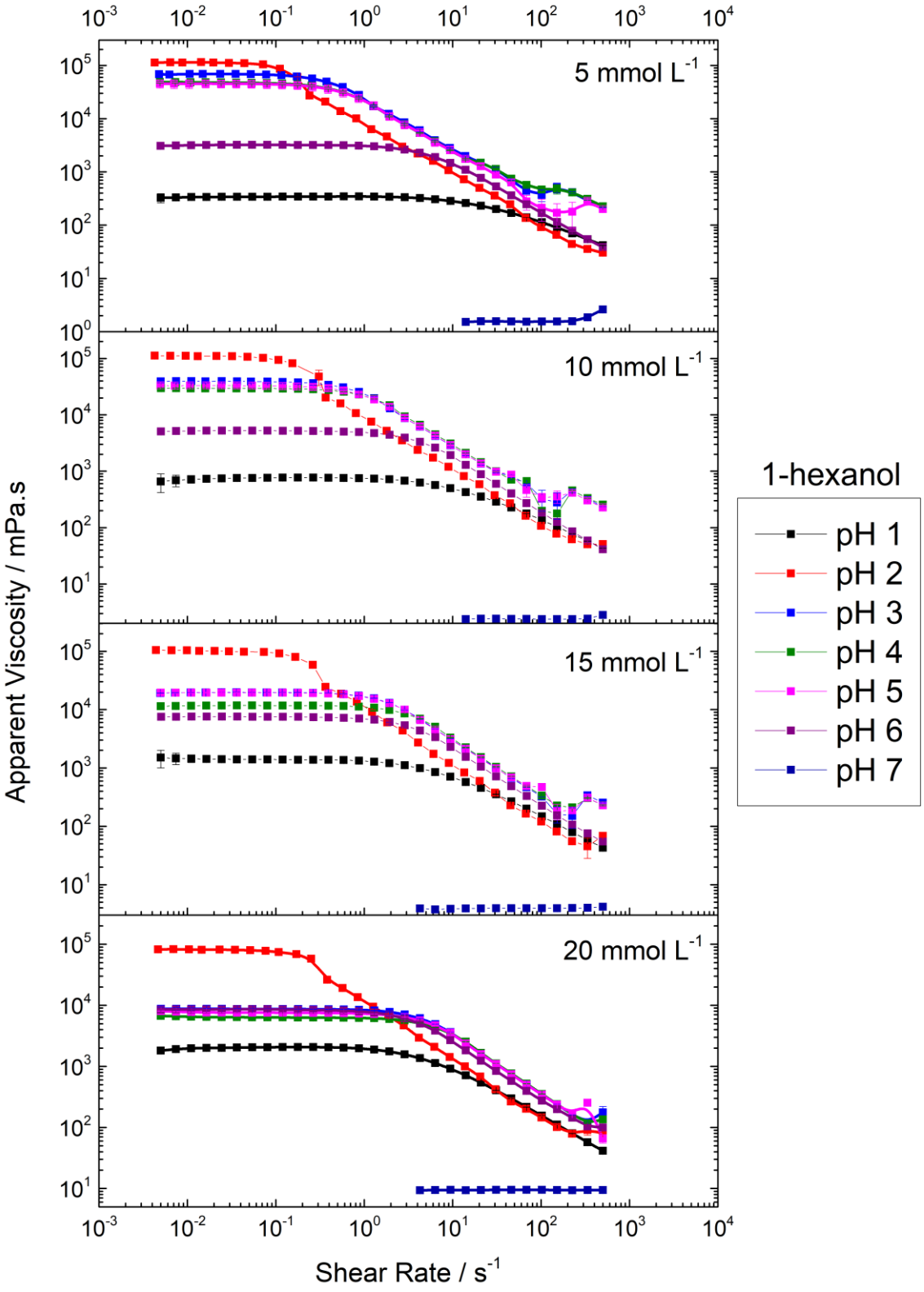

Figure D19. Flow curves for the solutions containing [PA]/[C_{16}TAB], with $[C_{16}TAB] = 100.0\ mmol\ L^{-1}$ and different concentration of hexanol and solution pH. The lines are only guide for the eyes and the values were obtained from at least a duplicate.

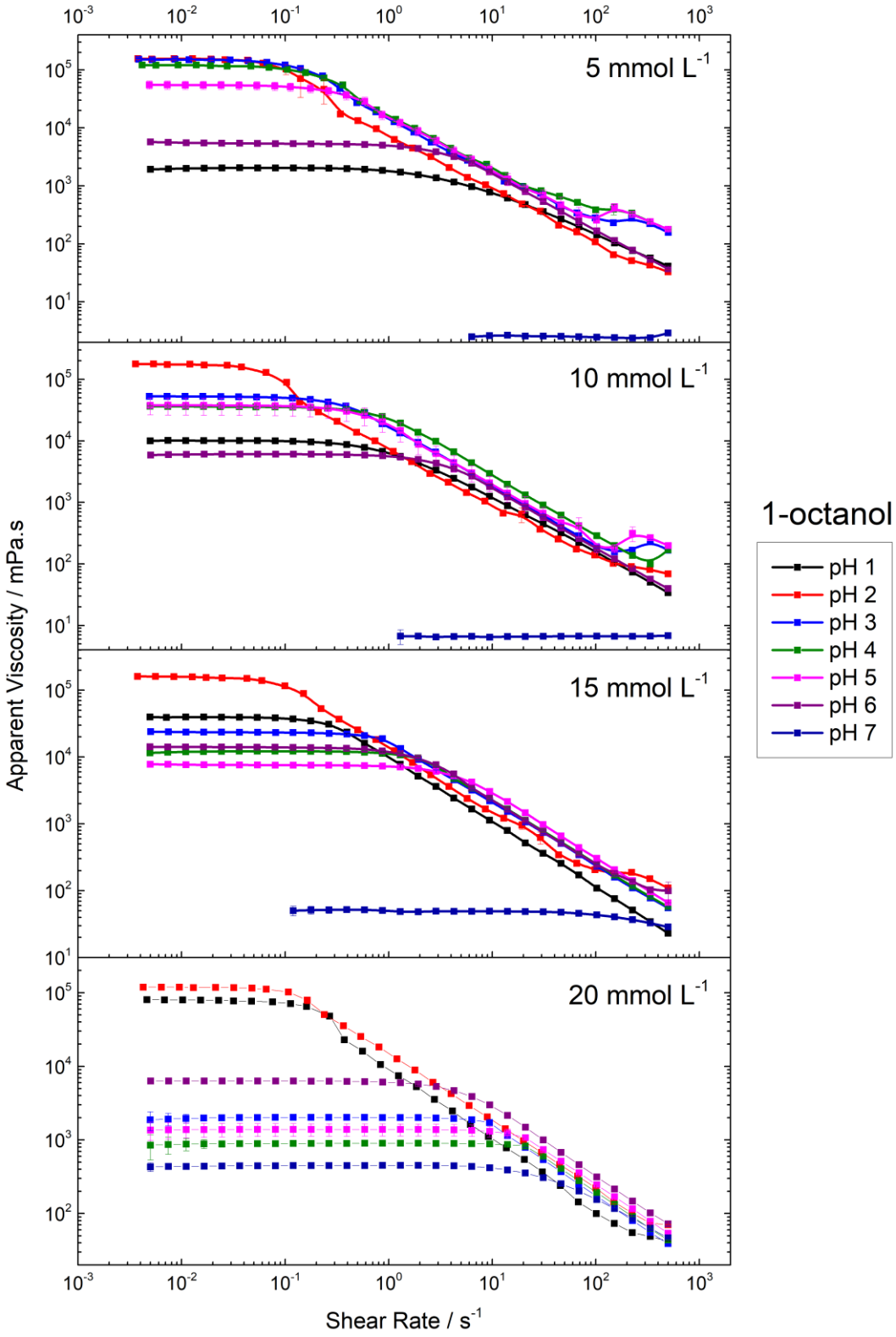

Figure D20. Flow curves for the solutions containing [PA]/[C_{16}TAB], with $[C_{16}TAB] = 100.0\ mmol\ L^{-1}$ and different concentration of octanol and solution pH. The lines are only guide for the eyes and the values were obtained from at least a duplicate.

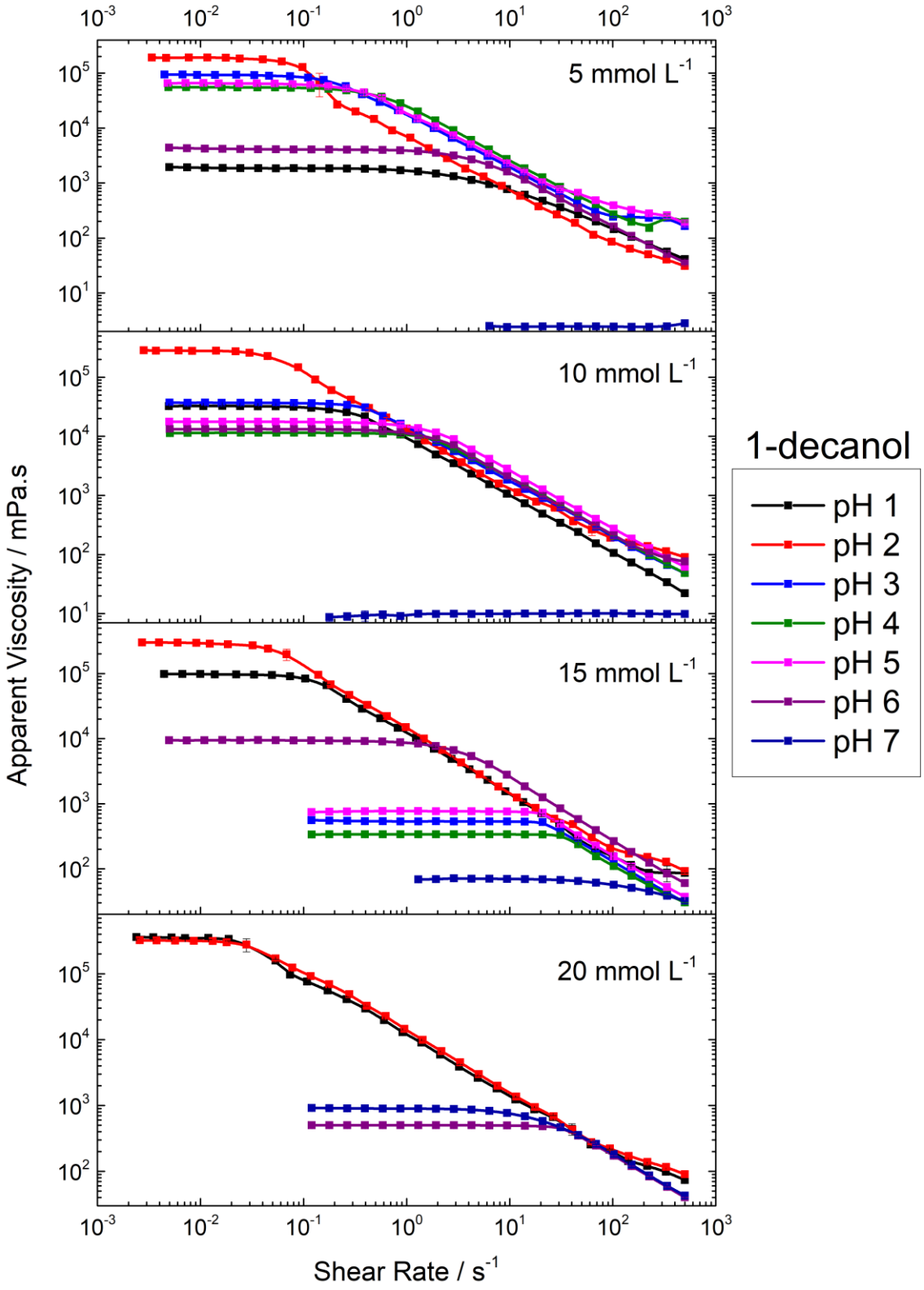

Figure D21. Flow curves for the solutions containing [PA]/[C_{16}TAB], with $[C_{16}TAB] = 100.0\ mmol\ L^{-1}$ and different concentration of decanol and solution pH. The lines are only guide for the eyes and the values were obtained from at least a duplicate.

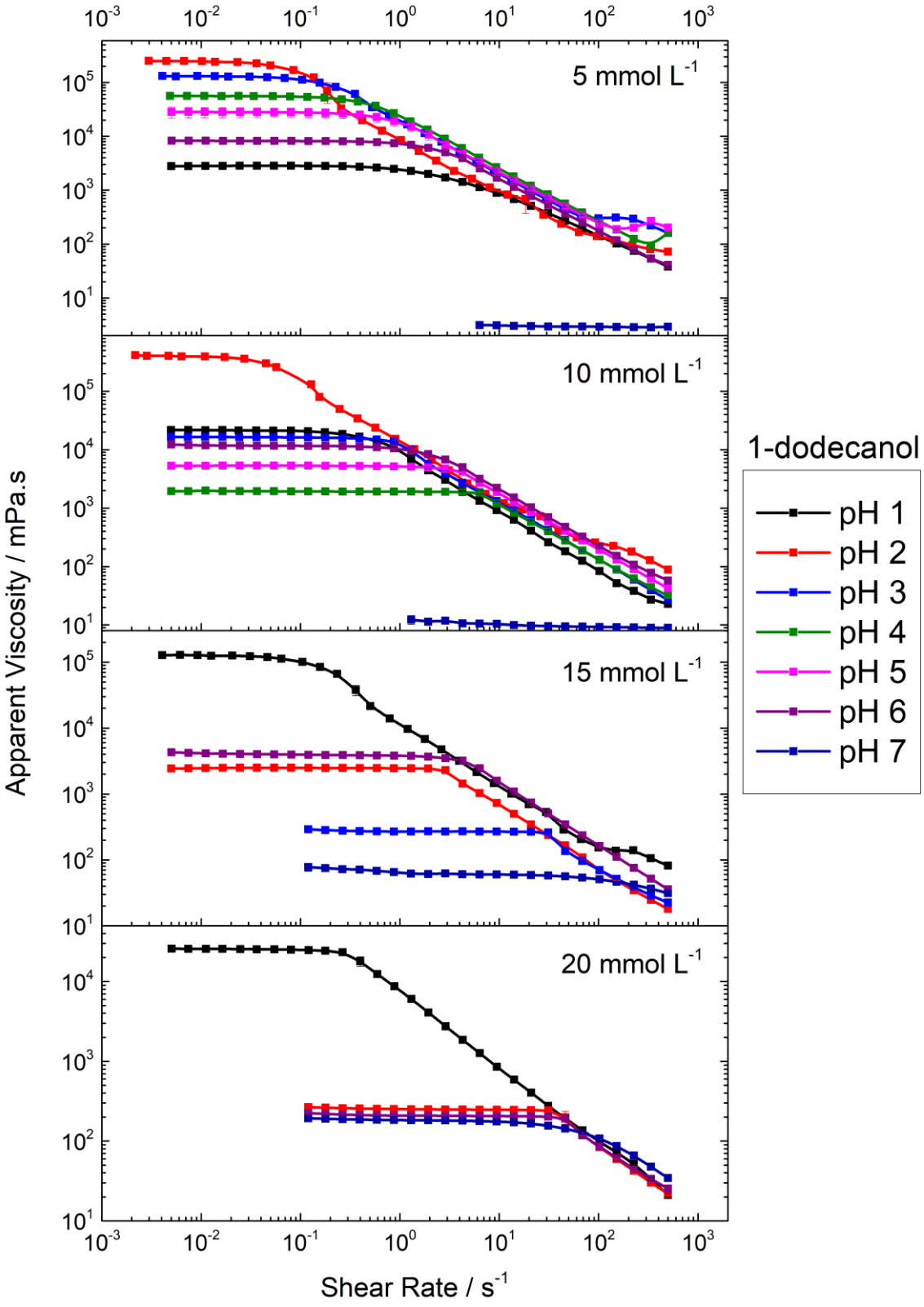

Figure D22. Flow curves for the solutions containing [PA]/[C_{16}TAB], with $[C_{16}TAB] = 100.0\ mmol\ L^{-1}$ and different concentration of dodecanol and solution pH. The lines are only guide for the eyes and the values were obtained from at least a duplicate.

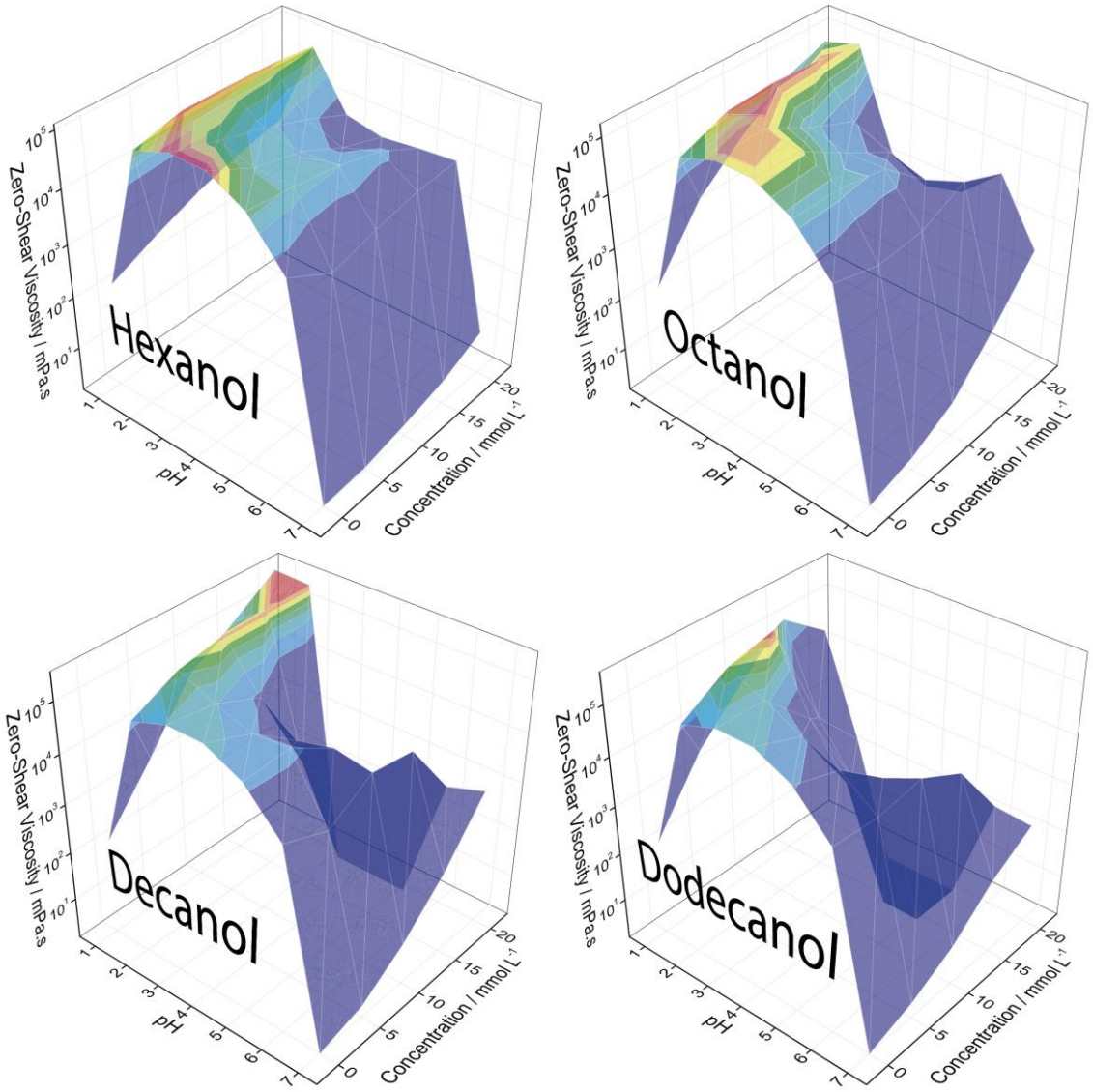

Figure D23. Surfaces showing the influence of the solution pH and alcohol concentration (hexanol, octanol, decanol and dodecanol) in the solution viscosity containing $[PA]/[C_{16}TAB] = 0.50$ with $[C_{16}TAB] = 100.0\ mmol\ L^{-1}$. The values were obtained from at least a duplicate.

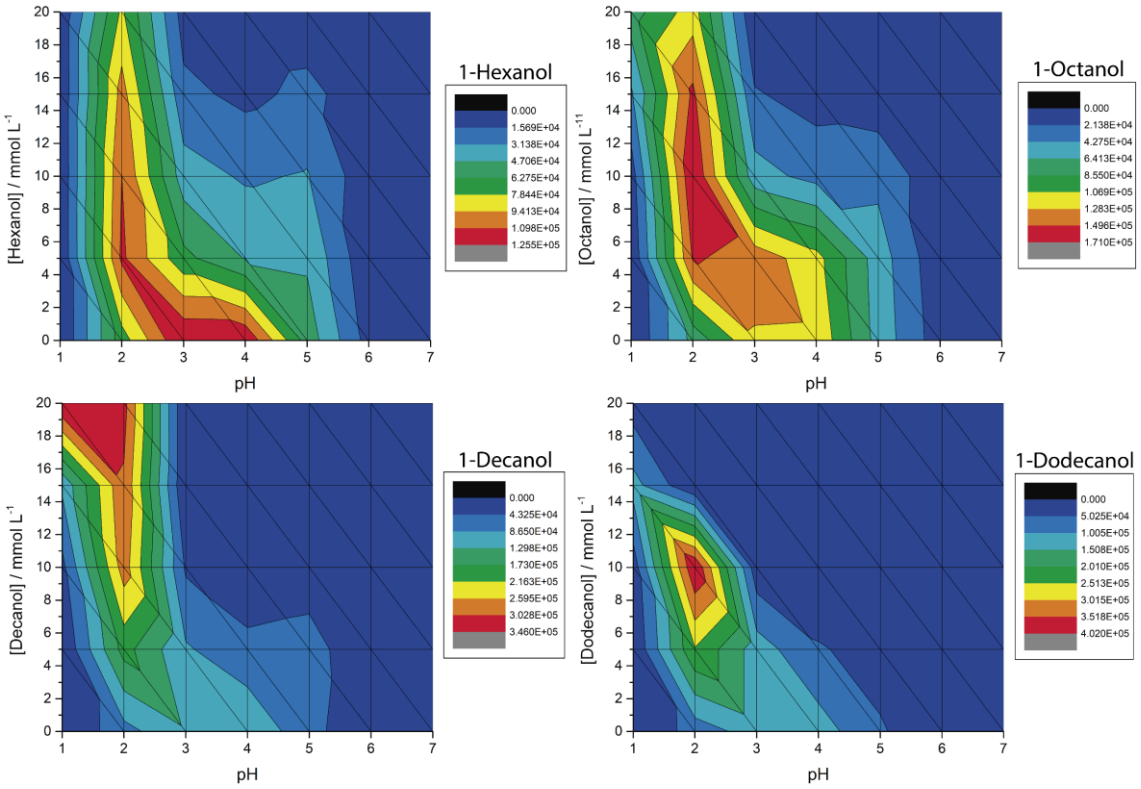

Figure D24. Contour maps for the solution viscosity as function of the alcohol concentration and solution pHs. The alcohols used were 1-hexanol, 1-octanol, 1-decanol and 1-dodecanol. The values were obtained from at least a duplicate.

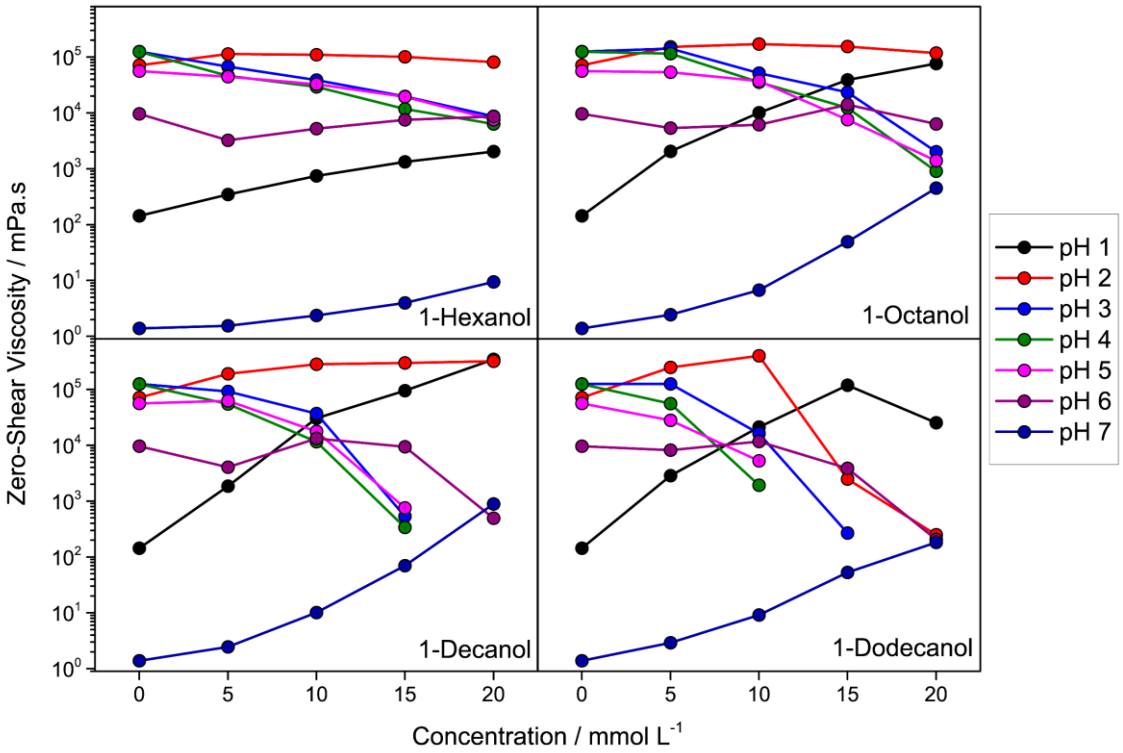

Figure D25. Zero-shear viscosity as function of the alcohol concentration for the solution containing $[PA]/[C_{16}TAB] = 0.50$, with $[C_{16}TAB] = 100.0\ mmol\ L^{-1}$ in different solution pH. The alcohols used were 1-hexagonal, 1-octanol, 1-decanol and 1-dodecanol. The lines are only guide for the eyes and the values were obtained from at least a duplicate.

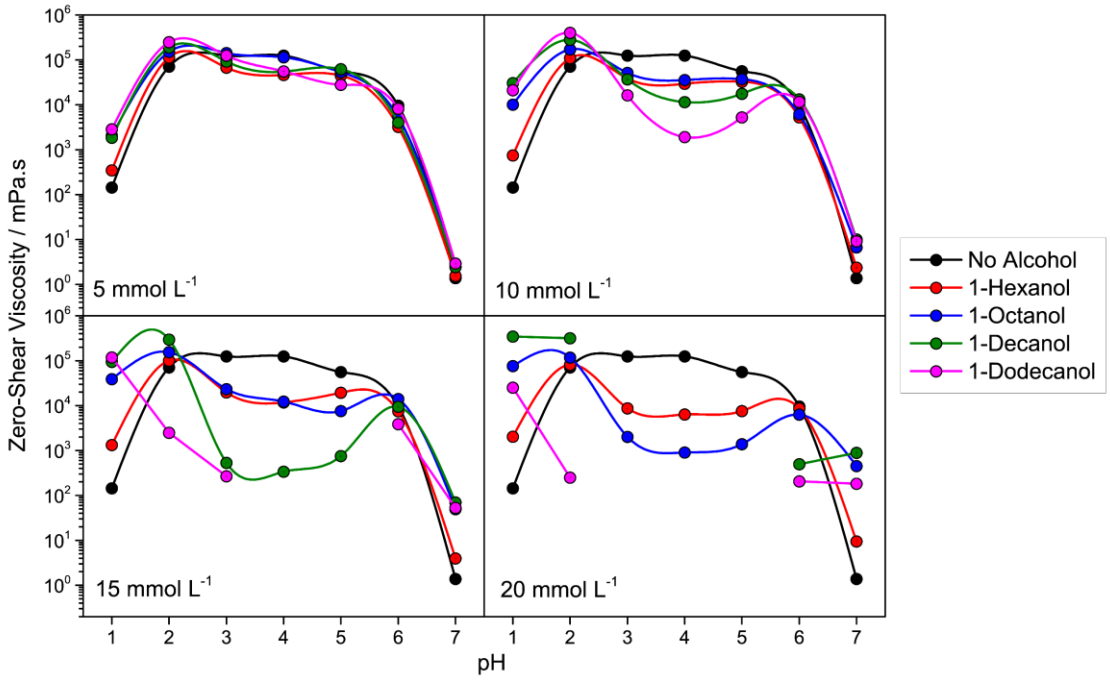

Figure D26. Zero-shear viscosity as function of the solution pH for the solution containing $[PA]/[C_{16}TAB] = 0.50$, with $[C_{16}TAB] = 100.0\, mmol\, L^{-1}$, in different alcohol concentrations. The alcohols used were 1-hexagonal, 1-octanol, 1-decanol and 1-dodecanol. The lines are only guide for the eyes and the values were obtained from at least a duplicate.

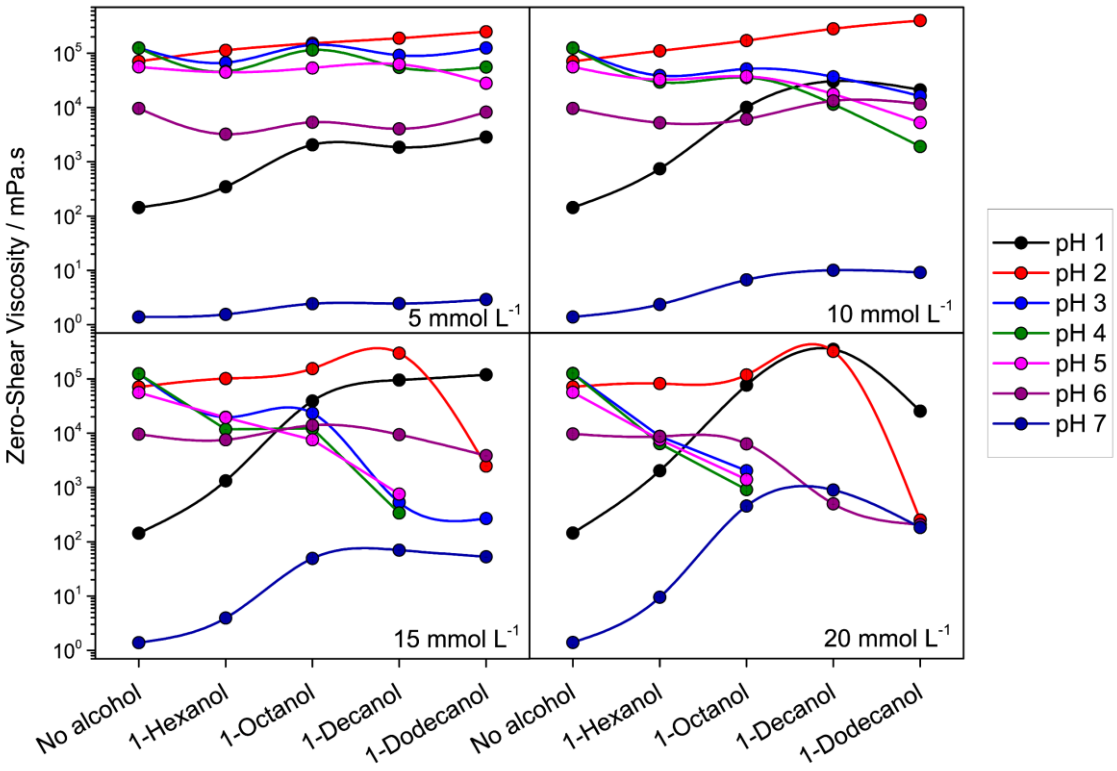

Figure D27. Zero-shear viscosity as function of alcohol added into the solution containing $[PA]/[C_{16}TAB] = 0.50$, with $[C_{16}TAB] = 100.0\, mmol\, L^{-1}$, in different alcohol concentrations and solution pH. The alcohols used were 1-hexagonal, 1-octanol, 1-decanol and 1-dodecanol. The lines are only guide for the eyes and the values were obtained from at least a duplicate.

Appendix E Static acid dissolution of carbonate outcrops investigated by time domain Nuclear Magnetic Resonance and X-ray tomography

Table E1. Volume (V) and surface area (S) for the carbonate outcrops before and after the acid dissolution with HCl (on the left) and HAc (on the right). The values were obtained by using µCT technique.

	HCl solution				HAc solution			
	Before dissolution		After dissolution		Before dissolution		After dissolution	
Rock	$V\ /\ mm^3$	$S\ /\ mm^2$	$V\ /\ mm^3$	$S\ /\ mm^2$	$V\ /\ mm^3$	$S\ /\ mm^2$	$V\ /\ mm^3$	$S\ /\ mm^2$
HPD	200.58	246.17	178.09	271.00	–	–	–	–
LPD	204.15	189.71	123.16	170.51	201.67	187.81	192.29	288.72
EDB	198.03	194.14	142.38	174.37	197.23	190.93	194.12	223.81
DP	198.68	228.83	131.12	175.67	189.29	201.07	144.81	237.53
EDW	199.78	218.17	136.44	152.52	199.24	199.42	162.08	286.74
IND	199.43	210.11	148.21	166.46	202.32	213.04	167.37	356.07

Table E2. Radii values calculated through the equations of volume (R_v) and surface (R_s) of a cylinder by using values presented in Table S1. The deformation parameter (d) is also presented. Values were calculated for samples before and after the acid dissolution in HCl.

HCl solution						
	Before dissolution			After dissolution		
Rock	R_v / mm	R_s / mm	d	R_v / mm	R_s / mm	d
HPD	3.49	4.16	0.16	3.29	4.45	0.26
LPD	3.52	3.46	0.02	2.73	3.21	0.15
EDB	3.47	3.52	0.02	2.94	3.26	0.10
DP	3.47	3.96	0.12	2.82	3.28	0.14
EDW	3.48	3.83	0.09	2.88	2.96	0.03
IND	3.48	3.73	0.07	3.00	3.15	0.05

Table E3. Radii values calculated through the equations of volume (R_v) and surface (R_s) of a cylinder by using values presented in Table S1. The deformation parameter (d) is also presented. Values were calculated for samples before and after the acid dissolution in HAc.

HAc solution						
	Before dissolution			After dissolution		
Rock	R_v / mm	R_s / mm	d	R_v / mm	R_s / mm	d
HPD	–	–	–	–	–	–
LPD	3.50	3.44	0.02	3.41	4.64	0.26
EDB	3.46	3.48	0.01	3.43	3.90	0.12
DP	3.39	3.61	0.06	2.96	4.06	0.27
EDW	3.48	3.59	0.03	3.13	4.62	0.32
IND	3.50	3.76	0.07	3.19	5.35	0.40

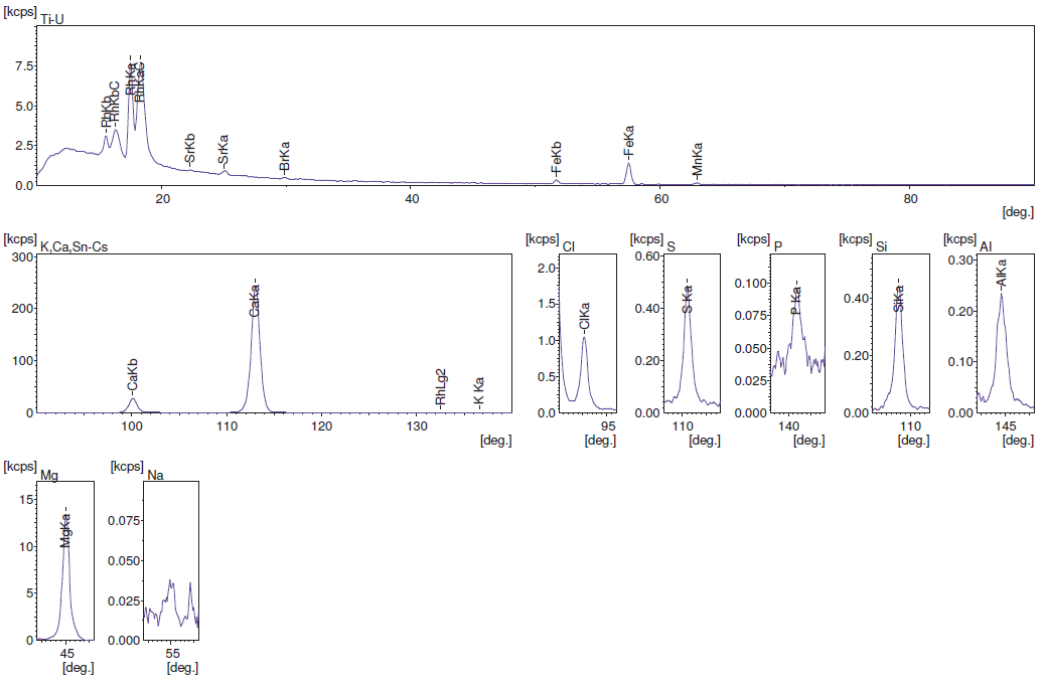

Figure E1. X-ray fluorescence spectrum of Silurian Dolomite (high permeability), HPD.

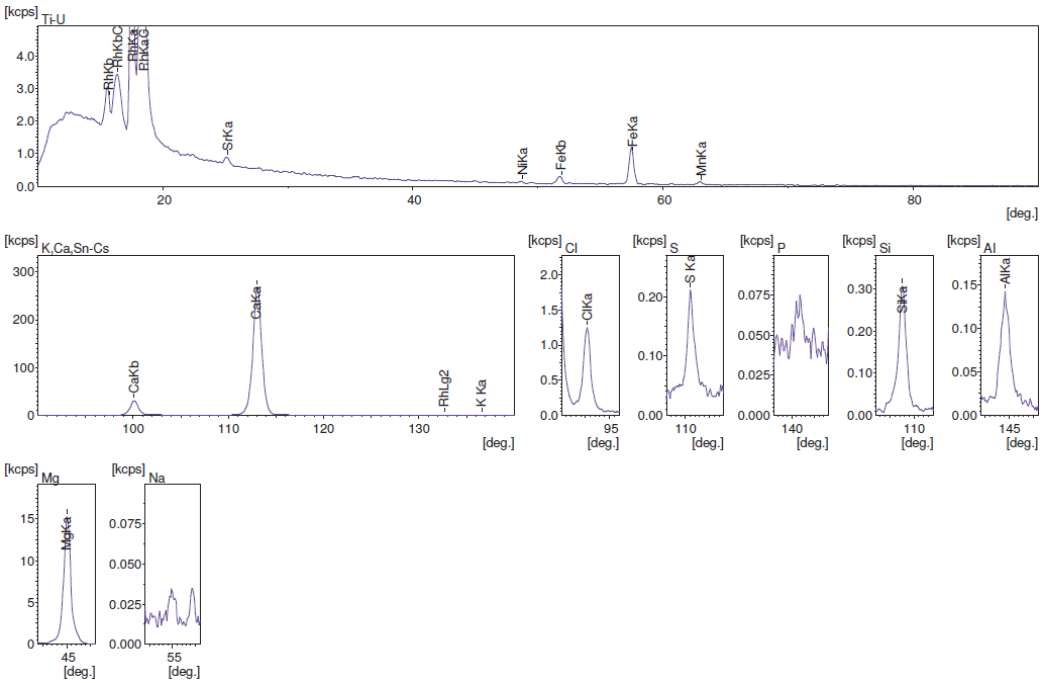

Figure E2. X-ray fluorescence spectrum of Silurian Dolomite (low permeability), LPD.

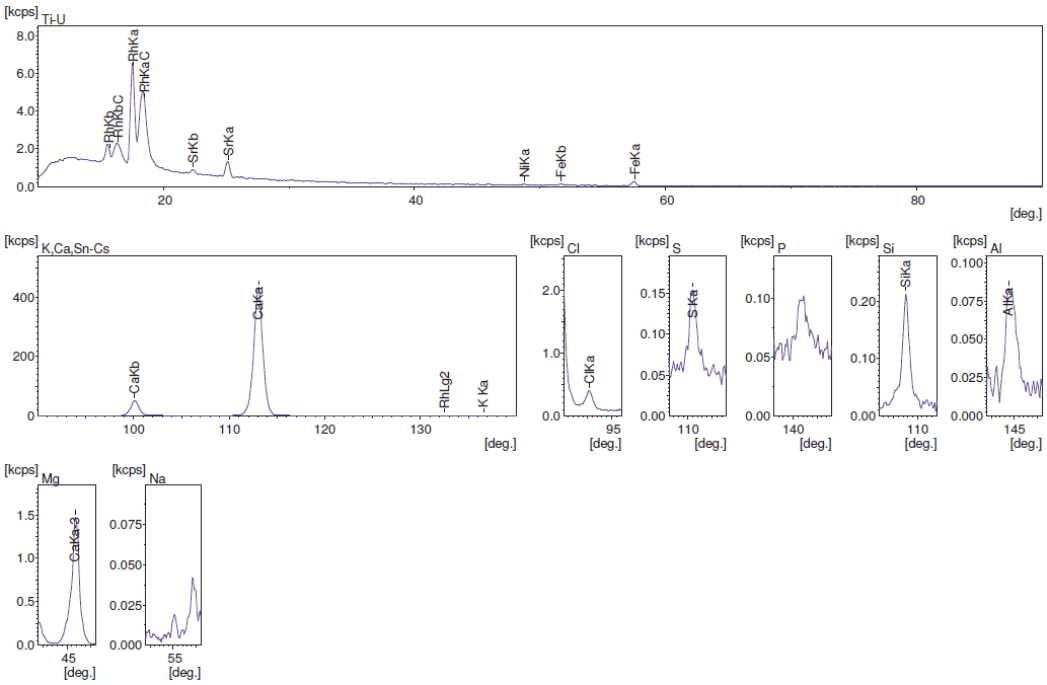

Figure E3. X-ray fluorescence spectrum of Desert Pink, DP.

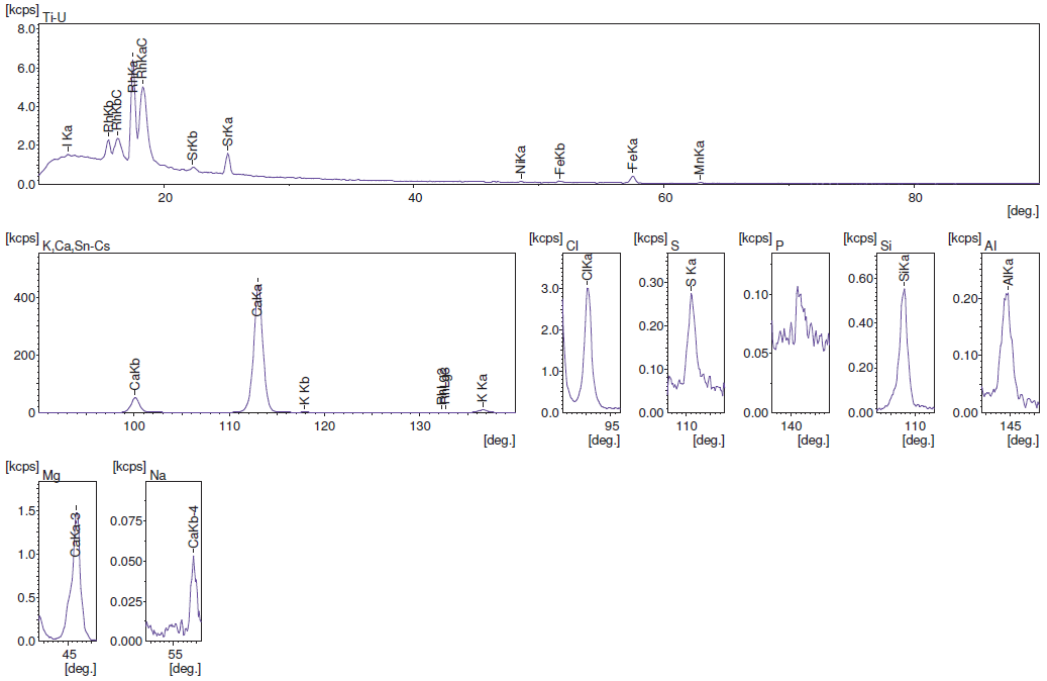

Figure E4. X-ray fluorescence spectrum of Edwards White, EDW.

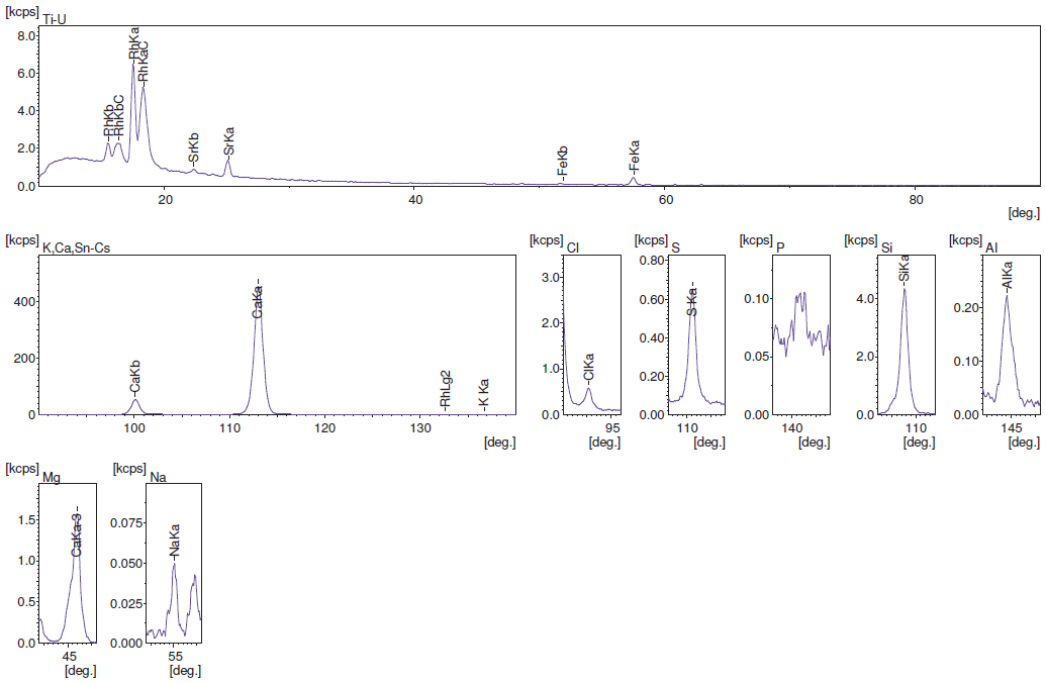

Figure E5. X-ray fluorescence spectrum of Indian Limestone, IND.

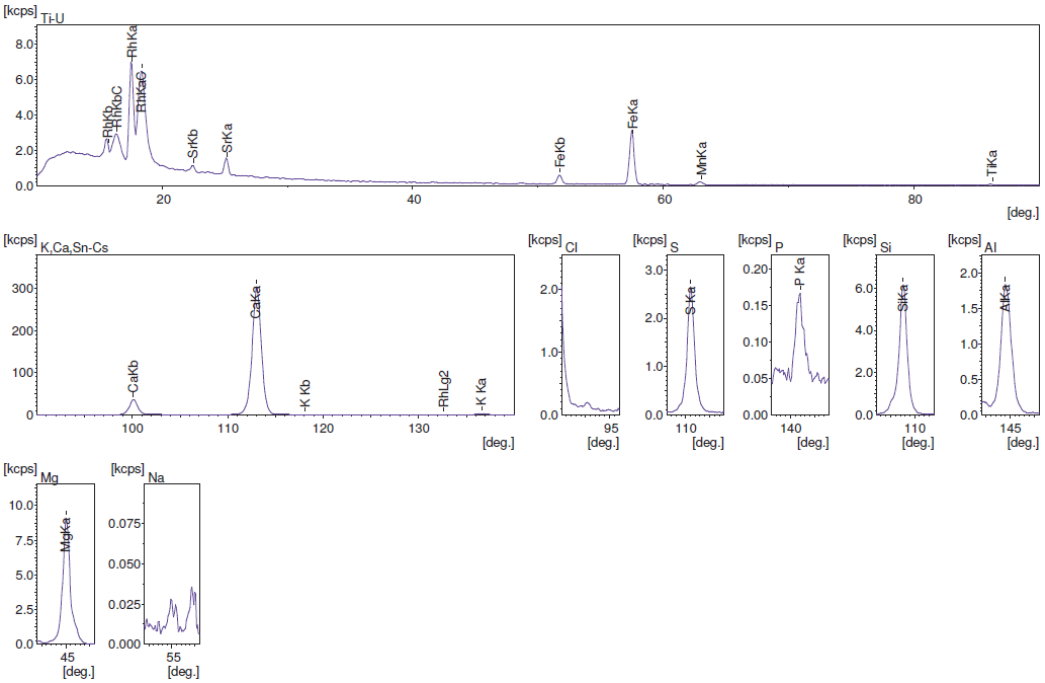

Figure E6. X-ray fluorescence spectrum of Edwards Brown, EDB.

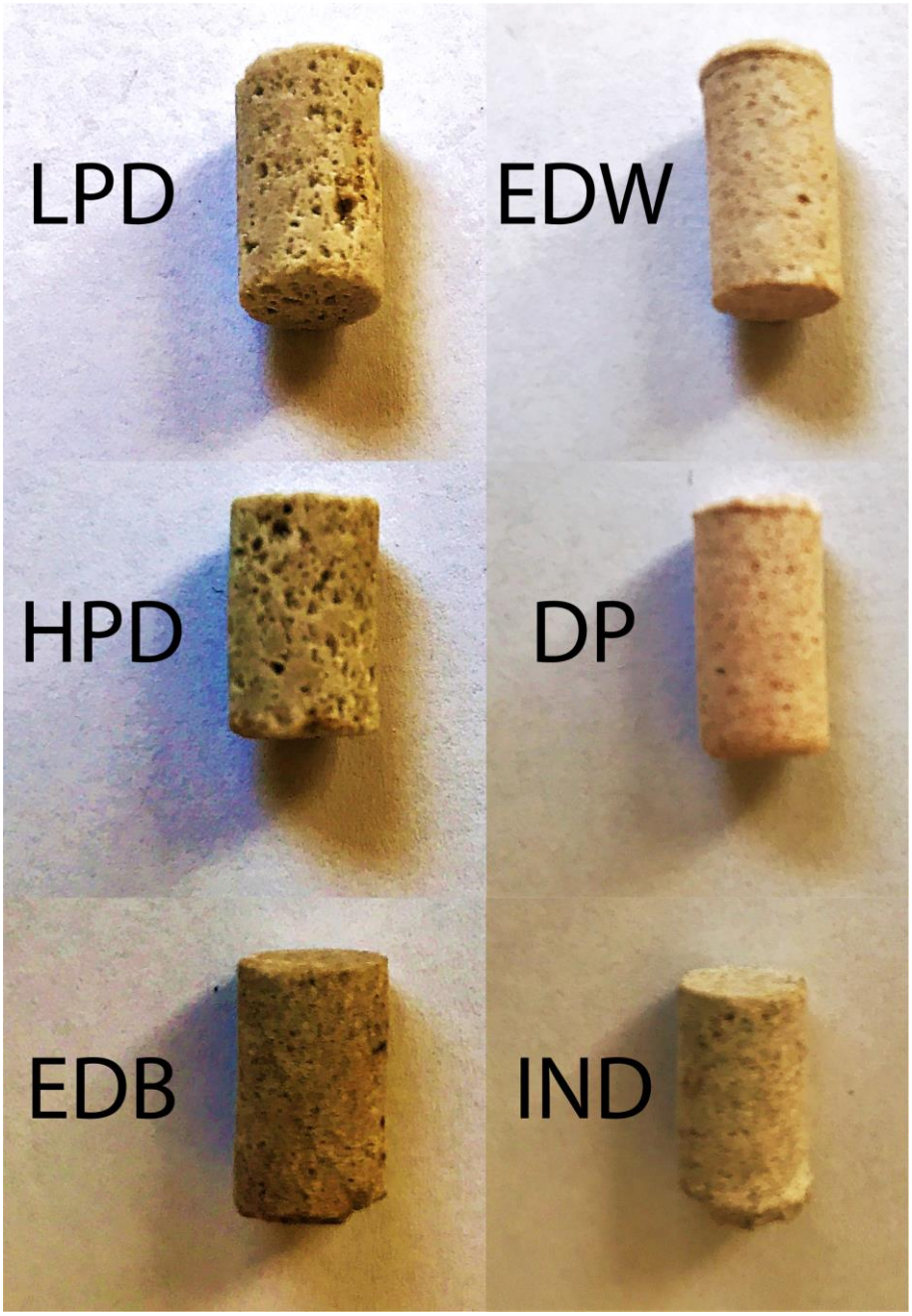

Figure E7. Photographs of the carbonate outcrops before the acid dissolution procedure.

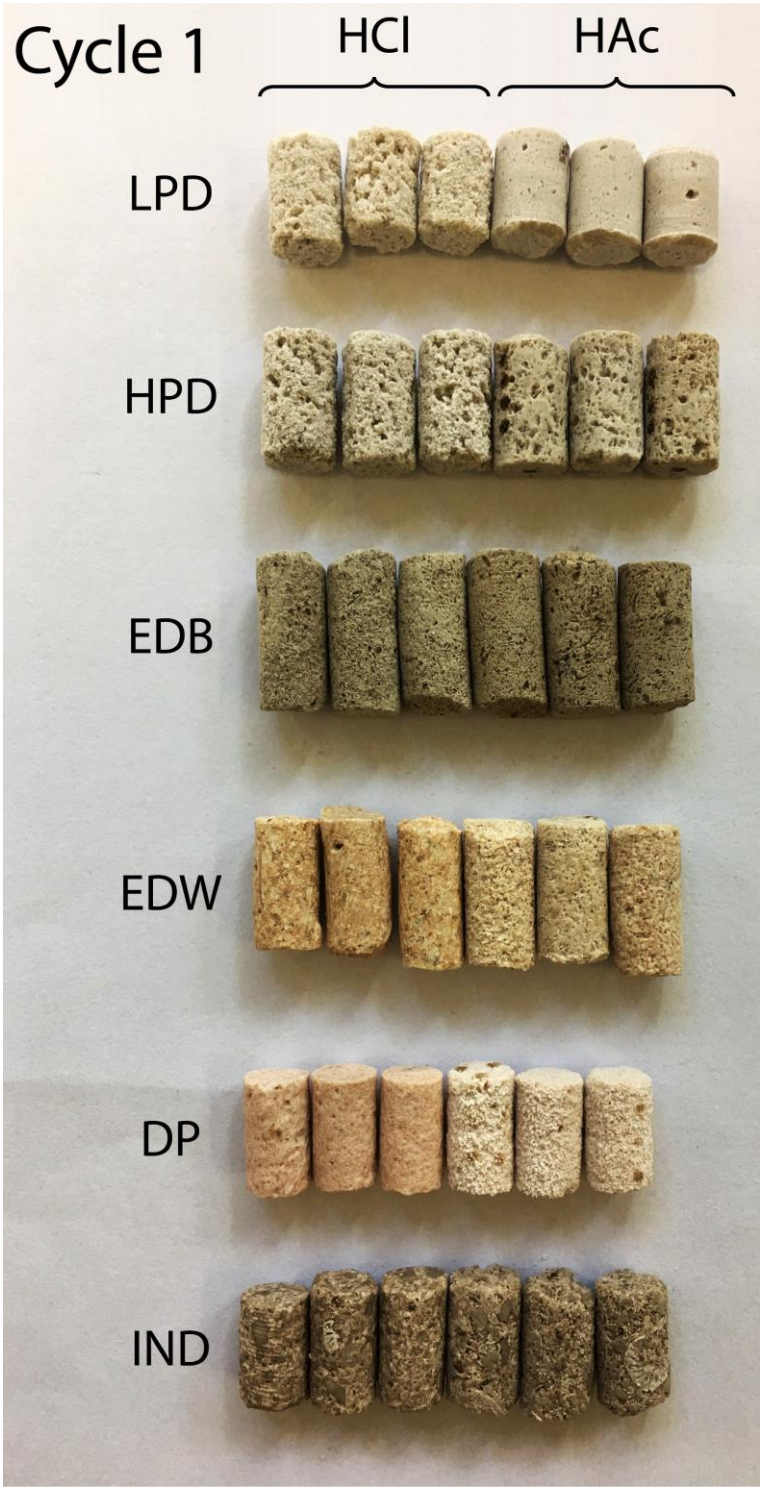

Figure E8. Photographs of carbonate outcrops after cycle 1 of acid dissolution. First three samples on the left were treated with HCl and the last three samples on the right were treated with HAc. Study was carried out in triplicate.

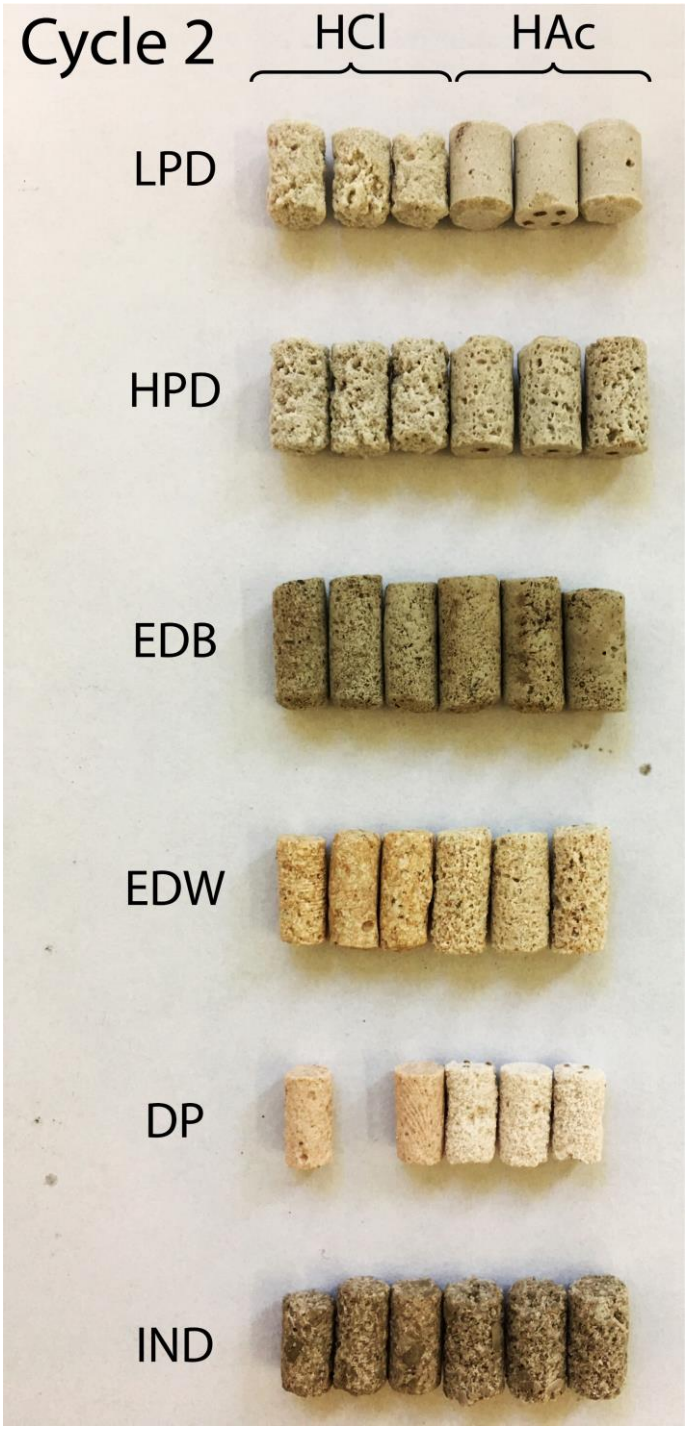

Figure E9. Photographs of carbonate outcrops after cycle 2 of acid dissolution. First three samples on the left were treated with HCl and the last three samples on the right were treated with HAc. Study was carried out in triplicate.

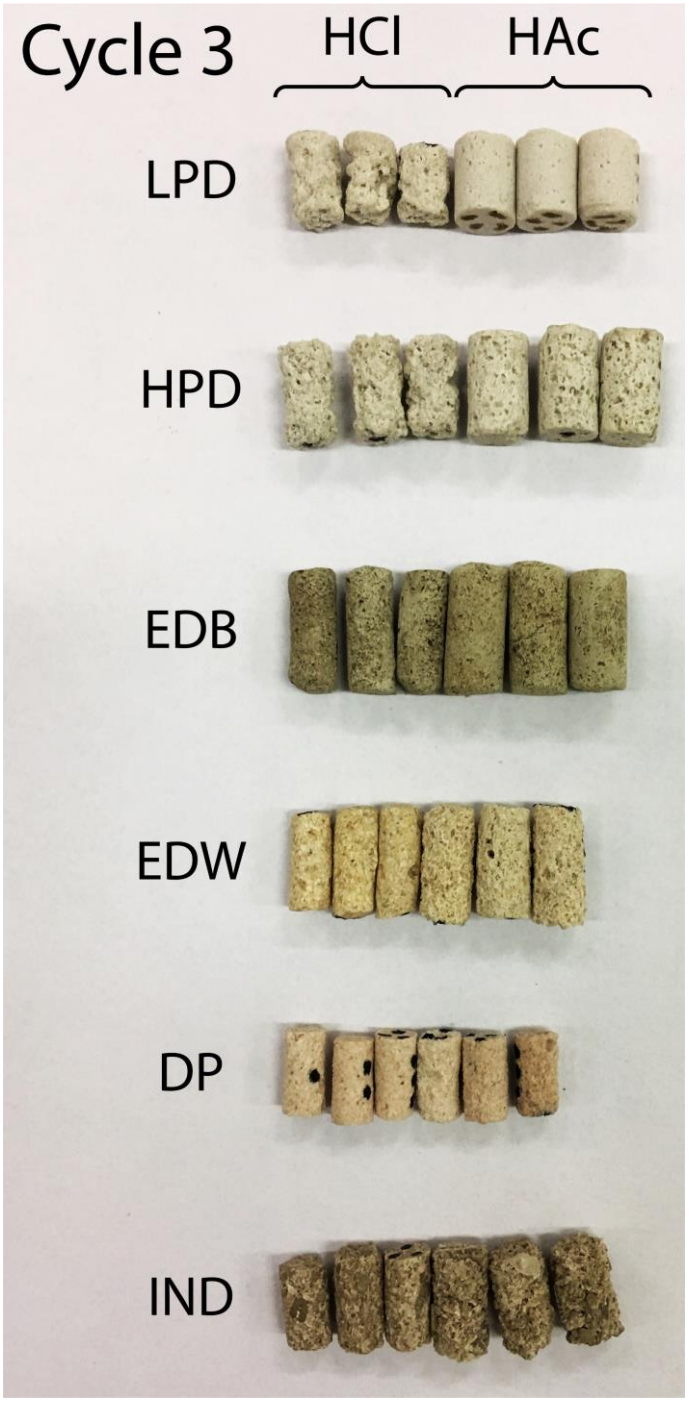

Figure E10. Photographs of carbonate outcrops after cycle 3 of acid dissolution. First three samples on the left were treated with HCl and the last three samples on the right were treated with HAc. Study was carried out in triplicate.

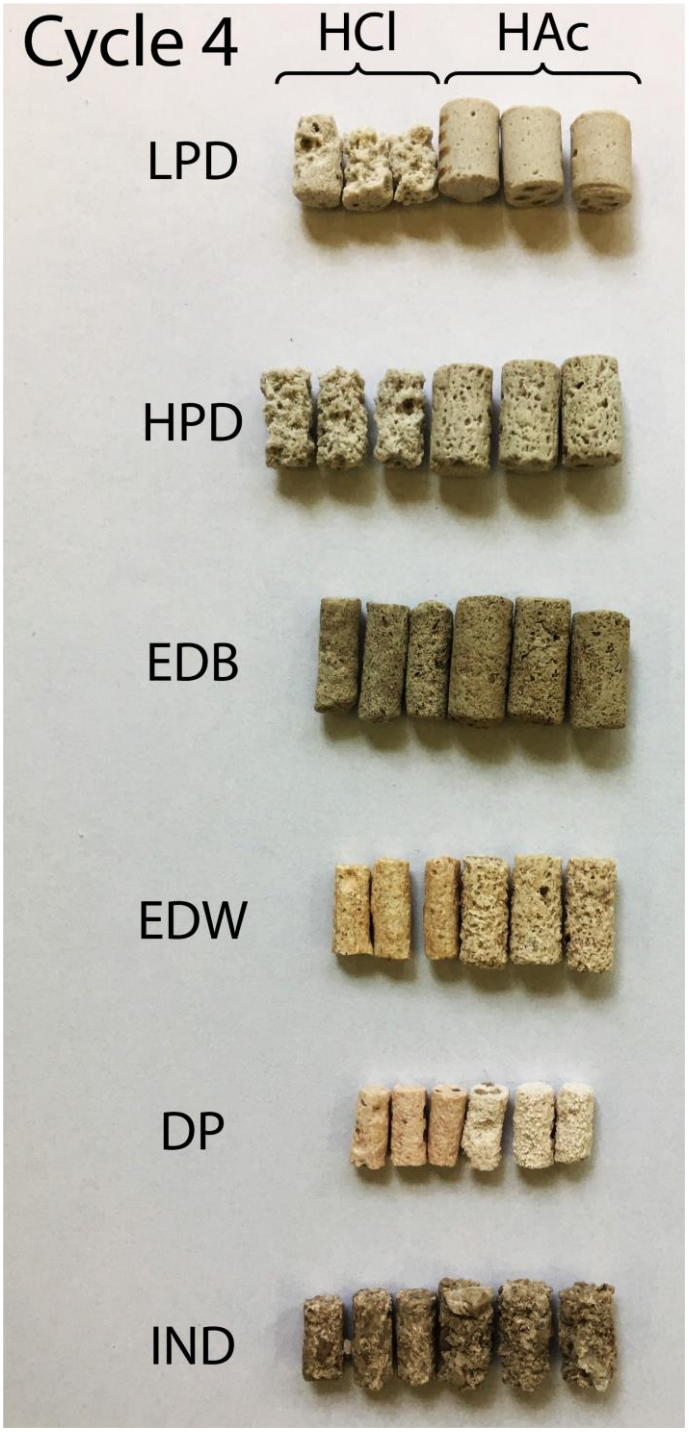

Figure E11. Photographs of carbonate outcrops after cycle 4 of acid dissolution. First three samples on the left were treated with HCl and the last three samples on the right were treated with HAc. Study was carried out in triplicate.

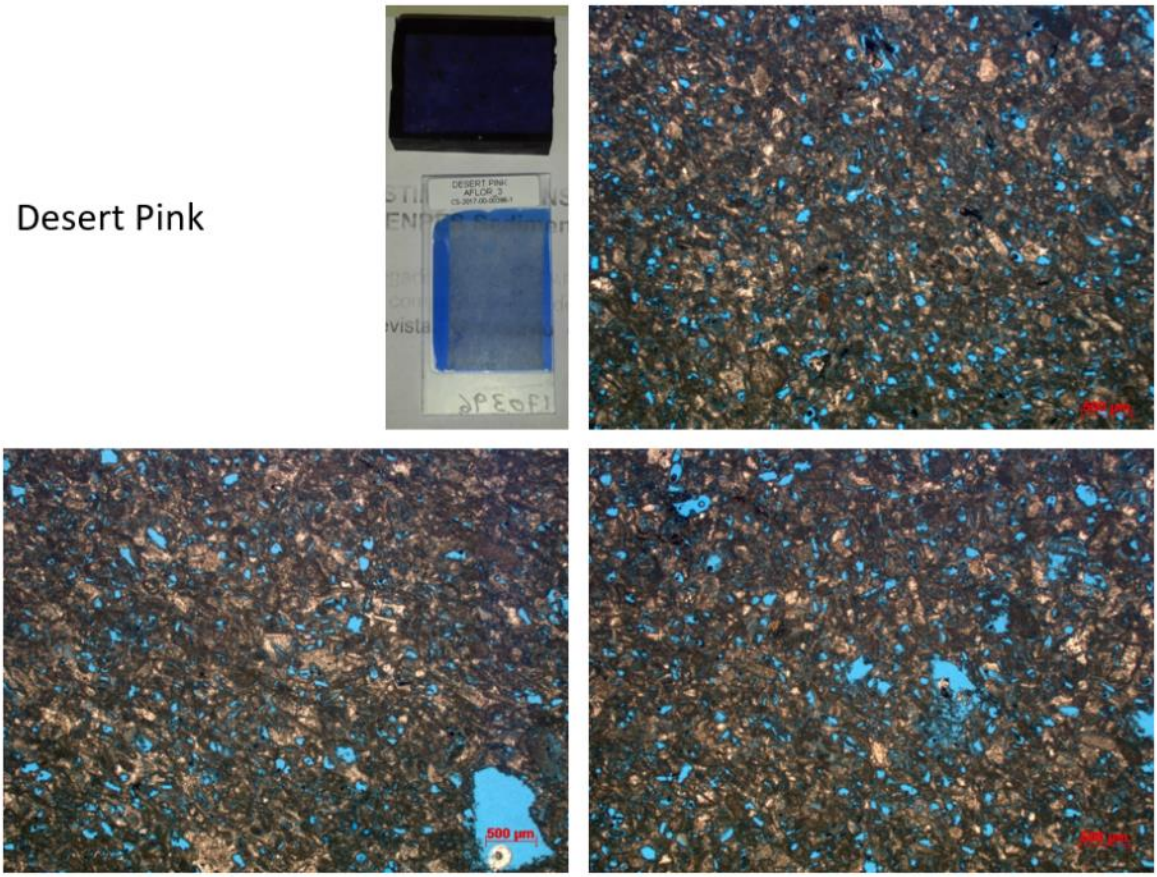

Figure E12. Microscopic images of thin sections for Desert Pink, DP. The scale pointed into the figures is for $500\ \mu m$.

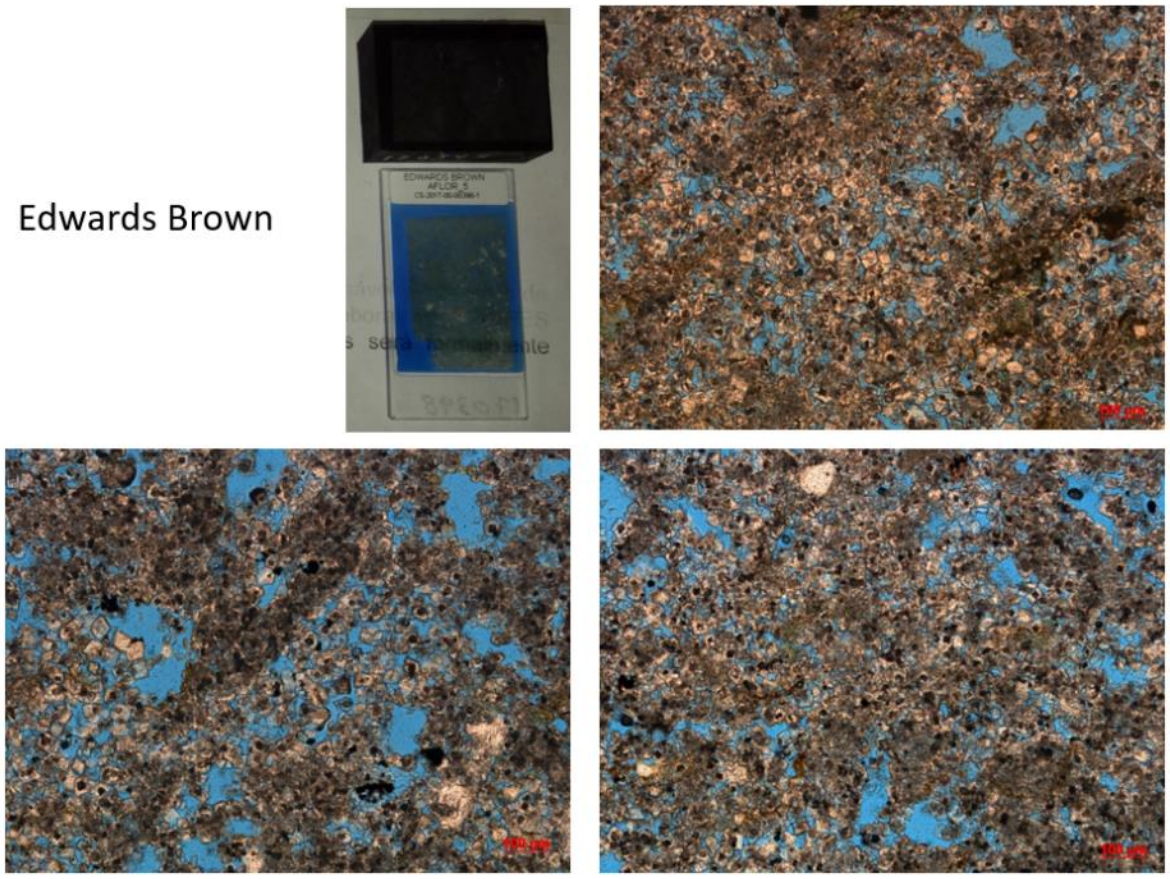

Figure E13. Microscopic images of thin sections for Edwards Brown, EDB. The scale pointed into the figures is for $500\ \mu m$.

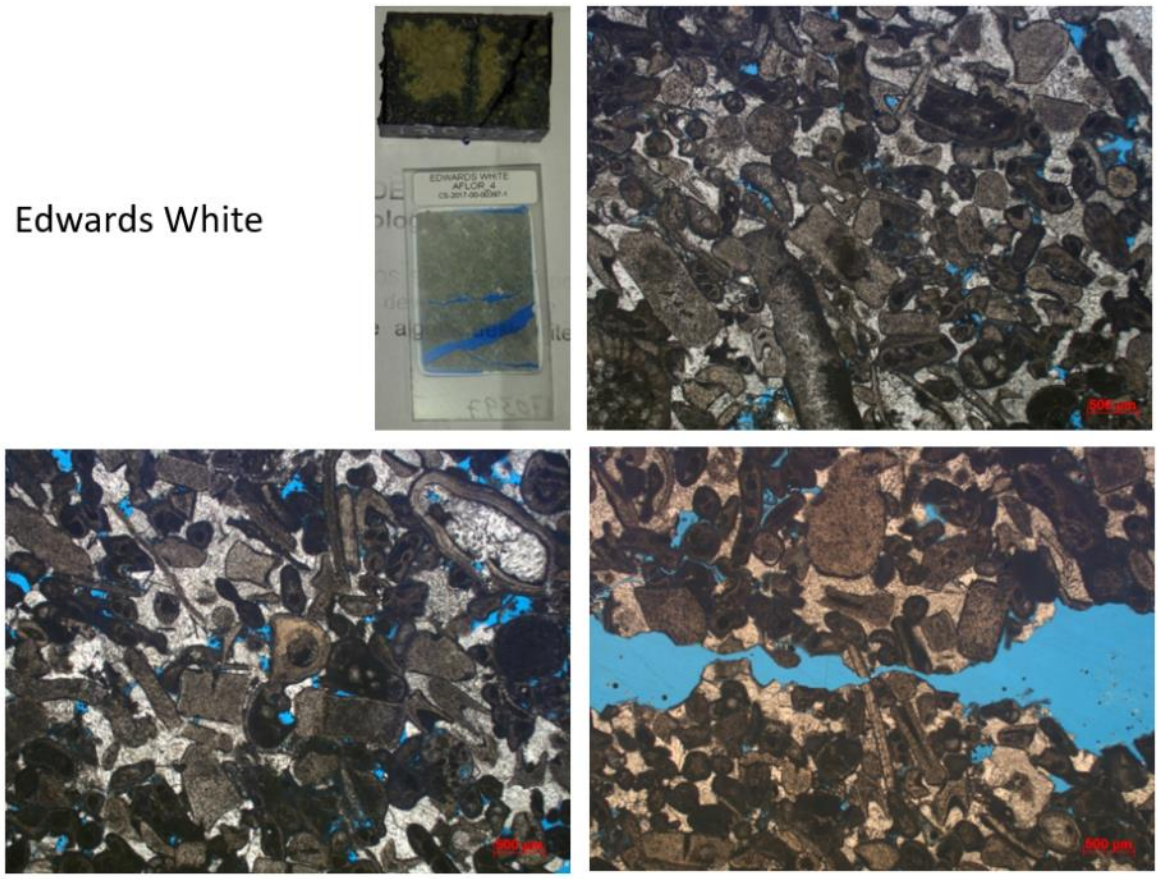

Figure E14. Microscopic images of thin sections for Edwards White, EDW. The scale pointed into the figures is for $500\ \mu m$.

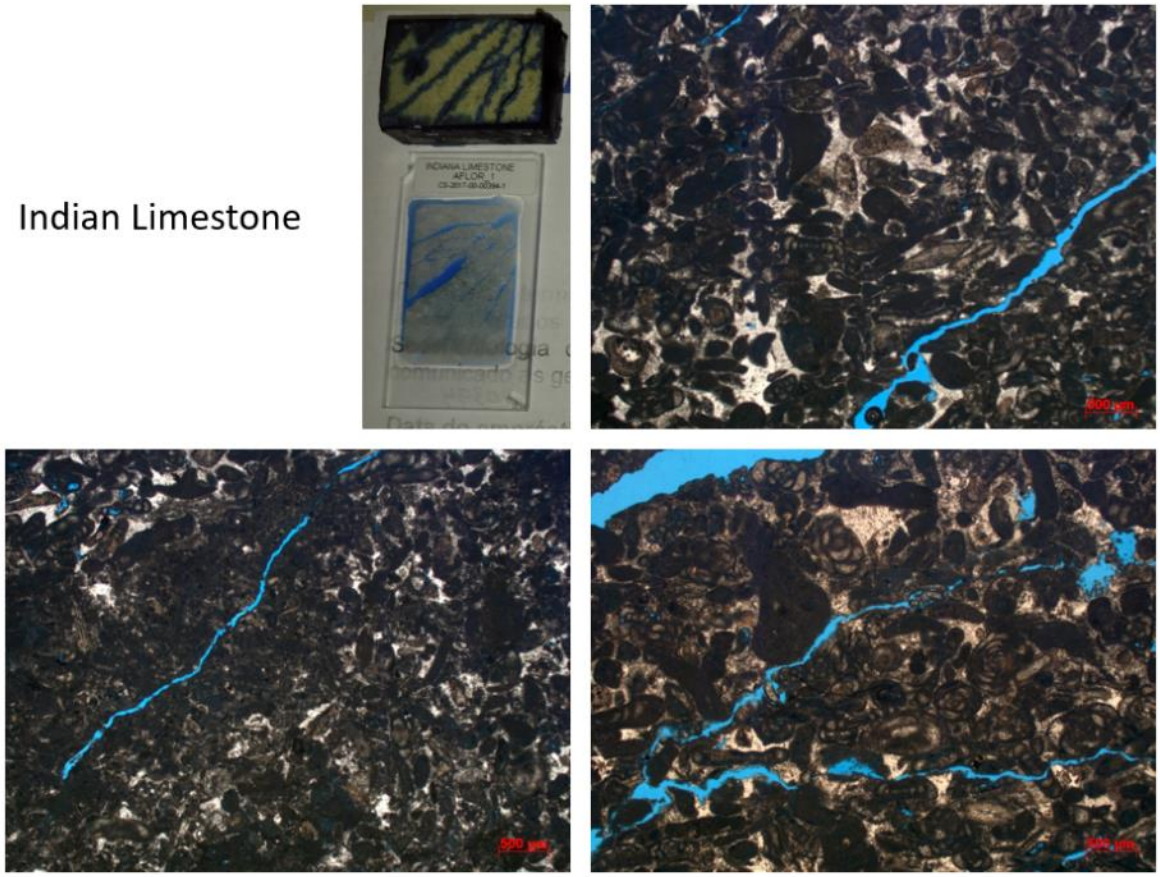

Figure E15. Microscopic images of thin sections for Indian Limestone, IND. The scale pointed into the figures is for $500\ \mu m$.

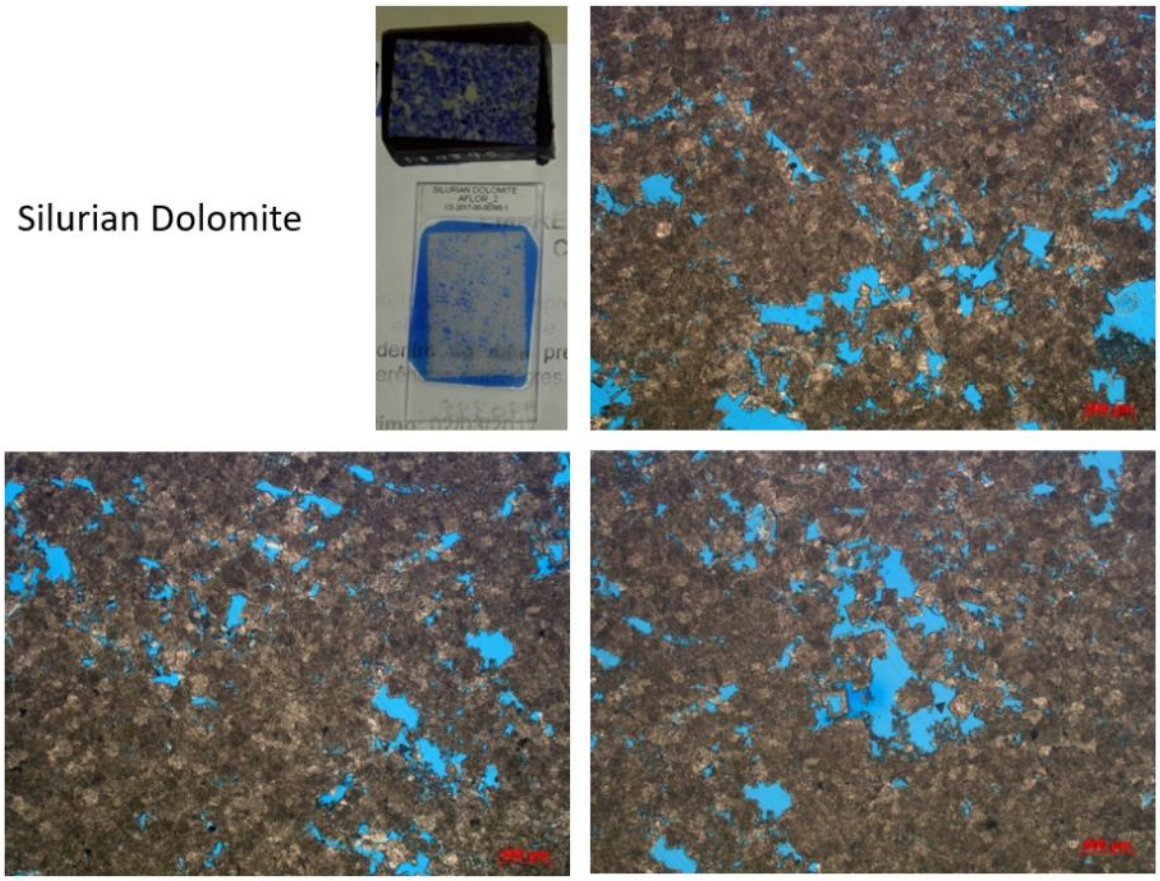

Figure E16. Microscopic images of thin sections for Silurian Dolomite. The scale pointed into the figures is for $500\ \mu m$.

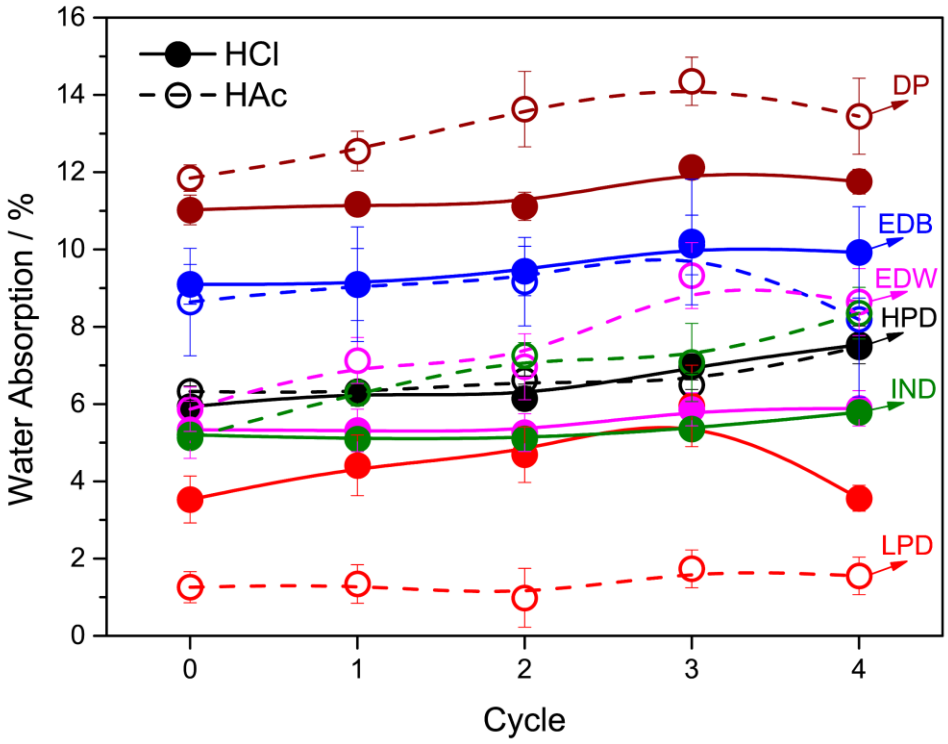

Figure E17. Amount of water incorporated as a function of the experimental cycle for each carbonate rock. Full symbols and continuous lines are for the results obtained for the samples treated with HCl and empty symbols and dashed lines for the samples treated with HAc. The color scheme is represented by the arrows and the respective abbreviations for each carbonate rock.

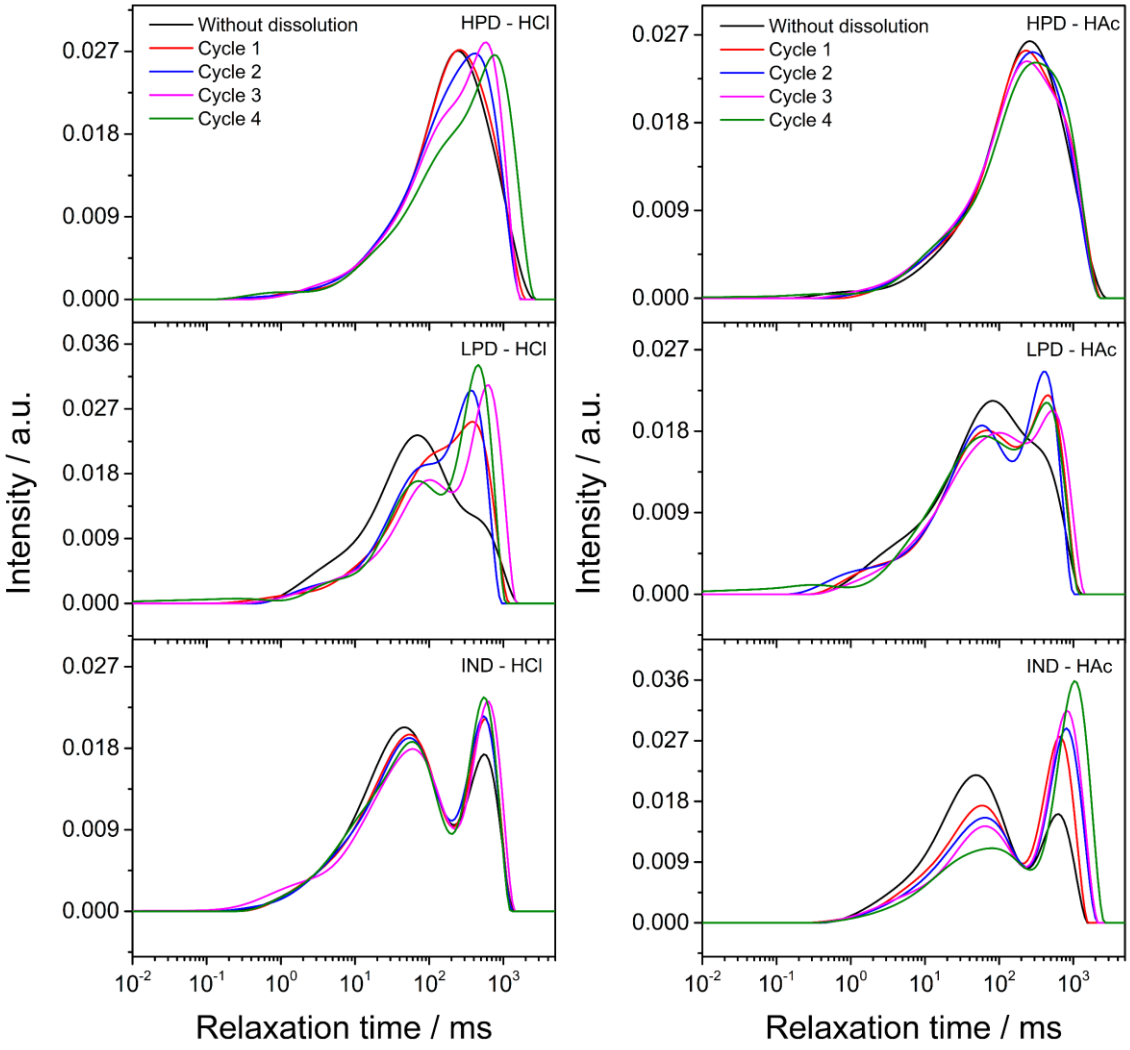

Figure E18. Transverse relaxation time distribution (T_2) after progressive cycles of acid dissolution. On the left are presented the results obtained in HCl solution and on the right are presented the results obtained in HAc. Carbonate rocks used were HPD, LPD and IND, from the top to the bottom in the image.

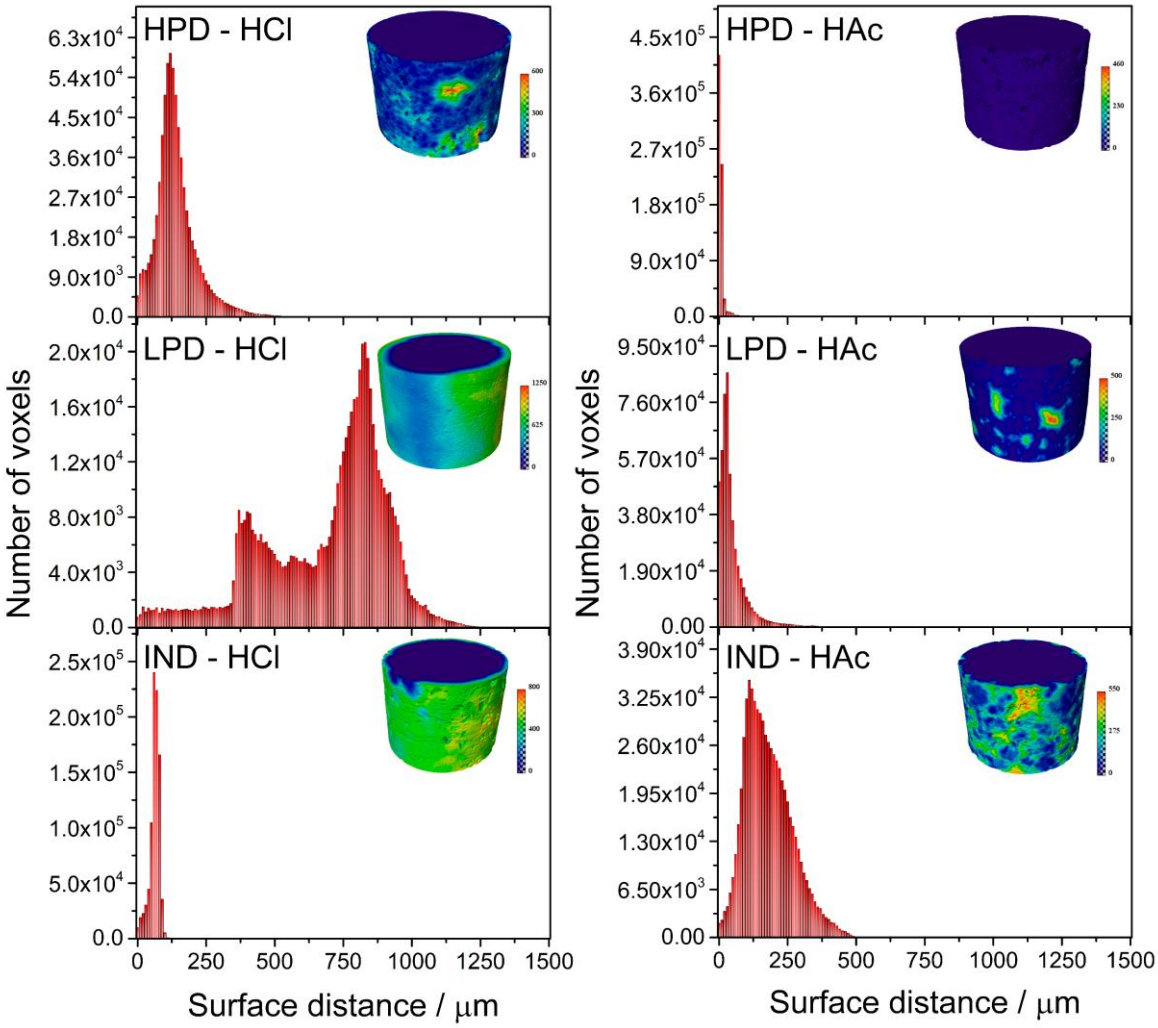

Figure E19. Heat map and points of distance between the treated surface and the original ones. On the left are presented data obtained treating the samples with HCl and on the right with HAc. From top to bottom are presented the results for HPD, LPD and IND outcrops.

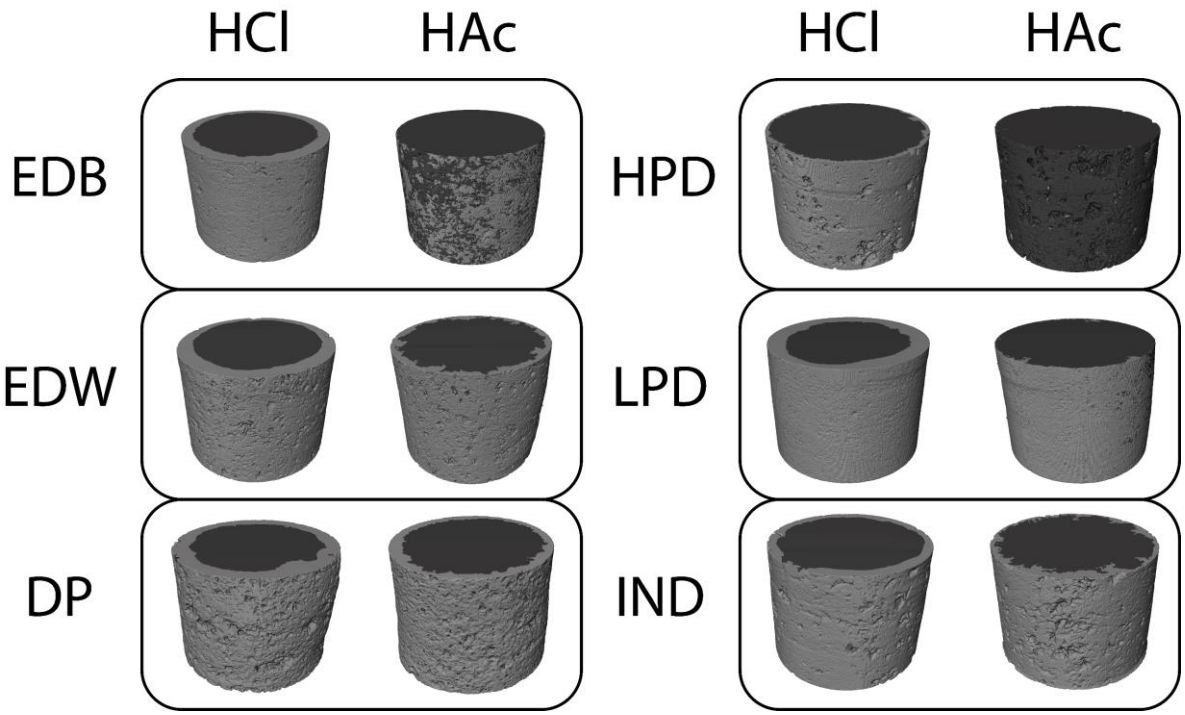

Figure E20. Micro computed tomography images obtained before and after acid dissolution. The procedures were carried out using HCl and HAc for half of t_{50}.

Appendix F Evaluation of a new formulation based on viscoelastic surfactant for acid stimulation in carbonates

Table F1. Parameters for zero-shear viscosity for the commercial diverting fluids (VES) and the different QuoVadis generations.

Acid diverting	$\eta_{0\%}$ / cP	η_{max} / cP	$\eta_{max}/\eta_{0\%}$	Neutralization at η_{max} / %	Efficiency range / %	Neutralization at phase separation / %
VES 1	17	616	36.2	60	50 – 70	70
VES 2	160,858	160,580	1.0	0	0 – 20	50
QV G1	335	1,809	5.4	40	20 – 50	60
QV G2	347	3,794	10.9	40	30 – 60	80
QV G3 A	26,264	26,264	1.0	0	0 – 10	50
QV G3 B	1,218	13,186	10.8	30	30 – 50	60
QV G3 C	32,055	66,433	2.1	10	10 – 30	60

Table F2. Parameters for $10\ s^{-1}$ for the commercial diverting fluids (VES) and the different QuoVadis generations.

Acid diverting	$\eta_{0\%}$ / cP	η_{max} / cP	$\eta_{max}/\eta_{0\%}$	Neutralization at η_{max} / %	Efficiency range / %	Neutralization at phase separation / %
VES 1	17	593	34.9	60	50 – 70	70
VES 2	888	1,065	1.2	30	0 – 30	50
QV G1	320	1,460	4.6	40	20 – 50	60
QV G2	340	2,590	7.6	40	30 – 60	80
QV G3 A	6,578	6,722	1.0	10	0 – 20	50
QV G3 B	1,049	5,004	4.8	40	30 – 50	60
QV G3 C	5,400	5,934	1.1	10	0 – 40	60

Table F3. Parameters for $100\ s^{-1}$ for the commercial diverting fluids (VES) and the different QuoVadis generations.

Acid diverting	$\eta_{0\%}$ / cP	η_{max} / cP	$\eta_{max}/\eta_{0\%}$	Neutralization at η_{max} / %	Efficiency range / %	Neutralization at phase separation / %
VES 1	17	222	13.1	60 and 70	50 – 70	70
VES 2	148	218	1.5	10	0 – 20	50
QV G1	164	400	2.4	60	20 - 60	60
QV G2	204	688	3.4	80	20 – 80	80
QV G3 A	704	911	1.3	30	20 – 30	50
QV G3 B	380	686	1.8	30	20 – 60	60
QV G3 C	644	875	1.4	60	10 – 20 and 50 – 60	60

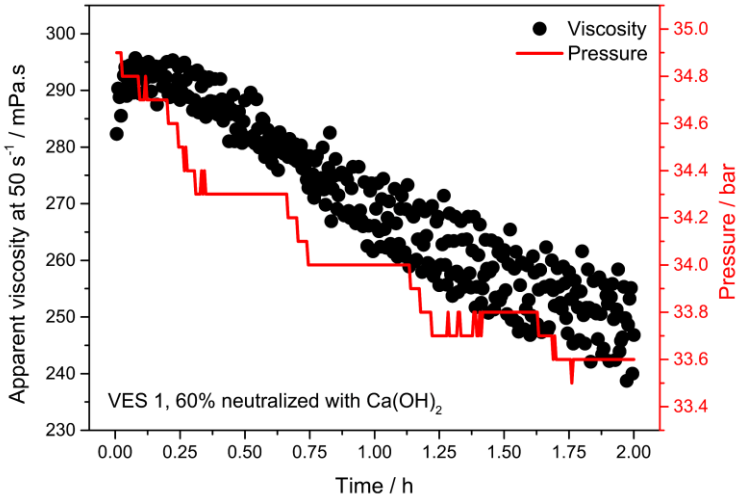

Figure F1. Apparent viscosity obtained at shear rate of $50\ s^{-1}$ for VES 1 60% neutralized with $Ca(OH)_2$ (left axis, black circles) and monitored pressure along the shear (right axis, red line) as a function of time.

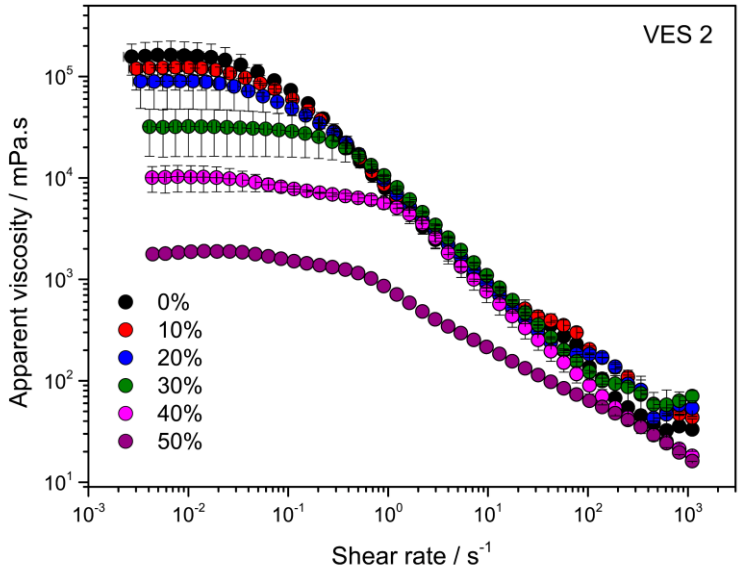

Figure F2. Flow curves, presenting the viscosity as function of the shear rate for acid VES 2 neutralized with $Ca(OH)_2$ up to 50%. Experiments were performed at $25\ °C$ and atmospheric pressure.

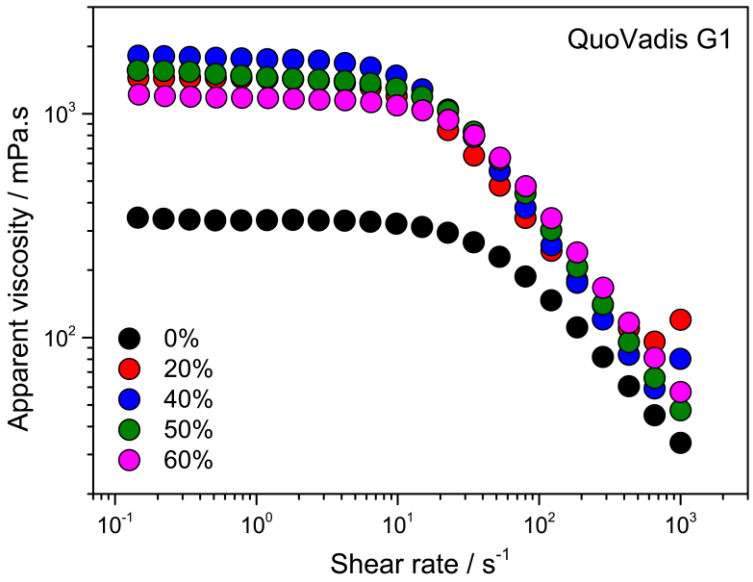

Figure F3. Flow curves, presenting the viscosity as function of the shear rate for QuoVadis G1 neutralized with $Ca(OH)_2$ up to 60%. Experiments were performed at $25\ °C$ and atmospheric pressure.

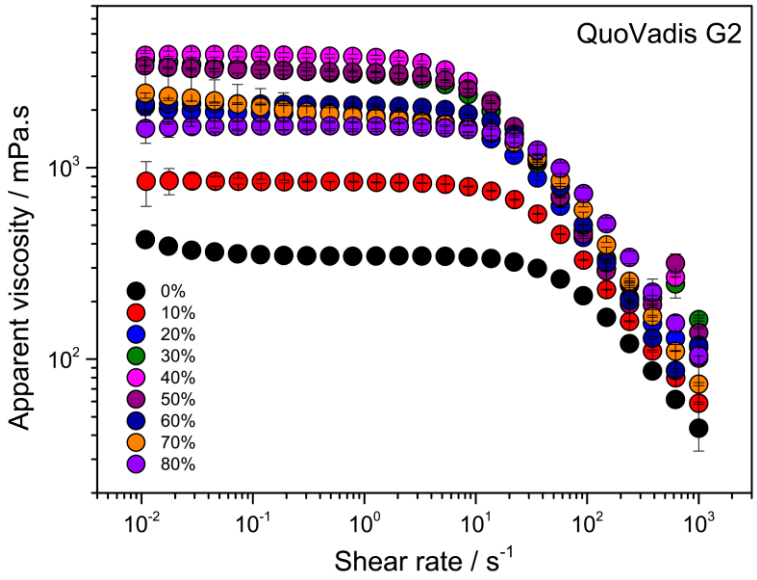

Figure F4. Flow curves, presenting the viscosity as a function of the shear rate for QuoVadis G2 neutralized with $Ca(OH)_2$ up to 80%. Experiments were performed at $25\ °C$ and atmospheric pressure.

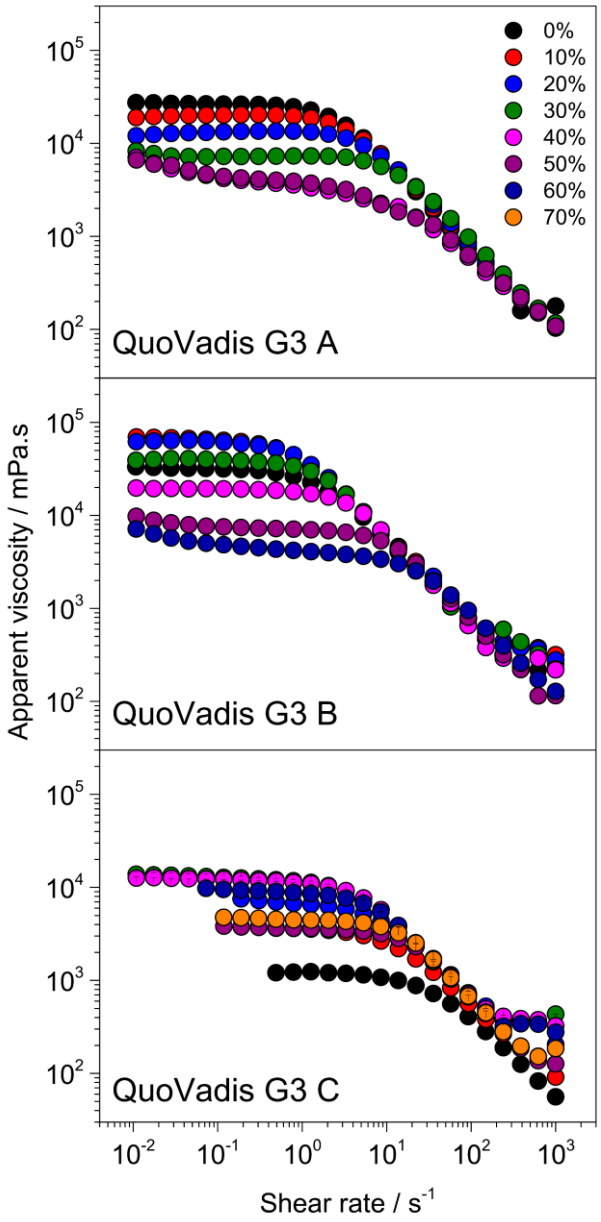

Figure F5. Flow curves, presenting the viscosity as a function of the shear rate for QuoVadis G3 and its different compositions neutralized with $Ca(OH)_2$ up to 70%. Experiments were performed at $25\ ^{\circ}C$ and atmospheric pressure.

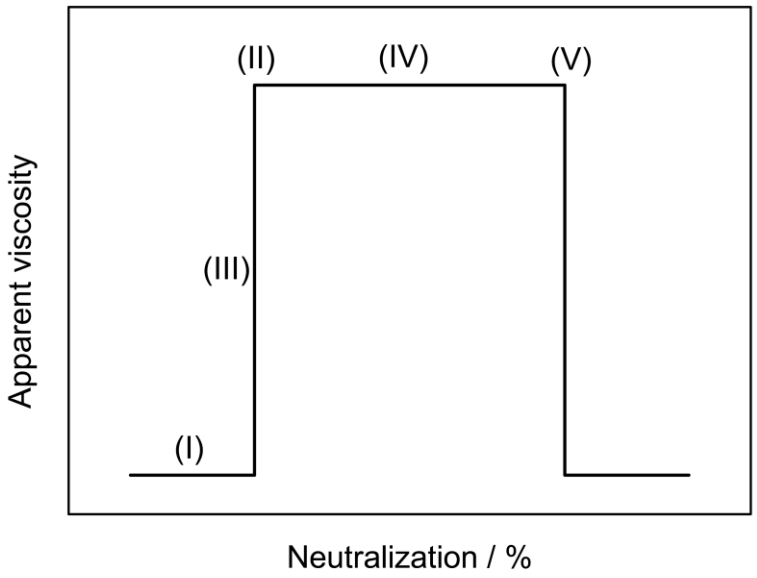

Figure F6. Illustrative scheme for an ideal diverting fluid regarding its viscosities variations as function of the neutralization percentage. Points indicated on the images are (I) the initial viscosity, prior to any neutralization; (II) maximum viscosity reached by the fluid; (III) increment in viscosity described by the ratio between the maximum viscosity and the initial viscosity; (IV) the efficiency range and; (V) the point where the viscosity starts to drop.

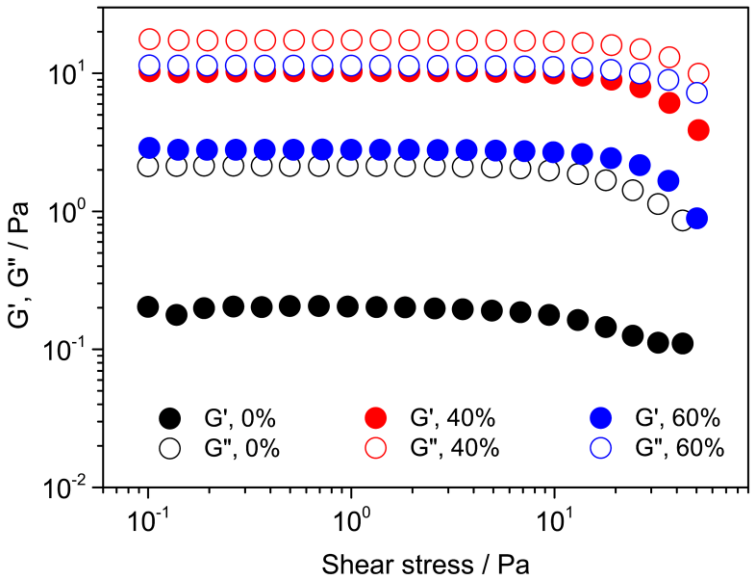

Figure F7. Oscillatory stress sweep showing G' and G" as function of the shear stress for QuoVadis G2 in 0, 40 and 60% of neutralization with $Ca(OH)_2$. Full and open symbols are for G' and G", respectively.

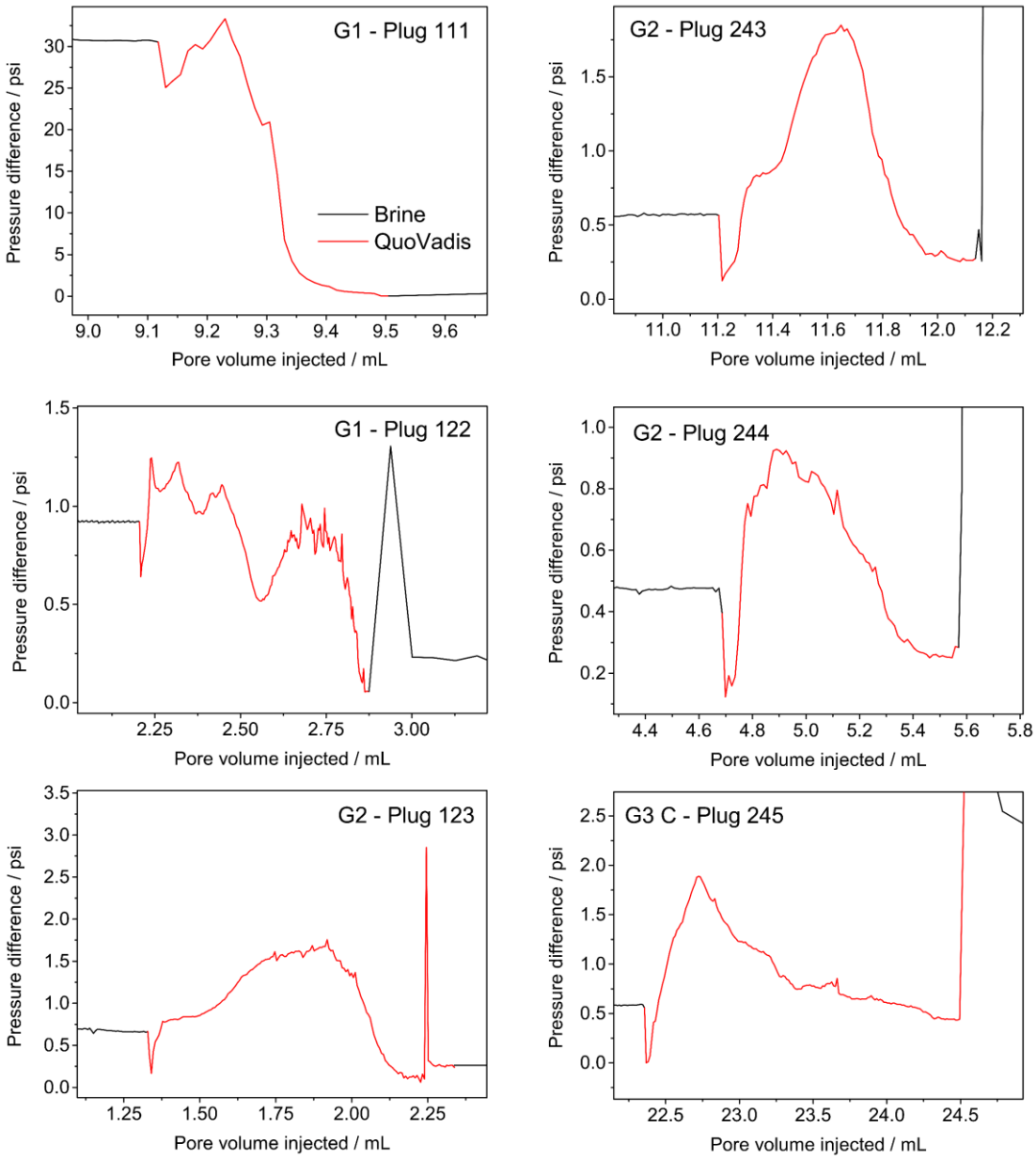

Figure F8. Core-flooding experiments carried out using QuoVadis fluids and different Indian Limestone carbonates. The QuoVadis generation and carbonate used were in each case is showed in the corner of each graph and the petrophysical properties can be found in Table 3.

Appendix G Permissions for using Figures from published articles

The files are attached below.

Copyright Clearance Center RightsLink®

Home | Help | Email Support | Manazael Jora

A systematic study of equilibrium structure, thermodynamics, and rheology of aqueous CTAB/NaNO3 wormlike micelles

Author: Matthew E. Helgeson,Travis K. Hodgdon,Eric W. Kaler,Norman J. Wagner
Publication: Journal of Colloid and Interface Science
Publisher: Elsevier
Date: 1 September 2010

Order Completed

Thank you for your order.

This Agreement between Manazael Jora ("You") and Elsevier ("Elsevier") consists of your license details and the terms and conditions provided by Elsevier and Copyright Clearance Center.

Your confirmation email will contain your order number for future reference.

Printable Details

License Number	4891340565595
License date	Aug 17, 2020

Licensed Content

Licensed Content Publisher	Elsevier
Licensed Content Publication	Journal of Colloid and Interface Science
Licensed Content Title	A systematic study of equilibrium structure, thermodynamics, and rheology of aqueous CTAB/NaNO3 wormlike micelles
Licensed Content Author	Matthew E. Helgeson,Travis K. Hodgdon,Eric W. Kaler,Norman J. Wagner
Licensed Content Date	Sep 1, 2010
Licensed Content Volume	349
Licensed Content Issue	1
Licensed Content Pages	12
Journal Type	S&T

Order Details

Type of Use	reuse in a thesis/dissertation
Portion	figures/tables/illustrations
Number of figures/tables/illustrations	1
Format	electronic
Are you the author of this Elsevier article?	No
Will you be translating?	No

About Your Work

Title	Wormlike micelles responsive to external stimuli and their applications in acid stimulation step of the oilfield industry
Institution name	University of Campinas, Brazil
Expected presentation date	Oct 2020

Additional Data

Portions	Fig. 1

Requestor Location

Manazael Jora
Rua Espanha 368

Requestor Location

SBO, 13455420
Brazil
Attn: Manazael Jora

Price

Total	0.00 USD

Tax Details

Publisher Tax ID	GB 494 6272 12

Total: 0.00 USD

CLOSE WINDOW ORDER MORE

Enthalpy measurements for the formation of salt-induced wormlike micelles using isothermal titration microcalorimetry

Author: Jie Liu,Bin Dong,Dezhi Sun,Xilian Wei,Suna Wang,Liqiang Zheng

Publication: Colloids and Surfaces A: Physicochemical and Engineering Aspects

Publisher: Elsevier

Date: 5 May 2011

Review Order

Please review the order details and the associated terms and conditions.

No royalties will be charged for this reuse request although you are required to obtain a license and comply with the license terms and conditions. To obtain the license, click the Accept button below.

Licensed Content

Licensed Content Publisher	Elsevier
Licensed Content Publication	Colloids and Surfaces A: Physicochemical and Engineering Aspects
Licensed Content Title	Enthalpy measurements for the formation of salt-induced wormlike micelles using isothermal titration microcalorimetry
Licensed Content Author	Jie Liu,Bin Dong,Dezhi Sun,Xilian Wei,Suna Wang,Liqiang Zheng
Licensed Content Date	5 May 2011
Licensed Content Volume	380
Licensed Content Issue	1-3
Licensed Content Pages	6
Journal Type	S&T

Order Details

Type of Use	reuse in a thesis/dissertation
Portion	figures/tables/illustrations
Number of figures/tables/illustrations	1
Format	electronic
Are you the author of this Elsevier article?	No
Will you be translating?	No

About Your Work

Title	Wormlike micelles responsive to external stimuli and their applications in acid stimulation step of the oilfield industry
Institution name	University of Campinas, Brazil
Expected presentation date	Oct 2020

Additional Data

Portions	Fig. 3

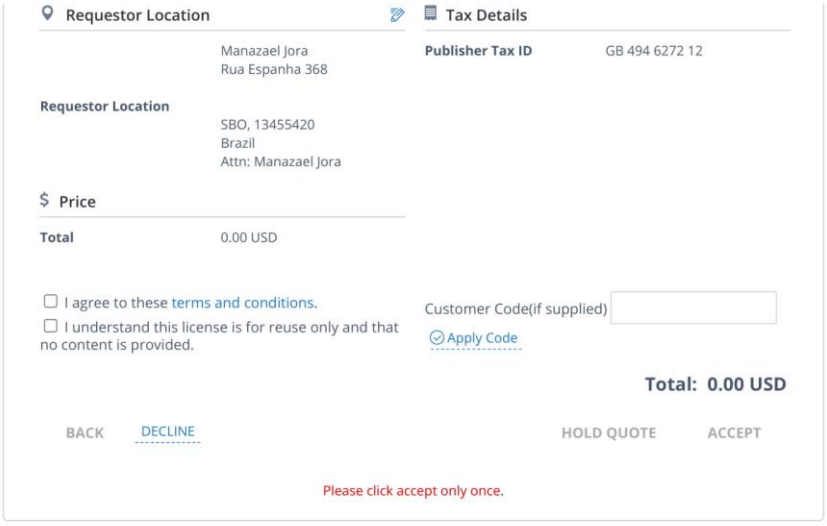

Requestor Location

Manazael Jora
Rua Espanha 368

Requestor Location

SBO, 13455420
Brazil
Attn: Manazael Jora

Price

Total 0.00 USD

Tax Details

Publisher Tax ID GB 494 6272 12

I agree to these terms and conditions.

I understand this license is for reuse only and that no content is provided.

Customer Code(if supplied)

Apply Code

Total: 0.00 USD

BACK DECLINE HOLD QUOTE ACCEPT

Please click accept only once.

Hydrophobicity of counterions as a driving force in the self-assembly process: Dodecyltrimethylammonium chloride and parabens

Author: Ana Kroflič,Bojan Šarac,Janez Cerkovnik,Marija Bešter-Rogač
Publication: Colloids and Surfaces A: Physicochemical and Engineering Aspects
Publisher: Elsevier
Date: 20 October 2014

Review Order

Please review the order details and the associated terms and conditions.

No royalties will be charged for this reuse request although you are required to obtain a license and comply with the license terms and conditions. To obtain the license, click the Accept button below.

Licensed Content

Licensed Content Publisher	Elsevier
Licensed Content Publication	Colloids and Surfaces A: Physicochemical and Engineering Aspects
Licensed Content Title	Hydrophobicity of counterions as a driving force in the self-assembly process: Dodecyltrimethylammonium chloride and parabens
Licensed Content Author	Ana Kroflič,Bojan Šarac,Janez Cerkovnik,Marija Bešter-Rogač
Licensed Content Date	20 October 2014
Licensed Content Volume	460
Licensed Content Issue	n/a
Licensed Content Pages	10
Journal Type	S&T

Order Details

Type of Use	reuse in a thesis/dissertation
Portion	figures/tables/illustrations
Number of figures/tables/illustrations	1
Format	electronic
Are you the author of this Elsevier article?	No
Will you be translating?	No

About Your Work

Title	Wormlike micelles responsive to external stimuli and their applications in acid stimulation step of the oilfield industry
Institution name	University of Campinas, Brazil
Expected presentation date	Oct 2020

Additional Data

Portions	Graphical abstract

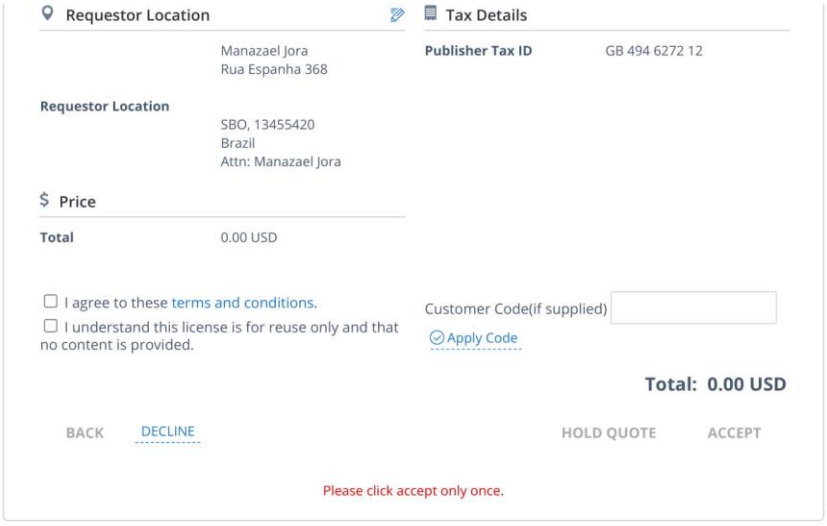

Requestor Location

Manazael Jora
Rua Espanha 368

Requestor Location

SBO, 13455420
Brazil
Attn: Manazael Jora

$ Price

Total 0.00 USD

Tax Details

Publisher Tax ID GB 494 6272 12

☐ I agree to these terms and conditions.
☐ I understand this license is for reuse only and that no content is provided.

Customer Code(if supplied)

Apply Code

Total: 0.00 USD

BACK DECLINE HOLD QUOTE ACCEPT

Please click accept only once.

Calorimetric and Light Scattering Investigations of the Transition from Spherical to Wormlike Micelles of C14TAB Triggered by Salicylate

Author: Thiago Heiji Ito, Roberta Kamei Rodrigues, Watson Loh, et al
Publication: Langmuir
Publisher: American Chemical Society
Date: Jun 1, 2015

The thermal signature of wormlike micelles

Author: Thiago Heiji Ito,Karl Jan Clinckspoor,Renato Nunes de Souza,Edvaldo Sabadini
Publication: The Journal of Chemical Thermodynamics
Publisher: Elsevier
Date: March 2016

Review Order

Please review the order details and the associated terms and conditions.

No royalties will be charged for this reuse request although you are required to obtain a license and comply with the license terms and conditions. To obtain the license, click the Accept button below.

Licensed Content

Licensed Content Publisher	Elsevier
Licensed Content Publication	The Journal of Chemical Thermodynamics
Licensed Content Title	The thermal signature of wormlike micelles
Licensed Content Author	Thiago Heiji Ito,Karl Jan Clinckspoor,Renato Nunes de Souza,Edvaldo Sabadini
Licensed Content Date	March 2016
Licensed Content Volume	94
Licensed Content Issue	n/a
Licensed Content Pages	6
Journal Type	S&T

Order Details

Type of Use	reuse in a thesis/dissertation
Portion	figures/tables/illustrations
Number of figures/tables/illustrations	1
Format	electronic
Are you the author of this Elsevier article?	No
Will you be translating?	No

About Your Work

Title	Wormlike micelles responsive to external stimuli and their applications in acid stimulation step of the oilfield industry
Institution name	University of Campinas, Brazil
Expected presentation date	Oct 2020

Additional Data

Portions	Fig. 2

Requestor Location

	Manazael Jora Rua Espanha 368
Requestor Location	SBO, 13455420 Brazil Attn: Manazael Jora

Tax Details

Publisher Tax ID	GB 494 6272 12

Price

Total	0.00 USD

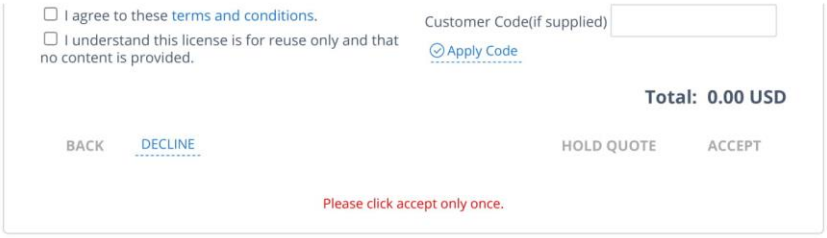

Viscosity Increase with Temperature in Cationic Surfactant Solutions Due to the Growth of Wormlike Micelles

Author: Gokul C. Kalur, Bradley D. Frounfelker, Bani H. Cipriano, et al
Publication: Langmuir
Publisher: American Chemical Society
Date: Nov 1, 2005

Copyright Clearance Center Marketplace™

Payment Details > **Review Details** > Confirmation Details

CUSTOMER INFORMATION

Billing Address

Mr. Manazael Jora
Rua Espanha 368
Sbo, 13455420
Brazil

+55 (19)981548943
manazaeljora@gmail.com

Customer Location

Mr. Manazael Jora
Rua Espanha 368
Sbo, 13455420
Brazil

PO Number (optional)

N/A

Payment options

Invoice

ORDER REVIEW

1. Soft matter

0.00 USD

ISSN	1744-6848	**Publisher**	ROYAL SOCIETY OF CHEMISTRY
Type of Use	Republish in a thesis/dissertation	**Portion**	Image/photo/illustration

LICENSED CONTENT

Publication Title	Soft matter	**Country**	United Kingdom of Great Britain and Northern Ireland
Author/Editor	Royal Society of Chemistry (Great Britain)	**Rightsholder**	Royal Society of Chemistry
Date	06/01/2005	**Publication Type**	e-Journal
Language	English	**URL**	http://www.rsc.org/Publishing/Journals/sm/index.asp

REQUEST DETAILS

Portion Type	Image/photo/illustration	**Distribution**	Worldwide
Number of images / photos / illustrations	1	**Translation**	Original language of publication
Format (select all that apply)	Print	**Copies for the disabled?**	No
Who will republish the content?	Academic institution	**Minor editing privileges?**	No
Duration of Use	Life of current edition	**Incidental promotional use?**	No
Lifetime Unit Quantity	Up to 499	**Currency**	USD
Rights Requested	Main product		

NEW WORK DETAILS

Title	Wormlike micelles responsive to external stimuli and their applications in acid stimulation step of the oilfield industry	**Institution name**	University of Campinas
		Expected presentation date	2020-10-26
Instructor name	Edvaldo Sabadini		

ADDITIONAL DETAILS

Order reference number	N/A	**The requesting person / organization to appear on the license**	Manazael Jora

REUSE CONTENT DETAILS

Title, description or numeric reference of the portion(s)	Figure 7	**Title of the article/chapter the portion is from**	2.4. Wormlike micelle fluids responsive to external stimuli
Editor of portion(s)	N/A	**Author of portion(s)**	Royal Society of Chemistry (Great Britain)
Volume of serial or monograph	N/A		
Page or page range of portion	Section 2.4	**Issue, if republishing an article from a serial**	N/A
		Publication date of portion	2020-10-26

Total Items: 1 **Total Due: 0.00 USD**

☐ I have read and accept CCC Terms and Conditions

Back

Reptation of living polymers: dynamics of entangled polymers in the presence of reversible chain-scission reactions

Author: M. E. Cates
Publication: Macromolecules
Publisher: American Chemical Society
Date: Sep 1, 1987

Linear rheology of entangled wormlike micelles

Author: Jean Francois Berret, Jacqueline Appell, Gregoire Porte
Publication: Langmuir
Publisher: American Chemical Society
Date: Nov 1, 1993

Scientific and technologic production

Published scientific articles:

(1) Jora, M. Z.; Cardoso, M. V. C.; Sabadini, E. Correlation between Viscosity, Diffusion Coefficient and Spin-Spin Relaxation Rate in 1H NMR of Water-Alcohols Solutions. J. Mol. Liq. 2017, 238, 341–346. https://doi.org/10.1016/j.molliq.2017.05.006.

(2) Jora, M. Z.; Cardoso, M. V. C.; Sabadini, E. Dynamical Aspects of Water-Poly(Ethylene Glycol) Solutions Studied by 1H NMR. J. Mol. Liq. 2016, 222, 94–100. https://doi.org/10.1016/j.molliq.2016.06.101.

(3) Jora, M. Z.; da Silva Barbosa, M.; de Alencar Simoni, J.; Sabadini, E. Solubility and Molar Enthalpy of Solution of Sucralose in H 2 O and D 2 O. Fluid Phase Equilib. 2018, 460 (15), 45–50. https://doi.org/10.1016/j.fluid.2017.12.028.

(4) de Souza, R. N.; Jora, M. Z.; Duarte, L. G. T. A.; Clinckspoor, K. J.; Atvars, T. D. Z.; Sabadini, E. A New Interpretation of the Mechanism of Wormlike Micelle Formation Involving a Cationic Surfactant and Salicylate. J. Colloid Interface Sci. 2019, 552, 794–800. https://doi.org/10.1016/j.jcis.2019.05.025.

(5) Jora, M. Z.; de Souza, R. nunes; Barbosa, T. M.; Tormena, C. F.; Sabadini, E. Probing the Formation of Wormlike Micelles Formed by Cationic Surfactant with Chlorobenzoate Derivatives. Langmuir 2019, 35 (52), 17046–17053. https://doi.org/10.1021/acs.langmuir.9b02173.

(6) Jora, M. Z.; de Souza, R. N.; Sabadini, E. Role of F, Cl, Br and I in the Wormlike Micelles Formation When Combining C14TAB with 4-Halogenbenzoates. J. Mol. Liq. 2020, 315, 113744. https://doi.org/10.1016/j.molliq.2020.113744.

(7) Souza, R. N. De; Gustavo, L.; Alves, T.; Jora, M. Z.; Dib, T.; Atvars, Z.; Sabadini, E. Thermal Behavior of Wormlike Micelles under Turbulent and Quiescent Regimes. Colloids Surfaces A 2020, 603 (June), 125271. https://doi.org/10.1016/j.colsurfa.2020.125271.

(8) Jora, M. Z.; Sabadini, E.; Raghavan, S. R. Light-Triggered Rheological Changes in a System of Cationic Wormlike Micelles Formulated with a Photoacid Generator. Langmuir 2020, acs.langmuir.0c01439. https://doi.org/10.1021/acs.langmuir.0c01439.

Patent application:

(1) Jora, M. Z.; de Souza, R. N.; da Silva Barbosa, M.; Speglich, C.; Sabadini, E. “COMPOSIÇÃO DE FLUIDO ÁCIDO DIVERGENTE PARA ESTIMULAÇÃO DE RESERVATÓRIO POR ACIDIFICAÇÃO MATRICIAL”. Process: BR 10 2020 006183 6. 2020/03/26.